
IWCN
International Workshop on Computational Nanotechnology
May 21-23, 2025
Salt Lake City, UT

Book of Abstracts

May 21st – 23rd IWCN

Conference Sponsors—Thank you!!!!

Gold: the John and Marcia Price College of Engineering, University of Utah

Silver: SILVACO

Tuesday 6-8 pm: Welcome and Tutorial

- **Tutorial:** Attracting Students to Semiconductors through Interactive Learning Experiences – a Tutorial by Gerhard Klimeck, Purdue University
- **Location**: Amphitheater

- **Welcome Reception:** hors d'oeuvres served in the Atrium

Attracting Students to Semiconductors through Interactive Learning Experiences – a Tutorial

Gerhard Klimeck*
Purdue University, Network for Computational Nanotechnology, West Lafayette, IN 47907, USA
*e-mail: gekco@purdue.edu

Semiconductor supply chain and security concerns have sparked a global race to re-shore semiconductor manufacturing. Projections indicate a shortage of 42,000 engineers in the U.S. who can architect, design, manufacture, and test chips [1]. These engineering functions are encapsulated in a complex modeling and simulation tool chain that extends from atoms to systems. The high barrier of entry into the field is evident, as we are not attracting and retaining enough students and we never truly use any of these tool chains for teaching. Many groups propose refining lectures and textbooks and hosting them on the web. However, I believe this approach is not much better than the VCR-taped lectures I experienced 30+ years ago. Instead, I advocate for interactive, immersive, project-driven learning to truly attract students into the field. In this tutorial, I will present several aspects of this approach.

nanoHUB has made device and materials modeling more accessible by offering Apps powered by advanced simulation engines in the nanoHUB cloud. Over 84,573 students have used these tools in 4,247 courses at 404 institutions. Overall we have identified clustered user behavior in 141,877 users at 1,448 institutions. The nanoHUB team initially developed user behavior analytics to demonstrate to NSF that scientific Apps in the cloud can be effectively used in education. This capability now guides educational design and provides feedback to faculty members.

A typical course in semiconductor devices follows a sequence that includes crystals, quantum mechanics, band structure, semi-classical carrier statistics, 1D drift diffusion models, PN junctions, bipolar junction transistors, MOS capacitors, and MOSFETs. nanoHUB offers numerous Apps and tools for these concepts, leading faculty to request recommendations. In response, Dragica Vasileska (ASU), student Xufeng Wang and I developed ABACUS [3], which consolidates these tools. As of January 2025, over 74,500 users from more than 1,690 institutions have utilized ABACUS and its constituent Apps. This tutorial will demonstrate several of the ABACUS and related tools.

Beyond ACACUS I also plan to share how I restructured the graduate level Semiconductor Device Fundamentals course in Electrical and Computer Engineering at Purdue University. I believe that this can be translated or adopted towards undergraduate students and even be introduced into first year engineering.

The course restructuring has been influenced by my personal learning experiences and observations of my students. I categorize students into two groups: the mathematically driven learners (which includes my younger self) and the hands-on, practical learners (reflecting my experience as a researcher and developer). As a mathematically inclined student, I could solve all the analytical problems presented to me. However, I realized that I lacked a "physical feeling" for concepts like the Fermi level or a degenerate semiconductor.

On the other hand, the practical learners, especially those in my online classes who are often full-time working engineers, struggle with math and physics. For them, traditional derivations and explanations completely fail to convey physical meaning. To address this, I replaced traditional exams with hands-on projects that provide real-world design experiences and enhance device understanding. There are 2 projects involving Quantum Dot Design and nanowire transistors. Both types of learners finish the course with a much better grasp of the subject matter. I hope to inspire others to adopt similar changes in their courses.

I would like to thank nanoHUB Technical Director Dr. Daniel Mejia for many discussions and amazing tool and analytics developments.

[1] www.semiconductors.org/chipping-in-sia-jobs-report/
[2] N K Madhavan, M Zentner, G Klimeck, "Learning and research in the cloud", *Nature Nano* 8, 786– (2013)
[3] X Wang, et al (2021), "ABACUS …," https:// nanoHUB .org/resources/abacus. (DOI: 10.21981/YYFZ-7868).
[4] Usage data: https://nanohub.org/dashboards/abacus

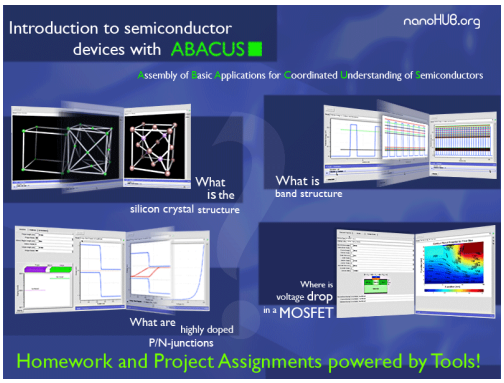

Fig. **1**. ABACUS splash screen highlighting typical semiconductor course topics from crystals to MOSFETS.

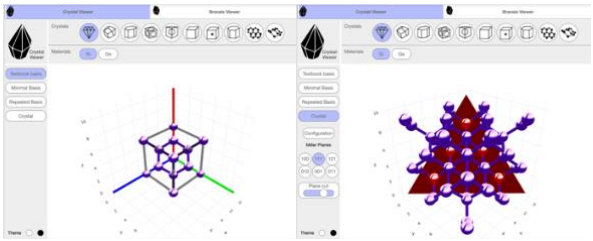

Fig. 2. Crystal viewer screen shots. (left) textbook unit cell that can be rotated. (right) crystal chunk with a Miller plane.

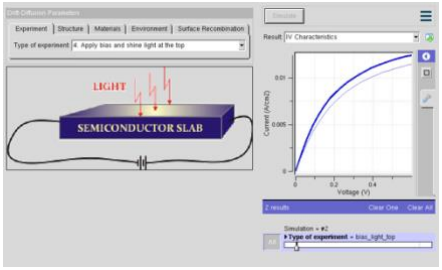

Fig. 3. Drift Diffusion Lab. Users can explore how illumination of a semiconductor increases the current and separates the hole and electron distribution across the device.

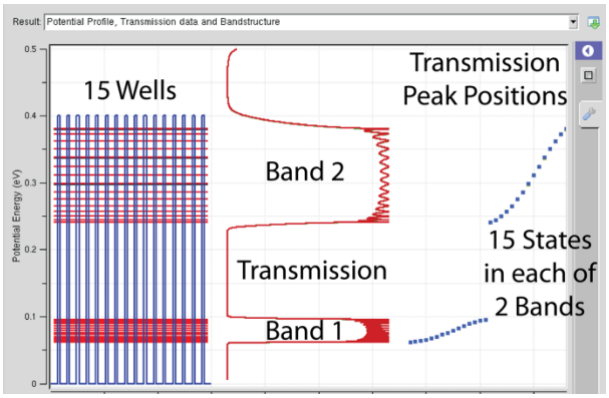

Fig. 4. How many atoms does it take to get bandstructure? Users can vary the number of barriers/wells and observe band formation visualized by transmission through barriers. The peak positions clearly identify the bands. Electrical engineers can relate to a band-pass filter.

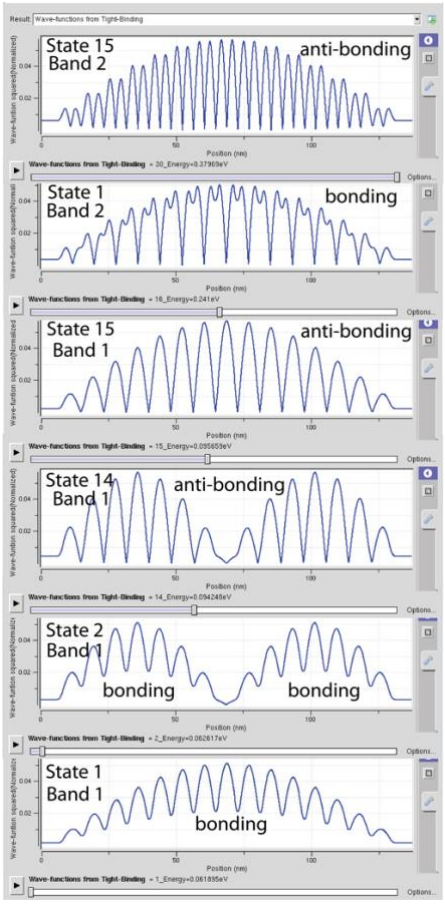

Fig. 5. Wavefunctions of the states in Figure 4 in a system of 16 barriers and 15 wells. The fist 15 states form a band. State 1 is the ground state of a particle in a box consistent of 15 "atoms". State 2 has two lobes. The states at the top of the band (typical valence bands) have the same envelopes as the bottom states but are anti-bonding. The concept of Bloch states emerges naturally.

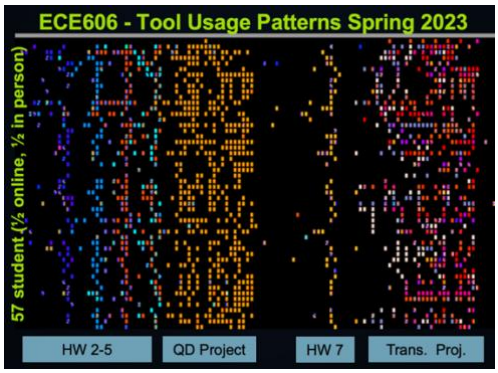

Fig. 6. Tool usage pattern of Purdue's ECE606 class in the spring of 2023. Dots indicate tool use on a specific day (horizontal axis) by the 57 class members who are vertically stacked. Dot colors designate a tool. The Quantum Dot (QD) Project spans several weeks. The nanowire transistor design project involves several different tools ranging from classical transport to fill atomistic quantum transport.

Wed. 9-10:30 Phonons I

Time	Type	Presenter	Title
9:05-9:35	**Invited**	Laura de Sousa Oliveira	Super-suppression of Long Mean-free-path Phonons in Nanoporous Silicon
9:35-9:50	Contributed	Sandip Dhruba	Investigation of thermal transport and dislocations in lattice-matched InGaAs/InAlAs superlattices by nonequlibrium molecular dynamics simulations
9:50-10:05	Contributed	Md Mobinul Haque	Thermal Conductivity of Nanowires : Machine Learning and Monte Carlo Insights
10:05-10:20	Contributed	Oreoluwa Adesina	Evaluating Thermal Transport at The Axial Junction of Si-Ge Composite Nanowires
10:20-10:35	Contributed	Shunda Chen	Impacts of Short-range Order on Thermal Conductivity of GeSn and Si-Ge-Sn Alloys

Super-suppression of Long Mean-free-path Phonons in Nanoporous Silicon

L. de Sousa Oliveira*, A. Davies*, N. Neophytos†, P. A. Greaney‡, S. A. Hosseini‡, I. Dickey‡
*Department of Chemistry, University of Wyoming, Laramie, WY 82071, USA
†School of Engineering, University of Warwick, Coventry CV4 7AL, UK
†Department of Mechanical Engineering, University of California Riverside, Riverside, CA 92521, USA
e-mail: Ldesousa@uwyo.edu

ABSTRACT

In 2020, using equilibrium molecular dynamics simulations, we identified specific nanoporous geometries that create narrow constrictions in the passage of phonons, leading to anticorrelated heat fluctuations [1]. These geometries were found to lower phonon transport to levels below the characteristic scattering length defined by the pore spacing, leading to a decrease in thermal conductivity by as much as 80% beyond what Matthiessen's rule would predict. Adjusting the size and arrangement of the pores offers control over phonon transport in these materials. In more recent work, we probed the nature of this phonon "super-suppression" with wavepacket molecular dynamics simulations [2], analyzed resonances in the power spectrum of the heat current autocorrelation function (HCACF), and developed an equilibrium ray tracing Monte Carlo model to help explain the observed anticorrelations in the heat flux of the porous geometries [3]. This model allowed us to detect the distinctive signatures that different types of correlated scattering leave in the HCACF, thereby clarifying the conditions required for diffusely scattered phonons to cancel their heat flow. With this model, we identified a region of experimentally accessible geometries likely to exhibit super-suppressed phonon transport.

MOTIVATION

Thermoelectric applications require materials to be thermally insulating and electrically conducting. In typical semiconductor materials, the majority of the heat is carried by long mean free-path phonons, which generally correspond to long wavelengths. Nanostructuring offers a route for minimizing thermal conductivity, and incorporating nanopores is a frequent nanostructuring technique. Nanoscale pores have been shown to significantly reduce phonon thermal transport in materials, often causing only minimal degradation to electron transport, which is ideal for thermoelectric applications. A comprehensive molecular dynamics study examining the role of geometry, such as pore size, shape, and distribution, in nanoporous silicon [4], led to the discovery of the examined unusual porous geometries with exceptionally low thermal conductivities.

METHODS

This study utilized molecular dynamics, non-equilibrium Green's function, and ray tracing Monte Carlo simulations. Thermal transport was evaluated within equilibrium molecular dynamics (MD) using the Green-Kubo method, and non-equilibrium MD wave packets generated from atom displacement and velocity profiles based on plane waves. The ray-tracing scheme was developed to simulate the trajectories of phonons undergoing diffuse elastic backscattering and compute their HCACF.

REFERENCES

[1] L. de Sousa Oliveira, S. A. Hosseini, P. A. Greaney, N. Neophytou, *Heat current anticorrelation effects leading to thermal conductivity reduction in nanoporous Si*, Physical Review B, 102 (2020), 205405.

[2] S. A. Hosseini, A. Davies, I. Dickey, N. Neophytou, P. A. Greaney, L. de Sousa Oliveira, *Super-Suppression of Long Phonon Mean-Free-Paths in Nano-Engineered Si due to Heat Current Anticorrelations*, Materials Today Physics 27 (2022): 100719.

[3] P. A. Greaney, S. A. Hosseini, L. de Sousa Oliveira, A. Davies, and N. Neophytou, *Super-suppression of long wavelength phonons in constricted nanoporous geometries*, Nanomaterials 14.9 (2024): 795.

[4] L de Sousa Oliveira, N. Neophytou. *Large-scale molecular dynamics investigation of geometrical features in nanoporous Si*, Physical Review B 100.3 (2019): 035409.

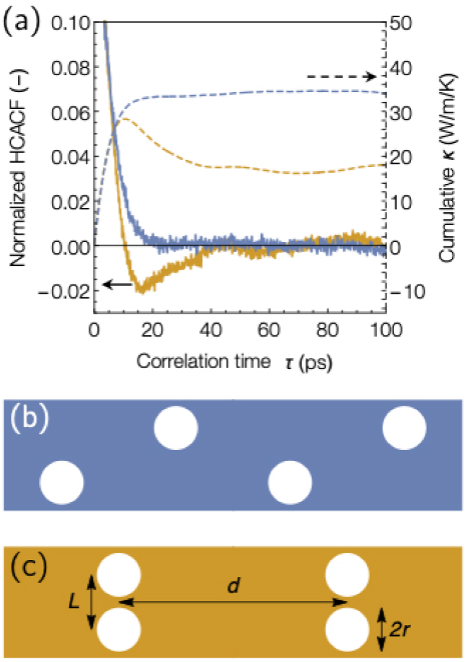

Fig. 1. Plot (a) shows the HCACF (solid lines, left-hand axis) and HCACF integral (dashed lines, right-hand axis) with the color-coding corresponding to the two porous geometry arrangements shown in (b) and (c). Both geometries have identical porosity, but the pores are offset in the blue geometry and stacked in the orange geometry. Figure adapted from [2].

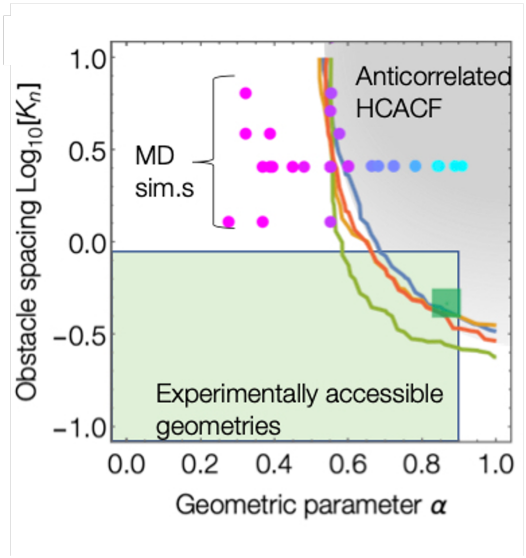

Fig. 2. The green-shaded region indicates geometries that can be experimentally accessed through fabrication methods. The green square represents pores with a 65 nm radius, arranged in a rectangular grid with long and short spacings of 400 nm and 150 nm, respectively, suggesting that the anticorrelation regime should be experimentally achievable. The circular points correspond to the geometries used in the molecular dynamics simulations conducted in this study. Figure adapted from [2].

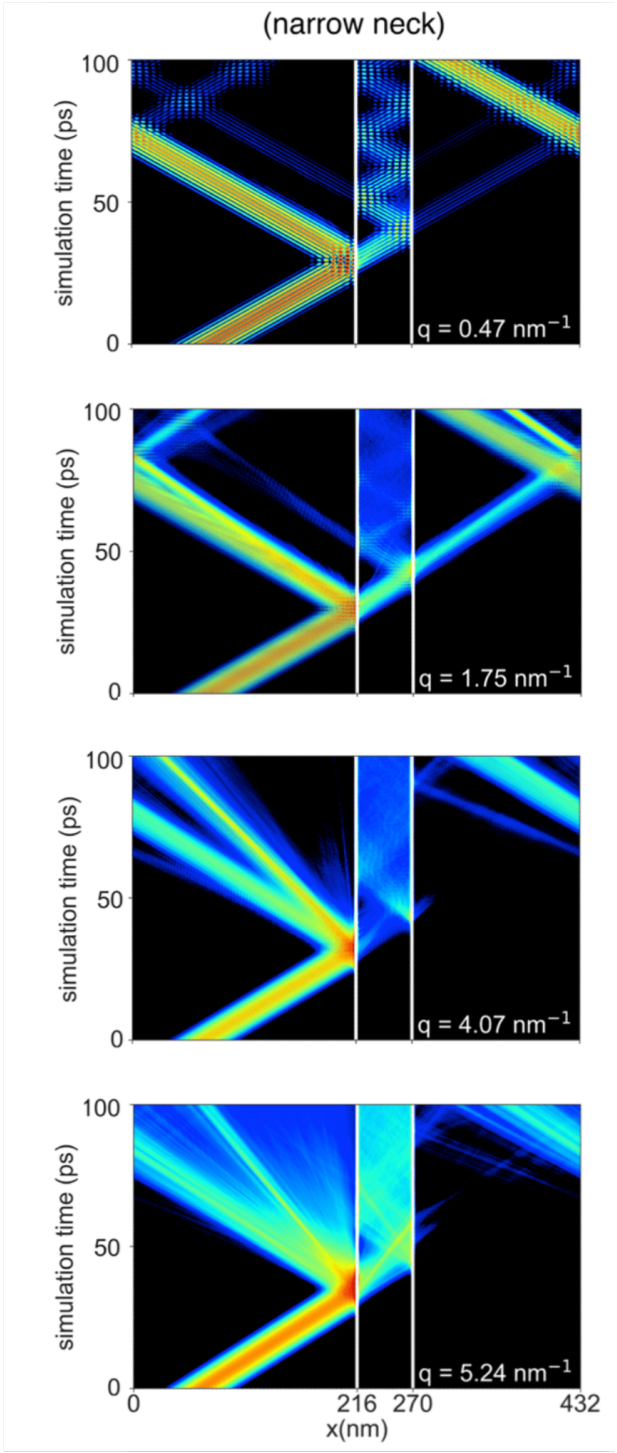

Fig. 3. A heatmap illustrating the time evolution of the wavepacket kinetic energies in the nanoporous geometry, displaying anticorrelated effects. The pore radius is 2 nm, with a neck size of 1.4 nm. White lines mark the pore locations along the transport direction. Each plot represents a wavepacket of a transverse acoustic mode centered at the specified wavevector. The distance between the pores is 54 nm. The wavepacket amplitudes are adjusted to maintain a temperature of 5 K in all simulations. Figure adapted from [2] and [3].

Investigation of thermal transport and dislocations in lattice-matched InGaAs/InAlAs superlattices by nonequlibrium molecular dynamics simulations

Sandip Dhruba and Irena Knezevic
Department of Electrical and Computer Engineering
University of Wisconsin-Madison, Madison, WI 53706, USA
dhruba@wisc.edu , irena.knezevic@wisc.edu

InGaAs/InAlAs superlattices are widely used in optoelectronic and thermoelectric devices, such as quantum cascade lasers (QCLs). High thermal conductivity is desired in the active region of QCLs to prevent the accumulation of heat which eventually leads to dislocation formation and catastrophic optical damage [1]. Many factors lower thermal conductivity, among them the slow anharmonic decay of optical phonons, mass-difference scattering, interface roughness, etc.

Mei and Knezevic investigated the thermal conductivity in the binary compounds InAs, GaAs and AlAs and their ternary alloys, $In_xGa_{1-x}As$ and $In_yAl_{1-y}As$ by equilibrium molecular dynamics (EMD) simulations [2]. However, in practice, QCLs often experience significant temperature fluctuations under nonequilibrium conditions owing to thermal runaway mechanisms. These fluctuations can cause certain regions to reach critical temperatures and stresses, leading to the formation of dislocations [3]. Hence, it is worthwhile to investigate this phenomenon using nonequilibrium molecular dynamics (NEMD). We have primarily accurately calculated the thermal conductivity of the InAs, GaAs, AlAs, $In_{0.53}Ga_{0.47}As$ and $In_{0.52}Al_{0.48}As$ at room temperature using the NEMD method and the values were very close to [2]. We were also able to successfully generate dislocations by applying compressive uniaxial strain to $In_{0.53}Ga_{0.47}As/In_{0.52}Al_{0.48}As$ superlattices, as shown in Fig. 1. Zinc blende semiconductors are known to show perfect dislocations with $1/2< 110 >$ burgers vectors which glide on $\{111\}$ planes. These perfect dislocations often dissociate into partial dislocations of type $1/6< 112 >$ creating stalking faults in the structure. Both types were observed in the simulation.

Thermal conductivities (TC) of InAs, GaAs, and AlAs, $In_{0.53}Ga_{0.47}As$ and $In_{0.52}Al_{0.48}As$ at room temperature were calculated by NEMD simulations in LAMMPS. The system, with periodic boundaries, was first equilibrated using NVT and NVE ensembles and then Langevin thermostats were applied to impose heat flux. TC for each simulation cell was determined using Fourier's Law, and bulk TC was calculated by extrapolating $1/\kappa$ vs $1/L$ graph as shown in Fig. 2b. Separately, compressive strain at a high strain rate was applied on superlattices made of random alloys of $In_{0.53}Ga_{0.47}As$ and $In_{0.52}Al_{0.48}As$ and dislocations were observed. Tensile strain was also applied to investigate the fracture mechanism.

In conclusion, the goal of this work is to do atomistic modeling of nucleation of dislocations because of nonequilibrium conditions and thermal stress in InGaAs/InAlAs superlattices. From primary simulations, it is clear that the binary potentials produce accurate results for thermal conductivity at nonequilibrium conditions and the superlattices also show the right type of dislocations under strain.

ACKNOWLEDGEMENT

This work was funded by the AFOSR Award No. FA9550-22-1-0407, Splinter Professorship, and Vilas Distinguished Achievement Professorship (IK). Calculations were performed at CHTC (UW-Madison).

REFERENCES

[1] Y. Sin, Z. Lingley, M. Brodie, B. Knipfer, C. Sigler, C. Boyle, J. D. Kirch, K. Oresick, H. Kim, and D. Botez, "Catastrophic degradation in high-power buried heterostructure quantum cascade lasers," in *CLEO: Science and Innovations*, pp. SW3N–3, Optica Publishing Group.

[2] S. Mei and I. Knezevic, "Thermal conductivity of ternary III-V semiconductor alloys: The role of mass difference and long-range order," vol. 123, no. 12, p. 125103.

[3] J. Souto, J. L. Pura, M. Rodríguez, J. Anaya, A. Torres, and J. Jimenéz, "Mechanisms driving the catastrophic optical damage in high-power laser diodes," in *High-Power Diode Laser Technology and Applications XIII*, vol. 9348, pp. 203–209, SPIE.

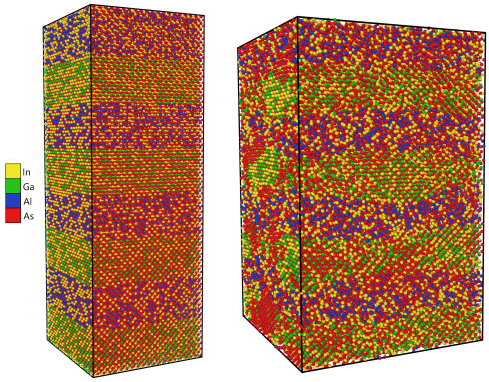

(a)

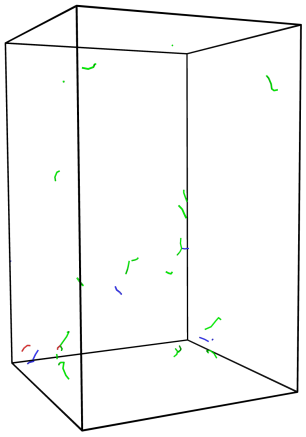

(b)

Fig. 1: Nucleation of dislocations in $In_{0.53}Ga_{0.47}As/In_{0.52}Al_{0.48}As$ superlattice by compressive strain at 800K. (a) A sample of $In_{0.53}Ga_{0.47}As/In_{0.52}Al_{0.48}As$ superlattice (left) and its strained picture (right) rendered in Ovito. (b) 1/2$<$ 110 $>$ (blue) 1/6$<$ 112 $>$ (green) type dislocations shown by dislcoation analysis (DXA) in Ovito.

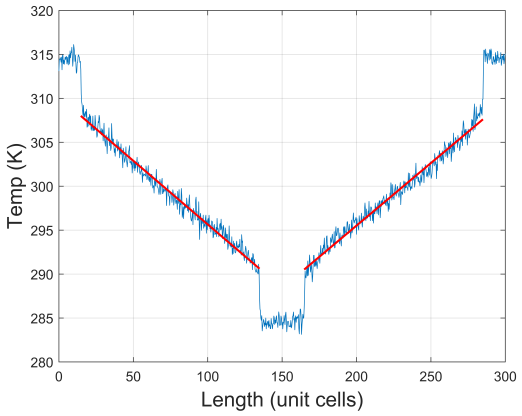

(a)

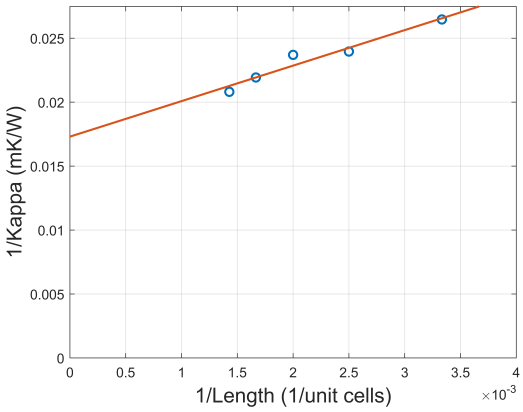

(b)

Fig. 2: Thermal conductivity calculation at room temperature by NEMD. (a) Sample steady-state thermal profile for a GaAs sample. (b) Variation of $1/\kappa$ with $1/L$ for GaAs at room temperature.

Thermal Conductivity of Nanowires: Machine Learning and Monte Carlo Insights

M. K. Eryilmaz and I. Knezevic
Department of Electrical and Computer Engineering
University of Wisconsin-Madison, Madison, WI 53706, USA
korkmaz2@wisc.edu, irena.knezevic@wisc.edu

The thermal conductivity of nanowires is critically influenced by their structural properties, such as width and surface-roughness parameters (rms roughness, correlation length, and correlation type). Accurate modeling of these dependencies is essential for optimizing nanowire applications in thermal management. In this work, we employ symbolic regression to derive explicit mathematical expressions that capture the thermal transport behavior of silicon nanowires (SiNWs) versus structural properties. By integrating Monte Carlo simulation data with advanced machine learning algorithms, we identify key parameter interactions and quantify their effects on thermal conductivity for temperature at and above 300 K and widths above 20 nm. Our approach offers a bridge between complex numerical models and analytical expressions. This presentation will highlight the methodology, key findings, and implications for both theoretical research and practical applications in thermal transport.

The ultralow measured thermal conductivities in intentionally roughened SiNWs have been reproduced in our phonon Monte Carlo simulations in the diffusive limit with exponentially correlated real-space rough surfaces similar to experimental findings [1,2]. In order to understand the behavior of thermal conductivity with respect to various physical properties of the nanowires, we employed data analysis and machine learning methods to infer mathematical expressions that would relate the termal conductivity to these properties.

Symbolic regression is a machine learning algorithm capable of uncovering analytical equations that describe data, which can result in interpretable models with strong generalization potential beyond the training dataset. In this work, we employ a neural-network-based symbolic regression framework called the Equation Learner (EQL) network [3] and combine it with our Monte Carlo results.

Thermal conductivity values of intentionally roughened silicon nanowires has been reproduced in phonon Monte Carlo simulations with exponentially correlated real-space rough surfaces, and the root mean squared (RMS) surface roughness, correlation length, wire width, temperature, surface area, volume and normalized geometric mean free path (N-GMFP) [1] of the nanowires are saved to be used as the dataset. This dataset was fed to the symbolic regression network in various combinations, and the network was fine tuned to fit the needs of the dataset and be able to produce mathematical expressions that are short and comprehendible. The final symbolic network was formed of two layers, each layer comprising function nodes loaded with identity, square, exponential, sinusoidal and product functions. The variables we fed in the algorithm stayed as variables through the process, and the result was finalized into a partial function of the input variables.

The relation of thermal conductivity with N-GMFP was observed to form compact equations with the two distinct parts of thermal conductivity vs. N-GMFP graph. The results agree with experimental data from literature [2].

ACKNOWLEDGEMENT

This work was funded by the AFOSR Award No. FA9550-22-1-0407, Splinter Professorship, and Vilas Distinguished Achievement Professorship (IK). Calculations were performed at CHTC (UW-Madison).

REFERENCES

[1] Maurer, L. N., Aksamija, Z., Ramayya, E. B., Davoody, A. H., & Knezevic, I. (2015). Universal features of phonon transport in nanowires with correlated surface roughness. *Applied Physics Letters*, *106*(13). https://doi.org/10.1063/1.4916962

[2] Hochbaum, A. I., Chen, R., Delgado, R. D., Liang, W., Garnett, E. C., Najarian, M., Majumdar, A., & Yang, P. (2008). Enhanced thermoelectric performance of rough silicon nanowires. *Nature*, *451*(7175), 163–167. https://doi.org/10.1038/nature06381

[3] Kim, S., Lu, P. Y., Mukherjee, S., Gilbert, M., Jing, L., Ceperic, V., & Soljacic, M. (2020). Integration of Neural Network-Based Symbolic Regression in deep Learning for scientific discovery. *IEEE Transactions on Neural Networks and Learning Systems*, *32*(9), 4166–4177. https://doi.org/10.1109/tnnls.2020.3017010.

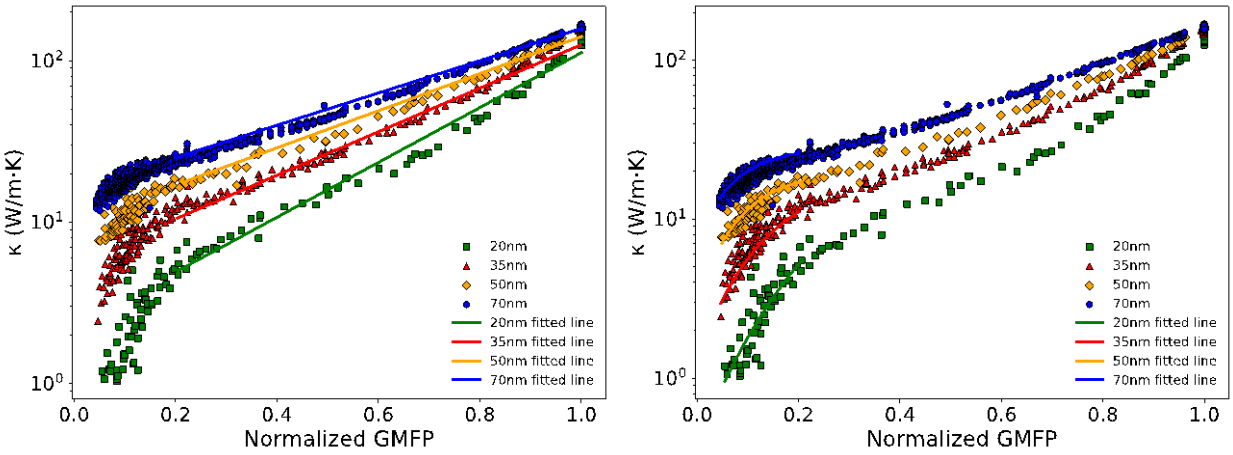

Fig. 1. Thermal conductivity versus normalized geometric mean free path as obtained from phonon Monte Caro simulation (symbols) and from symbolic regression (lines). The left panel highlights the fit for diffusive regime (small to moderate roughness or high normalized GMFP), and the right panel presents the fit for the localization regime (high roughness or low normalized GMFP).

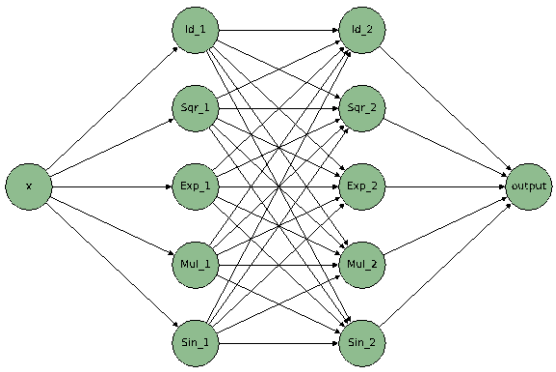

Fig. 2. The equation learner symbolic network schematic. This schematic has two layers of neurons that have identity, square, exponential, multiplication and sinusoidal activation functions in each of the two layers. More nodes with different functions can be added to these layers. [2]

Evaluating Thermal Transport at The Axial Junction of Si-Ge Composite Nanowires

Oreoluwa Adesina[1], Masoumeh Mahmoudi Gahrouei[1], Andres Lee[1], Riccardo Rurali[2], Laura de Sousa Oliveira[1]
[1]Department of Chemistry, University of Wyoming, 1000 E. University Ave, Laramie Wyoming 82071
[2]Institut de Ciència de Materials de Barcelona (ICMAB–CSIC), Campus de Bellterra, 08193 Bellaterra, Barcelona, Spain

ABSTRACT

In this work, thermal transport is calculated for silicon-germanium (Si-Ge) composite nanowires that have curved interfaces at the axial junction between the two materials. This is done for regular straight and bent (floppy) wire categories. In real-life nanowire forests, there will be some bent wires present. We use the Müller-Plathe method, which is based on non-equilibrium molecular dynamics (NEMD), with the Tersoff potential to model thermal transport in nanowires with lengths ranging between 100 – 550 nm for two wire diameters in LAMMPS. We consider a range of curvatures at the junction between Si and Ge. The interfacial resistance at the axial junctions is also evaluated. The direction of heat flow, relevant to thermal rectification applications, is also taken into account, i.e., geometries are modeled for heat flowing from Ge(hot) to Si(cold) and vice-versa.

INTRODUCTION

To further the development of different materials for applications in thermal management and several industrial uses, we need to understand thermal transport across interfaces fully. The mechanical and thermal attributes of solid systems can be strongly dependent on these interfaces if present. Interfaces can act as a barrier to efficient thermal transport. Thermal transport in small-scale heterogeneous systems is controlled by interfacial resistance because of the large surface-to-volume ratio. This study will further our understanding of phonon thermal transport and the role of boundary scattering at the interfaces of low-dimensional materials. Our choice of nanowires, Si and Ge can be experimentally [1] synthesized in several ways. A stringent minimization criterion is used to enforce bending in the second group of systems such that the bent wires are also structurally relaxed.

RESULTS

Thermal conductivity values calculated using the Müller-Plathe method, are plotted in Fig. **1** and Fig. **2** as a function of the wire length for all regular wire geometries. In addition to curved interfaces, the thermal conductivities of flat heterojunctions are also presented, labeled Si|hot| and Ge|hot|. In this set of data, we can easily observe that thermal conductivity (κ) increases with an increase in wire length, with some anomalies. Anomalies largely stem from the presence of resonating frequencies that lead to oscillations in the wires. For the bent counterparts (Fig. **4**), we observe an uncharacteristic decrease in thermal conductivity as length is increased with some outliers. This is likely the result of additional scattering due to the curvature of the nanowires.

In part due to limitations in the methodology employed, minimal changes are observed in the thermal conductivity of the wires due to interfacial curvature. Preliminary interfacial resistance calculations help shed light on the role of heterojunction curvature. We observe that notwithstanding the diameter being considered (5.43 or 10.86 nm), the resistance in Ge(hot) is lower than in Si(hot), as expected. It appears that, as a result, for thermal transport between Si(hot) and Ge(cold), larger curvatures (and thus interfacial surface areas) lead to slightly higher interfacial resistances, a trend that is not observed for transport between Ge(hot) and Si(cold), as shown in Fig. **5** and Fig. **6**. Further analysis is being conducted to fully understand these sets of results.

ACKNOWLEDGMENT

The scientific computing resources of this work was supported by the Advanced Research Computing Center (ARCC) at the University of Wyoming and the National Center for Atmospheric Research – Wyoming Supercomputer (WYOM0168) [2].

REFERENCES

[1] C.-W. Lin, S.-Y. Lin, S.-C. Lee, and C.-T. Chia, 'Structural and optical properties of silicon–germanium alloy nanoparticles', *J Appl Phys*, vol. 91, no. 4, pp. 2322–2325, 2002, doi: 10.1063/1.1433185.

[2] 'Computational and Information Systems Laboratory. 2023. Derecho: HPE Cray EX System (Wyoming-NCAR Alliance). Boulder, CO: National Center for Atmospheric Research.', doi: doi:10.5065/qx9a-pg09.

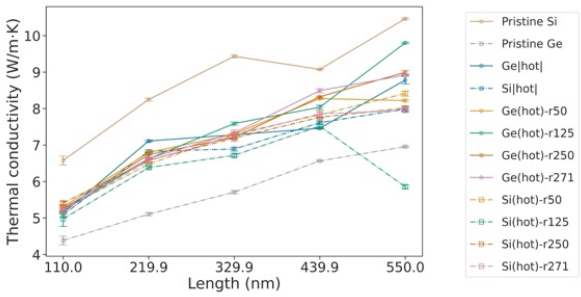

Fig. **1**. Size-dependent thermal conductivity of Ge(hot) and Si(hot) supercells with diameters of 5.43 nm for regular wires

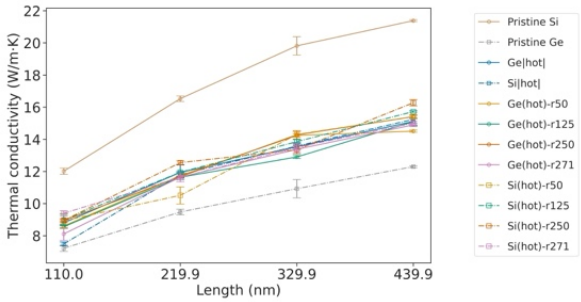

Fig. **2**. Size-dependent thermal conductivity of Ge(hot) and Si(hot) supercells with diameters of 10.8 nm for regular wires

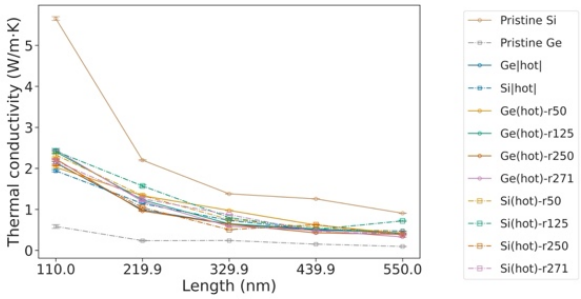

Fig. **3**. Size-dependent thermal conductivity of Ge(hot) and Si(hot) supercells with diameters of 5.43 nm for bent wires

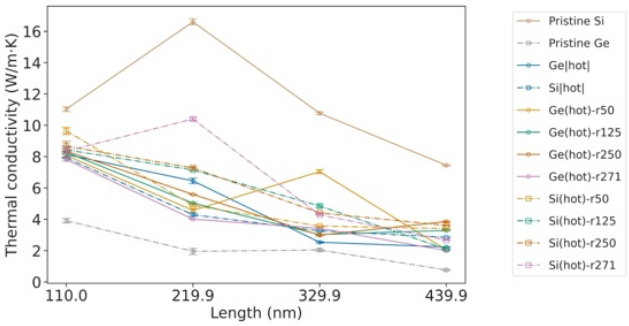

Fig. **4**. Size-dependent thermal conductivity of Ge(hot) and Si(hot) supercells with diameters of 10.86 nm for bent wires

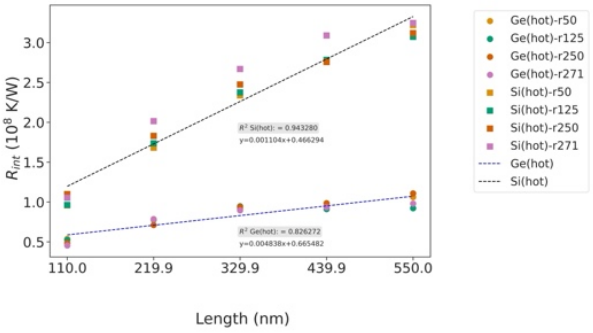

Fig. **5**. Interfacial resistance of Ge(hot) and Si(hot) across all sizes for 5.43 nm diameter wires for regular wires

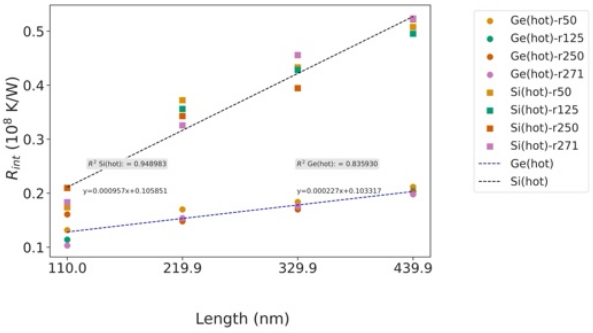

Fig. **6**. Interfacial resistance of Ge(hot) and Si(hot) across all sizes for 10.86 nm diameter wires for regular wires

Impacts of Short-range Order on Thermal Conductivity of GeSn and Si-Ge-Sn Alloys

Shunda Chen and Tianshu Li
Department of Civil and Environmental Engineering,
George Washington University, Washington, DC 20052, USA
e-mail: shdchen@email.gwu.edu, tsli@email.gwu.edu

GeSn and Si-Ge-Sn alloys are versatile, silicon-compatible materials for electronic, photonic, and topological quantum applications. Effective thermal management remains a challenge in these applications. Building on our recent studies [1]–[5] predicting complex short-range order in GeSn and Si-Ge-Sn alloys, we investigate the impact of the non-random alloying element distribution on their thermal conductivity using first-principles calculations. We find that the thermal conductivity of GeSn and Si-Ge-Sn alloys varies significantly with atomic ordering. We analyze the underlying mechanisms driving the variation, revealing the role of atomic ordering in phonon scattering and heat conduction. Our results suggest that short-range order may offer a new pathway for engineering the thermal properties of Group IV alloys, alongside its effects on electronic [1]–[6] and topological quantum properties [7], with implications for next-generation semiconductor technologies.

ACKNOWLEDGMENT

This work was partially supported by the Air Force Office of Scientific Research under Award No. FA9550-19-1-0341. It was also supported as part of the μ-ATOMS, an Energy Frontier Research Center funded by the U.S. Department of Energy, Office of Science, Basic Energy Sciences under Award No. DE-SC0023412. This research used resources of the National Energy Research Scientific Computing Center, a DOE Office of Science User Facility supported by the Office of Science of the U.S. Department of Energy under Contract No. DE-AC02-05CH11231 using NERSC Award No. BES-ERCAP0027056. The authors also acknowledge GW High Performance Computing for the computing support.

REFERENCES

[1] B. Cao, S. Chen, X. Jin, J. Liu, and T. Li, "Short-range order in GeSn alloy," *ACS Applied Materials & Interfaces*, vol. 12, no. 51, pp. 57 245–57 253, 2020. [Online]. Available: https://doi.org/10.1021/acsami.0c18483

[2] X. Jin, S. Chen, and T. Li, "Short-range order in SiSn alloy enriched by second-nearest-neighbor repulsion," *Phys. Rev. Mater.*, vol. 5, p. 104606, Oct 2021. [Online]. Available: https://link.aps.org/doi/10.1103/PhysRevMaterials.5.104606

[3] ——, "Coexistence of two types of short-range order in Si–Ge–Sn medium-entropy alloys," *Communications Materials*, vol. 3, no. 1, pp. 1–9, Sep. 2022. [Online]. Available: https://www.nature.com/articles/s43246-022-00289-5

[4] X. Jin, S. Chen, C. Lemkan, and T. Li, "Role of local atomic short-range order distribution in alloys: Why it matters in Si-Ge-Sn alloys," *Phys. Rev. Mater.*, vol. 7, p. L111601, Nov 2023. [Online]. Available: https://link.aps.org/doi/10.1103/PhysRevMaterials.7.L111601

[5] S. Chen, X. Jin, W. Zhao, and T. Li, "Intricate short-range order in GeSn alloys revealed by atomistic simulations with highly accurate and efficient machine-learning potentials," *Phys. Rev. Mater.*, vol. 8, p. 043805, Apr 2024. [Online]. Available: https://link.aps.org/doi/10.1103/PhysRevMaterials.8.043805

[6] X. Jin, S. Chen, and T. Li, "Enabling type I lattice-matched heterostructures in SiGeSn alloys through engineering composition and short-range order: A first-principles perspective," *IEEE Journal of Selected Topics in Quantum Electronics*, 2024. [Online]. Available: https://ieeexplore.ieee.org/abstract/document/10574300

[7] Y. Liang, S. Chen, X. Jin, D. West, S.-Q. Yu, T. Li, and S. Zhang, "Group IV topological quantum alloy and the role of short-range order: the case of Ge-rich $Ge_{1-x}Pb_x$," *npj Computational Materials*, vol. 10, no. 1, p. 82, 2024. [Online]. Available: https://www.nature.com/articles/s41524-024-01271-0

Wed. 11:00-12:30 Phonons 2

Time	Type	Presenter	Title
11:00-11:30 am	**Invited**	Keivan Esfarjani	Predicting Thermal Conductivity and Classifying Chemical Bonds using DFT and Machine Learning
11:30-11:45	Contributed	Shouhang Li	Phonon Thermal Transport Along the Chain Direction of Crystalline Polyethylene
11:45-12:00 pm	Contributed	Masoumeh Mahmoudi Gahrouei	Ab initio investigation of thermoelectric properties of two-dimensional MOFs
12:00-12:15	Contributed	David Mai	Applying POD-methods onto electron-phonon scattering in the Wigner equation
12:15-12:30	Contributed	Izak Baranowski	Modeling of Non-Equilibrium Phonons in Hot Carrier Solar Cells

Predicting Thermal Conductivity and Classifying Chemical Bonds using DFT and Machine Learning

Keivan Esfarjani

Dept. of Materials Science and Engineering, University of Virginia

Email: k1@virginia.edu

This talk details our development of computational tools for accurately predicting thermal conductivity from first-principles calculations. We utilize harmonic and anharmonic force constants, extracted from supercell DFT calculations, to model phonon transport. Applying this methodology to lanthanum-pnictides, we demonstrate a counterintuitive result: LaBi's thermal conductivity surpasses that of LaP, despite the lighter mass of phosphorus. We attribute this discrepancy to the strong anharmonicity in LaP, a consequence of its more metavalent La-P bonds. In the second part, we explore the nature of metavalent bonding itself. To remove any bias, we employ unsupervised machine learning classification on a broad material dataset. We identify four descriptors that effectively categorize five distinct bonding types, excluding weak Hydrogen and van der Waals interactions. This analysis provides new insights into chemical bonding beyond traditional classifications.

Phonon Thermal Transport Along the Chain Direction of Crystalline Polyethylene

Shouhang Li*, Philippe Dollfus*, Jérôme Saint-Martin*†, and Davide Romanin*
*Centre de Nanosciences et de Nanotechnologies, CNRS, Université Paris-Saclay,
10 Boulevard Thomas Gobert, 91120 Palaiseau, France
†SATIE, CNRS, ENS Paris-Saclay, Université Paris-Saclay, 91190 Gif-sur-Yvette, France
e-mail: shouhang.li@universite-paris-saclay.fr

ABSTRACT

It was once believed that the thermal conductivity (κ) in crystalline polyethylene (PE) is higher than 100 W/mK. Here, we applied the stochastic self-consistent harmonic approximation (SSCHA) [1] combined with phonon Boltzmann transport equation to predict the κ of PE. Our calculation scheme incorporates the quantum, thermal, and anharmonic effects in force constants. It is found that the room-temperature κ of PE is only $\sim$ 18 W/mK, which matches the previous thermoreflectance experiment well.

INTRODUCTION

Polymers have the properties of being lightweight, cost-effective to manufacture, and soft, thereby having great potential in LEDs, electronic packaging, flexible electronics, *etc*. The thermal conductivities in polymers are usually ≈ 0.2 W/mK, which is relatively low and becomes the bottleneck in many applications. To address this issue, it was proposed to achieve very high thermal conductivity (> 100 W/mK) by stretching and ordering polyethylene (PE) chains[2]. This inspires lots of theoretical studies to explore the upper limit of the thermal conductivity of PE, either by molecular dynamics simulation [3] or first-principles calculations [4], [5]. However, those theoretical predictions generally overestimate the κ for PE, which is incomparable to the time-domain thermoreflectance (TDTR) experiment[6].

THEORY AND METHOD

In this work, the SSCHA [1] is employed to obtain the temperature-dependent force constants (FCs). This method rigorously incorporates the quantum, thermal and anharmonic effects on FCs. The NequIP potential [7] is adopted to address the huge computing burden in SSCHA calculations. The thermal conductivity is obtained by solving the phonon Boltzmann transport equation using the exact diagonalization method [8].

RESULTS AND DISCUSSIONS

The lattice structure of PE is shown in Fig. 1(a). The phonon dispersions from harmonic approximation and the Hessian calculation including anharmonic effects are shown in Fig. 1(b). Overall, the phonon frequencies from theoretical prediction matches experimental results. There is a pronounced renormalization in the harmonic phonon frequency, which indicates there are large modifications in FCs. The κ along the chain direction of PE is shown in Fig. 2. The κ is mainly contributed by the high-frequency longitudinal acoustic phonons, which hold relatively large lifetime and group velocity. The κ predicted by our method matches the TDTR experiment well, while the classical DFT and the temperature-dependent effective potential method significantly overestimate the value.

ACKNOWLEDGMENT

We acknowledge support from the HPC resources of IDRIS, CINES, and TGCC under Allocation No. 2024-A0160914101 made by GENCI, as well as funding from the projects PLACHO (ANR-21-CE50-0008) and TyLDE (Grant No. ANR-23-CE50-0001-01) founded by ANR.

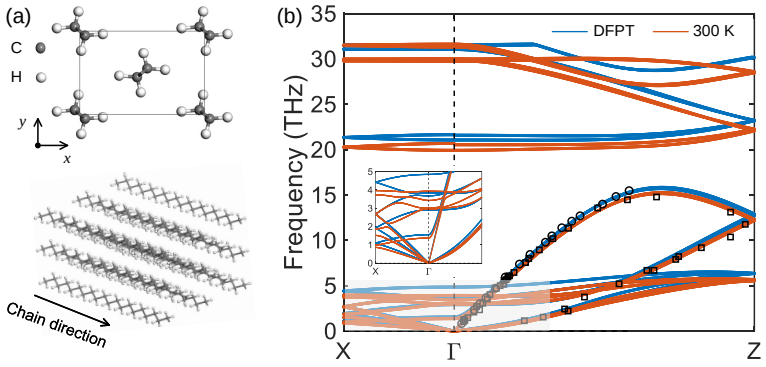

Fig. 1: (a) The lattice structure of crystalline PE. There are 4 carbon atoms and 8 hydrogen atoms in the unit cell. (b) The phonon dispersions from density functional perturbation theory (DFPT) and Hessian calculation at 300 K. The inset shows a zoomed-in region near the Γ-point. The black scatters are data from experiments respectively.[9], [10].

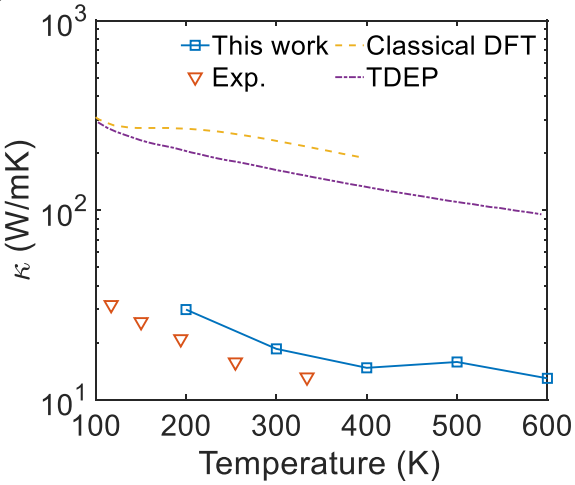

Fig. 2: The thermal conductivity along the chain direction of crystalline PE from this work, the TDTR experiment (Exp.)[6], the classical DFT [5], and the temperature-dependent effective potential method (TDEP)[4]. In classical DFT, force constants were extracted at 0 K using the finite difference method.

REFERENCES

[1] L. Monacelli, R. Bianco, M. Cherubini, M. Calandra, I. Errea, and F. Mauri, "The stochastic self-consistent harmonic approximation: calculating vibrational properties of materials with full quantum and anharmonic effects," *J. Phys.:Condens. Matter*, 33, 363001, 2021.

[2] S. Shen, A. Henry, J. Tong, R. Zheng, and G. Chen, "Polyethylene nanofibres with very high thermal conductivities," *Nat. Nanotechnol.*, 5, 251–255, 2010.

[3] X. Yu, D. Ma, C. Deng, X. Wan, M. An, H. Meng, X. Li, X. Huang, and N. Yang, "How does van der waals confinement enhance phonon transport?" *Chin. Phys. Lett.*, 38, 014401, 2021.

[4] N. Shulumba, O. Hellman, and A. J. Minnich, "Lattice thermal conductivity of polyethylene molecular crystals from first-principles including nuclear quantum effects," *Phys. Rev. Lett.*, 119, 185901, 2017.

[5] X. Wang, M. Kaviany, and B. Huang, "Phonon coupling and transport in individual polyethylene chains: a comparison study with the bulk crystal," *Nanoscale*, 9, 18 022–18 031, 2017.

[6] X. Wang, V. Ho, R. A. Segalman, and D. G. Cahill, "Thermal conductivity of high-modulus polymer fibers," *Macromolecules*, 46, 4937–4943, 2013.

[7] S. Batzner, A. Musaelian, L. Sun, M. Geiger, J. P. Mailoa, M. Kornbluth, N. Molinari, T. E. Smidt, and B. Kozinsky, "E (3)-equivariant graph neural networks for data-efficient and accurate interatomic potentials," *Nat. Commun.*, 13, 2453, 2022.

[8] L. Chaput, "Direct solution to the linearized phonon boltzmann equation," *Phys. Rev. Lett.*, 110, 265506, 2013.

[9] A. Schaufele and T. Shimanouchi, "Longitudinal acoustical vibrations of finite polymethylene chains," *J. Chem. Phys.*, 47, 3605–3610, 1967.

[10] L. Feldkamp, G. Venkataraman, and J. King, "Dispersion relation for skeletal vibrations in deuterated polyethylene," " in *Neutron Inelastic Scattering Vol. II. Proceedings of a Symposium on Neutron Inelastic Scattering*, 1968.

Ab initio investigation of thermoelectric properties of two-dimensional MOFs

Masoumeh Mahmoudi Gahrouei, Nikiphoros Vlastos, Oreoluwa Adesina, Ransell D'Souza, Emmanuel C. Odogwu, and Laura de Sousa Oliveira*

Department of Chemistry, University of Wyoming, 1000 E. University Ave, Laramie Wyoming 82071

e-mail: mmahmoud@uwyo.edu

ABSTRACT

Metal–organic frameworks (MOFs) have the potential to be used as thermoelectric materials. Thermoelectric materials enable direct conversion between thermal and electrical energy. The main motivation for this project is to further our knowledge of thermoelectric properties in MOFs and find which available self-consistent-charge density functional tight-binding (SCC-DFTB) method can best predict (at least trends in) the electronic, phononic and therefore thermoelectric properties of MOFs at a lower computational cost than standard density functional theory (DFT). In the case of the electronic properties, we compare SCC-DFTB/3ob and SCC-DFTB/mio (based on available Slater-Koster files), GFN1-xTB and GFN2-xTB against PBE and hybrid DFT (HSE06) for $Zn_3C_6O_6$, Zn-NH-MOF, $Ni_3(HITP)_2$ and $Cd_3C_6O_6$ MOFs for the monolayer and stacked AA, serrated and AB structures. We also calculate the phononic contribution to the thermal conductivity using SCC-DFTB/3ob(mio) and GFN-xTB. Our results suggest that while GFN-xTB is adequate to predict the MOFs' electronic properties, DFTB-mio and GFN2-xTB are adequate to predict the MOFs' phononic properties. We find that while $Zn_3C_6O_6$, Zn-NH-MOF and $Cd_3C_6O_6$ MOFs are predicted to have a higher power factor than the $Ni_3(HITP)_2$ MOF (one of the highest performing synthesized thermoelectric MOFs), thermal transport is substantially lower for Zn-NH-MOF, leading to the highest ZT among the group.

MOTIVATION

An estimated two thirds of all the energy produced in the world is wasted as heat. Thermoelectric (TE) materials can convert wasted heat into useful electricity and vice-versa. The challenge to create efficient TE materials lies in achieving simultaneously high electronic conductivity (σ), high Seebeck coefficient (S) and low thermal conductivity (κ) in the same solid [1]. These properties define the dimensionless TE figure of merit $ZT=(S^2\sigma/\kappa)T$, where T is the temperature. The research goal of this reasearch is to develop the fundamental knowledge to predict key quantitative (QSPR) structure-property relationships to inform the rational design of thermoelectric metal–organic frameworks (MOFs).

METHODS

We use the Vienna *Ab Initio* Simulation Package (VASP) [2-4], a computer program which uses density functional theory (DFT) for atomic scale materials modelling. Using VASP is computationally expensive. DFTB+ [5] is a fast and versatile software package, here used to implement SCC-DFTB and GNFn-xTB. These semiempirical methods lead to up to two orders of magnitude increase in speed with only a small loss in accuracy. All the electrical transport coefficients (*S* and *σ)* are determined by solving the Boltzmann transport equation as implemented in BoltzTraP2 [6]. Second-order force constant phonon properties using both DFT and SCC-DFTB/GFNn-xTB were determined through the PHONOPY code [7]. To get the third-order force constant phonon contributions to the thermal conductivity (κ_L), the PHONO3PY code was employed [8-9].

CONCLUSION

While GFN1-xTB electronic properties are closer to DFT-PBE, the phonon dispersions using GFN2-xTB and DFTB-3ob/mio better resemble those from DFT-PBE. We therefore expect that the lattice thermal conductivities from GFN2-xTB and, to a lesser extent, DFTB-3ob/mio are closer to DFT-PBE. Curiously, GFN2-xTB did not converge for most unstable geometries (i.e., those with negative phonon modes) and was found to converge for all but one of the stable geometries.

The $Zn_3C_6O_6$, Zn-NH-MOF, $Ni_3(HITP)_2$, and Cd3C6O6 maximum electrical conductivity, Seebeck coefficient, and PF computed with DFT and SCC-DFTB are shown in Fig 1. The phonon properties of the monolayer, AA-stacked and serrated Zn-NH-MOF MOF results have been presented here due to its high ZT results (Fig 2). This work has been published [10-11].

REFERENCES

[1] Sootsman, J. R.; Chung, D. Y.; Kanatzidis, M. G. New and Old Concepts in Thermoelectric Materials. *Angew. Chem. Int. Ed.* **2009**, *48* (46), 8616–8639.

[2] Kresse, G.; Hafner, J. Ab Initio Molecular Dynamics for Liquid Metals. *Phys. Rev. B* **1993**, *47* (1), 558.

[3] Kresse, G.; Furthmüller, J. Efficiency of Ab-Initio Total Energy Calculations for Metals and Semiconductors Using a Plane-Wave Basis Set. *Comput. Mater. Sci.* **1996**, *6* (1), 15–50.

[4] Kresse, G.; Furthmüller, J. Efficient Iterative Schemes for Ab Initio Total-Energy Calculations Using a Plane-Wave Basis Set. *Phys. Rev. B* **1996**, *54* (16), 11169.

[5] Hourahine, B.; Aradi, B.; Blum, V.; Bonafé, F.; Buccheri, A.; Camacho, C.; Cevallos, C.; Deshaye, M.; Dumitrică, T.; Dominguez, A. DFTB+, a Software Package for Efficient Approximate Density Functional Theory Based Atomistic Simulations. *J. Chem. Phys.* **2020**, *152* (12).

[6] Madsen, G. K.; Carrete, J.; Verstraete, M. J. BoltzTraP2, a Program for Interpolating Band Structures and Calculating Semi-Classical Transport Coefficients. *Comput. Phys. Commun.* **2018**, *231*, 140–145.

[7] Togo, A. First-Principles Phonon Calculations with Phonopy and Phono3py. *J. Phys. Soc. Jpn.* **2023**, *92* (1), 012001.

[8] Togo, A.; Chaput, L.; Tanaka, I. Distributions of Phonon Lifetimes in Brillouin Zones. *Phys. Rev. B* **2015**, *91* (9), 094306.

[9] Togo, A.; Chaput, L.; Tadano, T.; Tanaka, I. Implementation Strategies in Phonopy and Phono3py. *J. Phys. Condens. Matter* **2023**.

[10] Mahmoudi Gahrouei M, Vlastos N, D'Souza R, Odogwu EC, de Sousa Oliveira L. Benchmark Investigation of SCC-DFTB against Standard and Hybrid DFT to Model Electronic Properties in Two-Dimensional MOFs for Thermoelectric Applications. Journal of Chemical Theory and Computation. 2024 May 6;20(9):3976-92.

[11] Mahmoudi Gahrouei M, Vlastos N, Adesina O, de Sousa Oliveira L. Benchmark Investigation of SCC-DFTB Against Standard DFT to Model Phononic Properties in Two-Dimensional MOFs for Thermoelectric Applications. Journal of Chemical Theory and Computation. 2024 Nov 7;20(22):10167-78.

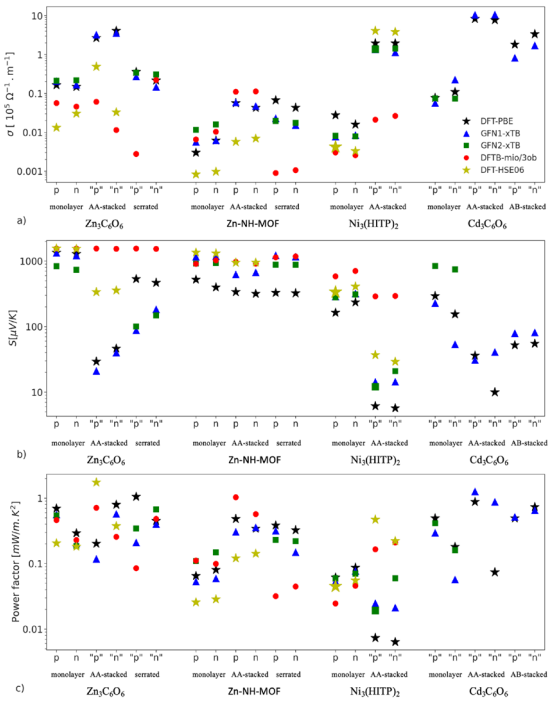

Fig. **1**. The maximum a) electrical conductivity (σ), b) the Seebeck coefficient (S) and c) the power factor (PF) of the $Zn_3C_6O_6$, Zn-NH-MOF, Ni_3(HITP), and $Cd_3C_6O_6$. The black stars, red circles, blue triangles, green squares, and yellow stars correspond to the DFT-PBE, DFTB, GFN1-xTB, GFN2-xTB and DFT-HSE06 results. Figure reproduced from [10].

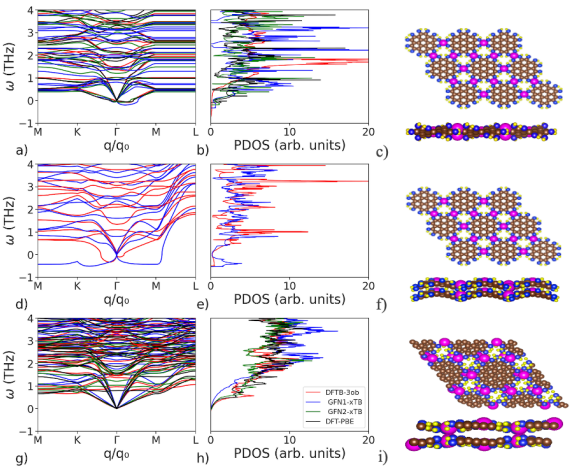

Fig. 2. a) The phonon dispersion and b) density of states of e) the wavy Zn-NH-MOF monolayer. f) The phonon dispersion and g) density of states of h) Zn-NH-MOF AA-stacked. i)The phonon dispersion and j) density of states of k) Zn-NH-MOF serrated. Zn, C, N and H are pink, brown, blue, and yellow, respectively. Figure reproduced from [11].

Applying POD-methods onto electron-phonon scattering in the Wigner equation

D. Mai and D. Schulz
Chair for Communication Technology, TU Dortmund, Otto-Hahn Straße 4, 44225 Dortmund, Germany
e-mail: david.mai@tu-dortmund.de

***Abstract*— For the computation of the nonballistic electron transport caused by i.e. electron-phonon scattering high performance computing methods are needed. Therefore, a Discontinuous Galerkin (DG) method is used to approximate the Wigner transport equation (WTE). To oppose the resulting high computation times, a Proper Orthogonal Decomposition (POD)-method is introduced and linked with DG.**

INTRODUCTION

Recently a variety of methods to model the electron transport have been developed [1]. Those models mostly neglect the electron-phonon scattering or use relaxation models. Preliminary work to model electron-phonon scattering has already been made by [2], but quantum mechanical effects are neglected. To gain the best sophisticated approach these approximations are examined and results based on a larger amount of phonon modes are discussed. Since the addition of the electron-phonon interaction emerge into high computing times and large memory requirements, Model Order Reduction (MOR) methods like the POD method are introduced to solve these problems and enable an examination of more precisely discretisation schemes [3]. An algorithm can be set up to model the scattering and to include the already mentioned methods.

MODEL

A Wigner-Weyl-transformation of the electron-phonon von Neumann equation results into the Wigner transport equation in the phase space. Through the electron-phonon interaction a hierarchy problem arise. This results in an approximation of the Wigner function based on 4^l phonon states $|n_q>$ with l representing the order of the hierarchy. The hierarchy problem is dissolved through approximations like the random phase approximation (RPA) and the Markov approximation. The DG method is now used in χ-direction. The phase space k regarding the charge carrier and the phase space q of the phonons is discretized which leads to a discrete modal spectrum. For the transient solution a Lawson method of fourth order is applied.

RESULTS

For a test device (Fig. 1) the hierarchy problem is solved for the second order. The expected electron density can be seen in Fig. 2, which is in agreement with results taken by assessing the ballistic transport [4]. Only through the sole consideration of the electron-phonon interaction, the scattering can be seen (Fig. 3). The observed carrier concentration is in agreement with former results in [2] and [5]. From first evaluations (Fig. 4) it can be concluded that the POD method results in a considerable time reduction down to a tenth and can be classified as a promising approach.

REFERENCES

[1] J. Weinbub, D. Ferry, *Recent advances in Wigner function approaches.* Applied Physics Reviews 5, 041104 (2018)
[2] M. Nedjalkov, D. Vasileska, D. K. Ferry, C. Jacoboni, C. Ringhofer, I. Dimov, and V. Palankovski, *Wigner transport models of the electron-phonon kinetics in quantum wires*, Physical Review B **74**, 035311 (2006).
[3] A. Chatterjee, *An introduction to the proper orthogonal decomposition*, CURRENT SCIENCE, VOL. 78, NO. 7 (2000).
[4] L. Schulz, and D. Schulz, *Complex Absorbing Potential Formalism Accounting for Open Boundary Conditions Within the Wigner Transport Equation*, IEEE Trans Nanotechnol 18 (2019), S. 830–838.
[5] R. Rosati and F. Rossi, *Scattering nonlocality in quantum charge transport: Application to semiconductor nanostructures*, Physical Review B **89**, 205415 (2014).

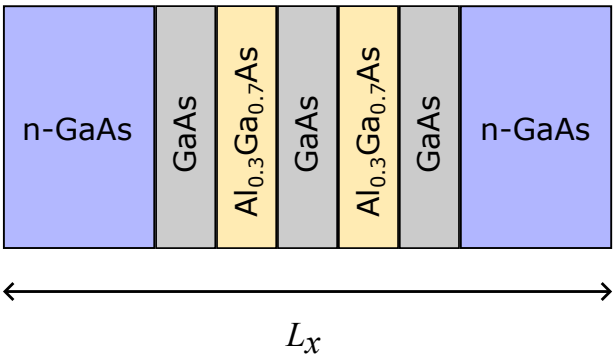

Fig. 1. Schematic GaAs/AlGaAs resonant tunneling diode with a width of L_x = 60 nm. At the edges of the structure the GaAs layer is highly doped. An $Al_{0.3}Ga_{0.7}As$ doublebarrier with 5 nm width is placed in the middle of an undoped GaAs layer with a 5 nm well between the barriers.

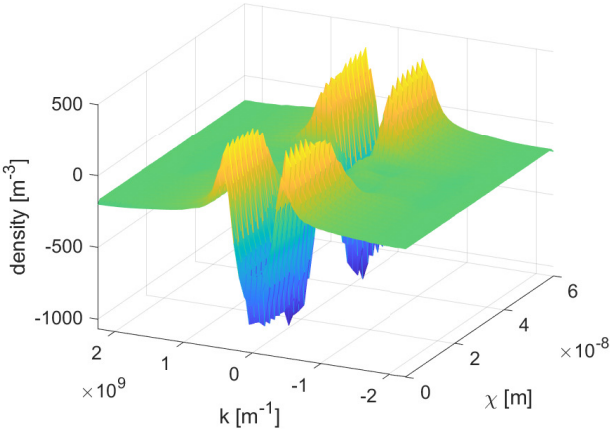

Fig. 3. The density of the scattered electrons is shown as a function dependent on the computation grid. For the q-discretisation N_q = 100 values are used. Two maxima are visible, which represent the creation of electrons at the wavenumber $k+q$ and $k-q$ respectively. The minimum at k=0 depicts the annihilation of an electron through the electron-phonon interaction.

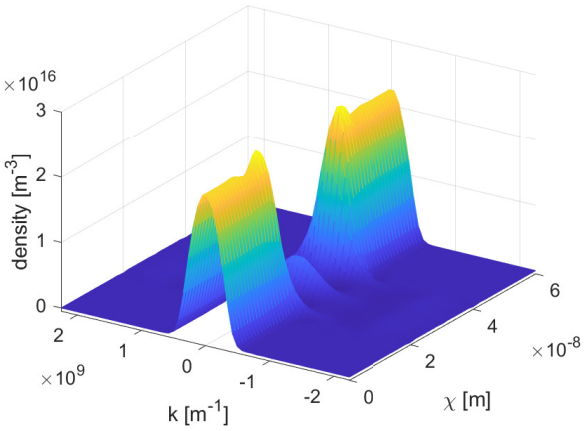

Fig. 2. The electron density within the RTD is shown as a function in dependence of the χ-coordinate and the k-coordinate. N_k = 60 values are considered for the k-discretisation.

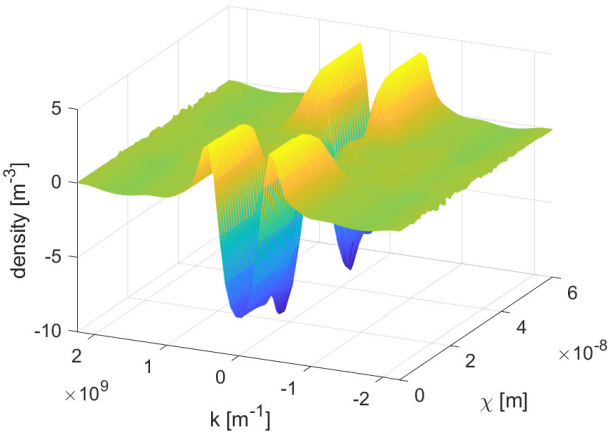

Fig. 4. The density of the scattered electrons is shown as a function of the computation grid. The solution is achieved through the POD method. For the q-discretisation the q phase space is divided into N_q = 11 values. 2750 snapshots are used to create a basis to reduce the order of the matrix of the system. The structure of the scattered electron density is in agreement with the solution gathered in Fig. 3. At the borders of the k-grid instabilities can be seen which shall be resolved through further investigations of the boundary conditions, which have to be adjusted to the expanded phase space $k+q$ and $k-q$.

Modeling of Non-Equilibrium Phonons in Hot Carrier Solar Cells

I. Baranowski, S.M. Goodnick, and D. Vasileska
School of Electrical, Computer, and Energy Engineering, Arizona State University, Tempe, AZ USA
e-mail: ibaranow@asu.edu

As fabrication techniques have improved and solar cell efficiencies are getting closer to the Shockley-Queisser limit, new designs which reconsider the fundamental assumptions of loss mechanisms are being explored. One such design is through hot-carrier solar cells in which the design of the cells is such that the photogenerated carriers are quickly extracted before the carriers have time to lose their excess energy to the lattice.

Reduced dimension systems have demonstrated in photo-luminescence (PL) measurements carrier temperatures in excess of the lattice temperature [1]. For 2D-MQW, it is theorized that the inhibited thermalization of carriers is due to the formation of a hot phonon bottleneck; as the phonon number N_{LO} increases, the rate of absorption and emission become approximately equal. This leads to an inhibition of the thermalization rate due to optical phonons. The dynamics of the system are not well understood, providing motivation for simulating these systems. Prior work has focused solely on the build up of polar LO phonons[2], however, the present work seeks to show that LA phonons could also play a role in the inhibition of carrier thermalization .

To simulate the system used in PL measurements, a modified Monte-Carlo (MC) method is used to solve the Boltzmann Transport Equation (BTE) with modifications to account for the build up of non-equilibrium phonons. The effects of confinement are included via the solution of a coupled non-parabolic Schrödinger-Poisson system. For recombination processes, an ABC model given as,

$$R(n) = An + Bn^2 + Cn^3 \tag{1}$$

is used, wherein the ABC coefficients are extracted from a fit to experimental measurements.

The non-equilibrium phonons are accounted for by introducing a discretized mesh of the phonon number $N_{LO}(\mathbf{q})$. When an emission or absorption event is selected in the MC, a value ΔN_{LO} is subtracted or added, respectively, for the corresponding $N_{LO}(\mathbf{q})$ value.

$$\Delta N_{LO} = \frac{2\pi}{\mathbf{q}^2 \Delta \mathbf{q} S} \tag{2}$$

This work also includes a discretization of the LA phonon branch. At the end of every synchronization time step, the decay and generation of LO phonons via Klemen's mechanism is modeled as:

$$\begin{aligned} \frac{\partial N}{\partial t} &= \Gamma_0 \left(G - \Gamma\right) \\ &= \Gamma_0 \left(N' N''(N_{LO}+1) - (N'+1)(N''+1)N_{LO}\right) \end{aligned} \tag{3}$$

where N' and N'' are the LA phonon modes which are coupled to the LO phonon mode to conserve both energy and momentum. As such, the dynamics of both the LA and LO phonons can be studied.

The simulations predict a possible phonon bottleneck resulting from a build up of both optical and acoustic phonons. This can be advantageous for designing an effective hot carrier solar cell.

References

[1] H. Esmaielpour, B. K. Durant, K. R. Dorman, V. R. Whiteside, J. Garg, T. D. Mishima, M. B. Santos, I. R. Sellers, J.-F. Guillemoles, and D. Suchet. Hot carrier relaxation and inhibited thermalization in superlattice heterostructures: The potential for phonon management. *Applied Physics Letters*, 118(21):213902, May 2021. [doi:10.1063/5.0052600].

[2] Y. Zou, H. Esmaielpour, D. Suchet, J.-F. Guillemoles, and S. M. Goodnick. The role of nonequilibrium LO phonons, Pauli exclusion, and intervalley pathways on the relaxation of hot carriers in InGaAs/InGaAsP multi-quantum-wells. *Scientific Reports*, 13(1):5601, Apr. 2023. [doi:10.1038/s41598-023-32125-2].

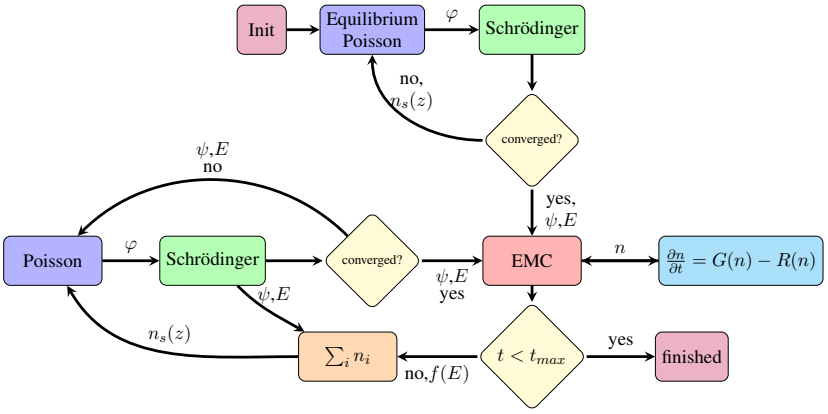

Fig. 1. Flowchart of the MC code

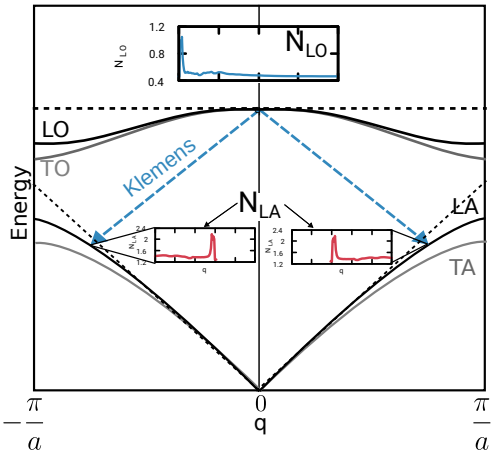

Fig. 2. Schematic diagram showing the considered LO phonon decay mechanism. The insets show the calculated phonon number vs wavenumber for the respective branch. Dotted lines show analytic dispersion used for LO and LA branches

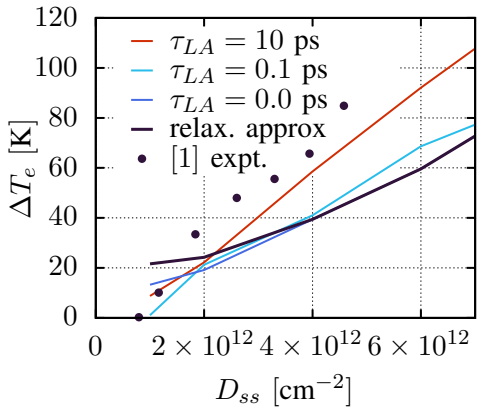

Fig. 3. Carrier temperature against steady-state sheet density for different acoustic phonon decay times compared to experimental results.

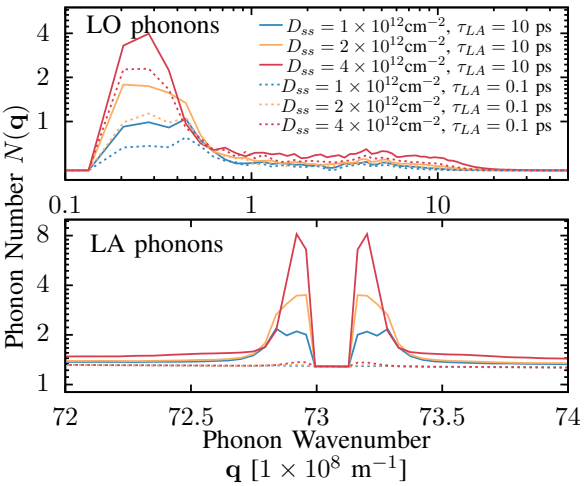

Fig. 4. Steady-state phonon number for both the acoustic and optical branches

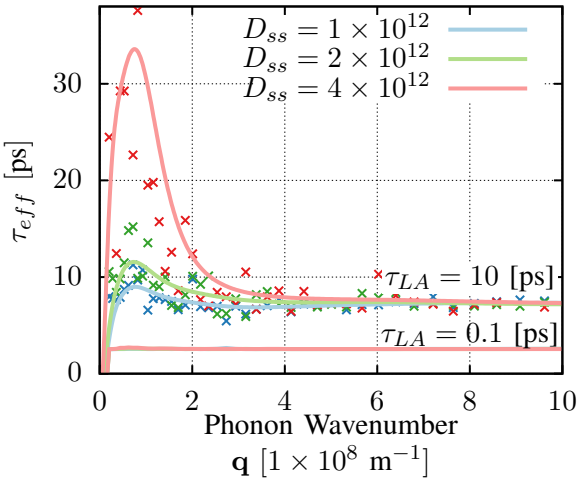

Fig. 5. Effective lifetimes for two different acoustic phonon decay times as a function of phonon wavenumber

Wednesday 2:00-3:30 pm Simulation Methods

Time	Type	Presenter	Title
2:00-2:30 pm	**Invited**	Giuseppe Romano	Differentiable Hydrodynamics Simulations: From Inverse Design to Automatic Material Properties Extraction
2:30-2:45	Contributed	Anders Winka	Investigation of thermalization effects and hot carriers in ultra-scaled electronic devices
2:45-3:00	Contributed	Denis Mamaluy	Phenomenological inelastic scattering model for electron transport in mesoscopic devices
3:00-3:15	Contributed	Bernhard Pruckner	Switching of Magnetization in Strained Noncollinear Antiferromagnet Mn_3Sn
3:15-3:30	Contributed	Khandakar Aaditta Arnab	KROGER: An Extended Calculation Framework for Realistic Defect Modeling in Semiconductors

Differentiable Phonon Hydrodynamic Simulations for Inverse Design and Material Property Extraction

Giuseppe Romano
Massachusetts Institute of Technology, 77 Massachusetts Avenue, Cambridge 02139, MA, USA
romanog@mit.edu

The geometry of a nanostructure strongly influences its transport properties, including its effective thermal conductivity. Nondiffusive phenomena—such as hydrodynamic transport—introduce novel mechanisms for tuning heat flow beyond what is captured by Fourier's law. However, engineering nanostructures for thermal applications remains challenging due to computational complexity. Most existing efforts rely on trial-and-error approaches or gradient-free methods, such as genetic algorithms, which suffer from slow convergence and poor scalability. In this talk, I will present our recent work on geometry optimization via differentiable programming. Our approach leverages automatic differentiation to compute gradients of a cost function with respect to the material's geometry, described through a density field. This enables efficient gradient-based optimization. We combine density-based topology optimization with the mode-resolved phonon Boltzmann transport equation (BTE) to design materials with a target effective thermal conductivity tensor. Our topology optimization approach is based on the *Transmission Interpolation Method* (TIM) [1], a novel scheme that connects material density to interfacial heat flux. In the second part of the talk, I will show how our differentiable BTE solver can be integrated with experimental data to extract key thermal properties. I will also highlight emerging directions at the intersection of thermal transport and differentiable programming, such as inverse-designed structures for analog computing [2]. The talk will conclude with an overview of the open-source software supporting our work.

[1] G. Romano, and S. G. Johnson. "Inverse design in nanoscale heat transport via interpolating interfacial phonon transmission." Structural and Multidisciplinary Optimization 65.10 (2022): 297.
[2] S. Caio and G. Romano. "Analog Computing with Heat: Matrix-vector Multiplication with Inverse-designed Metastructures." arXiv preprint arXiv:2503.22603 (2025).

Investigation of thermalization effects and hot carriers in ultra-scaled electronic devices

A. Winka, L. Deuschle, J. Cao, A. N. Ziogas, A. Maeder,
N. Vetsch, V. Maillou, M. Ciappa, M. Luisier
Integrated Systems Laboratory, ETH Zurich, Gloriastrasse 35, 8092, Zurich, Switzerland
e-mail: awinka@iis.ee.ethz.ch

Introduction. Decreasing the channel cross section of transistors enhances electron-electron (e-e) interactions, significantly affecting their performance. To capture these effects at an atomistic level the GW approximation [1] is usually the method of choice. Notably, it produces band gaps closer to experiments than density-functional theory. Going one step further, to describe the transport properties of nanoscale devices, the GW approximation should be combined with the non-equilibrium Green's function (NEGF) formalism [2]. In addition to renormalizing the bandstructure of semiconductors, the NEGF+GW approach changes the magnitude of electrical currents and the spectral distribution of electrons compared to the ballistic case. High-energy electrons in the drain of the transistor thermalize, generating hot carriers (HC) that can depassivate silicon-hydrogen (Si-H) bonds at the Si surface, degrading device performance [3]. Modeling HC and thermalization effects in nanoscale devices is thus crucial for device reliability. Hence, in this paper, we use an NEGF+GW approach [2] to study the formation of HC in the ultra-scaled silicon gate-all-around nanowire field-effect transistor (NWFET) of Fig. 1a and quantify this phenomenon.

Results. Figure 1b reports the I-V characteristics of the considered Si NWFET in the quasi-ballistic limit and with e-e interactions. The latter induce backscattering, reducing the ON-state current by 3.5$\times$ with respect to the quasi-ballistic case. More interestingly, they also alter the electron distribution, as can be seen in Fig. 2. Under quasi-ballistic conditions, electrons are accelerated by the applied electric field so that their kinetic energy on the drain side reaches the applied source-to-drain voltage Fermi level splitting, i.e. 0.6 eV. With e-e scattering, electrons thermalize, which broadens their distribution on the drain side. This effect can be better visualized in Fig. 3a, where the electron density is extracted in the drain region at three different gate voltages. Although the kinetic energy of many electrons clearly exceeds 1 eV, a negligible portion of them (less than 10^{14} cm^{-3}) have sufficiently high energy for Si-H bond depassivation through impact ionization. For this mechanism to occur, electrons with an energy larger than 3 eV, the Si nanowire band gap, would be required.

In Fig. 3b the electron occupancy function is plotted. In the ballistic case, the occupancy is given by two Fermi functions with a temperature of 300 K, one for the states injected from the source and one for states coming from the drain. In the presence of e-e scattering, the results cannot be fitted with a Fermi function because of the non-equilibrium situation. However, the high-energy range of the calculated occupancies follows a Boltzmann distribution function, from which a carrier temperature can be extracted. This quantity is presented in the inset of Fig. 3b. Temperatures up to 2,000 K are reached, in agreement with previous studies based on the Boltzmann Transport Equation [4].

Conclusion. Through NEGF+GW, we investigated the electronic properties of an ultra-scaled Si NWFET, highlighting the presence of hot carriers on the drain side of this device. While these HC are not expected to play a detrimental role in the structure examined here, it is important to have tools capable of predicting their influence from first-principles.

References. [1] L. Hedin, *Phys. Rev.* 139, A796–A823 (1965). [2] L. Deuschle et al., arXiv:2112.12986 [cond-mat.mes-hall] (2024). [3] S. E. Tyaginov et al., *ECS Trans.* 35, 321 (2011). [4] M. V. Fischetti and S. E. Laux, *J. Appl. Phys.* 89, 1205–1231 (2001).

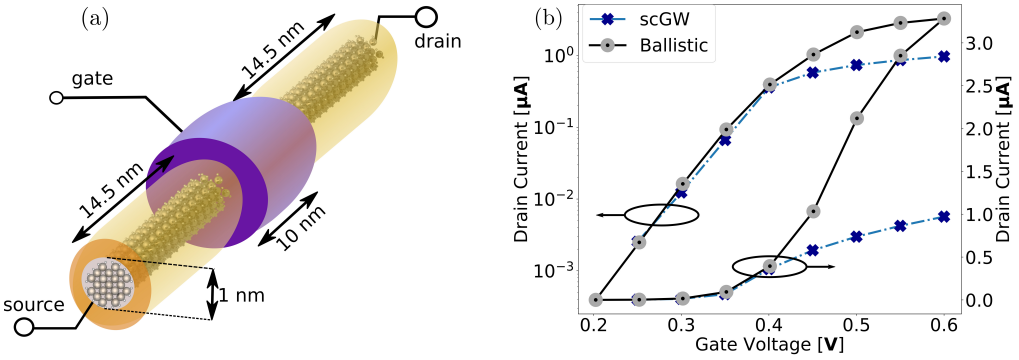

Fig. 1: (a) Schematic view of the silicon gate-all-around (GAA) nanowire field-effect transistor (NWFET) simulated in this work and its dimensions. (b) Transfer characteristics "I_d-V_{gs}" at V_{ds}=0.6 V for the GAA NWFET in (a). The quasi-ballistic current (black line with circles) was calculated in the presence of weak electron-phonon interactions at a phenomenological level to ensure convergence at high V_{gs}. Electron-electron (e-e) interactions are treated within the GW approximation (dashed-dotted line with crosses) [2].

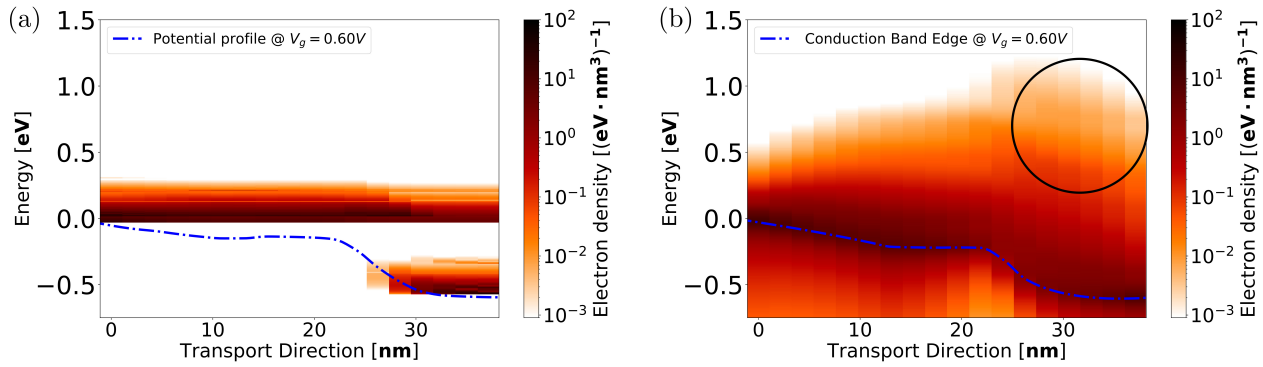

Fig. 2: Spatially- and energy-resolved (spectral) electron density in the Si GAA NWFET from Fig. 1 at V_{gs}=0.6 V and V_{ds}=0.6 V (a) in ballistic transport and (b) with e-e interactions. The spatial resolution corresponds to partial traces of the Green's function at different positions inside the device. The dash-dotted blue lines refer to the conduction band edge. The presence of hot carriers in (b) is indicated by a circle.

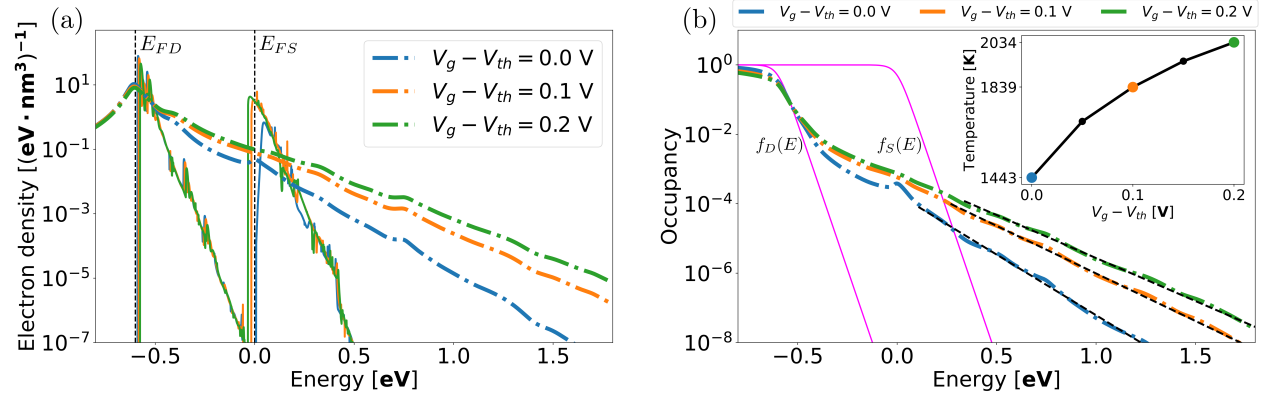

Fig. 3: Spectral (a) electron density and (b) electron occupancy function extracted at x=39 nm in Fig. 2(b) at three different V_{gs}-V_{th} voltages ($V_{th} = 0.4$V). Solid lines refer to the quasi-ballistic results and dash-dotted lines to results including e-e interactions. The occupancy functions are obtained by dividing the electron density by the density-of-states. The magenta lines in (b) correspond to the source and drain Fermi functions at 300 K. The black dashed lines are fits to the high-energy tales with a Boltzmann function $exp(-(E - E_F)/(k_B T))$, from which a temperature T can be determined. This quantity is shown in the inset of subplot (b).

Phenomenological inelastic scattering model for electron transport in mesoscopic devices

Denis Mamaluy* and Juan P. Mendez
Sandia National Laboratories, Albuquerque, New Mexico, *mamaluy@sandia.gov

Keywords: quantum transport, beyond-CMOS devices, inelastic scattering

We present a phenomenological inelastic scattering model that allows accurate quantum transport current calculations in semiconductor devices and is applicable to mesoscopic systems such as modern state-of-the-art transistors and beyond-CMOS devices. The model has no fitting parameters and is applicable to systems without significant self-heating effects. It is validated on silicon mobility and resistivity data in the wide range of temperatures (4K-500K), doping densities (10^{18}cm^{-3}-10^{21}cm^{-3}) and sheet doping densities (10^{10}-10^{15}cm^{-2}). When applied to IBM's Lgate=12nm, TSi=5nm GAAFET devices [1], it agrees well with the experimental I-V measurements.

Mesoscopic devices are not made of a single molecule, but still consist of many thousands or even millions of atoms. Just 1nm3 of Si contains about 120 of atoms and the simulation volume of the state-of-the-art GAAFET transistor is about (50nm)^3 or about 15 million atoms. Quantum transport simulation of such devices is challenging, but recent progress demonstrates [2-5] that numerically efficient first principles simulations with no fitting parameters can correctly predict the conductive properties of highly-conductive highly-confined Si:P/B systems at cryogenic temperatures, where elastic electrostatic scattering is very strong, but inelastic scattering effects can be ignored. In this work we introduce a model that allows sufficiently accurate and very simple description of inelastic scattering effects on the current in such mesoscopic systems, thus extending the range of efficient predictive quantum transport simulations to elevated and room temperatures. The idea is to approximate the current spectrum affected by the two-body inelastic scattering collisions by weighting the ballistic current spectrum with the ballisticity factor $B(E)$, $i_{eff}(E)=i_{ballistic}(E)\cdot B(E)$. The ballisticity factor is assumed to be proportional to the number of phonons with the comparable to electron energies. Effectively, the model dampens the computed ballistic current spectrum for those frequencies where phonon population is high, leaving the rest of the current spectrum unmodified. Remarkably, this exceptionally simple scheme for accounting of inelastic scattering provides an excellent match to the experiment, as can be seen from Figure 1, without using any fitting parameters. We show that the model also allows to recover the electron mobility values in silicon thin films for a wide range of temperatures and doping values as illustrated in Figure 3.

REFERENCES

[1] N. Loubet et al., *Stacked Nanosheet Gate-All-Around Transistor to Enable Scaling Beyond FinFET*, 2017 Symposium on VLSI Technology, Kyoto, Japan, pp. T230-T231, 2017.
[2] D. Mamaluy, J.P. Mendez, X. Gao, S. Misra, *Revealing quantum effects in highly conductive δ-layer systems*, Commun. Phys. 4, 205 (2021).
[3] J.P. Mendez, S. Misra, D. Mamaluy, *Influence of imperfections on tunneling rate in δ-layer junctions*, Phys. Rev. Applied 20, 054021 (2023).
[4] J.P. Mendez, D. Mamaluy, *Conductivity and size quantization effects in semiconductor δ-layer systems*. Sci Rep 12, 16397 (2022).
[5] J.P. Mendez, D. Mamaluy, *Uncovering anisotropic effects of electric high-moment dipoles on the tunneling current in δ-layer tunnel junctions*, Sci Rep 13, 22591 (2023)

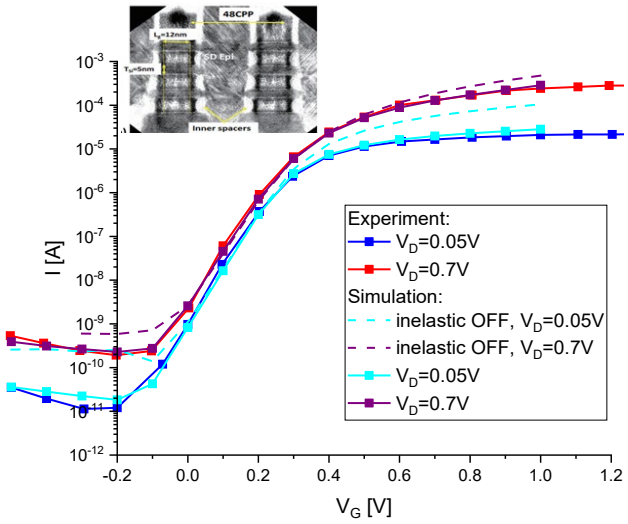

Fig. 1. Electrical characteristics of IBM's GAAFET [1] device: experimental measurements vs first principles simulation results. Dashed lines: no inelastic scattering (ballistic), solid lines: using the inelastic scattering model. Note that the current spectrum is effectively reduced for those energies, where phonon population is high, as a function of the gate voltage and the corresponding effective potential barrier, shown in Figure 2.

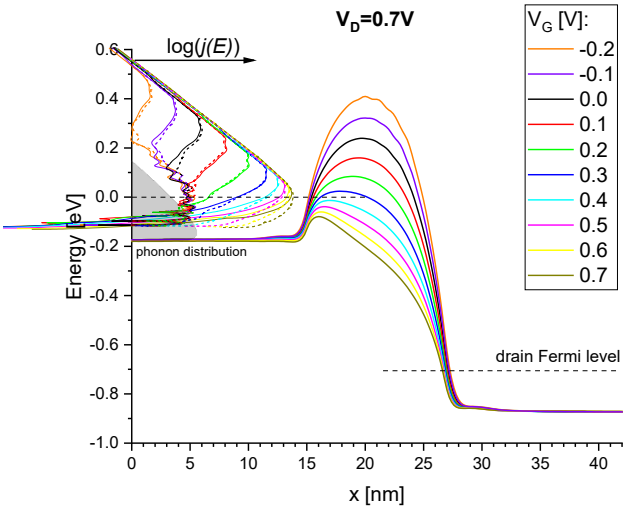

Fig. 2. Effective 1D potential (conduction band edge) from the source (left side) to the channel (middle) and the drain (right side) is shown for different gate voltages (solid color curves); V_D=0.7V. The current density spectrum j(E) is shown in semi-log scale for each gate voltage (solid color curves); the ballistic current spectrum case is also shown using the dashed lines; the grey area represents the phonon distribution $pDOS(E) \cdot f_{B-E}(E)$ expressed as a function of the electron energy.

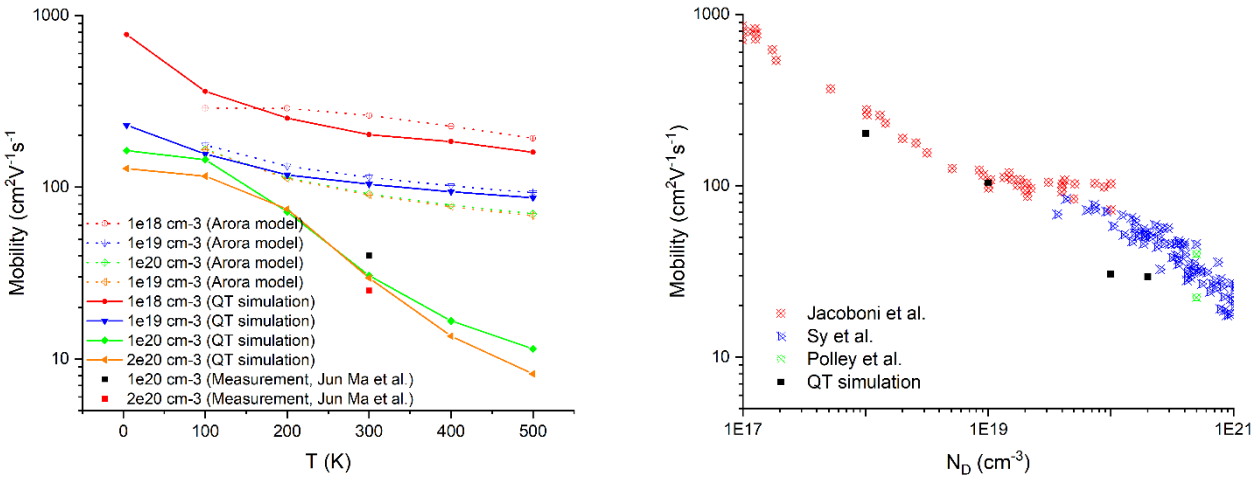

Fig. 3. Left panel: Comparison of the predicted electron mobilities vs temperature between our quantum transport simulations and the Arora model and experimental data for different doping densities; Right panel: Comparison of the electron mobilities predicted by our framework with experimental data at room temperature (300K). Note that here the computed mobility is extracted assuming a very thin (~5nm) silicon film, which lowers the mobility value compared to the bulk values for high temperatures and doping concentrations.

Switching of Magnetization in Strained Noncollinear Antiferromagnet Mn_3Sn

B. Pruckner*, W. Goes‡, S. Selberherr†, and V. Sverdlov*†
* Christian Doppler Laboratory for Nonvolatile Magnetoresistive Memory and Logic, at the
† Institute for Microelectronics, TU Wien, Gußhausstraße 27-29, A-1040 Wien, Austria
‡ Silvaco Europe Ltd., Compass Point, St Ives, PE27 5JL, Cambridge, United Kingdom
e-mail: pruckner@iue.tuwien.ac.at

Noncollinear antiferromagnets (nc-AFM) have been studied for their potential use as spin-polarizing layer in Spin-Orbit Torque Magnetoresistive Random Access Memory (SOT-MRAM) devices [1]. Experimentally shown SOT-induced magnetization switching of the nc-AFM Mn_3Sn between two distinct magnetic states, proves the potential of these materials to be also utilized as free magnetic layer in MRAM devices [2,3]. We study the magnetic behavior of the nc-AFM Mn_3Sn. Fig. 1a shows the structure of the Mn and Sn atoms, arrange in a two-dimensional Kagome lattice [2,3,4], with the Mn atoms carrying the magnetic moments $\mathbf{m_A}$, $\mathbf{m_B}$ and $\mathbf{m_C}$. The energy of the system is comprised of the interlayer and intralayer antiferromagnetic exchange energies acting between the Mn nearest neighbors, with $J_1 = 23.15$ meV and $J_2 = 17.53$ meV, the single-atom anisotropy $K = 0.19$ meV acting along $\mathbf{e_A}$, $\mathbf{e_B}$, $\mathbf{e_C}$, and the Dzyaloshinskii–Moriya-interaction $D = 0.833$ meV acting along $\mathbf{e_D} = \mathbf{e_y}$ [2]. When introducing epitaxial tensile strain, as shown in Fig. 1b, additional energy contributions arise: the modulated exchange energies $J_1 * (1 - \delta)$ and $J_2 * (1 - \delta)$, with the parameter δ accounting for the change in distance between two nearest neighbor Mn atoms, and a global uniaxial strain-induced anisotropy K_{strain}, caused by the displacement of Sn atoms neighboring the Mn atoms. The crystal symmetry of the unstrained Kagome lattice is broken, introducing a small net magnetic moment $\mathbf{m_{net}}$, as depicted in Fig. 1c. Fig. 2 shows the energy of the system over the polar angle of $\mathbf{m_{net}}$ from the z-axis and various strain strengths indicated with the δ parameter. With increasing strain we observe a six-, four-, and twofold energy of the system. At high strain only the two distinct stable states remain, with $\mathbf{m_{net}}$ pointing along positive or negative z-direction Fig. 1c shows the stable 'up' state with high strain.

Applying an external magnetic field along x-direction shifts the energy barriers, through the contribution of $\mathbf{m_{net}}$ to the energy, as depicted in Fig. 3. We show that the shifted energy barriers facilitate deterministic switching making the nc-AFM Mn_3Sn a potential candidate for the use as magnetic memory. We reduce the 6-spin model to an effective 3-spin model without neglecting interlayer nearest neighbor effects. We apply SOT-induced current generated in an adjacent Pt heavy metal layer and solve the coupled Landau-Lifshitz-Gilbert (LLG) equations for our system. We calculate the octupolmoment $\mathbf{m_{oct}} = \frac{1}{3}\left[\mathbf{M_{xy}}\mathbf{m_A} + \mathbf{R}\left(\frac{-2\pi}{3}\right)\mathbf{m_B} + \mathbf{R}\left(\frac{2\pi}{3}\right)\mathbf{m_C}\right]$ used as order parameter in nc-AFM materials [3].

Fig. 4 shows $\mathbf{m_{oct}}$, $\mathbf{m_{net}}$, and the energy, when an SOT-current in x-direction is applied. Fig. 4a shows the system without applied external field, Fig. 4b and Fig. 4c for an external field of $H_{ext,x} = 0.05$ T and $H_{ext,x} = 0.1$ T, respectively. A variation of the absolute value of $\mathbf{m_{net}}$ proportional to the energy is shown. The description of the system by an effective 1-Spin-LLG using the octupolmoment has been suggested [4]. However, as $\mathbf{m_{net}}$ is neglected, dynamic processes cannot be captured to a full extent, therefor a careful consideration of the energy of $\mathbf{m_{net}}$ and $\mathbf{m_{oct}}$ is necessary.

REFERENCES

[1] S. Hu et al., Nat.Comm. 13, 4447, 2022
[2] T. Higo et al., Nature 607, 474 , 2022
[3] J.-Y. Yoon et al. Nat.Mat. 22, 1106, 2023
[4] Z. He and L. Liu, Jour. Appl. Phys. 135, 093902, 2024

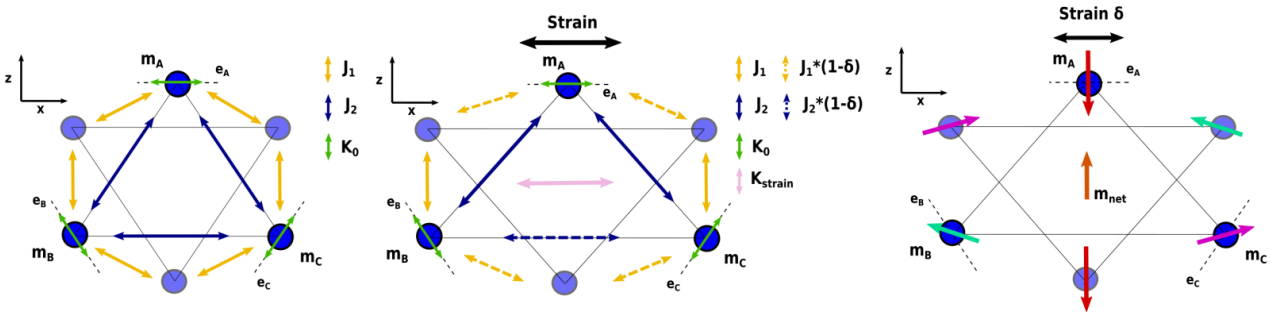

Fig. 1. Kagome lattice of the nc-AFM Mn_3Sn without (left) and with (center) tensile strain applied to the crystal lattice. (Right) The magnetic moments of the sublattices. In a strained state, a small nonzero net-magnetization $\mathbf{m_{net}}$ emerges.

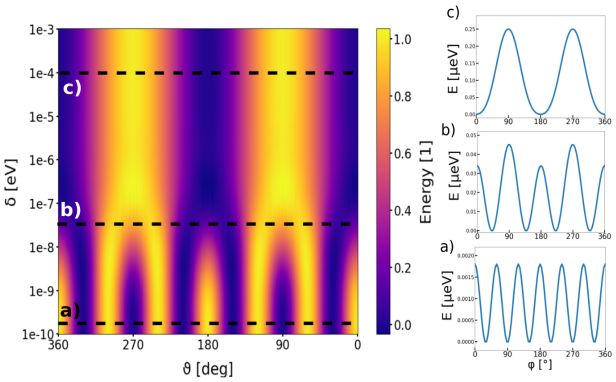

Fig. 2. The normalized energy for various applied strain values. For no and very small strains a sixfold energy profile can be observed (a). Increasing the strain leads to a fourfold (b) and twofold (c) energy profile.

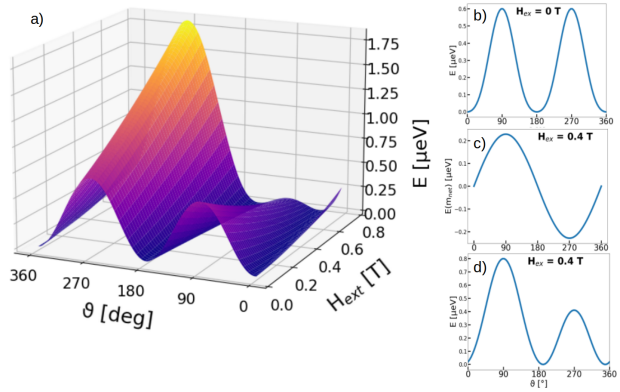

Fig. 4. a) The energy of the system over the polar angle of $\mathbf{m_{net}}$ with an external field applied along x-direction. (Right) The energy for b) no applied field, the energy of $\mathbf{m_{net}}$ in a field of $H_{ext,x} = 0.4T$, and the total energy for $H_{ext,x} = 0.4T$.

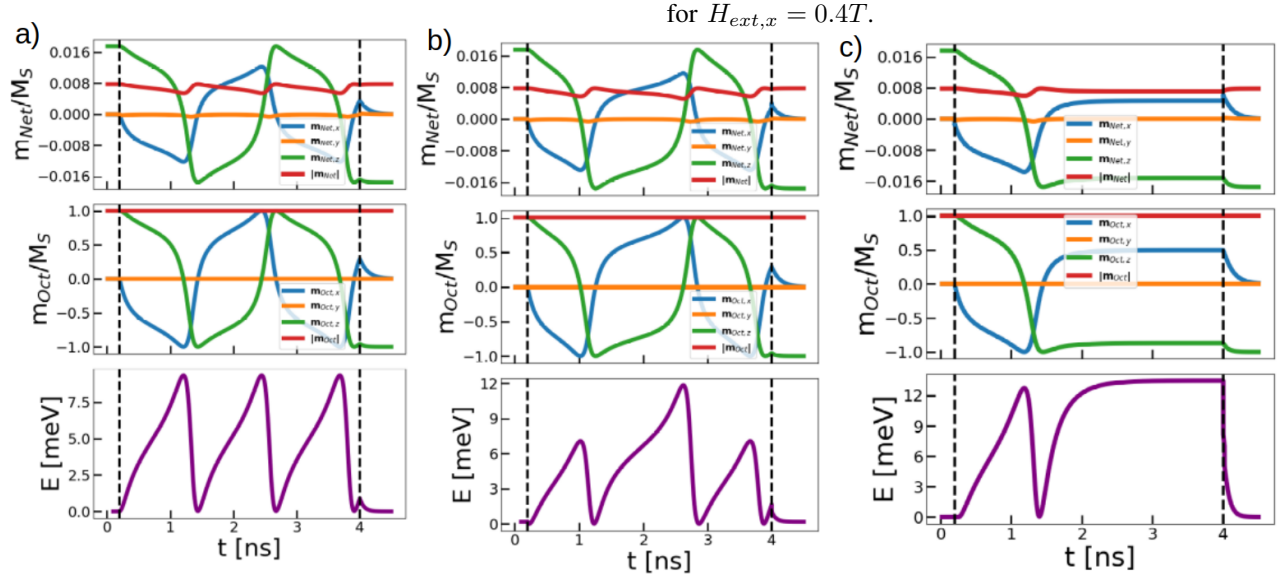

Fig. 3. $\mathbf{m_{net}}$, $\mathbf{m_{oct}}$, and the energy of the system displayed for an applied SOT-current of $9*10^{11}$ A/m² in x-direction. a) $H_{ext,x} = 0$ T, b) $H_{ext,x} = 0.05$ T, c) $H_{ext,x} = 0.1$ T. M_S is calculated to $1.5 * 10^6$ A/m by using the crystal parameters in [1].

KROGER: An Extended Calculation Framework for Realistic Defect Modeling in Semiconductors

Khandakar Aaditta Arnab[1], and Michael A Scarpulla[1,2]
[1.] Materials Science & Engineering, University of Utah
[2.] Electrical & Computer Engineering, University of Utah
Email: mike.scarpulla@utah.edu

Accurate defect modeling is essential for optimizing semiconductor materials for electronic applications. Here, we introduce KROGER [1], a robust computational framework that integrates density functional theory (DFT) with thermodynamic effects such as bandgap temperature dependence, chemical potentials, and defect vibrational entropy. KROGER enables precise predictions of defect equilibria, charge carrier compensation mechanisms, and kinetic trapping effects, providing valuable insights into material processing and defect engineering.

KROGER models full, partial, and constrained defect equilibria to capture the influence of growth and processing conditions on defect chemistry. Named after F.A. Kroger for his seminal work on point defect equilibria, KROGER processes large-scale datasets of DFT-computed formation energies for defects and complexes, allowing defect population predictions under real-world conditions. It accounts for self-trapped holes (STHs) and incorporates a quantum harmonic oscillator model to estimate defect vibrational entropy, which contributes energy corrections exceeding 1.5 eV per defect near the melting point.

To demonstrate its capabilities, we apply KROGER to β-Gallium Oxide (β-Ga_2O_3), an ultra-wide bandgap semiconductor with promising applications in power electronics. Accurate modeling of defects in β-Ga_2O_3 is crucial for optimizing its electrical properties and doping strategies. A key challenge in defect modeling is predicting defect concentrations under real-world synthesis conditions. Standard DFT-based formation energy calculations often predict full compensation of n-type doping by gallium vacancies (V_{Ga}), contradicting experimental findings. However, Sn-doped β-Ga_2O_3 crystals grown by edge-fed growth (EFG) at 2068°C with p_{O2} = 0.02 atm exhibit degenerate n-type conductivity with minimal compensation. By incorporating temperature-dependent bandgap corrections, realistic chemical potentials from the Ga-O binary phase diagram, and vibrational entropy effects, KROGER significantly improves agreement with experimental data.

In this study, we modeled 873 charge states of 259 defects, including native and impurity-related species involving 19 elements, to simulate the defect chemistry of β-Ga_2O_3 under EFG growth and oxygen annealing. KROGER accurately predicts unintentionally doped (UID), Sn-, Fe-, and Mg-doped EFG crystals by computing defect equilibria based on experimentally reported impurity concentrations. This approach provides insights into kinetic trapping mechanisms influencing dopant distributions and charge compensation. Additionally, we validate our results against deep-level optical spectroscopy (DLOS) data for V_{Ga}-related defects and experimental electron-donor concentration ratios in Sn-doped β-Ga_2O_3.

A key advancement is Sequential Quenching, bridging equilibrium and infinitely fast quenching models by incorporating defect-specific diffusion kinetics. This method allows semi-quantitative predictions of defect distributions in finite-sized samples subjected to realistic cooling rates. By freezing defects at distinct temperatures based on their diffusion constants, KROGER predicts spatial defect distributions across bulk crystals and thin films, enabling precise defect engineering strategies for optimizing material performance in power electronics.

This study highlights the necessity of integrating first-principles calculations with thermodynamic corrections to achieve predictive accuracy in defect modeling. KROGER provides a powerful and transferable framework for semiconductor defect engineering, setting a

benchmark for predictive modeling in electronic materials

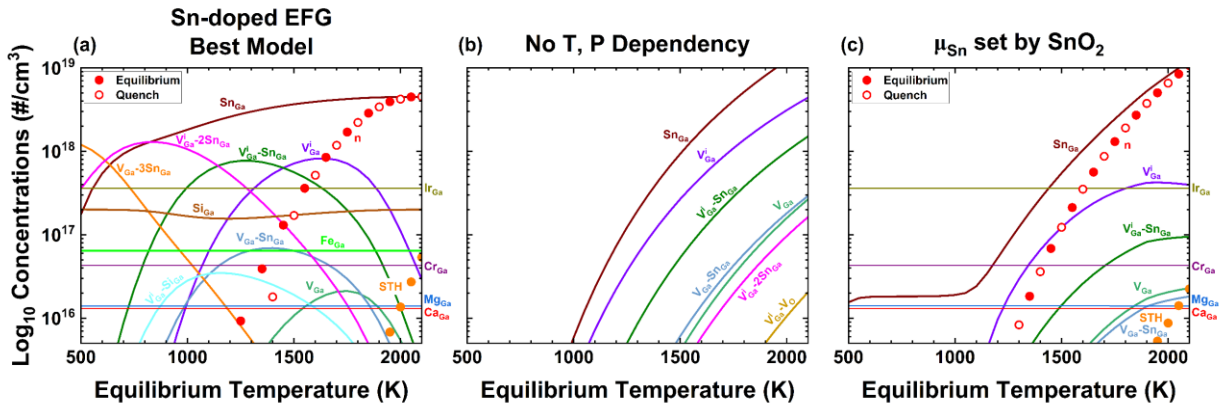

Fig. **1**. Defect Concentrations in Sn-Doped β-Ga_2O_3 Under Different Conditions. (a) Full temperature-dependent effects with fixed impurity concentrations at pO_2 = 0.02 atm, consistent with n-type conductivity and <1% compensation if native defects freeze-in by ~1950 K, (b) "O-rich, Sn-doped" conditions without temperature dependencies, incorrectly predicting insulating behavior with >99% compensation, (c) Sn solubility limited by equilibrium with SnO_2, requiring simultaneous freeze-in of native defects and Sn at ~1850 K, implying unlikely sensitivity to cooling rate. Evidence suggests kinetic trapping enables high [Sn] without SnO_2 precipitation.

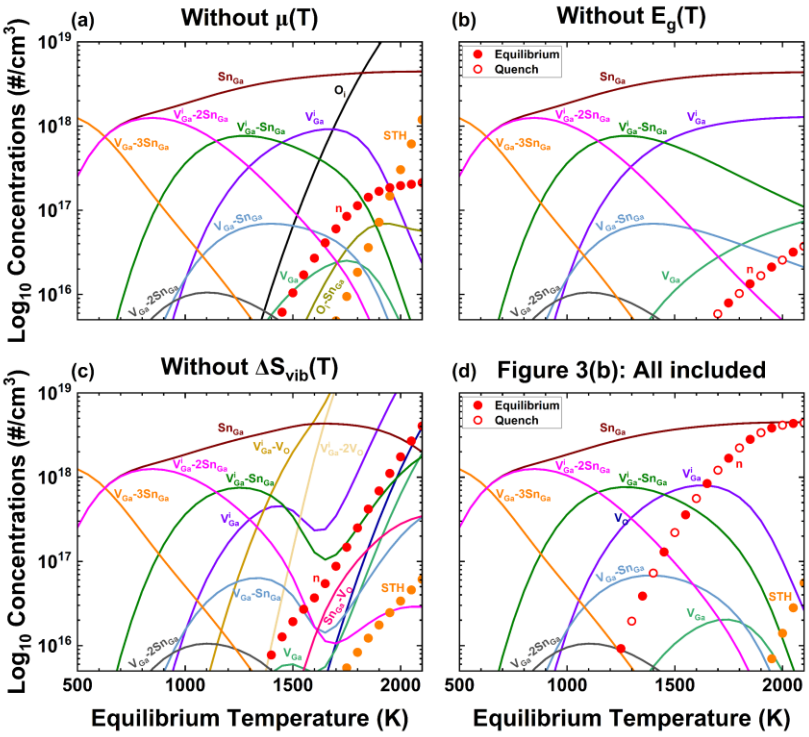

Fig. 2. Effects of omitting one temperature dependence at a time to investigate their importances. Conditions kept constant are [Sn]=4.5x10^{18} /cm^3 and f=0.40. (a) Adopting T-independent O-rich conditions as in Fig. 1(b) predicts O_i are the dominant compensating acceptors at high temperature and at no temperature does n=[Sn]. (b) Effect of E_g(T), N_C(T), and N_V(T) held constant at 300 K values, again there is no temperature where n=[Sn]. (c) Effect of omitting DS_{vib}(T) – here there is only one temperature at which n=[Sn] so coincidence would be required for agreement with experiments. Also, the concentrations of V_{Ga} and divacancy complexes increase to at% concentrations, which would be possible to measure. (d) Replication of Fig. 3(b) including all effects to facilitate side-by-side comparison.

[1] K. A. Arnab *et al.*, "Quantitative Modeling of Point Defects in $β$-Ga2O3 Combining Hybrid Functional Energetics with Semiconductor and Processes Thermodynamics,", *arXiv*: arXiv:2501.17373 (2025).

Wednesday 4:00-5:30 pm Molecular, Organic, and Optical

Time	Type	Presenter	Title
4:00-4:15 pm	Contributed	Patrizio Graziosi	Electron-phonon coupling and mobility modeling in organic semiconductors: a new and efficient methodology
4:15-4:30	Contributed	Zdenek Futera	Electron Transport in Biomolecular Junctions Studied by DFT and Tight Binding Approaches
4:30-4:45	Contributed	Muhamed Duhandžić	Charge carrier transport mechanisms in doped conjugated polymers
4:45-5:00	Contributed	Minsu Jeong	First-principles study of the quasi-Fermi level splitting in ferrocene-based molecular junctions
5:00-5:15	Contributed	Abdelilah Benali	Modeling strong light-matter interaction in polaritonic semiconductors as open systems
5:15-5:30	Contributed	Marcin Makowiec	NEGF computation of optical absorption in InAs/GaSb type-II superlattices

Electron-phonon coupling and mobility modeling in organic semiconductors: a new and efficient methodology

P. Graziosi, R. G. Della Valle*, and E. Venuti*
Institute for Nanostructured Materials, National Research Council, via Gobetti 101, 40129, Bologna, Italy
*Department of Industrial Chemistry, University of Bologna, via Gobetti 85, Bologna, Italy
e-mail: patrizio.graziosi@cnr.it

Abstract Submission

We have developed a first-principles method to calculate the electron-phonon coupling for specific modes and $\boldsymbol{q}$-points in the Brillouin Zone for crystalline organic semiconductors, which can be used to compute the corresponding mobility.

To validate our method, we compare the computed mobilities with available data for single crystals of naphthalene, anthracene and tetracene, finding a good agreement, especially when accounting for possible charged impurities.

Introduction

Organic Semiconductors (OSCs), based on abundant, eco-friendly, and cheap elements, have emerged as attractive candidates in several new electronic technologies. [1]

Two main approaches exist to describe charge transport in OCS: hopping and band transport via Boltzmann transport equation (BTE). The latter is particularly relevant for OSCs with orderly packed structures.

Here, we introduce a method to calculate and parametrize the electron-phonon coupling (EPC) in OSCs, and then use it to assess the mobility. We validate the overall method, Fig. 1, by comparing its results with experimental available data. [2]

Model

We employ DFT-VdW calculations using VASP, with the Phonopy package, to perform the simulations. The EPC at $\boldsymbol{q}$-point for phonon branch ν is computed as:

$$D_{\boldsymbol{q},\nu}^{n,n} = \frac{\partial t_W^n}{\partial r_{\boldsymbol{q},\nu}} , \qquad D_{\boldsymbol{q},\nu}^{n,m} = \frac{\partial \Delta_s^{n,m}}{\partial r_{\boldsymbol{q},\nu}} \qquad (1)$$

In (1), n and m are the band indexes, t_W^n is the transfer integral (¼ of the bandwidth) of band n, $\Delta_s^{n,m}$ the Davydov splitting between n and m, $r_{\boldsymbol{q},\nu}$ the average displacements of all the atoms along the eigenmode ($\boldsymbol{q}, \nu$). Then, we extract deformation potential values specific for band indexes and lattice phonon mode:

$$D_{n,m,\nu} = \frac{\sum_{\boldsymbol{q}} {D_{\boldsymbol{q},\nu}^{n,m}}^2 DOS_{\boldsymbol{q},\nu}}{\sum_{\boldsymbol{q}} DOS_{\boldsymbol{q},\nu}} \qquad (2).$$

The values in (2) are passed to the BTE solver *ElecTra* [3] to evaluate the charge mobility.

Validation

The calculation of the Raman spectra, Fig. 2, allows to validate the description of the electronic and vibrational structures. The comparison with experimental single crystal mobilities, Fig. 3-5, shows a very good agreement, which improves when we consider possible ionized defects, Fig. 6. Importantly, the method is more than one order of magnitude cheaper than DFPT-based approaches.

Conclusions

A method has been developed and validated, that combines DFT-level calculations and semiclassical transport simulations to compute the electron-phonon coupling and charge mobility in organic semiconductors. The accuracy of the method improves when including defects.

Acknowledgment

We acknowledge the CINECA award under the ISCRA initiative, funding from the European Union–Next-Generation EU via the Italian call PRIN 2022, project code 2022XZ2ZM8, "POLYPHON" and from M.M.B. s.r.l., Faenza (RA) Italy for the VASP license.

References

[1] Ö. H. Omar *et al.*, J. Mater. Chem. C 9, 13557 (2021).
[2] P. Graziosi *et al.*, Phys. Rev. Materials accepted, https://arxiv.org/abs/2407.18824.
[3] P. Graziosi *et al.*, Computer Physics Communications **287**, 108670 (2023).

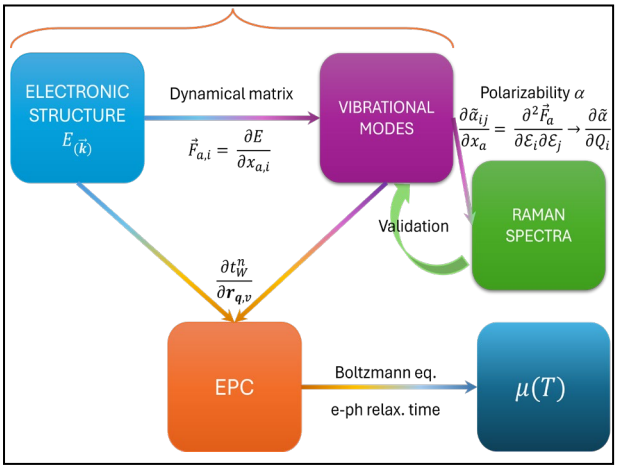

Fig. **1**. Scheme of the workflow from the electronic and phononic structure to the mobility μ.

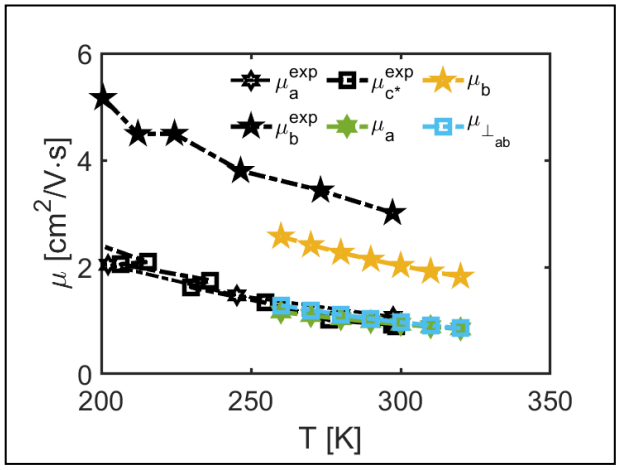

Fig. 4. Experimental and computed hole mobility of anthracene crystals along *a*, *b*, and c^* axes. [3]

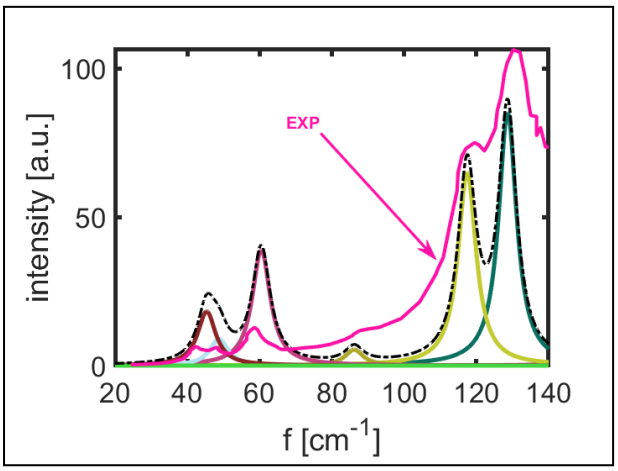

Fig. 2. Comparison of Raman spectra in the lattice phonons region of the bulk tetracene polymorph I; experimental (magenta) and computed (individual modes in colors and total in dash-dot black) spectra, ref. [3] and references therein.

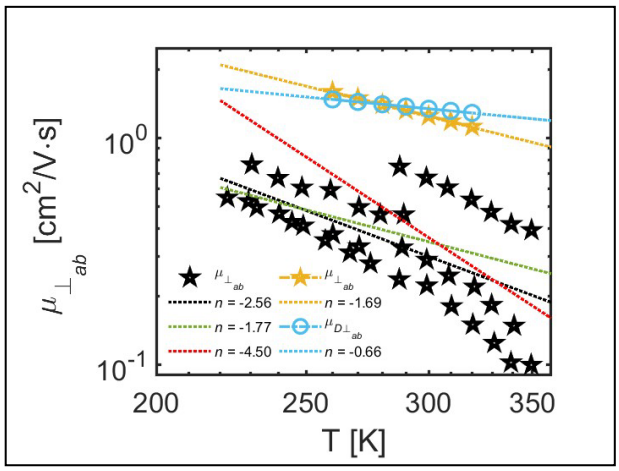

Fig. 5. Experimental vs computed hole mobility of tetracene crystals along the direction perpendicular to *ab* plane, $\mu_{\perp ab}$. The exponent of T^{α} fits are reported in the legend. μ_D is for the mobility evaluated from diffusivity via Einstein's relations. [3]

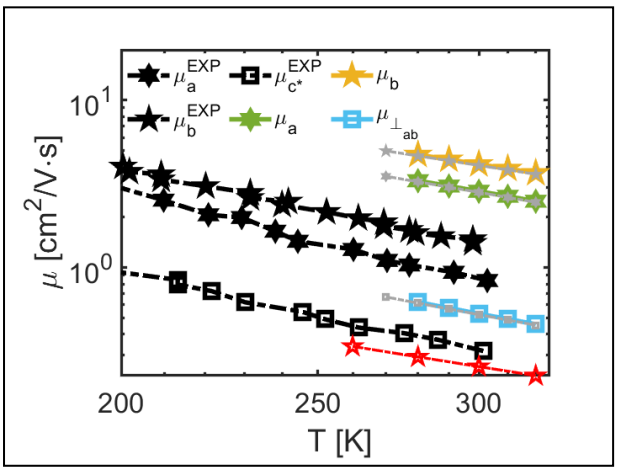

Fig. 3. Comparison of the hole mobility of naphthalene crystals along *a*, *b*, and $\perp_{ab}$ axes. In gray, elastic scattering with acoustic phonons is added; in red: μ_b from a computation based on DFPT which is ~ 30× more expensive, details in [3].

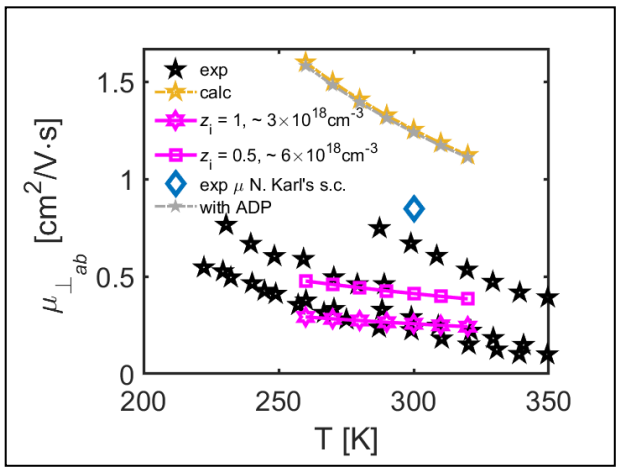

Fig. 6. Tetracene case as in Fig. 5, here magenta lines are for cases where scattering from ionized impurities of charge Z_i is included; Z_i = 0.5 mimics a charge spread over more sites, resembling extended charged defects, details in [3].

Electron Transport in Biomolecular Junctions Studied by DFT and Tight Binding Approaches

G. N. Jonnalagadda, L. Hronek, and Z. Futera
Faculty of Science, University of South Bohemia, Branišovská 1760,
370 05 České Budějovice, Czech Republic
e-mail: zfutera@prf.jcu.cz

INTRODUCTION

Biomolecular juntions can be nowadays almost routinely prepared and studied by scanning tunneling microscopy (STM) or atomic force microscopy (AFM) techniques. From theoretical point of view, the transport phenomena there can be described by quantum tunneling effects. However, the situation is more complex, when large redox-active biomolecules are investigated. While in a native aqueous environment, the electron flow through the system of redox sites proceeds by the thermally activated hopping mechanism, the temperature-independent currents of relatively high magnitudes were detected on protein/metal junctions, suggesting atypical long-range tunneling behavior. [1], [2]

METHODOLOGY

We investigate these electron-transport phenomena by means of computer simulations based on classical molecular dynamics (MD) as well as the first-principles description within the framework of density functional theory (DFT). [3], [4] While the incoherent hopping could be studied by combined quantum-mechanical/molecular-mechanical (QM/MM) techniques, [5] the coherent tunneling requires a quantum description of the whole interface models. Special care is taken to electronic–state alignment on the bio/metallic interfaces for which we apply the DFT+Σ scheme.

RESULTS

We systematically investigate these biomolecular junctions by quantum calculations based on tight-binding potentials (TB) and DFT. Different types of molecular junctions (benzene-1,4-diamine, benzene-1,4-dithiolate, Zn-porphyrin, Fe-heme) were investigated using non-equilibrium Green's function method (NEGF) and approximative approaches on the basis of Landauer formalism. Besides, electron transport properties of small redox proteins (STC, Cytochrome c, Cytochrome b_{562}, Azurin) in contact with gold electrodes were studied to elucidate the electronic states and transport conduction channels in such systems. [6]–[8] We show importance of the energy-level alignment on the bio/metallic contacts and discuss accuracy of different approaches to capture the transport phenomena.

REFERENCES

[1] K. Garg *et al.*, *Direct Evidence for Heme-Assisted Solid-State Electronic Conduction in Multi-Heme c-Type Cytochromes.* Chem.Sci. **9**, 7304 (2018)
[2] Z. Futera *et al.*, *Coherent Electron Transport across a 3 nm Bioelectronic Junction Made of Multi-Heme Proteins.* J.Phys.Chem.Lett. **11**, 9766 (2020)
[3] D. Biriukov, Z. Futera *Adsorption of Amino Acids at the Gold/Aqueous Interface: Effect of an External Electric Field.* J.Phys.Chem.C **125**, 7856 (2021)
[4] Z. Futera, *Amino-Acid Interactions with the Au(111) Surface: Adsorption, Band Alignment, and Interfacial Electronic Coupling.* Phys.Chem.Chem.Phys. **23**, 10257 (2022)
[5] O.V. Kontkanen, D. Biriukov, Z. Futera *Reorganization Free Energy of Copper Proteins in Solution, in Vacuum, and on Metal Surfaces.* J.Chem.Phys. **156**, 175101 (2022)
[6] Z. Futera, X. Wu, J. Blumberger *Tunneling-to-Hopping Transition in Multiheme Cytochrome Bioelectronic Junctions.* J.Phys.Chem.Lett. **14**, 445 (2023)
[7] K. Garg *et al. Shallow Conductance Decay Along the Heme Array of a Single Tetraheme Protein Wire.* Chem.Sci. **15**, 12326 (2024)
[8] G. N. Jonnalagadda, X. Wu, L. Hronek, Z. Futera *Structural, Solvent, and Temperature Effects on Protein Junction Conductance.* J.Phys.Chem.Lett. **15**, 11608 (2024)

FUNDING

The research is supported by Czech Science Foundation (GAČR) Grant No. 25-16698S.

Charge carrier transport mechanism in doped conjugated polymers

M. Duhandžić and Z. Akšamija
Materials Science and Engineering, University of Utah, 201 Presidents' Circle, 84112 Salt Lake City, UT, USA
e-mail: zlatan.aksamija@utah.edu

ABSTRACT

Carriers in conjugated polymers (CP) are localized over couple of molecular sites within the polymer chain. The inverse participation ratio (IPR) ranges between 1 in the tail to ~8 in the middle of the Gaussian density of states (DOS). Delocalized states deep in the DOS can be accessed through doping, which a priori leads to band-like transport. Conversely, dopant counterions create traps and an exponential tail in the density of states (DOS). However, the effect of doping on carrier delocalization is still not well understood. We capture transport properties of doped CPs by developing a tight-binding Hamiltonian that includes dopant-induced energetic disorder (DID) via Coulomb interactions. We show that carriers at the Fermi level localize with doping. This prohibits the occurrence of band-like transport in CPs. We anticipate our work to contribute to understanding of the underlying transport physics in CPs.

INTRODUCTION

Organic electronic materials are an environmentally friendly and low-cost alternative to inorganic semiconductors. Among them, conjugated polymers (CPs) are a broad family of organic semiconductors, and frequently employed as a platform for electronic devices. [1] Carrier transport in CPs occurs through phonon-assisted hopping between sites that are localized over several mer units. The number of units depends on the conformational disorder of the CP [2] and conjugation breaking. In the tail of the density of states (DOS) carriers are localized and the inverse participation ratio IPR = 1, while the IPR can be as high as ~8 in the middle of DOS. [3]

To increase their conductivity (σ), CPs are usually heavily (comparable to the density sites) doped. The increase in σ is attributed to carriers being more delocalized with doping and the transport changing from a hopping to band-like. Conversely, Coulomb interactions with dopant counterions impact carrier mobility by creating heavy tails in the DOS. However, the impact of dopants on delocalization and how that translates into carrier transport is not fully understood.

Here we show that doping localizes carriers close to the Fermi level and that the transport mechanism remains phonon-assisted hopping even at high doping. We include dopant-induced disorder (DID) via Coulomb interactions in our tight-binding (TB) Hamiltonian. We utilize perturbation theory to calculate the transition rates between states from eigenenergies and eigenfunctions. Then we solve Pauli master equation (PME) for site-occupational probabilities and compute transport properties of doped CPs. Our results stress the important role of DID in delocalization. Nevertheless, the effective IPR remains low (~2) even at high carrier concentrations (n).

MODEL

To capture the impact of doping, we add Coulomb interactions to the Gaussian disorder model according to the Arkhipov model [4] that includes carrier screening [5] of counterions with finite size R_d at a distance R_s from carriers. We set the resulting DOS as onsite energies of the TB Hamiltonian (20x20x20 sites) and the overlaps $t_{nk} = t$ as off diagonal elements. Solving for eigenvalues and eigenfunctions, we obtain the resulting DOS and wavefunctions. We calculate $\mathrm{IPR}_i = 1/\sum_j |V_j|^4$ for state i, where V_j are components of the eigenstate vector ψ_i. In order to understand the impact on the carriers that contribute to transport, we define the effective IPR as $\mathrm{IPR}_{eff} = \frac{1}{Z}\sum_i \mathrm{IPR}_i\, e^{-(E_i-E_F)/k_BT}$, where $Z = \sum_i e^{-(E_i-E_F)/k_BT}$ and E_F is the Fermi level. The transition rates can be calculated using [10]:

$$W_{ij} = \frac{\pi}{\hbar}\sum_q |M_{ij,q}|^2 \delta(E_i - E_j \pm \hbar\omega_q) \quad (1)$$

where $M_{ij,q} = u\langle\psi_i|dH/du|\psi_j\rangle$ is the electron-phonon coupling constant due to phonon mode q and displacement u [6]. In a nutshell, the phonon energy is $E = \hbar\omega\left(N(E) + \frac{1}{2}\right) = \frac{1}{2}m\omega^2 u(r)^2$. The phonon displacement contains two contributions given as the sum of distribution functions of downward and upward hops, $N(E) + 1$ and $N(E)$, respectively. Then in the continuum limit, for downward hops we obtain

$$W_{ij} = \frac{\pi\hbar}{\rho}\left|\left\langle\psi_j\left|\frac{dH}{du}\right|\psi_i\right\rangle\right|^2 \left(N(E_{ij}) + 1\right)\frac{D(E_{ij})}{E_{ij}}, \quad (2)$$

where $D(E_{ij})$ is the vibrational DOS and ρ mass density. Using these rates, we solve PME for the

distribution function and calculate σ and the Seebeck coefficient (α). [5]

RESULTS

The increase of overlap integral t, shifts and skews the DOS to higher energies as shown in Fig. 1a). t delocalizes carriers so that a large enough t leads to completely delocalized carriers and band-like transport. However, with DID the effective IPR is significantly lower as shown in Fig 1b). The effect of doping on delocalization overtakes and $\mathrm{IPR}_{eff} \approx 1$ even at high doping. The IPR at every energy is shown in Fig 1c) and d), for $R_s = 0.3$ nm and d) $R_s = 0.8$ nm, respectively. Below the Fermi level (thin solid lines), carriers are localized, while they remain delocalized deeper in the DOS.

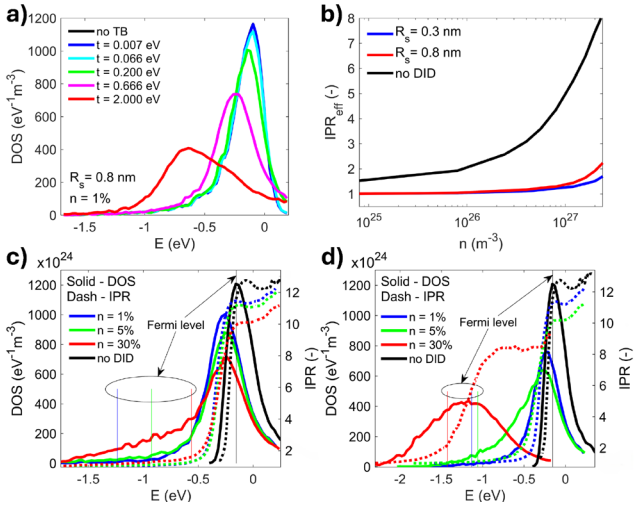

Fig. **1**. a) effect of overlap integral t on the DOS. Increasing t the DOS shifts and skews to higher energies. b) effective IPR with and without DID that shows carriers close to the Fermi level localize significantly with doping. DOS (left axis) and IPR (right axis) at different doping concentrations for c) $R_s = 0.3$ nm and d) $R_s = 0.8$ nm. The IPR at the Fermi level (thin solid lines) does not exceed 2 even at $n = 30\%$ in both cases.

An IPR_{eff} close to 1 indicates that the leading transport mechanism is carrier hopping between localized sites, even at high carrier concentrations. We test this hypothesis by comparing σ and α from the tight-binding (TB) to the same quantities simulated using phonon-assisted hopping (VRH) model (shown in Fig. 2 for a) $R_s = 0.3$ nm and b) $R_s = 0.8$ nm). $\sigma(n)$ and $\alpha(n)$ are essentially similar from both models. Qualitatively, in the TB model the Fermi level crossed the peak of the DOS at a lower n compared to the VRH, which is characterized by the change in sign of $\alpha(n)$ and a negative slope of $\sigma(n)$.

Although transition rates increase roughly as t^2, there is a trade-off between higher rates and the DOS being "too skewed", when the conductivity starts dropping with doping at $n < 50\%$. As a consequence, higher overlap does not necessarily increase conductivity (at every n) as shown in Fig. 3a) (left axis). At the point of conductivity drop, the Seebeck coefficient (α) changes sign, meaning that the Fermi level has crossed the peak of the DOS (right axis in Fig. 3a)), which confirms the previous statement. Both quantities are combined into the commonly plotted $\alpha(\sigma)$ curve shown in Fig. 3b). Qualitatively, the curve for realistic values of t (≈ 0.7 eV) is similar to the ones from simpler hopping models in which carriers are treated as completely localized. This is an important result that we anticipate will further advance the understanding of transport of doped organic semiconductors.

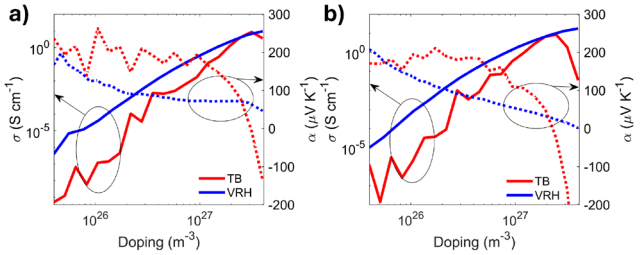

Fig. **2**. Compare of σ (left axis) and α (right axis) as a function of n simulated using the hopping (VRH) and our current (TB) model for a) $R_s = 0.3$ nm and b) $R_s = 0.8$ nm. Results indicate that hopping captures the underlying carrier transport physics in CPs.

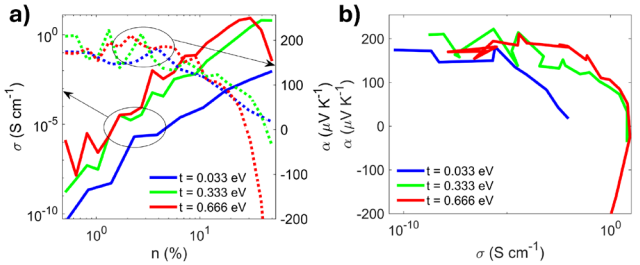

Fig. **3**. a) σ (left axis) and α (right axis) as a function of n that are combined in b) as $\alpha(\sigma)$. The switch in sign of α indicates that the Fermi level has crossed the peak of the DOS.

CONCLUSION

We utilize the TB Hamiltonian to simulate transport in doped CPs. We find that carriers localize with doping due to carrier-counterion Coulomb interactions and DID. Our results stress the importance of DID in carrier delocalization and we anticipate our work to be useful for further advancements in this field.

REFERENCES

[1] V. Leonov and R. J. M. Vullers, Journal of Renewable and Sustainable Energy **1**, 062701 (2009).

[2] N. Vukmirović and L.-W. Wang, The Journal of Physical Chemistry B **115**, 1792 (2011).

[3] D. Derewjanko *et al.*, Adv. Funct. Mater. **32**, 2112262 (2022).

[4] V. I. Arkhipov *et al.*, Physical Review B **71**, 045214 (2005).

[5] M. Duhandžić *et al.*, Physical Review Letters **131**, 248101 (2023).

[6] G. Zuo, H. Abdalla, and M. Kemerink, Physical Review B **93**, 235203 (2016).

First-principles study of the quasi-Fermi level splitting in ferrocene-based molecular junctions

Minsu Jeong, Jaeeun Kim, Ryong-Gyu Lee, Hyeonwoo Yeo, and Yong-Hoon Kim
Korea Advanced Institute of Science and Technology (KAIST), 291 Daehak-ro, Daejeon, 34141, Korea
e-mail: minsu.jeong@kaist.ac.kr

INTRODUCTION

While the splitting of quasi-Fermi levels (QFLs) represents a fundamental aspect in the finite-bias nonequilibrium operation of semiconductor devices [1], its atomic-level calculations remained a challenge due to the limitation in the standard approach combining density functional theory (DFT) and nonequilibrium Green's function (NEGF) formalisms. Another inherent shortcoming of the DFT-NEGF approach is its incapability of dealing with finite two-dimensional (2D) electrodes, because it requires semi-infinite electrode models. Both limitations can be overcome within the multi-scale constrained-search DFT (MS-DFT) formalism we recently developed [2,3]. In this report, we apply the MS-DFT formalism to ferrocene-based molecular junction sandwiched between metal and graphene electrodes [4,5], and analyze the transport properties of ferrocene.

MODELS & METHOD

Within the MS-DFT calculation for a semiconductor device, we assign the spatial origins of single-electron Kohn–Sham eigenstates within the junction system to the left electrode (L), channel (C), and right electrode (R) regions. Under the finite applied bias $V = (\mu_L - \mu_R)/e$, where μ_L and μ_R are the electrochemical potentials of L and R, respectively, the electrons in the C region are occupied by one group originating from L and right-traveling and the other group originating from R and left-traveling, resulting in QFL distributions within C [2].

RESULTS

In Fig.1, we modeled a ferrocene molecular junction system in contact with Au and graphene electrode. As shown in Fig.2, the junction shows the rectification operation due to the ferrocene formed an interface with graphene. Experimentally, the conductivity of junction increases/decreases depending on whether the Fe within the ferrocene undergoes reduction/oxidation, respectively [4,5]. In Fig.3 this charge transfer of Fe can be observed. Under a bias $V_{sd} = 1\,V$, Fe undergoes oxidation, resulting in low conductivity of the junction. As the bias decreases into $-1\,V$, the charge on Fe is depleted. It leads to increased conductivity in the molecular junction, so that the ferrocene junction exhibits diode operation. In Fig.4 and 5, the non-linear bias drop occurs at the gold-ferrocene and ferrocene-graphene junctions under positive and negative bias, respectively. This can be understood in terms of the hybridization of ferrocene with electrodes [3]. Under both biases, electrons are depleted from the HOMO state of ferrocene, effectively replacing the role of the gold/graphene electrode with its lower chemical potential. This depletion corresponds to the charge transfer of down/up state for $+1/-1V$ in Fig.3, respectively. At the graphene electrode under $V_{sd} = -1V$, a discrepancy arises between the electrochemical and electrostatic potential differences, with the applied electrostatic potential difference being smaller. This discrepancy is due to the quantum capacitance effect in graphene [3]. However, under positive bias, this quantum capacitance effect is absent. This occurs due to the hybridization of ferrocene with graphene, where ferrocene compensates for the lack of metallicity in graphene.

REFERENCES

[1] Shockley, W. & Read, W. T. Statistics of the Recombinations of Holes and Electrons, *Physical Review* **87**, 835-842 (1952).

[2] Lee, J., Yeo, H. & Kim, Y. H. Quasi-Fermi level splitting in nanoscale junctions from ab initio, *PNAS* **117**, 10142-10148 (2020).

[3] Kim, T. H., Lee, J., Lee, R.-G. & Kim, Y.-H. Gate- versus defect-induced voltage drop and negative differential resistance in vertical graphene heterostructures, *npj Computational Materials* **8** (2022).

[4] Jeong, H. *et al.* Redox-Induced Asymmetric Electrical Characteristics of Ferrocene-Alkanethiolate Molecular Devices on Rigid and Flexible Substrates, *Advanced Functional Materials* **24**, 2472-2480 (2013).

[5] Jia, C. *et al.* Redox Control of Charge Transport in Vertical Ferrocene Molecular Tunnel Junctions, *Chem* **6**, 1172-1182 (2020).

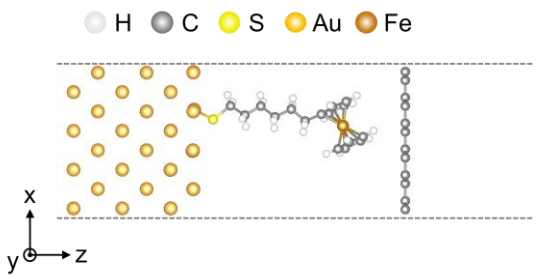

Fig. 1. Structure of ferrocenyl-alkanthiolate (ferrocene)-based molecular junction. We carried out MS-DFT calculations adopted the generalized gradient approximation PBE, double ζ-plus-polarization-level numerical atomic orbital basis sets, and the Troullier-Martins type norm-conserving pseudopotentials within the SIESTA software. The mesh cutoff of 200 Ry for the real-space integration was used. The k-point mesh was 3 x 3 x 1 Monkhorst-Pack grid.

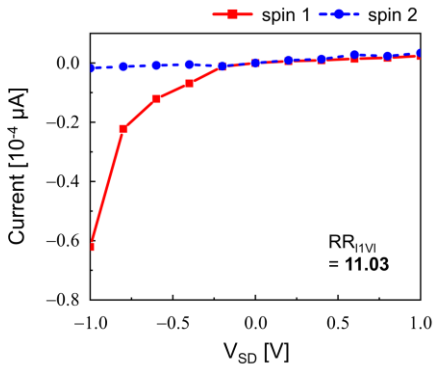

Fig. 2. The current–bias voltage (I-V) characteristics. calculated within MS-DFT. Red line with square and blue line with circles indicate the results corresponding to spin1 and spin2, respectively.

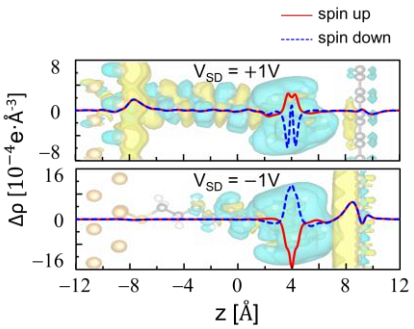

Fig. 3. The plane-averaged charge density differences or Landauer resistivity dipole $\Delta\rho$ for $V_{sd} = +1\,V$ (upper) and $V_{sd} = +1\,V$ (lower). It is defined as $\Delta\rho(r) = \rho^V(r) - \rho^0(r)$, where ρ^V and ρ^0 are the charge densities at the nonequilibrium and equilibrium conditions. Fe of the ferrocene locates at $z = 4$.

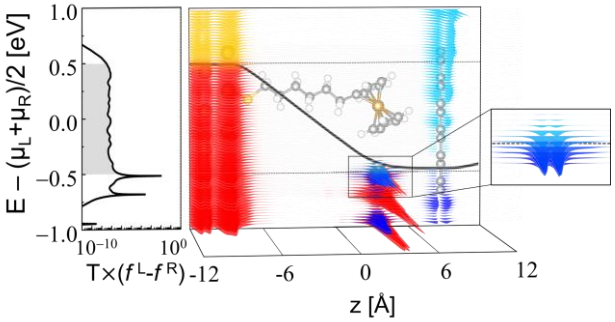

Fig. 4. Transmission, the non-equilibrium QFL profile and for $V_{sd} = +1\,V$ obtained from MS-DFT calculations. To account for the effect of the source-drain bias on electron transport, we multiply the transmission function by the bias window, $f^L - f^R$, which represents the difference in Fermi-Dirac distributions between the left and right electrodes. The red/blue color represents the electrons (occupied states, or QFL) originating from the left/right electrode, respectively. The orange and light blue color represent the unoccupied states. The red and blue peaks in the channel region (near $z = 4$) represent the states of ferrocene. The thin black dotted lines near $\pm 0.5\ eV$ indicate the chemical potential of source and drain electrode. The thick black line represents the plane-averaged bias-induced electrostatic potential change $\Delta\bar{v}_H$. It is defined as $\Delta\bar{v}_H(r) = \bar{v}_H^V(r) - \bar{v}_H^0(r)$, where $\bar{v}_H^V$ and $\bar{v}_H^0$ are the classical Hartree Coulomb potentials at the nonequilibrium and equilibrium conditions. The HOMO level is spin up/down for the -1/+1 V cases, respectively.

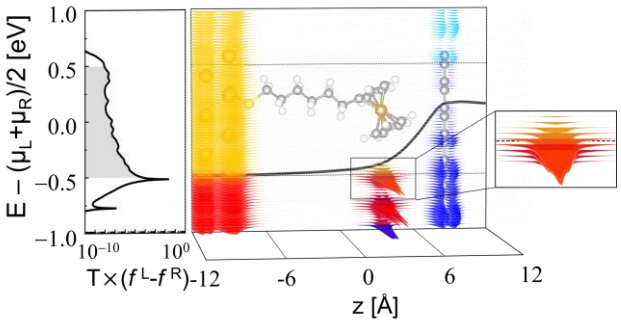

Fig. 5. Transmission, the non-equilibrium QFL profile and the plane-averaged bias-induced electrostatic potential change ΔV_H for $V_{sd} = -1\,V$ obtained from MS-DFT calculations.

Modeling strong light-matter interaction in polaritonic semiconductors as open systems

A. Benali, J. J. Seoane, X. Cartoixà, and X. Oriols
Department d'Enginyeria Electrònica, Universitat Autònoma de Barcelona, Spain
e-mail: abdelilah.benali@uab.cat

Introduction. The interaction between electrons ("matter") and electromagnetic fields ("light") within the same confined space has given rise to a new class of phenomena known as strong light-matter coupling regime : light and matter can no longer be treated as independent entities, but instead, they combine to form a hybrid physical entity known as a polariton which has already being implemented in various platforms. The goal of this work is to investigate polariton effects in semiconductor electron devices—specifically, quantum well heterostructures—at THz frequencies and room temperature (See Fig. 1(a)). We argue that this emerging phenomenon holds the potential to revolutionize electronics by naturally bridging electronics and photonics.

Although the quantum optics community has developed a robust understanding of the phenomenology of cavity quantum electrodynamics, and some experimental prototypes of operating at room temperature have been documented [1-4], the electronics community has largely overlooked these phenomena.

Model. The whole Hamiltonian of the light (q) and matter (x) (see Fig. 1(b) and 1(c)) is given by:

$$H = -\frac{\hbar^2}{2m}\frac{\partial^2}{\partial x^2} + V - \frac{\hbar\omega}{2}\frac{\partial^2}{\partial q^2} + \frac{\hbar\omega}{2}q^2 + \alpha q x,$$

where m is the electron mass, V is the potential profile of a quantum well, α is the coupling constant and ω the frequency of the optical cavity. A general solution of the Schrodinger equation is:

$$\Psi(x,q,t) = \sum_{n=0}^{N} \left(a_n(t)\phi_n(x)\psi_0(q) + b_n(t)\phi_n(x)\psi_1(q)\right),$$

where ϕ_n are the typical scattering states in tunneling scenarios (see Fig. 1(c)) and $\psi_{0/1}$ is the states of the light for $0/1$ photons (see Fig. 1(b)). Inside the quantum well, an electron in the ground state absorbs a photon and "jumps" to the exicted state, and then emits the photon into the cavity again (see Rabi oscillations in Fig. 2).

The typical polaritonic models found in the literature, such us Rabi and Dicke models, are developed for closed systems (i.e., the matter and the light do not escape from their cavities). However, a realistic physical system is never perfectly isolated and, in fact, intersubband polaritonic systems are based on electrons entering and leaving the quantum well. In this conferecne, we present a (semi) analytical formalism of the time evolution of such polaritonic systems in hetrostructures by seeking the energy eigenvalues and eigenestates of the whole polaritonic quantum systems.

We compute the traditional scattering states (which are energy eigenstates of the electron Hamiltonian alone, but not of the full electron-light Hamiltonian) as seen in Fig. 3. Then, we diagonalize the entire Hamiltonian to find the polaritonic energy eigenstates, which have a different spectrum from the electron-only states (see Fig. 1(d)). Once these eigenstates are known, we can analytically compute the full wavefunction evolution at any time to identify the optimal conditions for maximizing transmission (as an open system) and (Rabi) oscillations inside the well while electrons traverse the barrier region.

Conclusion. From the early days of electronics, the interplay between electrons and electromagnetic fields has played a fundamental role in technological advancements. In this conference, we demonstrate how this relationship can now be redefined through pure quantum interactions between light and matter, blending electronics and photonics for novel applications. By exploring this uncharted territory, our work aims to unlock the immense potential of polaritonic phenomena to sustain and transform semiconductor electronics.

Acknowledgement:

We acknowledge support from the Spain's Ministerio de Ciencia, Innovacion y Universidades under Grants PID2021-127840NB-I00 (MICINN/AEI/FEDER, UE) and PDC2023-145807-I00 (MICINN/AEI/FEDER, UE.

References

[1] D. K. Ferry, X. Oriols, J. Weinbub, IOP Publishing: Bristol, UK, (2023).
[2] C. F. Destefani, M. Villani, X. Cartoixa, M. Feiginov, and X. Oriols, PRB 106, 205306 (2022).
[3] T. Laurent et al. . Appl. Phys. Lett., 118(14), 141103 (2021).
[4] B. Limbacher et al. . Appl. Phys. Lett., 116(22), 221101 (2020).

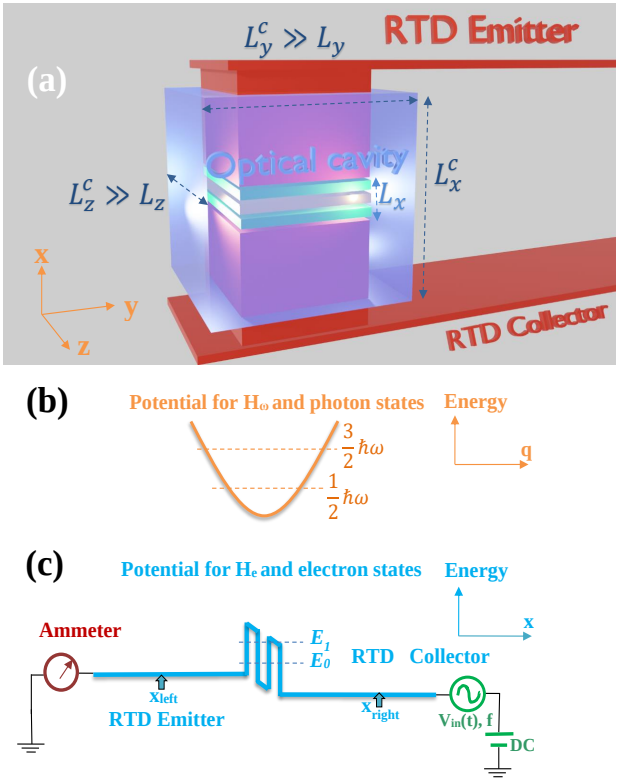

Fig. 1. (a) 3D spatial representation of the transport through a resonant tunneling diode (RTD) whose active region is inside a cavity, and whose transport direction size is much smaller than the lateral sizes, $L_y, L_z \gg L_x$. (b) zero-photon $|0\rangle$ and single-photon $|1\rangle$ states for the quantized single mode cavity field with energies $\hbar\omega/2$ and $3\hbar\omega/2$. (c) 1D-view of the RTD device showing ground $|0\rangle$ and first excited $|1\rangle$ electron states with energies E_0 and E_1; the light-matter interaction is effective only inside the active region, while a much larger simulation box is used to deal with open boundary conditions, with $X_{left,\,right}$ indicating the positions where wavepackets are initialized. (d) $|$electron,photon$\rangle$ states inside the RTD/cavity in the resonant strong coupling regime: state $|0,0\rangle$ almost unaffected; polaritonic states formed out of $(|0,1\rangle \pm |1,0\rangle)/\sqrt{2}$ split by $2E_r = 2\hbar\omega_r$ in comparison to the degenerate decoupled energies (dashed line); state $|1,1\rangle$ would create another polariton subspace, in a larger basis set, with state $|0,2\rangle$; $\omega_r = \alpha L_x/\hbar$ is the Rabi frequency.

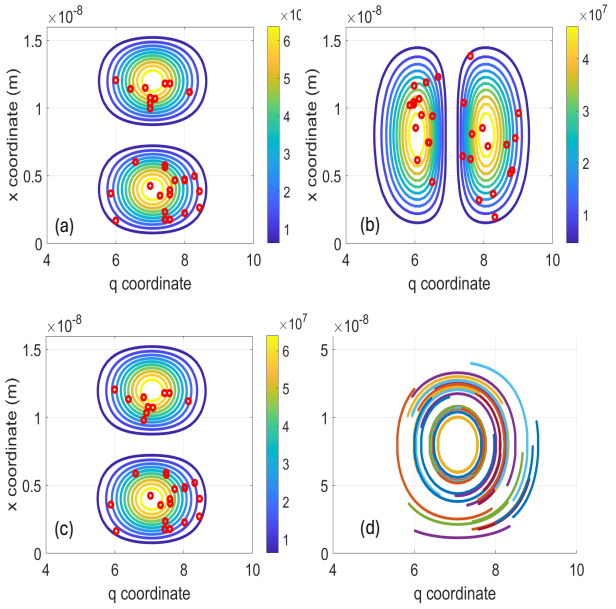

Fig. 2. Probability density of the wavefunction $\psi(x,q,t)$ in the $x-q$ configuration space at $t = 0fs$ (a), $t = 40fs$ (b), and $t = 80fs$ (c). Red circles indicate the positions of $M = 30$ Bohmian trajectories $x^j(t)$ and q^j (t) selected with random initial positions according to $\psi(x,q,0)|^2$. In (d), the continuous path of these trajectories is plotted, showing their (Rabi) oscillations.

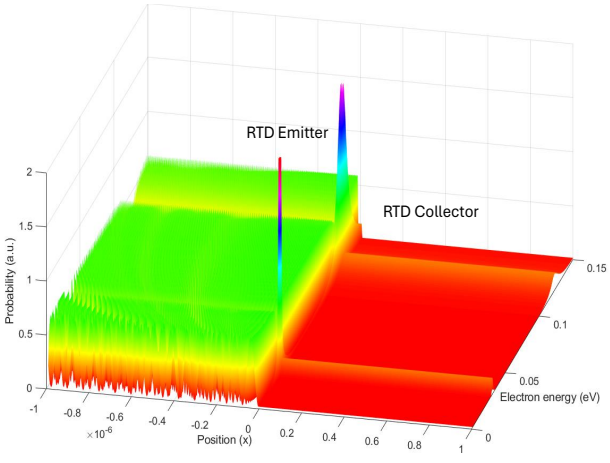

Fig. 3. Scattering states in the emitter, barrier and collector regions showing the openness of the RTD. These states are no longer energy eigenstates of the whole light matter system depicted in Fig. 1(d).

NEGF computation of optical absorption in InAs/GaSb type-II superlattices

M. A. Makowiec, and A. Kolek
Dep.of Electronics Fundamentals, Rzeszów UT, Al. Powst. Warszawy 12, 35-959 Rzeszów, Poland
e-mail: makum@prz.edu.pl

ABSTRACT

Optical properties of type-II broken gap semiconducting superlattice absorber are modelled within *interface layer approach*, using 8 band k·p Hamiltonian and nonequlibrium Greens function method. Good agreement with experiments over a wide range of temperatures for several structures is obtained for a common set of parameters, without the need for any adjustment. The studies cover the influence of scattering processes on absorption coefficient and miniband structure.

INTRODUCTION

In recent years, devices based on superlattice (SL) materials have attracted increasing attention. This is particularly true for the optoelectronics sector, which offers devices such as SL photo-detectors and quantum or interband cascade lasers. Due to their sophisticated architecture, complex band structure with nonparabolic dispersions, and technology-related features designing of such devices demands the use of numerical methods. Among them, the non-equilibrium Greens function (NEGF) method is one of the most advanced, since it is a fully quantum method. In the case of type-II SL (T2SL) absorbers, this method has been used to a very limited extent, mostly for studying the electronic transport [1][2]. In this paper the NEGF method is used for studying optical properties of T2SL InAs/GaSb absorbers. Results of numerical computations are compared with experiments showing good agreement. The benefits of the NEGF approach presented in the paper include, but are not limited to, studies of scattering-related features of the absorption coefficient and miniband tailing.

METHOD AND MODEL

The ingredient materials are modeled with the 8-band k·p Hamiltonian axially transformed to form two 4×4 uncoupled blocks [3]. Computations were performed separately for either of these blocks preserving the momentum representation for SL layers and the real space basis for the growth direction, z. The strain arising in SL structure was treated according to model solid theory [4]. All parameters were adopted from Vurgaftman's paper [5]. The size of simulated system was chosen to extend over two SL periods. The remaining part was accounted for through the boundary self-energies Σ_B which mimic the SL structure on both sides of the device. For this purpose the procedure of Ref. [6] formulated for multi-atomic layers of tight-binding Hamiltonians was adapted to SL case. The representative image of the simulated structure is depicted in Fig. 1. Results of the simulations are presented in Figs 2-6.

ACKNOWLEDGMENT

This research was supported by the National Science Centre, Poland, project No. UMO-2020/35/B/ST7/01830 (OPUS-19).

REFERENCES

[1] F. Bertazzi *et al*, *Nonequilibrium Green's Function Modeling of type-II Superlattice Detectors and its Connection to Semiclassical Approaches*, Phys. Rev. Appl. **14**, 014083 (2020).

[2] U. Aeberhard, *Theory and simulation of photogeneration and transport in Si-SiO$_x$ superlattice absorbers*, Nanoscale Res Lett **6**, 242 (2011).

[3] P.-F. Qiao, S. Mou, and S. L. Chuang, *Electronic band structures and optical properties of type-II superlattice photodetectors with interfacial effect*, Opt. Express **20**, 2319-2334 (2012).

[4] Van de Walle, *Band lineups and deformation potentials in the model-solid theory*, Phys. Rev. B **39**, 1871 (1989).

[5] I. Vurgaftman, J. R. Meyer, L. R. Ram-Mohan, *Band parameters for III–V compound semiconductors and their alloys*, J. Appl. Phys. **89**, 5815–5875 (2001).

[6] M. Luisier, A. Schenk, W. Fichtner and G. Klimeck, *Atomistic simulation of nanowires in the $sp^3d^5s^*$ tight-binding formalism: From boundary conditions to strain calculations*, Phys.Rev. B **74**, 205323 (2006).

[7] Y. Livneh *et al*, *K·p model for the energy dispersions and absorption spectra of InAs/GaSb type-II superlattice*, Phys.Rev. B **86**, 235311 (2012).

[8] J. V. Li et al, *Midinfrared type-II InAs/GaSb superlattice photodiodes toward room temperature operation*. Appl. Phys. Lett. **93**, 163505 (2008).

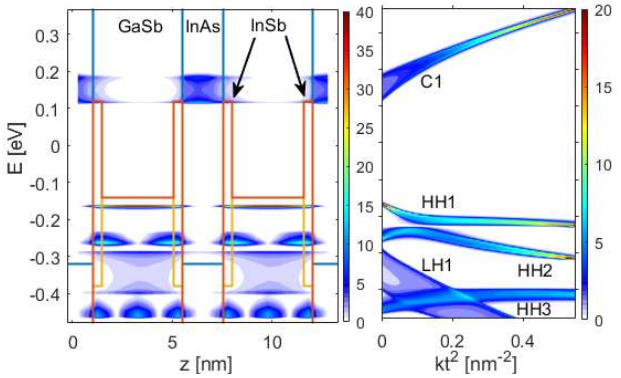

Fig. 1. Band diagram and position-resolved 1D density of states (left) and spatially averaged 1D density of states as a function of k^2 (right) calculated with the NEGF method for InAs/GaSb 25 Å/40 Å T2SL at 77 K. The arrows point at InSb layers, which are formed in SL with non-common-atom interfaces.

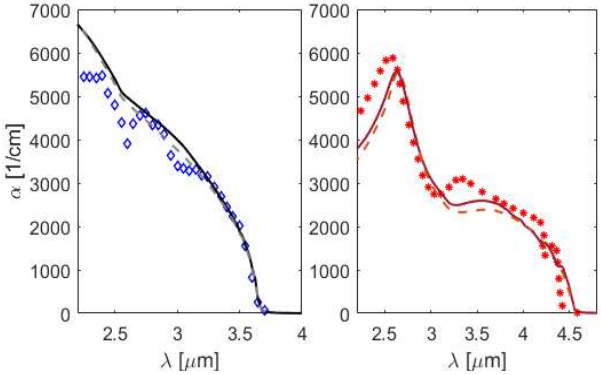

Fig. 2. Comparison between measured (symbols) and calculated (lines) absorption coefficient at 77 K for mid-wavelength infrared T2SL absorbers from Ref. [8] (left) and Ref. [7] (right). Calculations were performed using the NEGF method which includes (i) interface roughness scattering (IR) (dashed lines) and (ii) additional polar optical phonon scattering (solid lines). The main features of the absorption spectrum, its shape and magnitude as well as the cutoff wavelength agree very well.

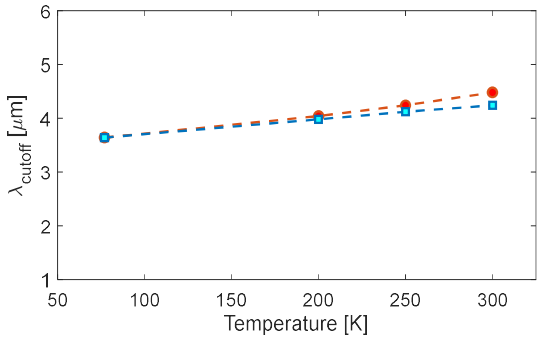

Fig. 3. Comparison between the cutoff wavelength of the absorption coefficient calculated using the NEGF method (circles) and experimental data [8] (squares) for an InAs/GaSb 18 Å/22 Å T2SL. Simulations for different temperatures were performed using identical set of parameters except of the lattice constant and the bandgap energy, for which the Varshni relation was used [5].

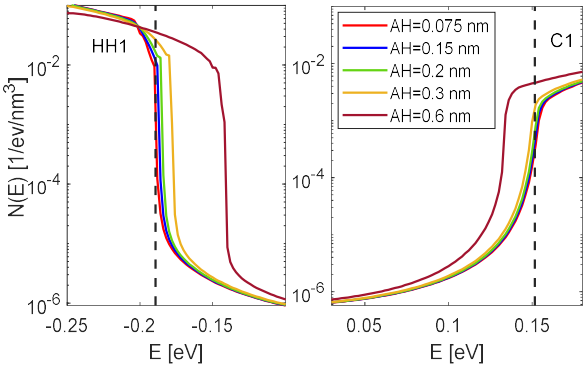

Fig. 4. Density of states calculated for an InAs/GaSb 18 Å/22 Å T2SL at 77 K. Dashed lines indicate edge of the C1 and HH1 minibands. Calculations were performed for different wales of asperity height (AH) of the interface roughness scattering included in NEGF method. With AH increasing, the bandgap narrowing (BGN) effect can be observed. In bulk materials such effect results from impurity scattering. The impact of IR-induced BGN on the absorption edge is shown in Fig. 5.

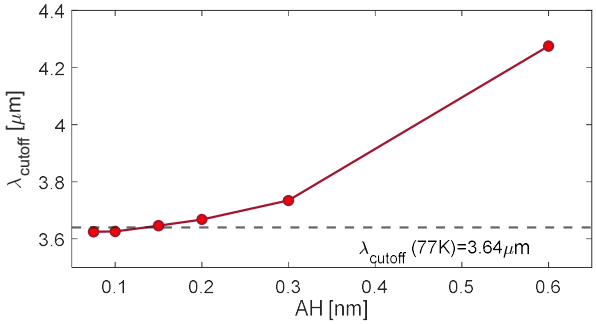

Fig. 5. The cutoff wavelength of the absorption coefficient calculated at 77 K using the NEGF method with interface roughness scattering for different values of asperity height (AH). The dashed line indicates the position of the absorption edge in experimental data [8].

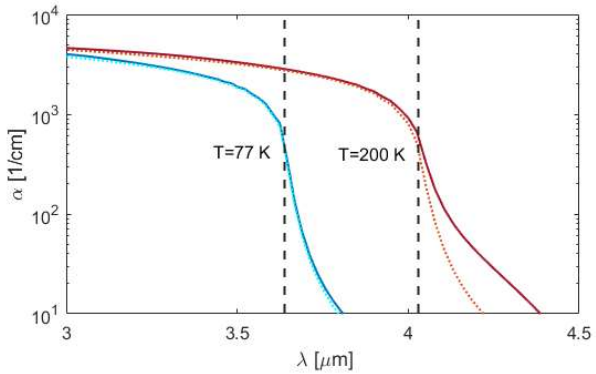

Fig. 6. Absorption coefficient calculated for an InAs/GaSb 18 Å/22 Å SL at 77 K (blue) and 200 K (red). Dotted lines represent data calculated with IR scattering, while solid lines represent data calculated with both IR and polar optical phonon scattering. Dashed vertical lines indicate the cutoff wavelength. The phonon contribution to the Urbach tail can be recognized at 200 K plot.

Wednesday 6:00-8:00 pm Poster Session

	Presenter	Title
1	Gerhard Klimeck	Changing the Typical Simulation Flow through Interactive Data Viewers and Drivers
2	Shuva Mitra	Theoretical modeling of twist-angle-dependent plasmon resonances in moire 2D materials
3	Mike Scarpulla	How Excess Carriers Change Steady State Concentrations of Point Defects
4	C.S. Soares	Design Considerations for a 5 nm n-FinFET using a Full-band Monte Carlo Simulator
5	Yeongjun Lim	Robust Mode Space Method for Heterostructure Transport Enabled by Machine Learning Approach
6	Min-Hui Chuang	A Calibrated Mobility Model for Monolayer Molybdenum Disulfide Device Simulation
7	Alan Carlos Junior Rossetto	Self-Heating and Hot Carrier Degradation Interaction in 28-nm FD-SOI pFETs
8	Dalton Zirbel	Theoretical modeling of quantum-well structures in dilute bismide optoelectronics
9	Nikiphoros Vlastos	Probing Light-Induced Isomerization Dynamics of Azobenzene Confined within Metal-Organic Frameworks: A Time-Dependent Density Functional Theory Investigation
10	Luca Gnoli	A computational approach to polymorphism in BDT organic semiconductors
11	Alathea Davies	Honeycomb-Kagome Band Structures of Highly Tunable Graphene-Like Covalent Organic Frameworks
12	Ali Jalali	Two-dimensional Magnetic Metal Organic Frameworks: Computational Study of Electron and Phonon Transport
13	Gowtham Nirmal Jonnalagadda	Electron Transport Mechanisms in Cytochrome b562 Junctions
14	David Mai	Importance of the Wigner equation for the analysis of the ballistic phonon transport
15	Aidan Belanger	Phonon Monte Carlo Investigation of Hydrodynamic Transport in Graphene Micro Ribbons
16	Alison Jensen	Atomistic Modeling Insights of Thermal Boundary Transport Between a Surrogate Fuel (CeO2) and a Fission Product (Pd)
17	Md Mobinul Haque	Elastic-Wave Modeling of Long-Wavelength Phonon Dynamics in Superlattice Nanowires With Rough Interfaces
18	Lucky K. Antonopoulos	A generalised framework for defining discrete Wigner functions via the Gottesman-Kitaev-Preskill code
19	V. Ganiu	Impact of Slope Limiters on DG Methods Solving Quantum-Liouville Type Equations
20	Xiaoyin Li	Topological Nodal-Point Superconductivity in Two-Dimensional Ferroelectric Hybrid Perovskites
21	Dongming Li	Nonlinear Eigenvalue Algorithms with Applications

Changing the Typical Simulation Flow through Interactive Data Viewers and Drivers

Daniel Mejia, Juan C. Verduzco, Alejandro Strachan, and Gerhard Klimeck*
Purdue University, Network for Computational Nanotechnology, West Lafayette, IN 47907, USA
*e-mail: gekco@purdue.edu

Computational device exploration is typically driven through few-point or a few swath-based simulations. This conventional research and learning process requires significant domain expertise to achieve meaningful results and has very high entry barriers to the field.

Our new *Interactive Data Viewers* enable the device community to turn this process around by starting the exploration from sets of available data and filling in simulation space gaps within the same environment. This flipped approach will accelerate both human and AI-driven exploration, enhance learning, and broaden participation. Although common in various research groups and in industry, no publicly available resource seems to allow such device exploration.

Two key challenges to achieving this vision are the data generation and data hosting. The FAIR (Findable, Accessible, Interoperable, and Reproducible) data principles [1] have laid out fundamental requirements for data stewardship. nanoHUB has paved the way for FAIR workflows, data generation, and hosting. In 2005, the nanoHUB team lowered the barrier to entry device design by creating scientific *Apps* that served as wrappers around complex simulation engines. At the same time, the team created the first scientific end-to-end user cloud before "cloud computing" became widely recognized. Since its inception, over 200,000 users have run millions of simulations on nanoHUB. Over 50% of simulation users are in formal classes and over 2,700 citations demonstrate research usage [2]. In 2010, we developed approaches to store simulation results to reduce compute load and to speed-up services [3]. To date, the platform has accumulated and curated 1.5 million datasets to 325 different Apps.

Figure 1 shows the modernized *PN-Junction App* [4] which runs web-native and retrieves data from our Sim2L [5] web service that runs the simulation tool *PADRE* [6]. Figure 1 depicts the coupled band edge diagram and I-V of a PN junction at high bias. Users can drag the voltage handle at the bottom to explore band edges as a function of bias. While standard textbooks use pages of mathematical derivations to explain ideal low voltage characteristics, they never show a realistic band diagram under high bias. Instead, they rely on pages of prose to discuss complex processes that cause non-ideal behavior (inset) without a real physical picture. With the new PN Junction Lab, students truly understand high bias behavior by running physics-based simulations.

Our *PNJunction Lab Exploration Tool, shown in Figure 2,* allows users to explore available PN Junction Lab results and populate the design space by requesting new simulations. New results generated in the active session are shown as green lines. Here we illustrate the resistive drop caused by the low doping in the P/N regions. The next user can visualize these new results without running new simulations in both Apps [3,7].

While nanoHUB app-generated data automatically follows FAIR principles, the development of simple and interactive front ends are needed to continue lowering barriers for use. We believe that this approach is applicable to most nanoHUB Apps and invite the community to contribute their simulation tools and scripts.

[1] M. D. Wilkinson, et al. (2016) "*The FAIR Guiding Principles for scientific data management and stewardship"*. Scientific data, 3(1), 1-9.
[2] N. K. Madhavan, M. Zentner, G. Klimeck, "Learning and research in the cloud", *Nature Nano* 8, 786– (2013)
[3] N Denny, M Zentner, D Mejia, G Klimeck, ""*Instant On" Science Gateways: An Introduction to Caching …..*", Gateways 2019, San Diego, California
[4] D Mejia, et al. "*PN Junction App*" https:// nanohub.org/ resources/pnjunctionapp. (DOI: 10.21981/ Q8D3-0502)
[5] Hunt, M., Clark, S., Mejia, D., Desai, S., Strachan, A. (2022). "*Sim2Ls: FAIR simulation workflows and data"*. Plos one, 17(3), e0264492.
[6] M R. Pinto, et al. "*PADRE*" https:// nanohub.org/ resources/padre. (DOI: 10.4231/D30C4SK7Z).~~).~~
[7] D Mejia, et al, "*PNJunction Lab Exploration Tool*" nanohub.org/resources/ex2pnjunction. (DOI: 10.21981/ 2E1V-AX20).

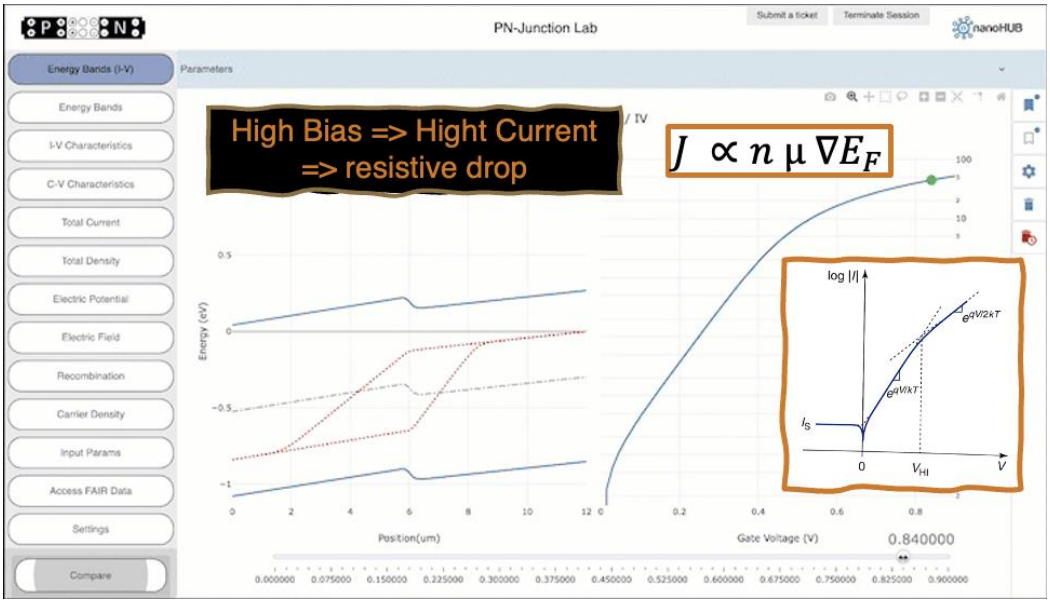

Fig. **1**. A moderately doped PN-junction at high bias in PN Junction App [3]. Users can change various device parameters and explore physical quantities (left panel). The App drives the Padre simulation engine which solves the problem though physics-based drift diffusion simulation [4] via a web service. The middle section shows a band edge diagram corresponding to the high bias current (green dot) on the I-V curve on the right. Users can change the voltage by dragging the slider on the bottom. The figure is augmented with an inset of a typical textbook indicating non-ideal device behavior. The equation suggests that under high current and insufficient charge density a Fermi level drop must occur. An increased carrier density induced by increased doping should compensate for a Fermi level drop. Users can increase the doping in the "Settings" button on the left and run a single simulation.

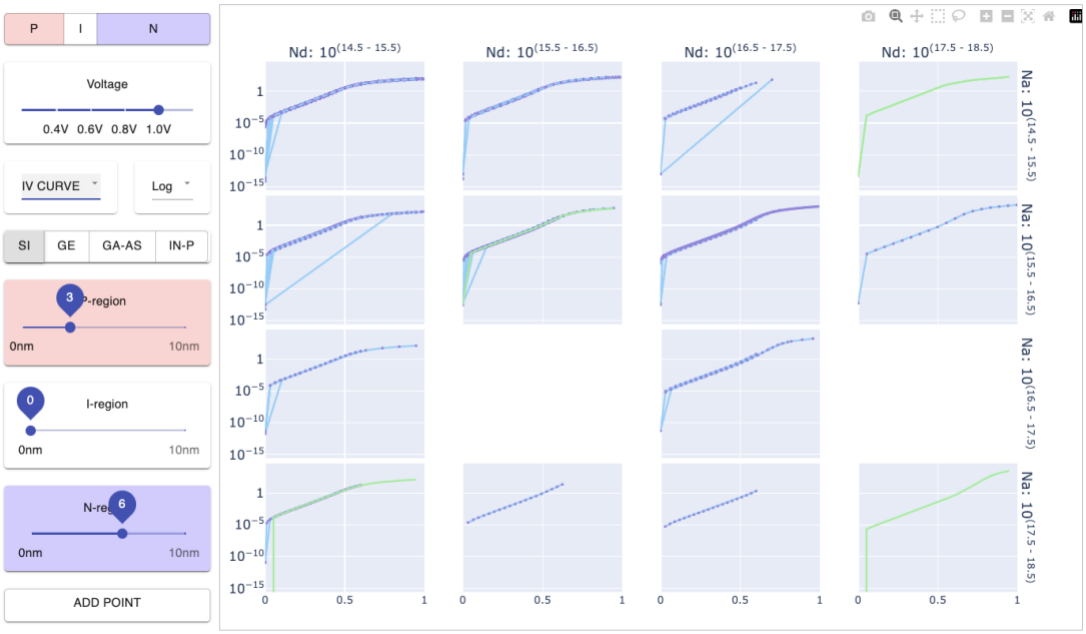

Fig. 2. View of the PN Junction Data App where we selected a high bias of 1V instead of the default value of 0.6V. The white spaces in the array of doping dependencies indicate a lack of data. The top right and bottom right quadrants were empty when we started this specific data view session. The bottom left was only filled to a bias of 0.6V. We then clicked on the "ADD POINT" button on the lower left and requested new doping data sets: ($Nd=10^{18}/cm^3$, $Na=10^{15}/cm^3$ top right), ($Nd=10^{15}/cm^3$, $Na=10^{18}/cm^3$ bottom left), ($Nd=10^{18}/cm^3$, $Na=10^{18}/cm^3$ bottom right), ($Nd=10^{16}/cm^3$, $Na=10^{16}/cm^3$). The generated results in this specific session are marked with green lines. A subsequent tool session by any other user will not see the distinction of green lines as they are now part of the available data sets. These new data sets are now also available precomputed in PN-Junction App (Fig. 1).

Theoretical modeling of twist-angle-dependent plasmon resonances in moiré 2D materials

Shuva Mitra and Irena Knezevic
Department of Electrical and Computer Engineering
University of Wisconsin-Madison, Madison, WI 53706, USA
smitra8@wisc.edu, irena.knezevic@wisc.edu

Moiré superlattices, formed by stacking two-dimensional (2D) materials with a twist angle between them or stacking two lattice-mismatched materials, have recently emerged as versatile platforms for exploring novel quantum phenomena [1]. In addition to the usual control parameters such as doping, gating, straining, and external electromagnetic fields, the twist angle provides additional control as the electronic properties of the materials highly depend on the twist angle. Figure 1 shows the emergence of moiré patterns in two single-layer graphene with a twist angle. The introduction of twist angle in moiré systems modifies the interlayer coupling and gives rise to flat electronic bands and miniband formation.

Surface plasmon polaritons, hybrid excitations that bear signatures of both electromagnetic waves and collective electron waves and are formed at the surface of materials, are highly sensitive to the electronic band structure and dielectric environment and can be generated in various structures such as nanoribbons and nanomeshes [2], [3]. Twist-angle-dependent bandstructure of moiré structures provides an ideal platform for plasmon generation and control. Plasmons in 2D materials can control light beyond the diffraction limit with potential applications ranging in nanophotonics, biological sensing, photovoltaics, and nonlinear optics.

In this work, we investigate plasmons in twisted moiré superlattices. By employing theoretical models based on tight-binding and continuum approximations, coupled with numerical simulation using the density matrix formalism, we aim to explore how the twist angle, interlayer coupling strength, and dielectric environment control plasmon dispersion, lifetime, and confinement. Figure 2 shows the angle-dependent bandstructure of twisted bilayer graphene calculated via the tight-binding model in the continuum limit. Furthermore, the presence of localized flat bands in certain twist angles, such as the magic angles in twisted bilayer graphene, can enhance the electron–electron interactions, potentially leading to exotic plasmonic modes. We hypothesize that the interplay between moiré-induced minibands and long-range Coulomb interactions will lead to tunable plasmonic modes with wavelengths far below the diffraction limit, making them suitable for extreme light confinement. By achieving controllable plasmonic resonance over wide infrared frequency range, twisted bilayer materials have potential nonlinear optics applications such as frequency comb generation. Additionally, the quantum nature of these plasmons in moiré systems could pave the way for hybrid quantum systems where plasmonic excitations couple with quantum emitters or other quasiparticles, such as excitons and phonons.

In conclusion, we presented a numerical study of plasmons in twisted bilayer 2D materials. Tuning the band structure and bandgap with twist angle provides a platform for generating tunable plasmons. This microscopic simulation results can be effective in designing in next-generation 2D material-based plasmonic and nonlinear optoelectronic devices.

ACKNOWLEDGMENT

This work was funded by NSF Award No. 2212011 ECCS, Splinter Professorship, and Vilas Distinguished Achievement Professorship (IK). Calculations were performed at CHTC (UW-Madison).

REFERENCES

[1] E. Y. Andrei and A. H. MacDonald, "Graphene bilayers with a twist," *Nat. Mater.*, vol. 19, no. 12, pp. 1265–1275, Dec. 2020.
[2] F. Karimi and I. Knezevic, "Plasmons in graphene nanoribbons," *Phys. Rev. B.*, vol. 96, no. 12, Sep. 2017.
[3] F. Karimi, S. Mitra, S. Soleimanikahnoj, and I. Knezevic, "Plasmon-enhanced optical nonlinearity in graphene nanomeshes," *Phys. Rev. B.*, vol. 108, no. 3, Jul. 2023.

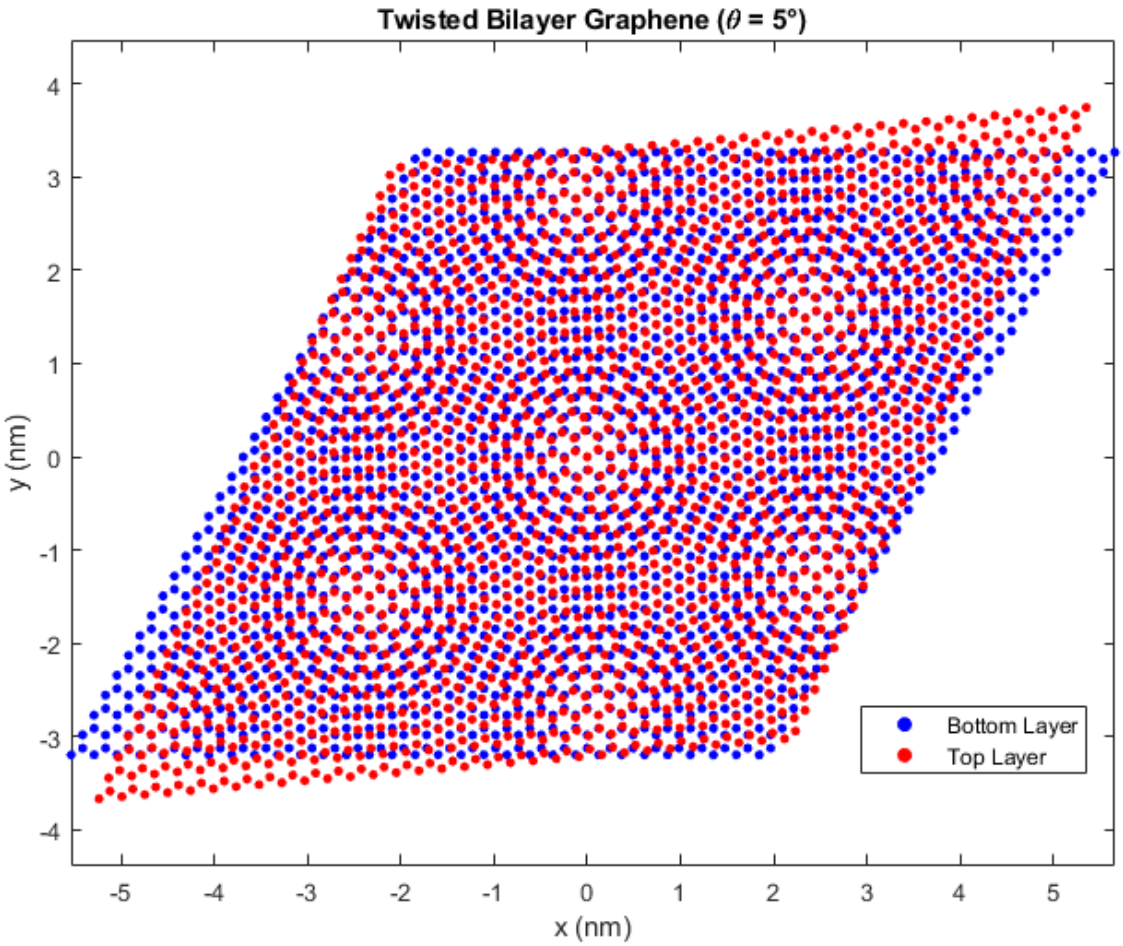

Fig. 1: Two graphene layers with a small twist angle between them creating a moiré pattern with large periodicity.

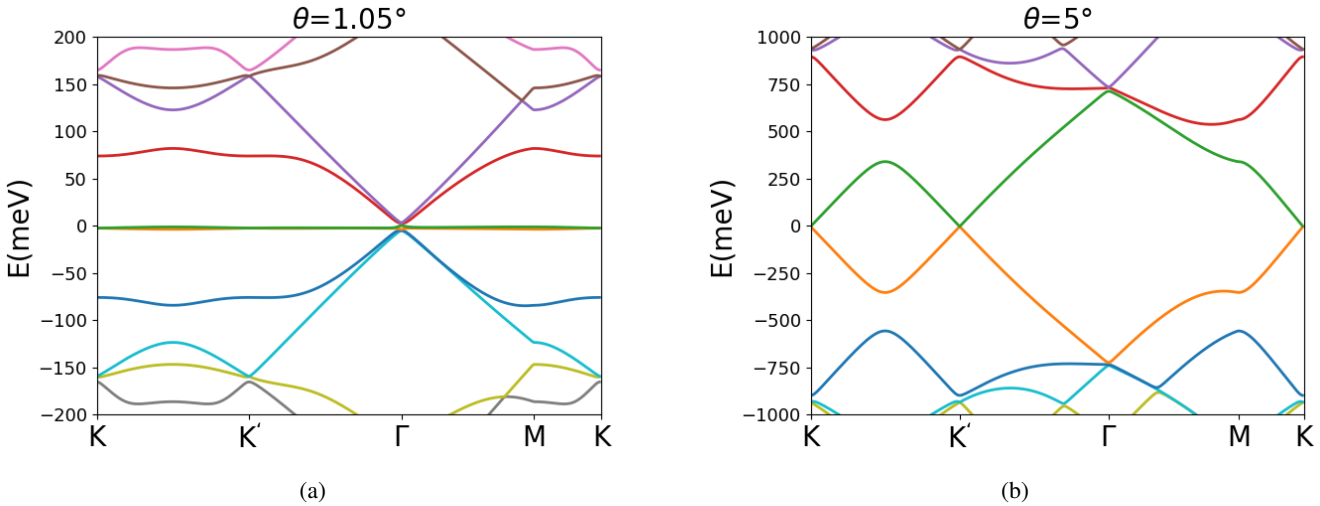

(a) (b)

Fig. 2: Twist-angle-dependent tunable bandstructure in bilayer graphene. (a) Flatbands at magic twist angle and (b) single-layer-graphene-like linear bands.

Design Considerations for a 5 nm n-FinFET using a Full-band Monte Carlo Simulator

C.S. Soares, M. Saraniti, and S.M. Goodnick
School of Electrical Computer and Energy Engineering, Arizona State University, Tempe, AZ, USA
e-mail: cdossan2@asu.edu

The industry substituted the planar transistor for the FinFET to continue Moore's law and avoid short-channel effects. The scaling rules for this transistor consist of increasing the fin height while reducing its width and the channel length. As the technology node advances, in addition to following the scaling rules, some design parameters should be considered to keep the desirable performance metrics and avoid short-channel effects. In this work, we investigate the role played by the source and drain doping density and the gate oxide interface quality in a state-of-the-art n-FinFET. To perform this study, a full-band cellular Monte Carlo simulator (CMC) [1] is employed.

In the CMC, the band structure of Si was calculated using the EPM, and the phonon dispersion was obtained using the 14-parameter model. The phonon scattering rate is calculated using the rigid-ion model. The ionized impurity scattering rate is obtained by assuming the Brooks-Herring approach and using Ridley's probabilistic screening for highly doped semiconductors. The impact ionization rate is estimated by the Keldysh model, and the difference between the energy states of the generated electron-hole pair is equal to the band gap. The roughness of the Si/SiO_2 interface is described as surface scattering using the Fuch's model. The Poisson equation is solved using a multigrid solver. The carrier-carrier interactions are taken into account in the solution of the Poisson equation.

The transport properties of electrons in Si were estimated to validate our transport model. Fig. 1 shows the electron velocity for a range of electric field, demonstrating that there is excellent agreement between the CMC and the experimental results [2]. Fig. 2 shows the low-field electron mobility in Si as a function of the doping density. The CMC results agree very well with the experimental [2] and empirical [3] results, while the MC simulation [4] diverges from the empirical results in the high doping range. Fig. 3 shows the structure of the 5-nm node n-FinFET. The Fin width and height are 5 and 50 nm, respectively, the EOT is 1.2 nm, and the channel length is 19 nm. The channel and substrate are p-doped ($N_A = 1 \times 10^{15} cm^{-3}$ and $N_A = 1 \times 10^{18} cm^{-3}$, respectively). Fig. 4 shows the $I_{DS} \times V_{GS}$ of transistors with S-D $N_D = 1 \times 10^{19} cm^{-3}$ and $N_D = 1 \times 10^{20} cm^{-3}$. The effect of source starvation is observed in the transistor with low doped S-D. Fig. 5 and Fig. 6 show, respectively, the $I_{DS} \times V_{GS}$ and $I_{DS} \times V_{DS}$ curves of FinFETs with different gate oxide qualities. The roughness of the oxide interface degrades the current and its impact is more pronounced in the sidewall interface.

The resistance of the S-D regions decreases by increasing N_D to $1 \times 10^{20} cm^{-3}$. The interfaces between Si and SiO_2, mainly the sidewall ones, should present high quality to prevent degradation of the on-current. As future work, the impact of strain on the transistor current will be investigated and the effective potential will be included to account for quantum confinement.

ACKNOWLEDGMENT

This work is supported by the Taiwan Semiconductor Manufacturing Company Ltd.

REFERENCES

[1] M. Saraniti and S. M. Goodnick, IEEE Transactions on Electron Devices 47, 1909-1916 (2000) doi: 10.1109/16.870571

[2] C. Jacoboni, C. Canali, G. Ottaviani, and A.A. Quaranta, Solid-State Electronics 20, 77-89 (1977). doi: 10.1016/0038-1101(77)90054-5

[3] G. Masetti, M. Severi and S. Solmi, IEEE Transactions on Electron Devices, 30, 764-769 (1983). doi: 10.1109/T-ED.1983.21207

[4] H. Kosina, G. Kaiblinger-Grujin, Solid-State Electronics 42, 331-338 (1998). doi: 10.1016/S0038-1101(97)00199-8

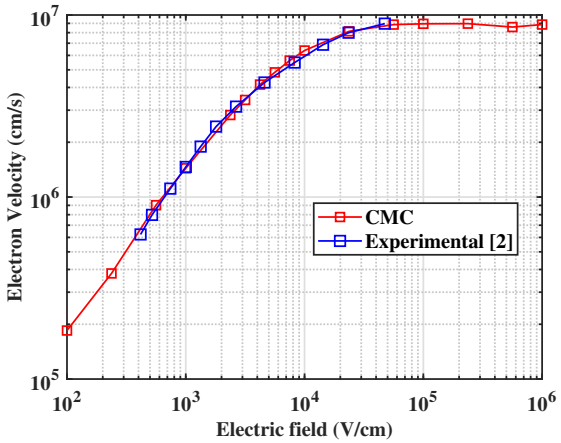

Fig. 1. Electron drift velocity as a function of electric field.

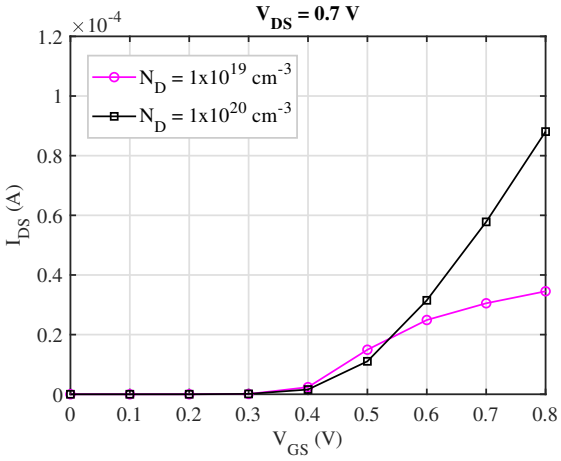

Fig. 4. $I_{DS} \times V_{GS}$ curves for FinFETs with distinct S-D doping.

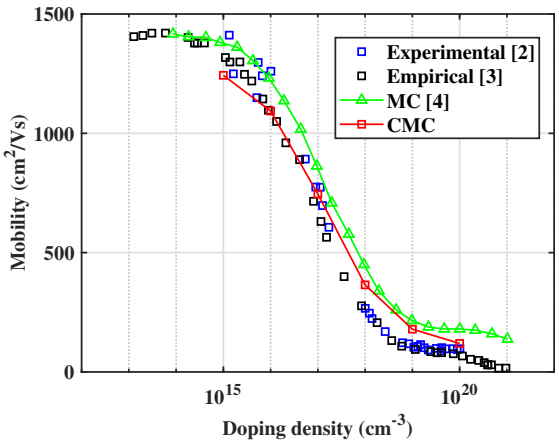

Fig. 2. Electron mobility as a function of doping concentration.

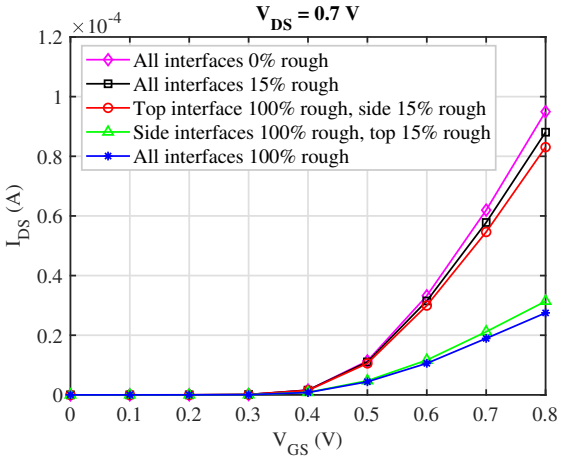

Fig. 5. Characteristic curves of FinFETs with different Si/SiO_2 interfaces.

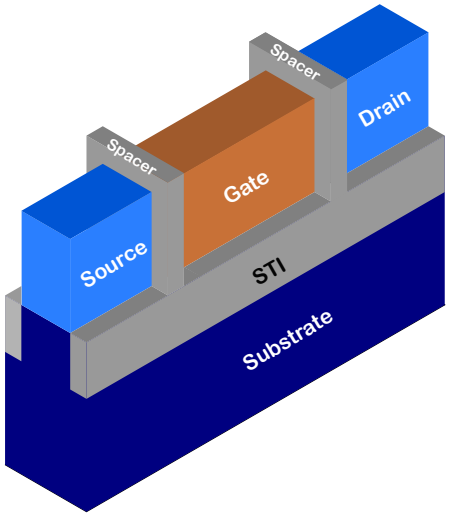

Fig. 3. Schematic of simulated 5-nm node FinFET.

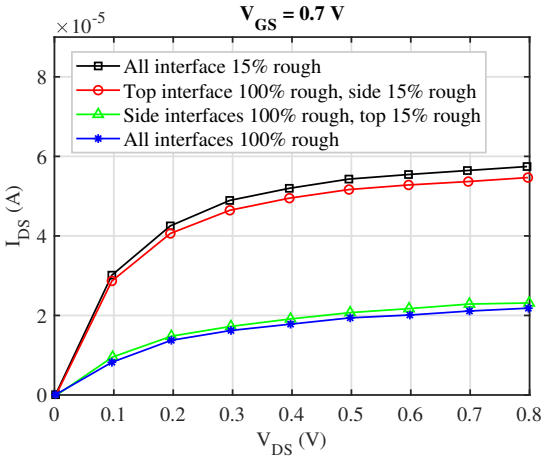

Fig. 6. Output curves of FinFETs with distinct Si/SiO_2 interfaces.

Robust Mode Space Method for Heterostructure Transport Enabled by Machine Learning Approach

Yeongjun Lim and Mincheol Shin
School of Electrical Engineering, Korea Advanced Institute of Science and Technology (KAIST),
Daejeon 34141, Republic of Korea
e-mail: mshin@kaist.ac.kr

INTRODUCTION

The non-equilibrium Green's function (NEGF) method combined with density functional theory (DFT) serves as a cornerstone of quantum transport simulation of nanodevices. However, its prohibitively high computational cost restricts its applicability to large-scale devices and parameter space explorations, posing a significant bottleneck for emerging nanoelectronic applications. The mode-space (MS) approach mitigates this issue by reducing the Hamiltonian dimensionality while preserving key transport characteristics [1,2]. Nevertheless, conventional MS methods struggle with non-orthogonal Hamiltonians, encountering challenges in basis selection and numerical stability leading to the need for manual efforts [2].

To address these limitations, we have developed a novel method that integrates parts of machine-learning (ML) techniques into the MS framework for homo-structure [3], which optimizes the transformation matrix U to improve computational efficiency while maintaining accuracy. Furthermore, we extend this approach to hetero-structures, where the complexity of multiple material interfaces introduces additional computational challenges.

METHOD

In this work, the transformation matrix U is initialized randomly and iteratively refined via a tailored network for the target system to accurately reproduce both the real and imaginary band structures and maximize the projectability between wavefunctions from the full and reduced Hamiltonians. By circumventing the need for manual basis selection, our approach overcomes conventional convergence issues, ensuring a stable and reliable transformation process.

For heterostructures, the device supercell is partitioned into fixed and trainable blocks as shown in Fig. 2 (a), allowing hierarchical optimization while maintaining computational efficiency. The final optimized U is then employed for NEGF-based transport simulations. The workflow of the method is shown in Fig. 1.

RESULTS AND DISCUSSION

We have applied our method to the GaSb/InAs broken-gap heterostructure depicted in Fig. 2 (a) for a tunnel FET simulation as shown in Fig. 3. The original full-Hamiltonian is obtained through DFT calculations. An optimal transformation matrix U is constructed to generate the reduced-size device Hamiltonian for transport simulations.

As shown in Fig. 2 (b), our method accurately reproduces the band structures of the target energy region. The reduced Hamiltonian for each cell has an average size of 59, approximately 9% of the original full-Hamiltonian size, as summarized in Table 1.

NEGF simulations confirm that our method faithfully reproduces key transport characteristics while significantly reducing computational cost. Fig. 4 (a) shows the band profile of the device at the ON-state, while Fig. 4 (b) presents the corresponding current spectrum demonstrating strong agreement with full-Hamiltonian results. These results demonstrate that our method accurately captures the complex tunneling properties within the hetero-junction, with high efficiency in transport simulations.

ACKNOWLEDGMENT

This research was supported by Basic Science Research Program of NRF Korea (RS-2023-00243425).

REFERENCES

[1] M. Shin, WJ. Jeong, and J. Lee, *Density functional theory based simulations of silicon nanowire field effect transistors,* J. Appl. Phys., **119**.15 (2016).
[2] M. Shin, *Hetero-structure mode space method for efficient device simulations.* J. Appl. Phys., **130**. 10 (2021).
[3] Y. Lim and M. Shin, *A Novel Machine-Learning Based Mode Space Method for Efficient Device Simulations*, SISPAD 2023.

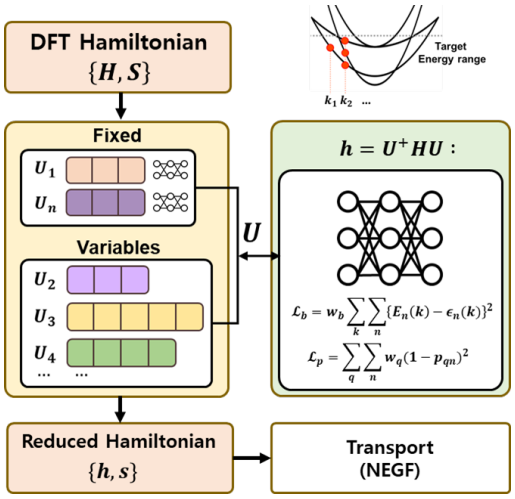

Fig. 1. Workflow of the proposed ML-assisted MS method for heterostructure transport simulations.

HAMILTONIAN REDUCTION

	L	JL2	JL1	JR1	JR2	R
Original H	616	616	616	616	616	616
Reduced H	50	50	70	70	58	58

Table 1. The sizes of the original Hamiltonian and the reduced Hamiltonian for the cells used in the transport simulation among the supercell cells in Fig. 2(a).

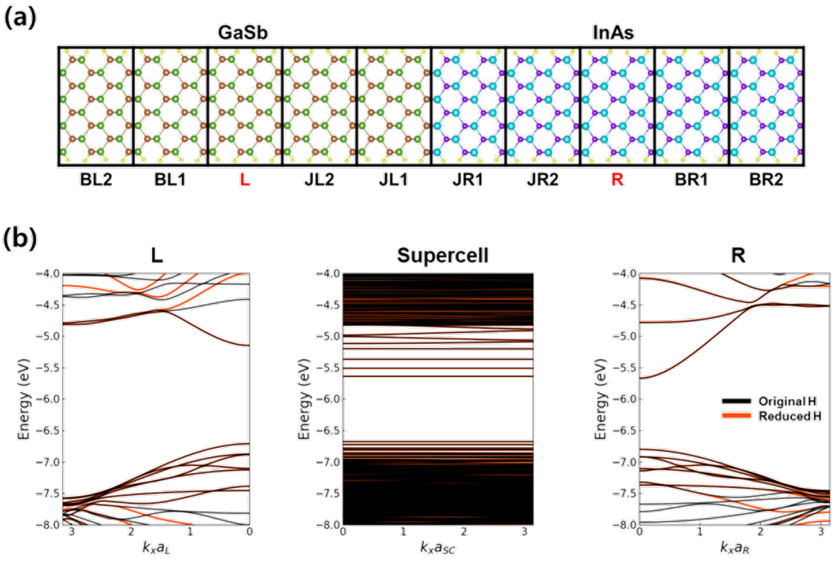

Fig. 2. (a) Atomistic configuration of 1.8 nm-thick GaSb/InAs hetero-juntion supercell with 160 Ga, 160 Sb, and 80 H atoms. The periodic boundary condition is imposed on the structure. For the heterostructure MS method, the L and R blocks are fixed, while remaining blocks are trainable. (b) Band structures of the L cell (GaSb), R cell (InAs), and 10-cell supercell (GaSb/InAs). a_L, a_R, a_{SC} represent the lateral lengths of the L cell, R cell and the supercell, respectively. The band structures are calculated at the longitudinal wave vector k_y = 0. The black and red lines represent the band structures obtained from original and reduced Hamiltonian, respectively.

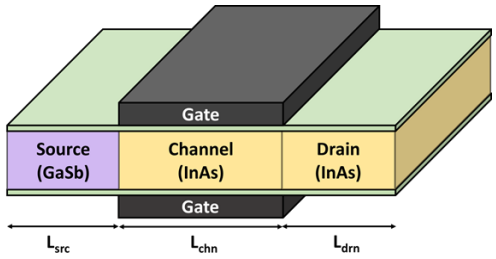

Fig. 3. Schematic of the simulated GaSb/InAs hetero-junction tunnel-FET of Fig. 2(a). The lengths of source, channel, and drain regions are 10 nm, 10 nm, and 20 nm respectively.

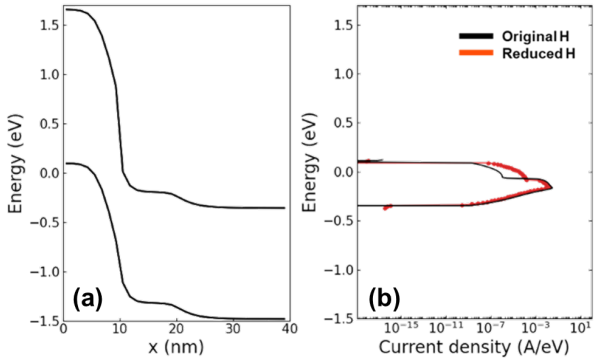

Fig. 4. (a) Band profiles and (b) comparison of the calculated current spectrum at ON-state using the original Hamiltonian (black line) and the reduced Hamiltonian (red dotted line). The applied drain bias V_{ds} is 0.5 V.

A Calibrated Mobility Model for Monolayer Molybdenum Disulfide Device Simulation

Yueh-Ju Chan[1,2], Min-Hui Chuang[1,2], Chieh-Yang Chen[1,2], and Yiming Li[1-3,*]
[1]Parallel and Scientific Computing Laboratory; [2]Institute of Communications Engineering; [3]Department of Electronics and Electrical Engineering, National Yang Ming Chiao Tung University, 1001 Ta-Hsueh Rd., Hsinchu 300093, Taiwan. *E-mail: ymli@nycu.edu.tw

Abstract

This work reports a physical-based mobility model including remote phonon and coulomb scatterings for device simulation of monolayer (ML) molybdenum disulfide (MoS_2) devices. The results adding with electronic structure of ML MoS_2 using density functional theory (DFT) simulation as well as calibrating the contact resistance can properly fit edge contact gate-all-around (GAA) nanosheet (NS) and top contact back gate (BG) FETs well.

Introduction

Recent studies have showed when MoS_2 is deposited on high-κ thin layer oxide, such as HfO_2 and Al_2O_3, it exhibits a higher mobility [1-2]. MoS_2 devices may have superior characteristics and have been studied as a potential candidate for advanced CMOS technologies [3-4]. Computationally, MoS_2 devices are simulated by DFT with nonequilibrium Green's function (NEGF) [5] which provides the most accurate results; however, huge computational resources limit studies of complicated cases. Thus, integrating DFT calculation into device simulation, after validation with results of DFT and NEGF, enables us to explore devices effectively [6].

This study implements a physical-based model by carefully calibrating with Boltzmann transport equation (BTE) for ML MoS_2 device simulation. By adding tunneling gap and contact resistance, we do further calibrate the results with fabricated devices.

The Device Simulation

The results of DFT simulated ML MoS_2 are listed in Table 1. We model the mobility based on remote coulomb scattering (RCS) and remote phonon scattering (RPS) and enhance the accuracy of device simulation by calibrating the results with BTE based on coulomb and phonon scatterings [7, 8] (Fig. 1). It is then applied to device simulation of edge contact GAA NS and top contact BG FETs [3, 7] (Fig. 2). For metal contacts, different simulations are considered for edge and top contact, respectively, devices. In the edge contact, contact resistance is included at the source and drain (S/D), while in the top contact, Wentzel-Kramers-Brillouin (WKB) tunneling with a Schottky contact is used at the interface between the S/D and the varying tunneling gap. The Schottky barrier height between S/D and MoS_2 channel is -0.05 eV. The thickness of tunneling gap (Fig. 3), based on the relaxation of DFT simulation, considers Antimony (Sb) and Bismuth (Bi) contacts.

Results and Discussion

According to the BTE transport, coulomb impurities scattering could be the most significant effect in MoS_2 mobility. If positive charge appears in the channel of MoS_2, due to the 2-D properties of MoS_2, showing screening potential at both sides of the oxide. This causing the coulomb impurity scattering appears. For the coulomb impurity scattering using remote coulomb scattering, we have

$$\mu_{rcs} = \mu_{rcs0}\left(\frac{c}{c_0}\right)^{\gamma_{rcs}} \quad (1)$$

where μ_{rcs} and μ_{rcs0} are the factors for calibration, c is the electron density, and $c_0 = 1.4\times10^{19}$ cm^{-3}. For the phonon scattering, based on conventional phonon scattering μ_{ph} with remote phonon scattering, it is

$$\mu_{rps} = \frac{\mu_{rps0}}{\left(\frac{F_\perp}{10^6\ \mathrm{V/cm}}\right)^{\gamma_{rps}}} \quad (2)$$

$$\mu_{ph\_theory} = {\mu_{ph}}^{-1} + {\mu_{rps}}^{-1} \quad (3)$$

where $F_\perp$ is the transverse field, μ_{rps0} and γ_{rps} are the calibration factor. Matthiessen rule in Eq. (3) adding coulomb and phonon mobility in Fig. 1(b) shows the result that could calibrate with BTE under the values of calibration factors in Table 2.

The mobility and electronic structure from DFT are used for device simulation of edge contact 40 nm gate length GAA NS FET (listed in Table 3). By adding the contact resistance from S/D showing with the calibration on phonon mobility factor matches the I_D-V_G curve (Fig. 4). We then explore the fabricated top contact devices. Due to the ultrathin body of MoS_2, making the top contact of S/D forming an inevitable tunneling gap. Using the First-principle method for relaxation between the metal and MoS_2, Fig. 5 shows the results of top contacts of Sb and Bi. The tunneling gap of two semimetal contact are equal to 3Å and 5Å. By using the calibration of phonon scattering, the calibration of I_D-V_G curve of contact with Sb and Bi are fitting well. The detail results for the calibration of BG FET are listed in Table 4.

Conclusion

We have reported a physical-based mobility model based on remote coulomb and phonon scatterings for ML MoS_2 device simulation. Considering the effects of contact resistance, we have fitted the fabrication results of edge contact GAA NS FET and top contact BGFET by calibrating the phonon scattering factors. Mentioned of the top contact of BGFET, we adding tunneling gap can lead to further simulating the transfer length and contact length.

Table 1. Listed of DFT simulated electronic structures including bandgap, electron affinity, effective mass, dielectric constant, and channel thickness.

Electrical Properties	ML MoS_2	silicon
Band gap (E_g)	1.78 eV	1.12 eV
Electron affinity (χ_e)	4.26 eV	4.08 eV
Effective mass (m_e^*)	4.59 m_0	0.19 m_0
Dielectric constant (ε)	4.8 ε_0	11.7 ε_0
Channel thickness (t_{ch})	0.65 nm	5 nm

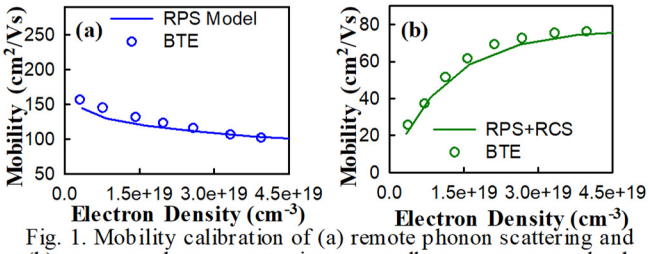

Fig. 1. Mobility calibration of (a) remote phonon scattering and (b) remote phonon scattering as well as remote coulomb scattering, comparing with BTE model [7, 8].

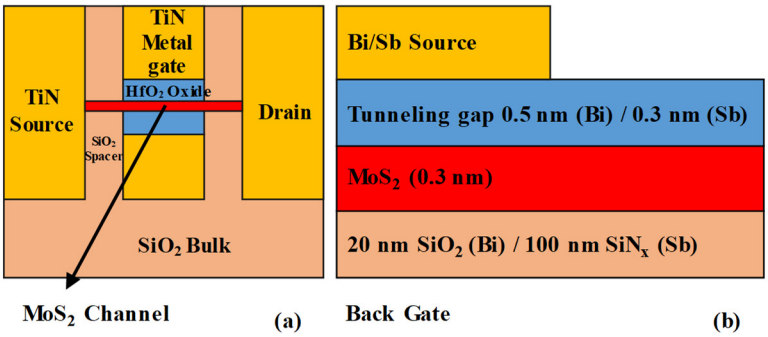

Fig. 2. Schematic plot of the (a) edge contact GAA NS FET and (b) top contact BG FET, where the detail properties of the structure are listed in Table 3.

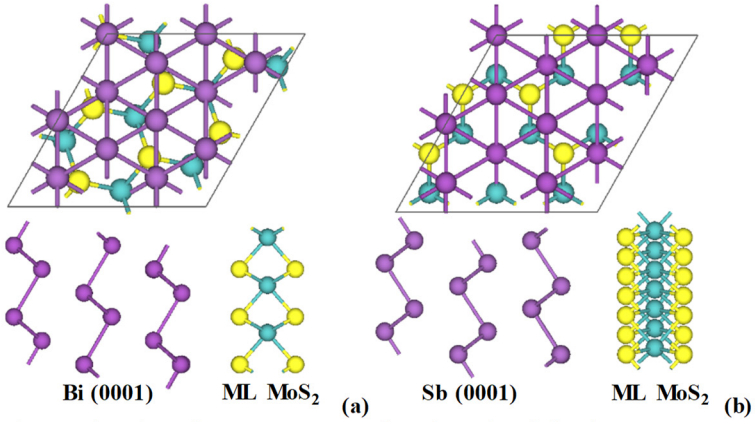

Fig. 3. Relaxation of top contact properties of (a) Bi and (b) Sb.

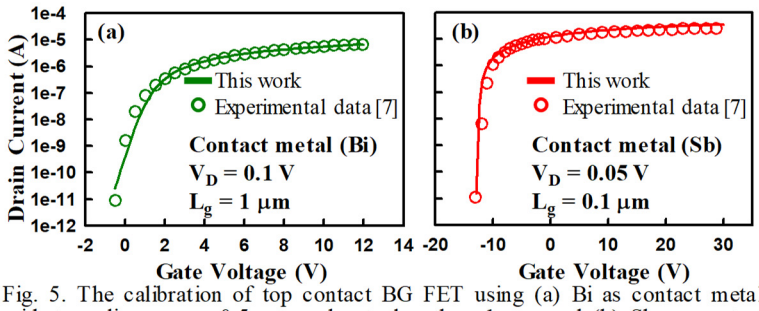

Fig. 5. The calibration of top contact BG FET using (a) Bi as contact metal with tunneling gap = 0.5 nm and gate length = 1 μm and (b) Sb as contact metal with tunneling gap = 0.3 nm and gate length = 0.1 μm.

Table 2. The extracted parameters of the remote coulomb scattering and the remote phonon scattering of the explored mobility of the ML MoS_2, calibrating with BTE model.

Factors	Value
μ_{rcs0}	8
μ_{rps0}	280
g_{rcs}	1.15
g_{rps}	0.5
μ_{ph}	350

Table 3. The detail structure parameters of edge contact GAA NS FET.

Parameter	Value
L_g	40 nm
W	50 nm
t_{ox}	5 nm
EOT	0.9 nm

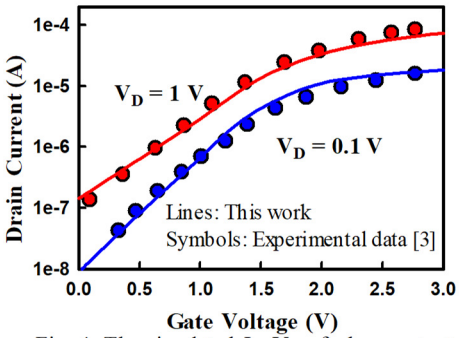

Fig. 4. The simulated I_D-V_G of edge contact GAA NS FET at linear (V_D = 0.1 V) and saturation (V_D = 1 V) regions.

Table 4. List of the calibrated parameters of Bi and Sb BG FETs.

Metal	Bi	Sb
Interface traps (cm^{-2}/eV)	1.2×10^{13}	3×10^{12}
Fixed charge (cm^{-3})	-8×10^{11}	6×10^{12}
SBH (eV)	-0.05	-0.05
Oxide	20-nm SiO_2	100-nm SiN_x

ACKNOWLEDGMENT

This work was supported in part by the National Science and Technology Council (NSTC), Taiwan, under Grant NSTC 113-2221-E-A49-094 and Grant NSTC 113-2218-E-006–019-MBK, and in part by the 2025 JDP of TSMC.

REFERENCES

[1] K. F. Mak et al., Phys Rev Lett, vol. 105, p. 136805, 2010. [2] B. Radisavljevic et al., Nature Nanotech, vol. 6, Art. no. 3, 2011. [3] Y.-Y. Chung et al., in IEDM, Feb. 2022, p. 34.5.1-34.5.4. [4] X. Xiong et al., in IEDM, Feb. 2021. [5] Y. Yoon et al., Nano Lett., vol. 11, p. 3768–3773, 2011. [6] A. Pon et al., in EDSSC, p. 1–3, 2019. [7] D. M. Sathaiya et al., in IEDM, Feb. 2022, p. 28.4.1-28.4.4. [8] Z. Jin et. al., Phys. Rev. B, 90, 045422, 2014.

Self-Heating and Hot Carrier Degradation Interaction in 28-nm FD-SOI pFETs

A.C.J. Rossetto, C.S. Soares*, D. Vasileska*, and G.I. Wirth†
Universidade Federal de Pèlotas, Pelotas RS, Brazil
*Arizona State University, Tempe AZ, USA
†Universidade Federal do Rio Grande do Sul, Porto Alegre RS, Brazil
e-mail: alan.rossetto@inf.ufpel.edu.br

Self-heating effect (SHE) and hot carrier degradation (HCD) are two significant and well-known reliability issues in CMOS technology. Both these effects degrade device parameters such as drain current and transconductance, the former being the performance degradation due to temperature effects, while the latter is due to the build-up of defects in the device structure. SHE becomes critical in structures with poor thermal conductivity — such as SOI and thin-film transistors—, while HCD depends directly on the electric field along the channel. Nevertheless, these effects are far from independent mechanisms. Even though their interplay is minimal for *n*-channel devices, it is known that SHE accelerates HCD in *p*-channel FETs [1]. To investigate the underlying relationship between SHE and HCD, electrothermal Monte Carlo simulations were carried out for a 28-nm technology FD-SOI pFET. The device structure of interest, depicted in Fig. 1, has a physical channel length of 30 nm, width of 80 nm, silicon film thickness of 7 nm, gate oxide thickness of 1.2 nm, and a 25-nm layer of BOX over a 50-nm thick *p*-type silicon substrate. Simulated $I_{DS} \times V_{GS}$ characteristic for one MC seed is shown in Fig. 2 and compared to available experimental data [2]. The results present good agreement for the entire bias range, yet mainly for the strong inversion region, which is the most relevant in the context of this work. Non-isothermal simulations were carried out using the framework presented in [3] considering a bias point of $V_{GS} = V_{DS} = -0.9$ V and 300 K fixed-temperature thermal boundaries at the back, source, and drain contacts. Both temperature and thickness of the silicon film were accounted for when considering the thermal conductivity degradation, which reaches no more than 7 $\mathrm{W/mK}$ for the temperature range of the device, in contrast to the 130 $\mathrm{W/mK}$ bulk value used in the substrate. The lattice (acoustic phonon) temperature T_L, depicted in Fig. 3, reaches up to 328 K at the drain side of the channel. At the same point, optical phonon temperature T_{OP} may exceed 380 K under the same circumstances, evidencing the non-equilibrium between the phonon baths. Increased T_L and T_{OP} enhances all types of scattering mechanisms, i.e., acoustic phonon (ACOU) and non-polar optical phonon emission (E) and absorption (A) for holes residing in all three valence bands (heavy hole (HH), light hole (LH) and split-off (SO)), as depicted in Fig. 4. In our framework, increased T_{OP} enables more carriers to interact with the optical phonon bath and eventually absorb energy. Fig. 5 depicts the hole energy distribution for the entire device. Even though the energy tends to decrease slightly on average for non-isothermal simulation due to enhanced phonon emission scattering, the increase in phonon absorption events results in even higher energies for some carriers, extending the tail of the distribution. These carriers will likely contribute to HCD since their energy surpasses the impact ionization threshold of 1.8 eV. Moreover, they can also increase their contribution to BTI by occupying charge traps whose energy level was once unreachable. Fig. 6 depicts how the energy distribution evolves as a function of the position along the device length ($L_{tot} = 48$ nm). At the source ($L_{tot}/6$), where T_L and T_{OP} are smaller, there is almost no difference between isothermal and non-isothermal results. However, as the position moves towards the hot spot ($2L_{tot}/3$) and beyond ($5L_{tot}/6$), the increase in the distribution tail due to SHE becomes evident.

REFERENCES

[1] M. Jin et al., IRPS (2016). DOI: 10.1109/IRPS.2016.7574505.

[2] M. Casse et al., IEDM (2022). DOI: 10.1109/IEDM45625.2022.10019322.

[3] A.C.J. Rossetto et al., J. Comput. Electron. **20**, 1644 (2021). DOI: 10.1007/s10825-021-01740-5.

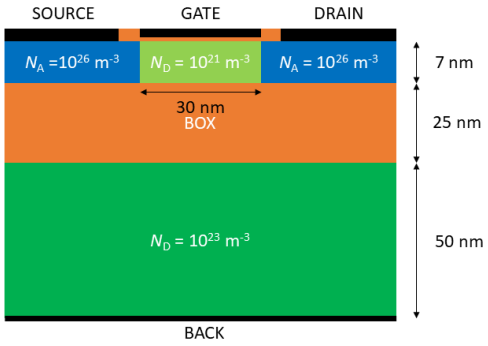

Fig. 1. PMOS FD-SOI case-study structure.

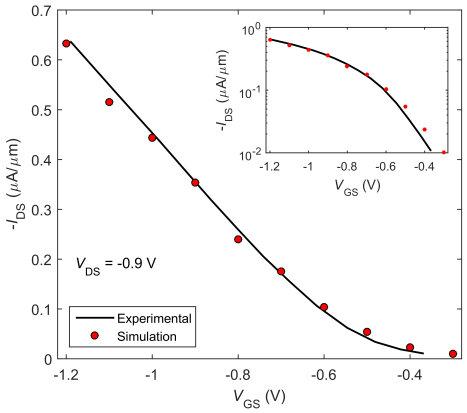

Fig. 2. $I_{DS} \times V_{GS}$ characteristics for the case-study device.

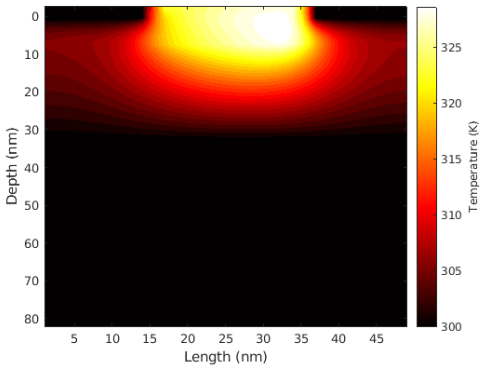

Fig. 3. Lattice temperature profile averaged along the device width.

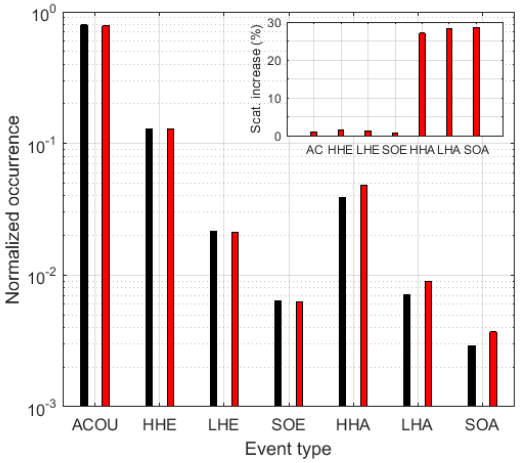

Fig. 4. Normalized occurrence of scattering events for each mechanism in isothermal and non-isothermal simulation.

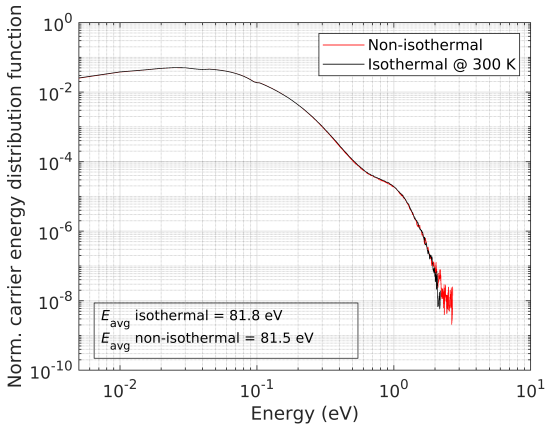

Fig. 5. Normalized hole energy distribution function for isothermal (black) and non-isothermal (red) simulation considering the entire device.

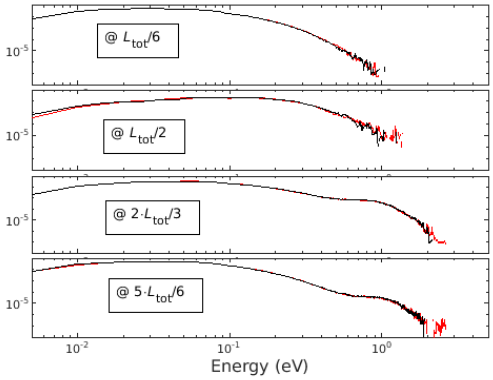

Fig. 6. Normalized hole energy distribution function for isothermal (black) and non-isothermal (red) simulation at different positions along the device length.

Theoretical modeling of quantum-well structures in dilute bismide optoelectronics

D. E. Zirbel and I. Knezevic
Department of Electrical and Computer Engineering
University of Wisconsin–Madison, Madison, WI 53706, USA
dzirbel@wisc.edu, irena.knezevic@wisc.edu

Dilute III–V-bismide alloys are promising candidates for developing high-power and high-efficiency midwave infrared (MWIR) optoelectronic devices. Currently, this spectral range is dominated by quantum and interband cascade lasers (QCLs and ICLs). However, these structures are very complicated and suffer from high temperature sensitivity due to Auger recombination. Bismide alloys allow for uniquely large spin-orbit split-off energies [1], which suppresses Auger recombination and thus temperature sensitivity. Additionally, the 3–4 μm waveband remains difficult to achieve with existing technologies. The quaternary alloy $In_yGa_{1-y}As_{1-x}Bi_x$ shows promise in filling this spectral gap with quantum-well devices based on the mature InP platform.

Introducing bismuth to III–V alloys dramatically raises the valence band due to a valence band anti-crossing (VBAC) interaction [2]. To accurately model these alloys, we utilize a 12-band $\mathbf{k} \cdot \mathbf{p}$ Hamiltonian [3]. This model allows for numerically efficient calculation of the alloys' band structures given a small number of parameters. As an example, Fig. 1 shows the bulk band structure of $In_{0.50}Ga_{0.50}As_{0.92}Bi_{0.08}$ calculated with this model and Fig. 2 shows calculated bandgaps for differing compositions of the alloy.

Two challenges with bismide alloys are the difficulty of incorporating large amounts of bismuth and managing the strain introduced to the system. To increase the emission wavelength of the device without raising the required bismuth concentration, one can increase the width of the quantum well. However, if the well material is strained, there is a restriction on how wide the well can be before relaxation occurs. These challenges can be overcome by using a graded quantum-well structure. One such example that we have explored is shown in Fig. 3. The barrier layers and outer-well layers are lattice-matched to the InP substrate, while the center layer is compressively strained. This center layer is sufficiently thin to avoid relaxation. The outer-well layers widen the well and lower the energy of bound electron states, while the center layer confines holes at a higher energy. These effects combine to reduce the energy gap of the well and increase the emission wavelength of the device. Fig. 4 shows the band diagram of this structure, with a calculated emission wavelength of 3.4 μm.

In conclusion, this work aims to accurately model optoelectronic devices implementing III–V-bismide alloys. Additionally, we aim to develop devices that can detect and emit light in the difficult 3–4 μm waveband. Preliminary results suggest this is possible with bismuth concentrations of less than 10% and strain of less than 1% by utilizing a graded quantum-well structure.

Acknowledgment

This work was funded by the Splinter Professorship and Vilas Distinguished Achievement Professorship (IK).

References

[1] S. Jin and S. J. Sweeney, *InGaAsBi alloys on InP for efficient near- and mid-infrared light emitting devices*, Journal of Applied Physics **114**, 213103 (2013).

[2] K. Alberi, J. Wu, W. Walukiewicz, K. M. Yu, O. D. Dubon, S. P. Watkins, C. X. Wang, X. Liu, Y. J. Cho, and J. Furdyna, *Valence-band anticrossing in mismatched III–V semiconductor alloys*, Phys. Rev. B **75**, 045203 (2007).

[3] C. A. Broderick, M. Usman, and E. P. O'Reilly, *Derivation of 12- and 14-band k · p Hamiltonians for dilute bismide and bismide-nitride semiconductors*, Semiconductor Science and Technology **28**, 125025 (2013).

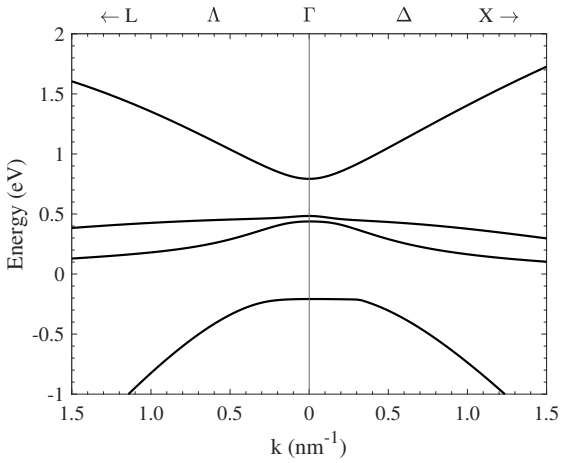

Fig. 1. Bulk band structure of $In_{0.50}Ga_{0.50}As_{0.92}Bi_{0.08}$ on InP calculated using a 12-band $\mathbf{k}\cdot\mathbf{p}$ Hamiltonian near the Γ point. Note the small bandgap and large spin-orbit split-off energy.

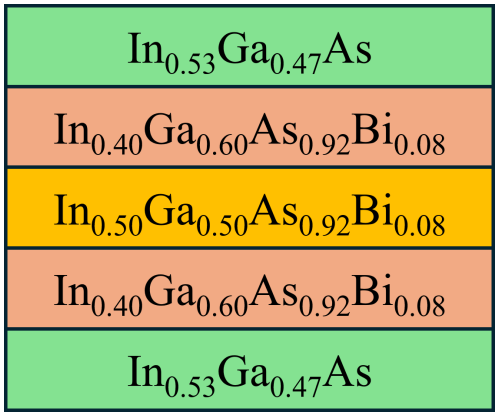

Fig. 3. Quantum-well structure explored in this work. The $In_{0.53}Ga_{0.47}As$ barrier layers and $In_{0.40}Ga_{0.60}As_{0.92}Bi_{0.08}$ well layers are lattice-matched to the InP substrate, while the $In_{0.50}Ga_{0.50}As_{0.92}Bi_{0.08}$ well layer is compressively strained.

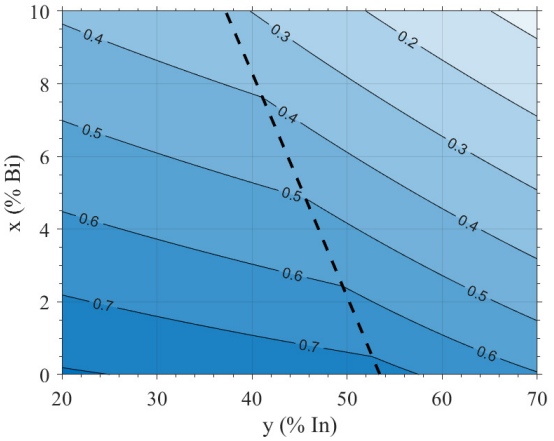

Fig. 2. Calculated bandgap (in eV) of bulk $In_xGa_{1-x}As_{1-y}Bi_y$ on InP. Solid lines show constant energy compositions and the dashed line shows lattice-matched compositions.

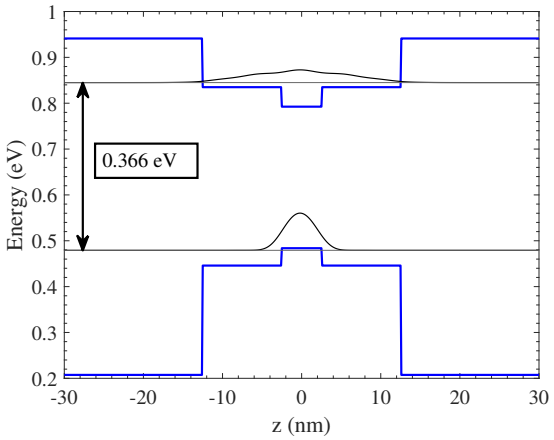

Fig. 4. Band diagram of the explored quantum-well design. Theoretical emission wavelength of 3.4 μm with less than 1% strain in the 5 nm well.

Probing Light-Induced Isomerization Dynamics of Azobenzene Confined within Metal-Organic Frameworks: A Time-Dependent Density Functional Theory Investigation

Nikiphoros Vlastos[*], Nicholas Gindulis[**], and Laura de Sousa Oliveira[***]
University of Wyoming, Laramie, Wyoming 1000 E. University Dr, 82071, USA
[*]Department of Physics, University of Wyoming, USA
[**]Department of Chemical Engineering, University of Wyoming, USA
[***]Department of Chemistry, University of Wyoming, USA
e-mail: nvlastos@uwyo.edu

Abstract Submission

Metal-organic frameworks (MOFs) have garnered significant attention for their tunable structures and potential applications in chemistry, physics, and materials science. Among these, metal-organic responsive frameworks (MORFs)[1] offer new opportunities by leveraging light-actuated behavior for applications in sensing, catalysis, drug delivery, and carbon capture. This research focuses on azobenzene, a prototypical photoisomerizing molecule, and its behavior under confinement within MOFs. Using time-dependent density functional theory (TD-DFT), we investigate the trans-to-cis and cis-to-trans photoisomerization pathways and how they are influenced by external factors such as excitation wavelength, solvent effects, and steric constraints.

We have completed ground-state optimizations of azobenzene in vacuum, benzene, and water, as well as excited-state calculations for the first two singlet states in vacuum. All calculations have been performed using the Gaussian16 software [2]. Our results are consistent with prior studies, both experimental and computational, particularly those by Crecca and Roitberg [3], in confirming that the trans isomer is more stable than cis by ~0.6 eV, and that the cis to trans isomerization barrier in the ground state is 1.08 eV.e explore the role of conical intersections, electronic relaxation pathways, and quantum yield variations to better understand the dominant isomerization mechanisms under different conditions. By elucidating the influence of confinement on electronic structure and isomerization efficiency, this study aims to help establish design principles for optimizing MORFs for practical applications. We anticipate to further present calculations of azobenzene within a 3D-MOF to further explore the impacts of constraint in the isomerization process.

Acknowledgment

We would like to express our sincere thanks to the University of Wyoming's Research Scholar Program for providing funding for this research. The scientific computing resources of this work were supported by the Advanced Research Computing Center (ARCC) at the University of Wyoming and the National Center for Atmospheric Research Wyoming Supercomputer (NWSC), allocation WYOM0181.

References

1. Manion, CA, Arlitt, R, Tumer, I, Campbell, MI, & Greaney, PA. "Towards Automated Design of Mechanically Functional Molecules." *Proceedings of the ASME 2015 International Design Engineering Technical Conferences and Computers and Information in Engineering Conference. Volume 2A: 41st Design Automation Conference*. Boston, Massachusetts, USA. August 2–5, 2015. V02AT03A004. ASME. https://doi.org/10.1115/DETC2015-46078
2. Gaussian 16, Revision C.01, M. J. Frisch, G. W. Trucks, H. B. Schlegel, G. E. Scuseria, M. A. Robb, J. R. Cheeseman, *et al.*, Gaussian, Inc., Wallingford CT, 2016.
3. Christina R. Crecca and Adrian E. Roitberg, *Theoretical Study of the Isomerization Mechanism of Azobenzene and Disubstituted Azobenzene Derivatives*, *The Journal of Physical Chemistry A* **2006** *110* (26), 8188-8203 DOI:10.1021/jp057413c

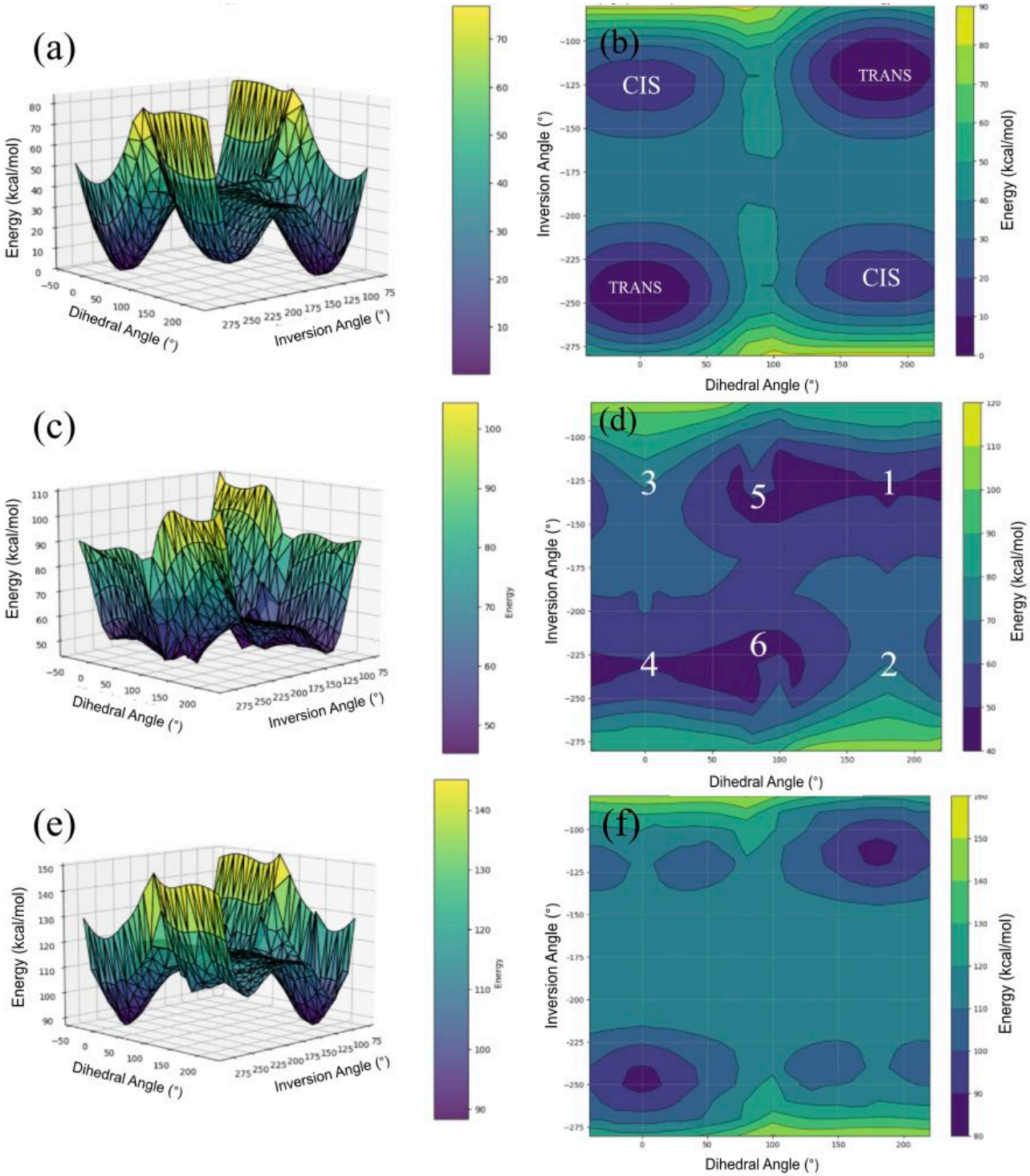

Figure 1 (a) Potential energy surface and (b) contour map of the ground state of Azo. The cis and trans minima are also labeled. (c) Potential energy surface and (d) contour map of the first excited state of Azo. Points 1 and 4 represent where the molecule is on the S1 surface after excitation from the ground-state trans minima, whereas excitation from the ground-state cis minima will place in the molecule at points 2 and 3. Points 5 and 6 represent the S1 minima as well as mark the location of the S1/S0 conical intersection. (e) Potential energy surface and (f) contour map of the second excited state of Azo. All angles are in degrees and energy is in kcal mol-1, relative to the energy of the ground state trans isomer.

A computational approach to polymorphism in BDT organic semiconductors

L. Gnoli, E. Venuti*, and P. Graziosi
Institute for Nanostructured Materials, National Research Council, via Gobetti 101, 40129, Bologna, Italy
*Department of Industrial Chemistry, University of Bologna, via Gobetti 85, Bologna, Italy
e-mail: lucagnoli@cnr.it

Abstract Submission

We have implemented a novel first-principles methodology to investigate how the molecular packing in organic semiconductors (OSC) affects the resulting mobility. We exploit polymorphism to disentangle the role of solid-state packing from other effects.

We identify the parameters driving the mobility and possible limitations in the use of the bare transfer integral to rank the OSC mobility.

Introduction

OSCs are revolutionizing electronics with their flexibility, lightweight nature, potential low-cost, enabling innovative applications ranging from flexible displays to bio-integrated devices. [1]

One of the main challenges for the worldwide use of OSCs is the predictive understanding of the inter-relationship between solid-state packing and device performance.

Here, we exploit polymorphism, i.e. same molecule with different crystalline packing, to isolate the role of molecular packing from effects due to the chemical nature. We chose BDT-based systems for their rich polymorphism (Fig. 1).

Model

We combine DFT-VdW calculations using VASP, Phonopy package, and in-house routines. For every phonon branch ν_i , we compute the related electron-phonon coupling (EPC) at every high symmetry $\mathbf{q}_k$ point from the bandwidth modulation (intra-band) or the modulation of the Davydov splitting (inter-band). The modulations are computed with respect to the displacement along each eigenmode ($\mathbf{q}_k$ ν_i)[2] Then, for each band index and lattice phonon mode, we perform a DOS-weighted average over the BZ to extract a deformation potential value to be passed to the transport code *ElecTra* [3] to evaluate the charge mobility μ, with a protocol validated for OSCs. [2]

Results

We computed for three different polymorphs of 3,7-bis(methylseleno)benzo-[1,2-b:4,5-b′]diselenophene (FOXDUU) the phonon dispersions (Fig. 2), and DOS (Fig. 3), which show remarkable differences in the low frequency region. We extracted the maximum μ by projecting it along the crystal orientations. We find that the transfer integrals, Fig. 4, can offer a rough ranking but a better descriptor is based on the ratio between bandwidth and effective EPC, evaluated from the square root of the ratio between the squared EPC and the mode frequency (Fig. 5). We computed anisotropic in-plane mobility and compared the computed and experimental μ values for the first polymorph, [4] obtaining a good agreement (Fig.6)

Conclusion

A new methodology was applied to polymorphic OSCs to unveil the impact of solid-state packing on μ. The conduction parameters extracted from the simulations suggests that the brickwork packing favors mobility with respect to π-pitched packing. More in general, we show that the packing geometry acts at the level of electronic structure bandwidth and EPC strength.

Acknowledgment

We acknowledge the CINECA award under the ISCRA initiative, funding from the European Union–Next-Generation EU via the Italian call PRIN 2022, project code 2022XZ2ZM8, “POLYPHON” and from M.M.B. s.r.l., Faenza (RA) Italy for the VASP license.

References

[1] Ö. H. Omar *et al.*, J. Mater. Chem. C 9, 13557 (2021).
[2] P. Graziosi *et al.*, Phys. Rev. Mater. accepted, https://arxiv.org/abs/2407.18824.
[3] P. Graziosi *et al.*, Comput Phys Commun **287**,108670 (2023).
[4] H. Takenaka *et al.*, Chem. Mater. **17**, 6696 (2019).
[5] K. Takimiya *et al.*, Chin. J. Chem. 40, 2546 (2022).

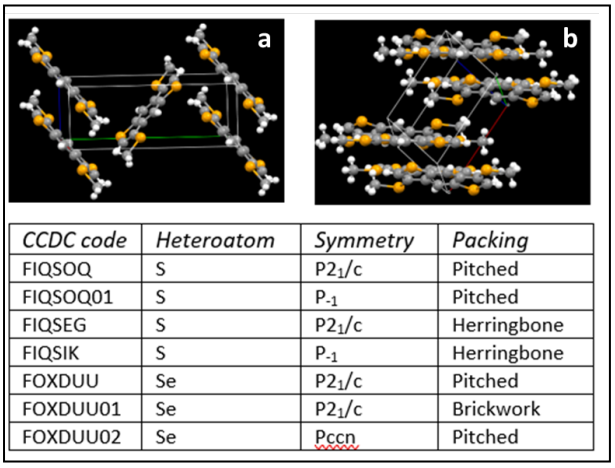

CCDC code	Heteroatom	Symmetry	Packing
FIQSOQ	S	$P2_1/c$	Pitched
FIQSOQ01	S	P_{-1}	Pitched
FIQSEG	S	$P2_1/c$	Herringbone
FIQSIK	S	P_{-1}	Herringbone
FOXDUU	Se	$P2_1/c$	Pitched
FOXDUU01	Se	$P2_1/c$	Brickwork
FOXDUU02	Se	Pccn	Pitched

Fig. **1**. Examples of "pitched" (a) and "brickwork" (b) molecular packings, and table of the investigated polymorphs.

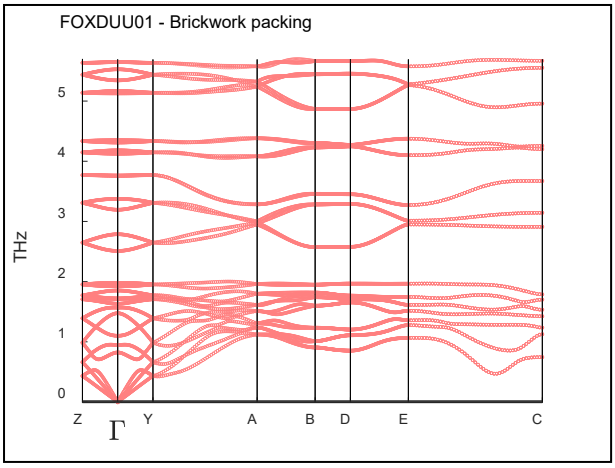

Fig. 2. Phonon dispersions of the FOXDUU01 polymorph

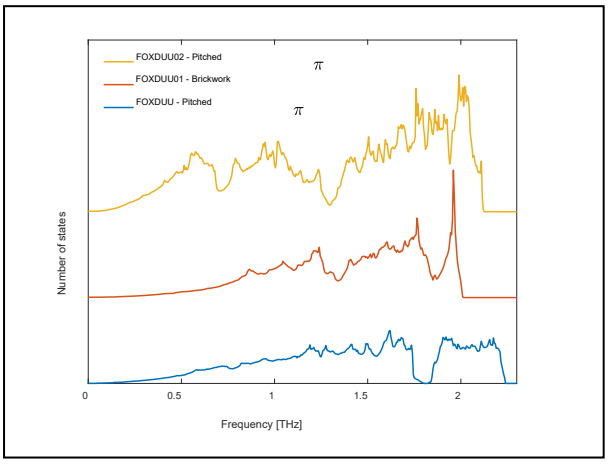

Fig. 3. Phonon DOS of the three FOXDUU polymorphs showing that the FOXDUU02 polymorph has higher phonon DOS at low energy

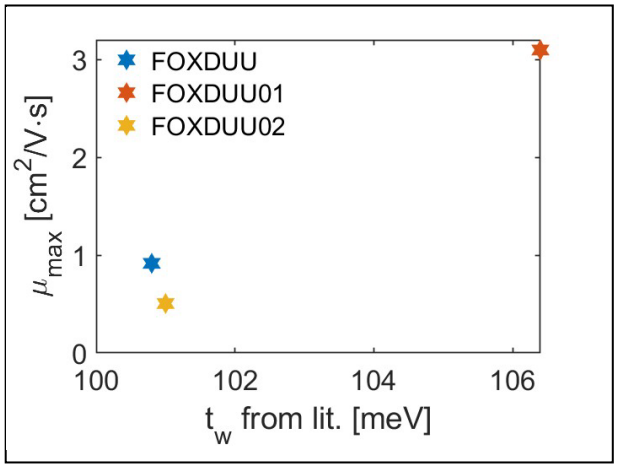

Fig. 4. Example of the computed hole mobility for three BDT polymorphs vs the transfer integral computed in dimers. [4-5]

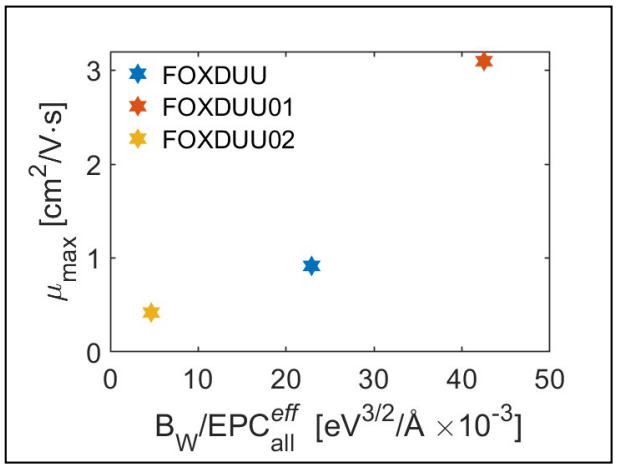

Fig. 5. Mobility of three polymorphs vs the ratio of bandwidth and effective EPC (both *intra*- and *inter*-band processes are accounted for), which appears to be a good ranking descriptor.

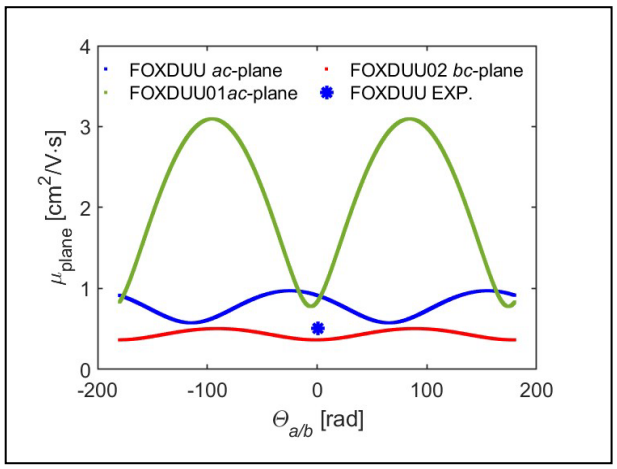

Fig. 6. Anisotropy of the in-plane hole mobility for the three FOXDUU polymorphs. The asterisk indicates the experimental mobility measured in [4]

Honeycomb-Kagome Band Structures of Highly Tunable Graphene-Like Covalent Organic Frameworks

A. E. Davies, I. M. Valdez, J. O. Hoberg, and L. de Sousa Oliveira
University of Wyoming, Department of Chemistry, Laramie, Wyoming
e-mail: adavies2@uwyo.edu

ABSTRACT

Graphene has transformed the field of materials science since 2004 [1]. Its unique electronic properties encouraged an explosion of research into the electron transport properties of two-dimensional materials. Covalent organic frameworks (COFs) emerged around the same time and were of great interest due to their incredible structural and chemical versatility, as well as permanent porosity and high surface area [2]. As structure determines property, 2D COFs exhibit a range of electron transport behaviors, many of which are present in other 2D materials. One of the most intriguing behaviors is the appearance of topological flat bands and graphene-reminiscent Dirac points at the band edges in π-conjugated hexagonal 2D COFs resulting from a combined honeycomb-Kagome sub-lattice [3]. It has been demonstrated that these unique band structures can produce topological superconductors, quantum Hall effects, and ferromagnetism [4].

In 2024, the Hoberg and Oliveira groups at the University of Wyoming published a novel synthesis route that used the three-fold Pictet-Spengler reaction to produce a highly π-conjugated COF from pyranoazacoronene (PAC) nodes [5]. This publication demonstrated the diversity and tunability of PAC COFs with two separate linker molecules (dihydroxyterephthaldehyde and dihydroxynaphthaldehyde) and three functional groups (methoxy, hydroxy, and phenyl rings). The honeycomb-Kagome lattice of these COFs manifests in the band structure (see Figure 1 for an example of a hydrogen functionalized benzene-linked PAC COF), as has been seen in previous works [3].

This study uses extended density functional tight binding to explore the electron transport properties of PAC COFs with 26 functional groups with different electron donating and withdrawing capabilities, combined with six distinct highly-conjugated linkers, two of which are from the original study. The PAC node, molecular precursors for the linkers, and a list of the functional groups are shown in Figure 2. These linkers vary in both conjugation length and conjugation linearity to the node, producing "bent" and "linear" conjugation pathways between pairs of nodes which noticeably impact the band gap. Across the 174 structures, the band gap ranges from 0.4 to 1.9 eV, highlighting the tunability of this series of COFs (the band gap trends across all linkers and functional groups are plotted in Figure 3). The honeycomb-Kagome nature of these band structures is further characterized through spin-orbit coupling calculations and molecular orbital analysis of the molecular precursors.

ACKNOWLEDGEMENTS

We would like to acknowledge generous support from NSF-DMREF grant #2118592, as well as the University of Wyoming, School of Computing, Graduate Scholars Fellowship. Calculations were performed on the Advanced Research Computing Center, Beartooth and Medicine Bow Computing Environments at the University of Wyoming.

REFERENCES

[1] K. .S. Novoselov *et al.*, Science **306**, 5751, (2004).
[2] A. P. Côté *et al.*, Science **310** 5696, (2005).
[3] S. Thomas *et al.*, Chem. Mater. **31**, 9, (2019).
[4] Q. Gao *et al.*, Phys. Chem. Chem. Phys. **26**, 3, (2024).
[5] K. Coe-Sessions, A. E. Davies *et al.*, J. Am. Chem. Soc. **146**, 48, (2024).

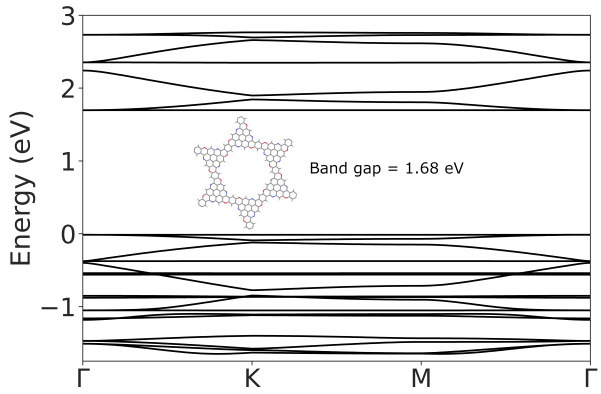

Fig. 1. The hydrogen-functionalized band structure of the benzene-linked PAC COF. The valence and conduction band edges display prominent combined honeycomb-Kagome features, which are present in all of the PACs COFs.

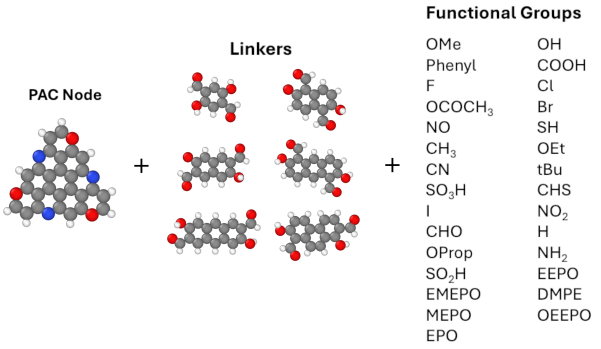

Fig. 2. Molecular precursors showing the generation of PACs COFs, including the PAC node (left column) the selection of six possible conjugated linkers (center column), and 29 functional groups (right column). The functional groups are labeled following the pyCOFBuilder software terminology.

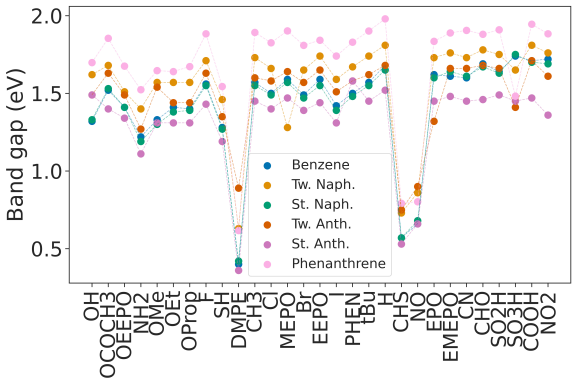

Fig. 3. Band gap trends across all structures with the functional groups labeled in the x-axis following the pyCOFBuilder software terminology. Each linker is labeled by a different color, as indicated in the legend.

Two-dimensional Magnetic Metal Organic Frameworks: Computational Study of Electron and Phonon Transport

A. Jalali, N. Vlastos, M. Mahmoudi Gahrouei, L. de Sousa Oliveira
Department of Chemistry, University of Wyoming, 1000 E. University Ave, Laramie Wyoming 82071
e-mail: ajalali@uwyo.edu

INTRODUCTION

Magnetic metal organic frameworks (MOFs) are excellent candidates for electronic and spintronic applications due to their tunable structures, high porosity, and, in some cases, strong electron correlation. MOFs provide structural flexibility through precise tuning of their electronic and magnetic properties by selecting specific ligands and metal nodes [1]. These materials exhibit diverse charge transport mechanisms such as band-like conduction facilitated by π-conjugated linkers and hopping transport mediated by metal centers [2, 3]. MOFs have an inherently low thermal conductivity due to their high porosity and weak bonding [4]. Suppressing heat conductivity while maintaining reasonable charge transport is advantageous for achieving a higher thermoelectric figure of merit (ZT). Understanding both electron and phonon transport in magnetic MOFs is essential for evaluating their performance in electronic and thermoelectric devices. This study aims to provide a benchmark study of electron and phonon transport behavior in transition metal-based 2D MOFs.

METHODOLOGY

We investigate the electronic and phononic transport properties of magnetic MOFs using self-consistent charge density functional tight binding (SCC-DFTB) and density functional theory (DFT). For electronic transport, we examine essential electronic properties such as band structure, density of states (DOS), electrical conductivity, and Seebeck coefficient in MOFs with transition metal nodes like Fe, Co, and Ni. Phonon transport calculations, including lattice thermal conductivity, are also obtained, allowing us to provide estimates for the thermoelectric figure of merit (ZT) of such MOFs. In addition, we begin exploring strategies such as doping to enhance charge mobility since MOFs exhibit low intrinsic electrical conductivity. Electron mobility is estimated via the Boltzmann transport equation within the constant relaxation time approximation.

CONCLUSION

By benchmarking SCC-DFTB against DFT, we aim to quantitatively evaluate the trade-off between computational efficiency and predictive accuracy in modeling both electron and phonon transport in magnetic 2D MOFs.

ACKNOWLEDGMENT

The authors acknowledge the computational resources provided by the University of Wyoming.

REFERENCES

[1] V. Rubio-Giménez, S. Tatay, and C. Martí-Gastaldo, Electrical conductivity and magnetic bistability in metal–organic frameworks and coordination polymers: charge transport and spin crossover at the nanoscale, Chemical Society Reviews **49**, 5601 (2020).

[2] T. Musho and N. Wu, Ab initio calculation of electronic charge mobility in metal–organic frameworks, Physical Chemistry Chemical Physics **17**, 26160 (2015).

[3] M. Kozlowska, Y. Pramudya, M. Jakoby, S. Heidrich, L. Pan, B. S. Richards, I. A. Howard, C. Wöll, R. Haldar, and W. Wenzel, Crystalline assembly of perylene in metal–organic framework thin film: J-aggregate or excimer? Insight into the electronic structure, Journal of Physics: Condensed Matter **33**, 034001 (2020).

[4] B. Huang, A. McGaughey, and M. Kaviany, Thermal conductivity of metal-organic framework 5 (MOF-5): Part I. Molecular dynamics simulations, International Journal of Heat and Mass Transfer **50**, 393 (2007).

Electron Transport Mechanisms in Cytochrome b_{562} Junctions

Gowtham Nirmal Jonnalagadda, Xiaojing Wu*, Lukas Hronek, and Zdenek Futera
Faculty of Science, University of South Bohemia, Branisovska 1760,
370 05 Ceske Budejovice, Czech Republic.
* Laboratoire de Chimie, ENS de Lyon 46, allée d'Italie, 69364 Lyon, France
e-mail: jonnag00@jcu.cz

INTRODUCTION

Cytochrome b_{562} (Cyt b_{562}) (Fig. 1) is a small redox-active heme protein that has served as a key model system for understanding biological electron transfer processes. Electron transport in such proteins plays a crucial role in various biochemical functions, including respiration and enzymatic catalysis. Investigating its transport properties in protein-metal junctions provides valuable insights into charge transfer mechanisms relevant to bioelectronic interfaces. Recent experimental studies have demonstrated the conductive properties of Cyt b_{562} on gold surfaces [1], but a deeper theoretical understanding of its charge transport mechanism is necessary. This study presents a comprehensive theoretical analysis of electron transport in Cyt b_{562} based junctions using a multiscale computational approach, examining both coherent and incoherent transport processes.

METHODOLOGY

To model electron transport, molecular dynamics (MD) simulations were employed to generate junction geometries under both vacuum-dried (Fig. 2) and solvated conditions (Fig. 3), where the protein was covalently bound to gold contacts in various configurations [2]. Charge transport was analyzed through two mechanisms: coherent tunneling, studied using the Landauer-Büttiker formalism within the Density Functional Theory (DFT) framework [3], and incoherent hopping, modeled using the semi-classical Marcus theory. [3], [4]

RESULTS

The study identified tunneling as the dominant charge transport mechanism, explaining experimental observations of Cyt b_{562} junctions. The tunneling exhibited an exponential but shallow distance dependence, highlighting the significance of structural orientations and protein-electrode contacts in determining conductance. While solvation effects had only a minor influence on electronic properties, primarily through adsorption arrangements, temperature dependence was crucial. The hopping mechanism showed a strong temperature dependence, whereas the tunneling currents remained nearly unaffected, reinforcing the role of coherent transport in these systems. [5]

FUNDING

The research is supported by Czech Science Foundation (GACR) Grant No. 20-02067Y.

REFERENCES

[1] M. Elliott, D.D. Jones *Approaches to Single-molecule Studies of Metalloprotein Electron Transfer Using Scanning Tunneling Probe-based Techniques.* Biochem. Soc. Trans. **46**, 9 (2018).

[2] Z. Futera *et al. Coherent Electron Transport across a 3 nm Bioelectronic Junction Made of Multi-heme Proteins.* J. Phys. Chem. Lett. **11**, 9766 (2020).

[3] Z. Futera, X. Wu, and J. Blumberger *Tunneling to Hopping Transition in Multiheme Cytochrome Bioelectronic Junctions.* J. Phys. Chem. Lett. **14**, 445 (2023).

[4] O.V. Kontkanen, D. Biriukov, Z. Futera *Reorganization Free Energy of Copper Protein in Solution, in Vacuum and on Metal Surfaces.* J. Chem. Phys. **156**, 175101 (2022).

[5] G.N. Jonnalagadda, X. Wu, L. Hronek, and Z. Futera *Structural, Solvent, and Temperature Effects on Protein Junction Conductance* J. Phys. Chem. Lett. **15**, 11608 (2024).

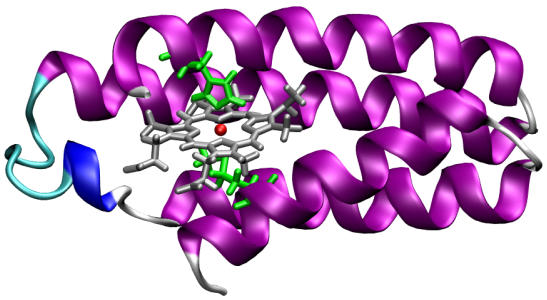

Fig. 1. Crystal structure of cytochrome b_{562} (PDB id 2BC5)

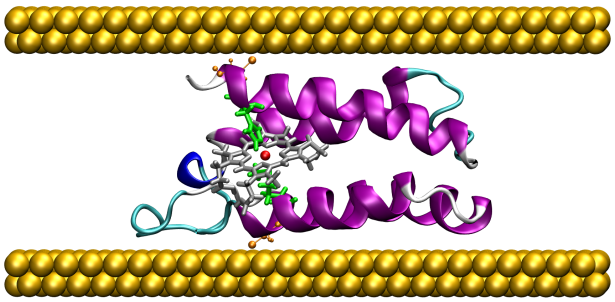

Fig. 2. Vacuum lying junction structure of Cyt b_{562}

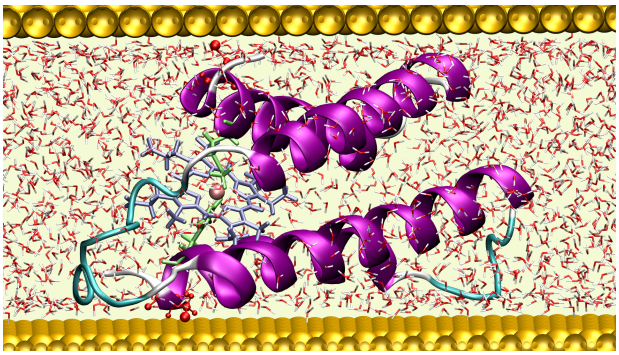

Fig. 3. Solvent lying junction structure of Cyt b_{562}

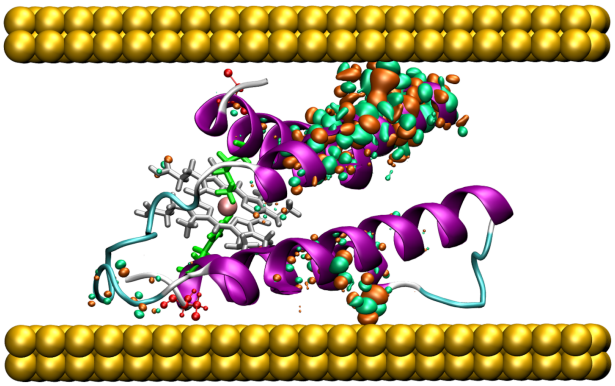

Fig. 4. Dominant conduction channel on the solvated lying structure of Cyt b_{562}

Importance of the Wigner equation for the analysis of the ballistic phonon transport

D. Mai and D. Schulz
Chair for Communication Technology, TU Dortmund, Otto-Hahn Straße 4, 44225 Dortmund, Germany
e-mail: david.mai@tu-dortmund.de

***Abstract*— Usually the computation of the ballistic phonon transport is approximated through Boltzmann type equations (BTE). Especially for hot electro-effects a more precise depiction of the phonon dispersion is needed to correctly apply processes like Umklapp scattering. This can be achieved through a Wigner transport equation (WTE) for phonons.**

INTRODUCTION

Mostly the Boltzmann equation is used to develop models for the phonon transport [1], even a Wigner equation has been proposed [2]. Those methods are using a linear approximation of the phonon dispersion resulting in an inaccurate representation of it. A precise depiction of the dispersion can be achieved through an inclusion of higher order phonon Hamiltonians into the Wigner equation. The phonon dispersion of acoustic phonons in homostructures and heterostructures is examined through BTE and WTE and those methods are compared. Of course optical phonons can be adressed with the proposed method.

MODEL

For demonstration purposes a Hamiltonian is introduced considering inversion symmetry, with which the von Neumann equation can be set up with coordinates r_1, r_2. Through the multiplication of the Hamiltonian with a locally varying function $s(r_1)$ and $s(r_2)$ respectivly, heterostructures can be described. We arrive at

$$\frac{\partial}{\partial t}\hat{\rho} = \sum_{n=0}^{N} c_n (s(r_1)\nabla_{r^1}^{2n} - s(r_2)\nabla_{r^2}^{2n})\hat{\rho} \qquad (1)$$

Utilizing a transformation onto center of mass coordinates r, r', the Wigner-Weyl transformation results into the formulation of a Wigner function $f(r, k)$ in the phase space. The Boltzman equation can be established through the consideration of only the first order derivative in eq. (1). A central differencing scheme is used in r-direction. The boundary condition in the real space are set through Perfectly Matched Layers (PML) [3] and a transient calculation is achieved using matrix exponantials, which can be approximated by applying Model Order Reduction methods like Krylow-subspace methods.

RESULTS

A simple Si material for homostructures and a Si/SiGe-junction are being used to compare the mentioned BTE and WTE. The latter material system can be found in Hetero-Bipolar-Transistors (HBT) for instance. The Wigner function of the phonons is shown in Fig. 1 using the Boltzmann equation and in Fig. 2 using phonon Hamiltonians up to the third order as for example. Especially near the edges of the first Brillouin zone differences between these approaches can be seen. While Fig. 2 displays a precise depiction of the phonon dispersion, the Boltzmann equation only shows a linear dependence on k. A similar behaviour can be seen from Fig. 3 and Fig. 4 for heterojunctions.

CONCLUSION

The use of a Wigner transport equation is needed to precisely reproduce the phonon dispersion especially near the edges of the first Brillouin zone as needed in investigations linked with processes when the nonballistic phonon transport is considered.

REFERENCES

[1] Baoyi Hu, Wenlong Bao, Guofu Chen, Zhaoliang Wang, Dawei Tang, *Boltzmann transport equation simulation of phonon transport across GaN/AlN interface*, Computational Materials Science 230 (2023), 112485.

[2] Simoncelli, M. and Marzari, N. and Mauri, F., *Wigner Formulation of Thermal Transport in Solids*, PhysRev X 12, 041011 (2022)

[3] Steven G. Johnson, *Notes on Perfectly Matched Layers (PMLs)*, arXiv, 2108.05348 (2021).

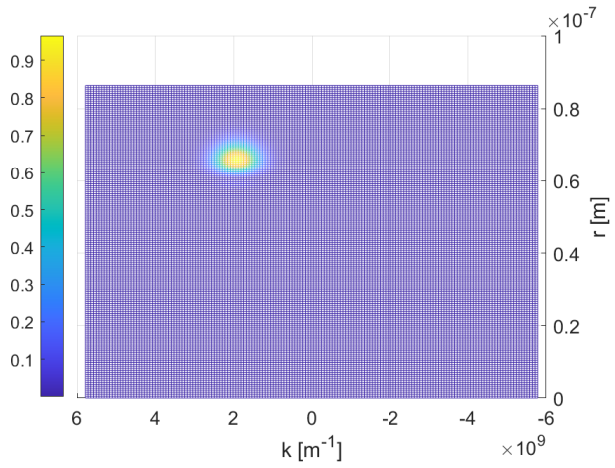

Fig. 1. A Gaussian distribution is set for all k in a Si material. The propagation of $f(r,k)$ using the BTE is shown. The yellow surface indicates the maximum of the distribution while the blue surface indicates a minimum. A linear dependence on k is visible.

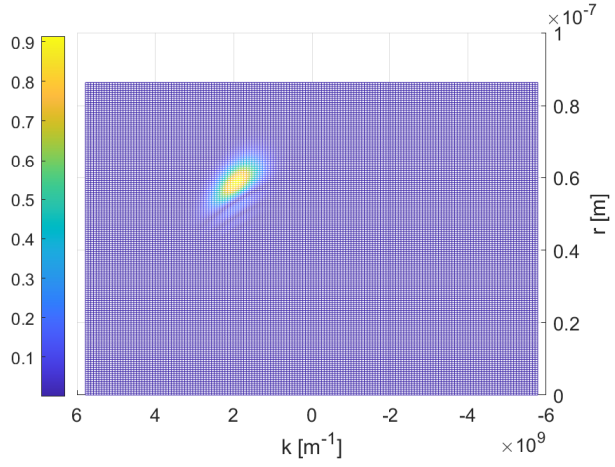

Fig. 2. A Gaussian distribution is set for all k in a Si material. The propagation of $f(r,k)$ using the WTE including Hamiltonians up to the third order is shown. The yellow surface indicates the maximum of the distribution while the blue surface indicates a minimum. The phonon dispersion towards the edges of the k-grid is visible.

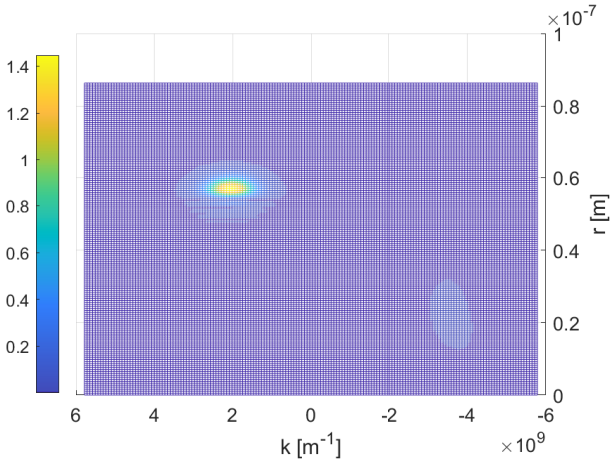

Fig. 3. A Gaussian distribution is set for all k in a $Si/Si_{0.9}Ge_{0.1}$ junction. The junction is set in the middle of the r-grid at 43nm. The propagation of $f(r,k)$ using the BTE is shown. The yellow surface indicates the maximum of the distribution while the dark blue surface indicates a minimum. Similar to the distribution in Fig. 1 a linear dependence on k is visible. However, through the junction an increasing maximum is shown and a part of the distribution is reflected, seen at the edges of the k-grid in light blue. The propagation velocity also decreases in the SiGe material.

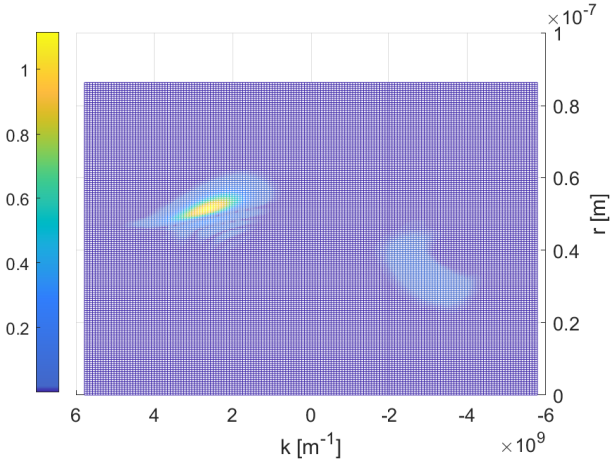

Fig. 4. A Gaussian distribution is set for all k in a $Si/Si_{0.9}Ge_{0.1}$ junction. The junction is set in the middle of the r-grid at 43nm. The propagation of the waves using the WTE is shown. The orange/yellow surface indicates the maximum of the distribution while the dark blue surface indicates a minimum. Similar to the distribution in Fig. 2 and in contrast to Fig. 3, the phonon dispersion is visible. However, through the junction a small increase of the maximum is shown and a part of the distribution is reflected, seen at the edges of the k-grid in light blue. The propagation velocity also decreases in the SiGe material as in Fig. 3 for the BTE.

Phonon Monte Carlo Investigation of Hydrodynamic Transport in Graphene Micro Ribbons

Aidan Belanger, and Zlatan Aksamija
Materials Science and Engineering Department, University of Utah,
Salt Lake City, Utah, 84112-0063, USA
e-mail: aidan.belanger@utah.edu

ABSTRACT

Using the Monte Carlo method to solve the Peierls-Boltzmann Transport Equation with boundaries, we simulate thermal transport in graphene micro ribbons. Our phonon dispersion and scattering rates were obtained from first principles with which we explore the interplay between normal, umklapp, and boundary scattering in the hydrodynamic transport regime.

INTRODUCTION

When normal scattering events (momentum conserving) dominate umklapp (momentum reversing) and impurity scattering, the thermal transport becomes hydrodynamic, resembling that of a fluid through a viscous damping term [1]. Graphene has been predicted to have a relatively wide window of temperatures over which hydrodynamic thermal transport can be observed (50-300K) [2]. Although hydrodynamic transport was first demonstrated in the 1960's [4], our capacity to harness this phenomena is only just beginning to be explored. Recently, limited thermal rectification attributed to normal scattering was experimentally demonstrated in a graphite Tesla valve structure [5].

This hydrodynamic transport regime (being non-Fourier) can be accurately modeled through solving the Peierls-Boltzmann Transport Equation (PBTE). Including boundaries when solving the PBTE becomes computationally expensive when using deterministic or iterative techniques [1]. To model the thermal transport in a computationally efficient way, we use the Monte Carlo (MC) simulation method in which phonons are generated from sampling the probability distributions of their energy, momenta and branch polarization and tracked through space [6]. We track phonons in free space and with boundaries (with solely normal and solely umklapp scattering) to examine the influence of boundaries on thermal transport in the hydrodynamic regime.

MODEL

From the interatomic force constants generated by first-principles in VASP [7], we generate a phonon dispersion (see Fig. 1), as well as normal and umklapp phonon scattering rates (see Fig. 2) with the finite displacement supercell approach in Phono3py [8]. With the energy and branch of the phonon assigned through the MC method, the scattering rates are computed by interpolating the lifetime values from Phono3py and dividing those lifetimes by a random number between 0 and 1, to add randomness to the scattering events.

The probability that a phonon is emitted in the scattering process is computed from Fermi's Golden Rule,

$$P(q,q') = \frac{2\pi}{\hbar}|V|^2 n_\lambda \left(n'_\lambda + \frac{1}{2}m\frac{1}{2}\right)(n''_\lambda + 1)\delta_{\pm q+q',q''+G}\,\delta(\omega_\lambda \pm \omega'_\lambda - \omega''_\lambda). \quad (1)$$

In our work, we approximate the delta function in (1) with a lorentzian distribution whose height is inversely proportional to the remaining energy and whose width is determined from the scattering rates of the phonons, $\Gamma'+\Gamma''$, $\delta = \frac{[\hbar(\Gamma'+\Gamma'')]^2}{\hbar^2(\omega_\lambda \pm \omega'^{\prime}_\lambda - \omega''_\lambda)^2 + [\hbar(\Gamma'+\Gamma'')]^2}$. Boundary scattering is treated as either diffusive or specular, using MC sampling of specular probability to determine which scattering event occurs, using the equation, $p_{spec(q)} = e^{-4(\Delta qN)^2}$. The diffusion coefficient is computed at the end of the MC simulation by integrating the velocity autocorrelation, $D = \int_0^\infty \langle V_t V_0 \rangle \, dt$.

The phonon positions after a few nanoseconds of flight time in Fig. 3, and a histogram of their one dimensional travel distances in Fig. 4, show LA and TA phonons with low umklapp scattering rates. Examining the diffusion coefficient in Fig. 5 demonstrates that these modes are responsible for a long transition time between ballistic and diffusive thermal transport. By adding boundaries, the phonon mean free paths are interrupted resulting in a much faster onset of the diffusive transport regime, as shown in Fig. 6.

REFERENCES

[1] M. Raya-Moreno, J. Carrete, and X. Cartoixà, "Hydrodynamic signatures in thermal transport in devices based on two-dimensional materials: An ab initio study," *Phys. Rev. B*, vol. 106, no. 1, p. 014308, Jul. 2022, doi: 10.1103/PhysRevB.106.014308.

[2] S. Lee, D. Broido, K. Esfarjani, and G. Chen, "Hydrodynamic phonon transport in suspended graphene," *Nat. Commun.*, vol. 6, no. 1, Art. no. 1, Feb. 2015, doi: 10.1038/ncomms7290.

[3] K. Ghosh, A. Kusiak, and J.-L. Battaglia, "Phonon hydrodynamics in crystalline materials," *J. Phys. Condens. Matter*, vol. 34, no. 32, p. 323001, Jun. 2022, doi: 10.1088/1361-648X/ac718a.

[4] J. A. Sussmann and A. Thellung, "Thermal Conductivity of Perfect Dielectric Crystals in the Absence of Umklapp Processes," *Proc. Phys. Soc.*, vol. 81, no. 6, p. 1122, Jun. 1963, doi: 10.1088/0370-1328/81/6/318.

[5] X. Huang *et al.*, "A graphite thermal Tesla valve driven by hydrodynamic phonon transport," *Nature*, vol. 634, no. 8036, pp. 1086–1090, Oct. 2024, doi: 10.1038/s41586-024-08052-1.

[6] S. Mei, L. N. Maurer, Z. Aksamija, and I. Knezevic, "Full-dispersion Monte Carlo simulation of phonon transport in micron-sized graphene nanoribbons," *J. Appl. Phys.*, vol. 116, no. 16, p. 164307, Oct. 2014, doi: 10.1063/1.4899235.

[7] J. Hafner, "Ab-initio simulations of materials using VASP: Density-functional theory and beyond," *J. Comput. Chem.*, vol. 29, no. 13, pp. 2044–2078, 2008, doi: 10.1002/jcc.21057.

[8] A. Togo, "First-principles Phonon Calculations with Phonopy and Phono3py," *J. Phys. Soc. Jpn.*, vol. 92, no. 1, p. 012001, Jan. 2023, doi: 10.7566/JPSJ.92.012001.

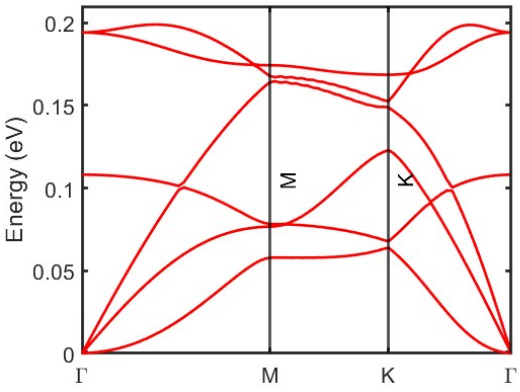

Fig. 1 Phonon dispersion of graphene as generated by Phono3py using a 71x71x1 grid of q points from the force constants of a 5x5x1 supercell of graphene.

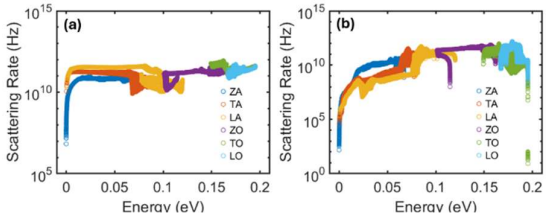

Fig. 2 (a) normal scattering rates and (b) umklapp scattering rates of graphene at 300K interpolated over a dense momentum space using a dataset provided by Phono3py.

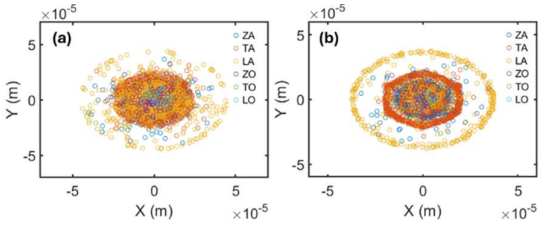

Fig. 3 Phonon positions after random initialization in 1um area and 2 ns of simulation. Implementing (a) normal scattering and (b) umklapp scattering of graphene at 300K.

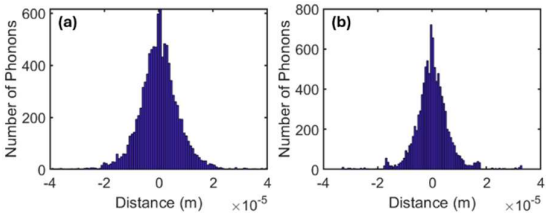

Fig. 4 Histograms of the phonon travel distance along the x direction after random initialization in 1 um area and 2 ns of simulation without boundaries. Implementing (a) normal scattering and (b) umklapp scattering of graphene at 300K.

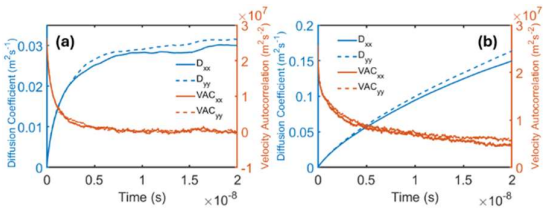

Fig. 5 The diffusion coefficient and its corresponding velocity autocorrelation in the x and y directions over 20 ns with (a) normal and (b) umklapp scattering. No boundaries are enforced in either simulation.

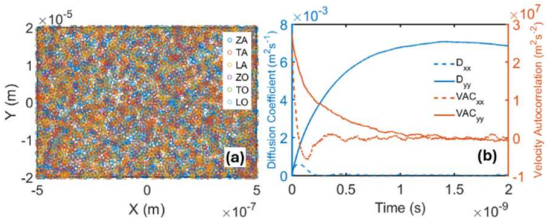

Fig. 6 Using the full scattering rates, (a) the phonon positions in a 1 um by 40 um ribbon after 2 ns of flight time and (b) the diffusion coefficient and velocity autocorrelation in the x and y directions throughout 2 ns of flight time in the ribbon.

Atomistic Modeling Insights of Thermal Boundary Transport Between a Surrogate Fuel (CeO_2) and a Fission Product (Pd)

A. Jensen*, O. Adesina*, J. Harter†, L. de Sousa Oliveira*
*Department of Chemistry, University of Wyoming, Laramie, WY
†Idaho National Laboratory (INL), Idaho Falls, ID
e-mail: ajense28@uwyo.edu

Abstract

Nuclear power offers a reliable and scalable solution to meet the growing global demand for sustainable electricity. Numerous daughter products are generated during the fission process in nuclear fuels. Thermal transport in nuclear fuels is complex and not entirely understood, in large part because of the impact of these fission products (FPs) on fuel structure. Precise modeling is crucial for advancing nuclear systems; however, while first-principles atomistic models provide detailed insights into molecular-level transformations, they are typically restricted to simplified frameworks. On the other hand, empirical models tend to introduce significant uncertainties, especially when employed for predictions. One challenging aspect of modeling thermal transport is the limited understanding of thermal boundary resistance (TIR). TIR is difficult to accurately quantify via experiment, and few concrete theories exist to evaluate the true effect it has on thermal transport [1]. By combining first principles and semiempirical atomistic modeling approaches, we investigate thermal transport at the boundary between nuclear fuels (or fuel surrogates) and FPs. In the end, the primary goal of these initial calculations is to guide the formulation of a physics-based finite element method with full spectral resolution to model thermal boundary transport. This approach aims to accurately model thermal transport across interfaces, aligning with atomistic model outcomes, and moving beyond the diffuse and acoustic mismatch models.

In this study, we investigate uranium dioxide (UO_2), the UO_2 surrogate cerium(IV) oxide (CeO_2), and palladium (Pd), a metallic fission product. In summary, we (1) conduct benchmark calculations to compare semiempirical tight binding with density functional theory for Pd and CeO_2, (2) carry out Pd-CeO_2 semiempirical equilibrium molecular dynamics to model the interface between palladium and CeO_2, and (3) perform some preliminary mesoscale modeling of palladium inclusions within a CeO_2 matrix with the finite element transport code *Griffin* [2], written using the MOOSE (Multiphysics Object Oriented Simulation Environment) [3] framework, developed and maintained at Idaho National Laboratory.

Acknowledgment

The computations conducted in this study are carried out on the National Center for Atmospheric Research-Wyoming Supercomputer (WYOM0168) [4].

References

[1] Zhang, P., Yuan, P., Zhai, S., Zeng, J., Xian, Y., Qin, H., and Yang, D. *A Theoretical Review on Interfacial Thermal Transport at the Nanoscale*, Small, (2018).

[2] Wang, Y., Prince, Z., Park, H., Calvin, O., Choi, N., Harter, J., and others *Griffin: A MOOSE-based reactor physics application for multiphysics simulation of advanced nuclear reactors*, Annals of Nuclear Energy **211**, 110917 (2025).

[3] Lindsay, A., Gaston, D., Permann, C., Miller, J., and others *2.0 - MOOSE: Enabling massively parallel multiphysics simulation*, SoftwareX **20**, 101-202 (2022).

[4] NCAR *Computational and Information Systems Laboratory, Cheyenne: hPE/SGI ICE XA System*, National Center of Atmospheric Research, Boulder, CO, (2019).

Elastic-Wave Modeling of Long-Wavelength Phonon Dynamics in Superlattice Nanowires With Rough Interfaces

Md Mobinul Haque and I. Knezevic
Department of Electrical and Computer Engineering, University of Wisconsin – Madison
Madison, WI 53706
e-mail: haque6@wisc.edu; irena.knezevic@wisc.edu

To differentiate the effect of phonon-phonon scattering and phonon-interface scattering on the thermal conductivity in silicon nanowires (SiNW), long wavelength phonon dynamics has been considered, as phonon-phonon interactions are infrequent for long wavelength (low-energy) phonons. Experimental measurements on SiNWs have shown that, their thermal conductivity below the Casimir limit can be explained with phonon-surface scattering [1]. Using the elastic-medium finite-difference time-domain (FDTD) technique, we can accurately model the dynamics of long wavelength lattice waves and their interaction with interfaces. Previously we presented the application of this model to calculate thermal conductivity in III-V superlattice (e.g. InGaAs/InAlAs) and in rough SiNW. The calculated cross plane thermal conductivity showed good agreement with experimental data at low temperature. For this work we propose to apply our model to extract long wavelength phonon lifetime for a rough superlattice nanowire, which will provide valuable insight on the effect of surface and interlayer roughness in the thermal transport of such superlattice nanowires.

To model the phonon dynamics in the rough interfaces, we start from our previously developed FDTD code [2]. Here, the elastic-wave equation is solved with the velocity-stress formulation using FDTD technique. To generate the rough superlattice interfaces and boundaries with a particular RMS roughness and correlation length, two types of autocorrelation functions (ACF) will be considered, namely gaussian and exponential. For the superlattice structure, AlGaAs/GaAs superlattice will be constructed with rough interfaces, but the general formulation and code can be used to simulate any structure with appropriate parameters.

To simulate the transport in the nanowires, we will use a Gaussian wave-packet as the excitation, which will be launched from the central region of the superlattice and will propagate through the rough interfaces toward the boundaries. Depending on the roughness properties used (i.e., rms roughness and correlation length), the Fourier transform of this wave, which peaks around the launch frequency and its harmonics, will experience significant broadening. Then, we will use Lorentzian fitting for each prominent peak to obtain the full-width half max (FWHM) of the peaks which contains the information about the phonon scattering lifetime. We can run the simulation for various launch frequencies to determine the lifetime versus frequency characteristics as indicated in Fig. 1(b) for the case of rough silicon nanowire.

In conclusion, we use our FDTD code to solve the elastic-wave equation to investigate the long wavelength phonon dynamics in rough superlattice nanowires and extract phonon lifetime versus frequency power law dependance.

ACKNOWLEDGEMENT

This work was funded by the AFOSR Award No. FA9550-22-1-0407, Splinter Professorship, and Vilas Distinguished Achievement Professorship (IK). Calculations were performed at CHTC (UW-Madison).

REFERENCES

[1] J. Lim, K. Hippalgaonkar, S. C. Andrews, A. Majumdar and P. Yang, *Nano Lett.* 12, 5, 2475 (2012).
[2] L. N. Maurer, S. Mei, and I. Knezevic, *Phys. Rev. B* 94, 045312 (2016).

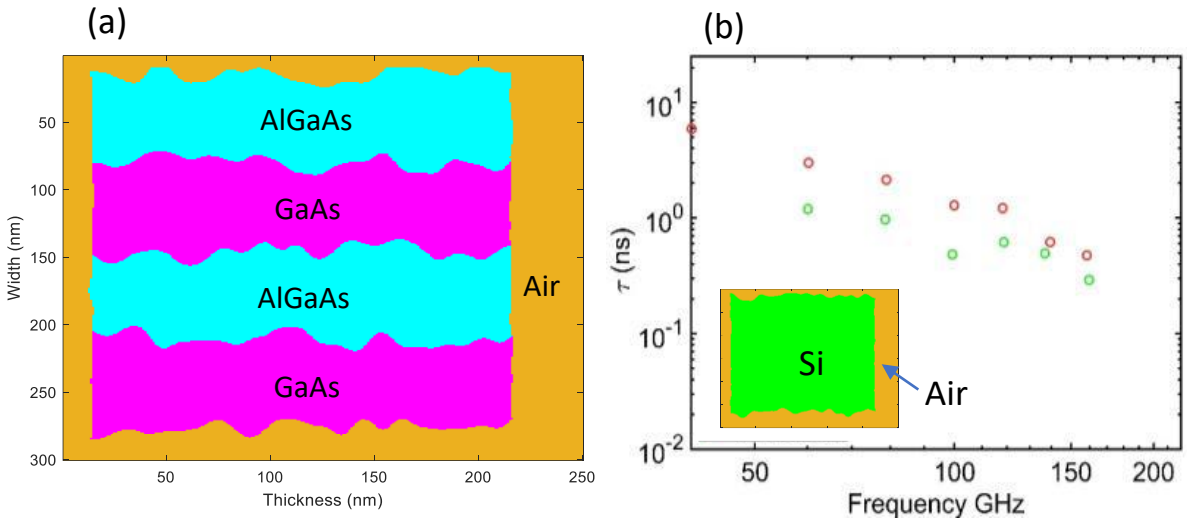

Fig. 1. (a) 2D cross section of the rough superlattice nanowire to be simulated. The RMS roughness and correlation length parameters are 5 and 10 nm respectively. (b) Representative plot of phonon lifetime versus frequency for a rough silicon nanowire. The green open dots represent RMS roughness of 1 nm and the red open circles represent RMS roughness of 5 nm. For both the cases, correlation length was 20 nm.

A generalised framework for defining discrete Wigner functions via the Gottesman-Kitaev-Preskill code

Lucky K. Antonopoulos (Lucky.K.Antonopoulos@gmail.com), Dominic G. Lewis, Nicholas Funai, Jack Davis, Nicolas C. Menicucci
Center for Quantum Computation and Communication Technology
School of Science, RMIT University, Melbourne, Victoria 3000, Australia

Wigner functions (WFs) are a useful tool in quantum mechanics to represent states and operators in phase space. Additionally, for states, the negativity of the WF can be a resource for quantum computing [1]. However, unlike the uniquely defined continuous WF (CWF), for discrete systems, there are many definitions of a discrete WF (DWF), each defined over some subset of dimensions (even, odd, or prime and prime power) [1–3], and sizes of phase space.

In this work, we construct a general framework for deriving DWFs based on a $d \times d$ sized phase space (a lattice with d^2 number of points) from a DWF defined over a doubled (a lattice of size $2d \times 2d$ and so $4d^2$ number of points) phase space. We construct the doubled DWF by focusing on a $2d \times 2d$ sized unit cell for the CWF of a Gottesman-Kitaev-Preskill (GKP) [4, 5] encoded state, where such a DWF(i.e., a doubled one) contains redundant information. This doubled DWF is the same as what Leonhardt [6], Feng et al [5], and Hannay et al [7] have defined.

To remove this redundancy and construct a distinct $d \times d$ DWF, we use cross-correlations between the doubled DWF and a choice of stencil $M \in \mathcal{M}$ ($\mathcal{M}$ is a special class of maps) where these Ms average the information present in the doubled phase space in some manner and before the phase space is halved. we call these M-DWFs. By identifying a subset of maps, we show that our general framework reproduces the DWFs defined by Wootters' [2], Gross [8], Leonhardt [6], and Cohendet [3]. Additionally, and interestingly, we prove that one of our maps called the Coarse grain map (CGM) produces a working DWF for all even dimensions and is based on a $d \times d$ sized lattice, i.e., with no need to double the phase space size.

Additionally, We further find that these different DWFs can be straightforwardly related to one another through the use of a super operator framework in such a way that the properties from one DWF definition can be related to analogous properties in a different definition.

By providing a straightforward procedure from the CWF to a DWF through the GKP code and creating a general framework, we begin to establish common ground amongst the plethora of DWFs in the literature as well as further generalise the definition of a DWF.

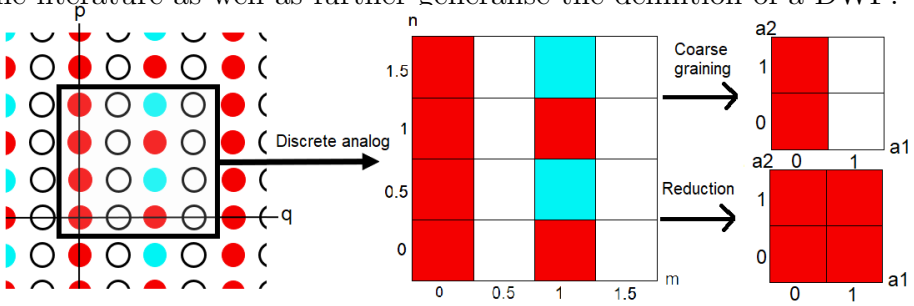

Left: CWF of a $d = 2$ logical-0 GKP state with a unit cell indicated. White spaces are zero-valued, while red and blue are equivalent positive and negative values. Middle: The associated $2d \times 2d$ DWF. Right: Coarse grain mapped DWF and reduction mapped DWF.

References

[1] Robert Raussendorf, Cihan Okay, Michael Zurel, and Polina Feldmann. The role of cohomology in quantum computation with magic states. *Quantum*, 7:979, April 2023.

[2] William K Wootters. A Wigner-function formulation of finite-state quantum mechanics. *Annals of Physics*, 176(1):1–21, May 1987.

[3] O. Cohendet, P. Combe, M. Sirugue, and M. Sirugue-Collin. A stochastic treatment of the dynamics of an integer spin. *Journal of Physics A: Mathematical and General*, 21(13):2875, July 1988.

[4] Daniel Gottesman, Alexei Kitaev, and John Preskill. Encoding a qubit in an oscillator. *Physical Review A*, 64(1):012310, June 2001.

[5] Lingxuan Feng and Shunlong Luo. Connecting Continuous and Discrete Wigner Functions Via GKP Encoding. *International Journal of Theoretical Physics*, 63(2):40, February 2024.

[6] Ulf Leonhardt. Discrete Wigner function and quantum-state tomography. *Physical Review A*, 53(5):2998–3013, May 1996.

[7] J. H. Hannay and M. V. Berry. Quantization of linear maps on a torus-fresnel diffraction by a periodic grating. *Physica D: Nonlinear Phenomena*, 1(3):267–290, September 1980.

[8] D. Gross. Hudson's theorem for finite-dimensional quantum systems. *Journal of Mathematical Physics*, 47(12):122107, December 2006.

Impact of Slope Limiters on DG Methods Solving Quantum-Liouville Type Equations

V. Ganiu, B. Arnaut, J. Neu, and D. Schulz
Chair for Communication Technology, TU Dortmund, Otto-Hahn-Str. 4, 44227 Dortmund, Germany
e-mail: valmir.ganiu@tu-dortmund.de

ABSTRACT

This work enhances the Discontinuous Galerkin (DG) method for solving Quantum-Liouville type equations by applying slope limiters with an approximate Riemann solver. Particularly, the moment limiter outperforms other conventional approaches in accuracy and runtime. Slope limiters applied onto the numerical results in combination with the self-consistent combination of Poisson's equation reduces the runtime by up to 31 %, improving the overall computational efficiency.

I. INTRODUCTION

DG methods for the approximation are more efficient than standard methods (e.g., finite volume techniques) for solving quantum transport equations but can suffer from instabilities at cell interfaces [1]. This challenge is addressed by approximate Riemann solvers (RS), providing a unique solution [2]. This work focuses on improving an approximate RS coupled with a slope limiter (SL). Section II introduces the Liouville-von Neumann equation (LVNE), the DG method, and the SL briefly. Section III analyzes the impact of the promising candidate for SLs and summarizes the results.

II. FUNDAMENTALS

This work utilizes the Liouville-von Neumann equation (LVNE) in center-of-mass coordinates χ and ξ, expressed as $\partial_t \rho(\chi,\xi,t) = \{\imath\hbar/m \cdot \partial_\chi \partial_\xi + q/(\imath\hbar)[V(\chi+\xi/2) - V(\chi-\xi/2)]\}\rho(\chi,\xi,t)$, where ρ is the statistical density, q is the electron charge, and V represents the device potential and external bias [3]. The DG method along with a Fourier Transformation of the ξ coordinate arriving at a phase space representation, discussed in detail in [3], is then applied using an upwinding numerical flux. However, gradients at cell junctions remain and require smoothing. To address this, the problem-independent (PI), the total variation diminishing (TVD), and moment limiters will be applied and evaluated, providing varying levels of smoothing from mild to distinctive [4]. To solve the Poisson's equation, the Gummel algorithm is used ensuring self-consistency.

III. NUMERICAL EXPERIMENTS AND DISCUSSION

The foundation is a double-barrier GaAs/AlGaAs resonant tunneling diode (RTD) with a flatband potential (Fig. 1). Results from the DG algorithm were compared to the reference solution obtained via the QTBM, with the relative error calculated as the $L^p \in p = 1, 2, \infty$ norm. All simulations utilizing the DG method were carried out with a N_χ x N_ξ = 76 x 80 sized grid. Fig. 2 through 4 illustrate the effects of the PI, moment, and TVD slope limiters, respectively. Tab. I summarizes the errors and runtimes for each limiter. The moment limiter achieves both the smallest error and the fastest runtime, ensuring an efficient DG scheme. Finally, Fig. 5 presents the total runtime of the self-consistent Poisson loop. As external bias increases, fewer iterations are needed to meet the error threshold, resulting in runtime savings of up to 31 %.

REFERENCES

[1] Randall J. LeVeque. *Numerical Methods for Conservation Laws*. Springer Science & Business Media, 1992.
[2] P.L. Roe. Approximate riemann solvers, parameter vectors, and difference schemes. *J. Comp. Phys.*, 135(2):250–258.
[3] V. Ganiu and D. Schulz. Efficiency analysis of discontinuous galerkin approaches for the application onto quantum liouville-type equations. *J. Comput. Electron.*, 23(4):718–727, June 2024.
[4] L. Zou. Understand slope limiter – graphically, 2021.

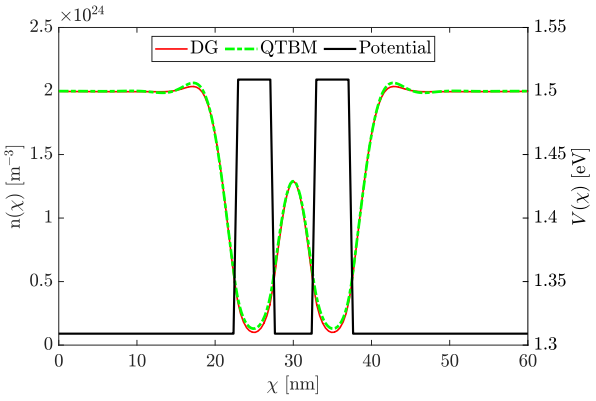

Fig. 1. Flatband potential profile of the resonant tunneling diode (RTD), as well as the statistical density derived with the QTBM (green) and DG (red). An overall good agreement between the proposed scheme and the QTBM as the reference method can be observed.

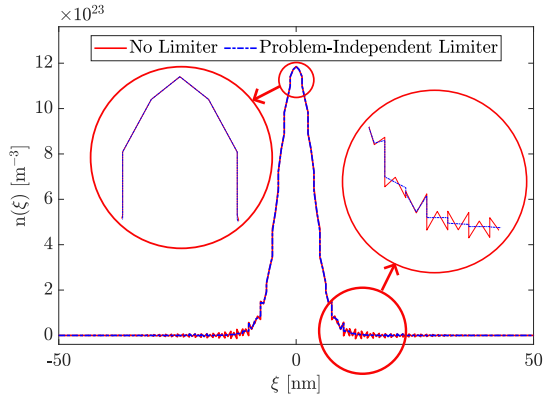

Fig. 2. Unprocessed (red) and processed (purple) results of the problem-independent limiter. The maximum at $\xi = 0$ nm is well preserved and around $\xi = 10$ nm a significant limiting of oscillations can be observed.

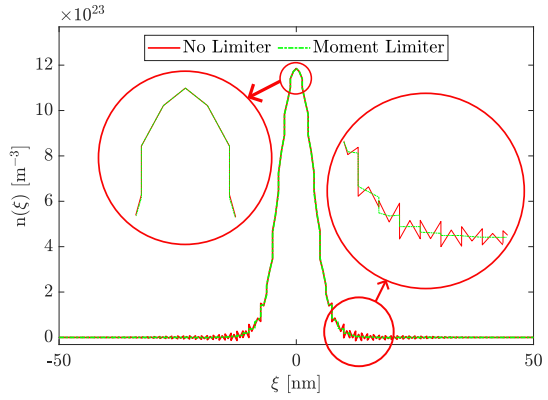

Fig. 3. Unprocessed (red) and processed (green) results of the moment limiter. The maximum at $\xi = 0$ nm is well preserved and around $\xi = 10$ nm a significant limiting of oscillations can be observed. Here, the smoothing is more distinctive than the problem-independent limiter in Fig. 2.

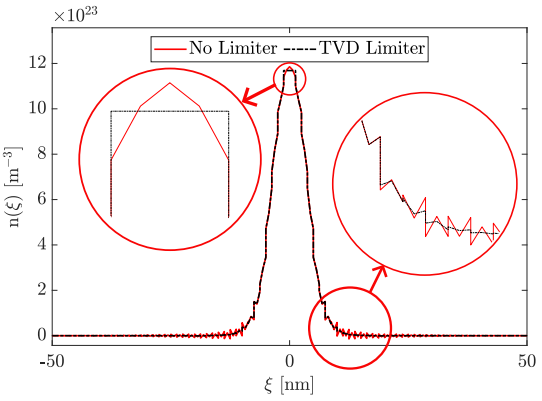

Fig. 4. Unprocessed (red) and processed (black) results of the TVD limiter. The maximum at $\xi = 0$ nm is *not* preserved and around $\xi = 10$ nm the least limiting of oscillations can be observed compared to the previous results.

TABLE I

L^p-ERROR AND RUNTIME FOR THE SLOPE LIMITERS APPLIED TO THE ξ-DOMAIN. WITH 0.06 S, THE MOMENT LIMITER IS THE MOST EFFICIENT WHILE ALSO PROVIDING THE SMALLEST ERROR.

	No Limiter	**PI**	**Moment**	**TVD**
L^1-Error	11.62 %	8.58 %	7.89 %	8.04 %
L^2-Error	7.83 %	7.38 %	7.25 %	7.46 %
L^∞-Error	8.07 %	8.07 %	8.07 %	9.36 %
Runtime		0.13 s	0.06 s	0.07 s

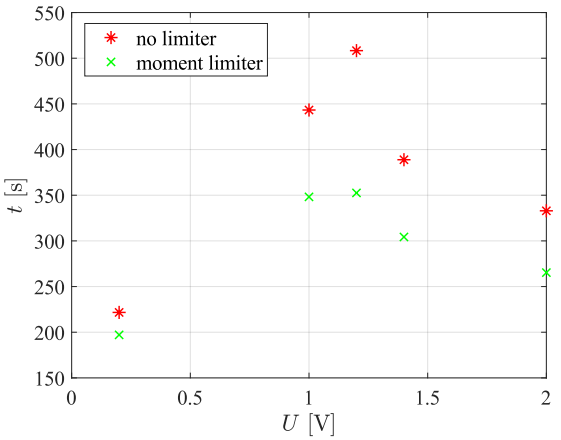

Fig. 5. Runtime comparison of the self-consistent while loop to solve Poisson's equation. Utilizing the moment slope limiter decreases the number of iterations needed to reach the desired convergence resulting in a reduction of the runtime.

Topological Nodal-Point Superconductivity in Two-Dimensional Ferroelectric Hybrid Perovskites

Xiaoyin Li[1], Shunhong Zhang[2], Xiaoming Zhang[3], Zeev Valy Vardeny[4], Feng Liu[1]*
[1]Department of Materials Science and Engineering, University of Utah, Salt Lake City, Utah 84112, United States
[2]International Center for Quantum Design of Functional Materials, University of Science and Technology of China, Hefei, Anhui 230026, China
[3]College of Physics and Optoelectronic Engineering, Ocean University of China, Qingdao, Shandong 266100, China
[4]Department of Physics & Astronomy, University of Utah, Salt Lake City, Utah 84112, United States
*e-mail: fliu@eng.utah.edu

INTRODUCTION

Topological superconductors (TSCs) are of great interest for hosting Majorana modes, which are non-Abelian quasiparticles promising for fault-tolerant quantum computing. While intrinsic TSCs are rare, extrinsic TSCs can be obtained in heterostructures by combining conventional superconductors with materials exhibiting spin-momentum locking, such as Rashba spin-orbit coupling (SOC) semiconductors [1, 2]. Although several candidate materials have been proposed, experimental realization remains challenging due to difficulties in synthesizing materials with suitable thickness and orientation, fabricating high-quality interfaces, and the typically small nontrivial superconducting gap, which hinders the detection of Majorana modes.

OBJECTIVE

This work [3] aims to identify new material candidates that overcome the challenges above. We find that two-dimensional (2D) hybrid organic-inorganic perovskites (HOIPs) offer promising features, such as structural diversity, strong SOC, and weak van der Waals interactions, for realizing TSC. Motivated by these advantages, we explore the potential of TSC in 2D HOIPs, focusing on utilizing the previously unexplored anisotropic SOC present in ferroelectric 2D HOIPs.

RESULTS

Figure 1 compares isotropic Rashba SOC and anisotropic SOC, along with their realized topological superconducting (TSC) and nodal-point superconducting (NSC) phases after including s-wave superconducting pairing and Zeeman splitting. Isotropic SOC leads to a fully gapped TSC with Majorana modes on all sample edges, while anisotropic SOC results in NSC with topologically protected nodal points and Majorana modes on specific edges. Using first-principles calculations (Fig. 2) and tight-binding modelling (Fig. 3) on a specific material with room-temperature ferroelectricity, BA_2PbCl_4 (BA = benzylammonium), we demonstrate the emergence of NSC and Majorana edge modes in 2D HOIPs. Furthermore, the intrinsic ferroelectricity of such 2D HOIPs offers additional tunability, enabling control of NSC phases and Majorana modes at ferroelectric domain walls as well as edges (Fig. 4).

CONCLUSION

We proposed and demonstrated 2D ferroelectric HOIPs as promising candidates to realize NSC and gapless Majorana modes, waiting for experimental realization. Also, NSC is protected by spatial symmetries of 2D HOIPs, therefore more exotic topological superconducting states could be found in this class of materials.

REFERENCES

[1] J. D. Sau, R. M. Lutchyn, S. Tewari, S. Das Sarma, Phys. Rev. Lett. **104**, 040502 (2010).
[2] R. M. Lutchyn, J. D. Sau, S. Das Sarma, Phys. Rev. Lett. **105**, 077001 (2010).
[3] X. Li, S. Zhang, X. Zhang, Z. V. Vardeny, F. Liu, Nano Lett. **24**, 2705-2711 (2024).

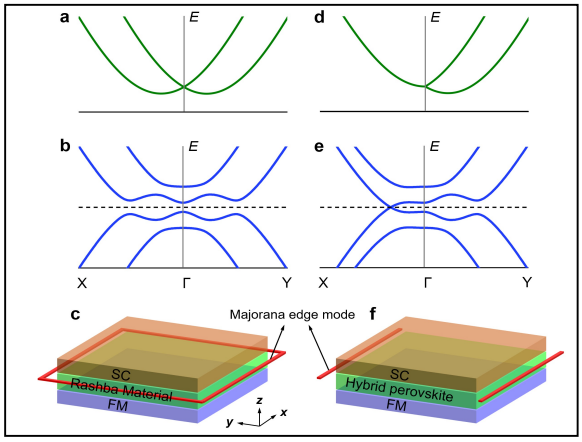

Fig. 1. Schematics of topological superconductivity (TSC) vs topological nodal-point superconductivity (NSC) based on non-centrosymmetric semiconductors with isotropic vs anisotropic SOC. Isotropic SOC: (a) The SOC-related split electronic band structure. (b) BdG quasiparticle band structure. (c) The Majorana edge mode. Anisotropic SOC: (d)-(f) Same as in (a)-(c) but for the two-dimensional hybrid organic-inorganic perovskite with anisotropic SOC.

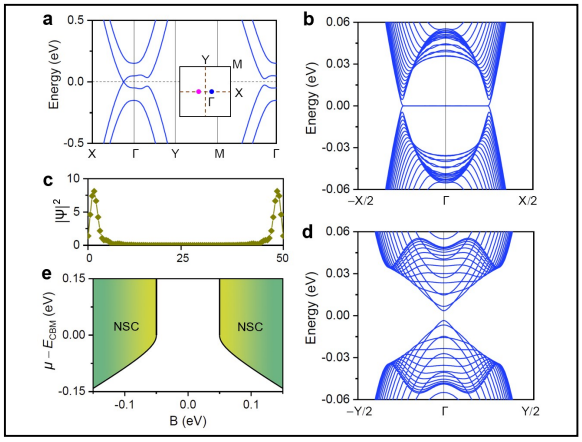

Fig. 3. NSC in BA_2PbCl_4 monolayer. (a) BdG quasiparticle band structure along high-symmetric k paths. Inset plots two nodal points in the Brillouin zone, whose chirality is shown by different colors (purple/blue for +/−). (b) and (c) BdG band structure of a nanoribbon terminated along y-direction and real-space distributions of emerged gapless Majorana modes. (d) BdG band structure of a nanoribbon terminated along x-direction. (e) NSC phase diagram in the parameter space of chemical potential μ and Zeeman field B with a fixed $\Delta = 0.05$ eV. For (a)-(d), $\mu = 1.23$ and $B = 0.1$ eV. The widths of the two nanoribbons are both 50 unit-cells.

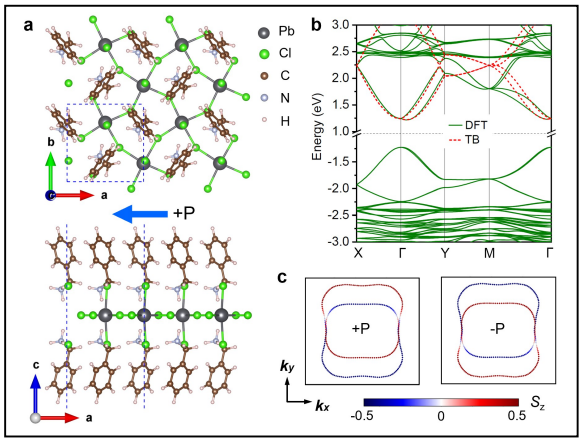

Fig. 2. Atomic and electronic structure of the ferroelectric BA_2PbCl_4 monolayer. (a) Top and side views of atomic structure. The blue arrow (+**P**) indicates the direction of ferroelectric polarization. (b) Electronic band structure along high-symmetric k paths of the Brillouin zone. (c) Conduction band energy contours (E = 1.58 eV) of the BA_2PbCl_4 monolayer with opposite polarization direction (+**P** and −**P**). The S_z component of spin is mapped by the color bar, while the S_x and S_y components are constrained to zero by crystal symmetry.

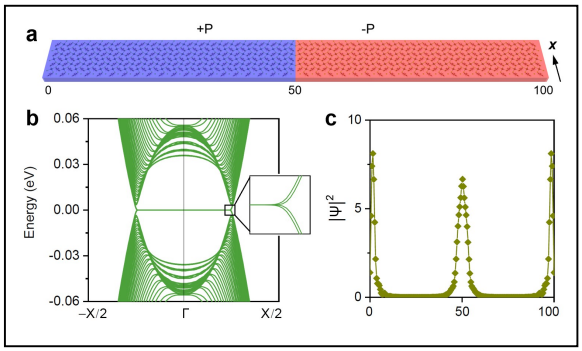

Fig. 4. Domain-wall Majorana modes in the BA_2PbCl_4 monolayer. (a) Illustration of ferroelectric two-domain structure, which is terminated along y-direction and periodic along x-direction. The widths of the left and right domains are both 50 unit-cells. (b) BdG band structure of the two-domain structure proximate to an s-wave SC ($\Delta = 0.05$ eV) and a FM with y-direction magnetization (B = 0.1 eV), showing the emergence of four gapless Majorana modes. (c) Real-space distributions of the four Majorana modes, peaking at the outer edges as well as the inner domain wall.

Nonlinear Eigenvalue Algorithms with Applications

Dongming Li*, and Eric Polizzi*†
*Department of Electrical and Computer Engineering, University of Massachusetts, Amherst, MA, USA
†Department of Mathematics and Statistics, University of Massachusetts, Amherst, MA, USA
e-mail: dongmingli@umass.edu, epolizzi@engin.umass.edu

Eigenvalue problems in which the coefficient matrices depend nonlinearly on the eigenvalues arise in a large variety of applications. Eigenvalues λ associated with eigenvectors $\mathbf{x}$ are then solutions of the following general form:

$$\mathbf{T}(\lambda)\mathbf{x} = 0. \tag{1}$$

This formulation includes the common linear eigenvalue problem as a special case, letting
$\mathbf{T}(z) = z\mathbf{B} - \mathbf{A}$,
as well as the polynomial case letting
$\mathbf{T}(z) = \sum_{m=0}^{M} z^m \mathbf{A}_m$.
Most often, however, numerical modeling of physical systems gives rise to the following non-linear eigenvalue form:

$$\mathbf{T}(z) = z\mathbf{S} - (\mathbf{H} + \mathbf{\Sigma}(z)), \tag{2}$$

where $\mathbf{H}$ represents the Hamiltonian, $\mathbf{S}$ is the mass matrix (i.e. $\mathbf{S} = \mathbf{I}$ using orthogonal basis functions), and $\mathbf{\Sigma}$ is a non-linear matrix with z. We note that $\mathbf{T}(z)^{-1}$ is the Green's function $\mathbf{G}(z)$ of the system. Depending on the applications, $\mathbf{\Sigma}$ has different meaning, for example:

- In quantum transport modeling (NEGF), $\mathbf{\Sigma}$ represents the self-energy functions that guarantee transparent/open/absorbing boundary conditions with the contact reservoirs.
- In electronic structure GW modeling, $\mathbf{\Sigma}$ represents the exact exchange and correlations terms that must be including to accurately predict bandgaps of materials in many-body perturbation theory (we note that only the correlation part is non-linear).
- In domain decomposition approach, $\mathbf{\Sigma}$ may represent a Schur complement arising while attempting to express a linear eigenvalue problems into a reduced system size (including the notable example of the Slater APW approach).

A common strategy for addressing these problems is linearization, which approximates the term $\mathbf{\Sigma}(z)$. However, this approach can introduce errors that compromise accuracy. Moreover, linearization often leads to larger systems and may necessitate the use of less robust numerical methods, such as the graphical or spectral method for GW. Our goal is to enable the direct solution of the non-linear problem (2) in a way that is: (i) robust, requiring no approximations; (ii) broadly applicable, with a general approach independent of the specific form of the non-linearity; and (iii) efficient, ensuring numerical scalability and high performance. This is made possible by enhancing the FEAST eigenvalue algorithm to naturally incorporate non-linear effects. FEAST reformulates the eigenvalue problem into a series of independent linear system solves at specific contour points. Using contour integration along $\mathbf{\Gamma}$, it iteratively refines the solution space via inversion residual subspace iterations. The nonlinear FEAST algorithm involves performing the following contour integrations along Γ for $k = 0$ and $k = 1$:

$$\mathbf{Q}_k = \frac{1}{2\pi\imath} \oint_{\Gamma} z^k \Big(\mathbf{X} - \mathbf{T}^{-1}(z)\mathbf{R}\Big)(z\mathbf{I} - \mathbf{\Lambda})^{-1}\, dz. \tag{3}$$

Using $\mathbf{Q}_k$, one can construct a reduced eigenvalue problem using Rayleigh–Ritz method [1], [2], [3].

We apply this new nonlinear eigenvalue algorithm to address the three problems described above. Our findings outlines, in particular, the importance of considering nonlinear eigenvalue problems in GW approximations to accurately obtain both HOMO and LUMO states.

References

[1] B. Gavin, A. Miedlar and E. Polizzi, Journal of Computational Science 27, 107, (2018).
[2] J. Brenneck and E. Polizzi, arXiv:2007.03000, (2020).
[3] D. Li and E. Polizzi, Phys.Rev. B 111 (4), 045137, (2025).

		G_0W_0@PBE			
	Molecule	Graphical solution	Spectral functions	Nonlinear FEAST	Deviation
HOMO	He	−23.66	−23.69	−23.69	0.03
	H_2	−15.91	−15.92	−15.92	0.01
	Ne	−20.75	−20.78	−20.78	0.03
	LiH	−6.94	−6.97	−6.97	0.03
	Li_2	−5.05	−5.02	−5.02	−0.03
	CO	−14.08	−14.09	−14.09	0.01
	F_2	−15.03	−15.07	−15.07	0.04
LUMO	He	2.06	1.91	1.91	0.15
	H_2	2.57	1.95	1.95	0.62
	Ne	2.45	2.16	2.16	0.29
	LiH	0.47	0.32	0.32	0.15
	Li_2	−0.03	−0.09	−0.09	0.06
	CO	0.35	0.21	0.21	0.14
	F_2	−1.40	−1.59	−1.59	0.19

Fig. 1: Nonlinear FEAST G_0W_0 results using Kohn-Sham PBE as the starting point, compared to conventional methods (spectral functions and graphical solutions), HOMO and LUMO energies in eV (Extracted from [3])

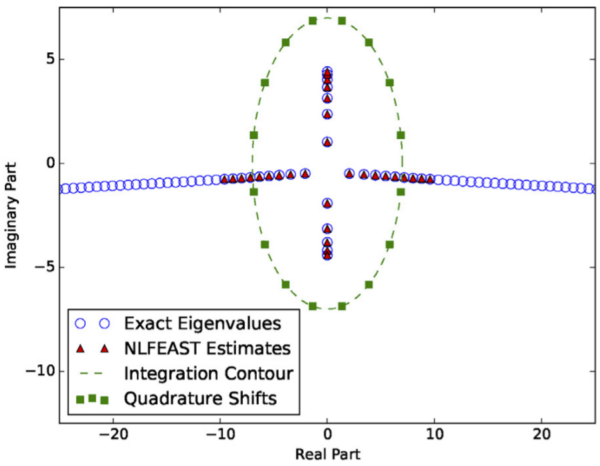

Fig. 2: All scattering resonances from a quantum transport problem. The nonlinear FEAST scheme is using a search subspace size of $m_0 = 30$ to capture all of the 22 eigenvalues inside of the integration contour, plus the eight (8) eigenvalues that are closest to the integration contour while still being outside of it. (Extracted from [1])

Fig. 3: FEAST algorithm for solving generalized non-linear eigenvalue systems $\mathbf{T}(\lambda)\mathbf{x} = 0$ of size n. We note that at the first iteration where $\mathbf{R}$ is not known, $\mathbf{Y}_j$ can directly be obtained by solving the linear system $\mathbf{T}(z_j)\mathbf{Y}_j = \mathbf{X}$.

Input:
Contour Γ containing m wanted eigenvalues
Set of quadrature nodes and weights $\{z_j, \omega_j\}$
Subspace (random) $\mathbf{X}_{n\times m_0} = \{\mathbf{x}_1, \ldots, \mathbf{x}_{m_0}\}$ with $m_0 \geq m$
While $\{\mathbf{r}_i\}$ not converged for all λ_i inside Γ
Solve $\mathbf{T}(z_j)\mathbf{X}_j = \mathbf{R}$ for all contour nodes j
Compute $\mathbf{Y}_j = (\mathbf{X} - \mathbf{X}_j)(z_j\mathbf{I} - \mathbf{\Lambda})^{-1}$
Compute $\mathbf{Q}_0 = \sum_j \omega_j \mathbf{Y}_j$ and $\mathbf{Q}_1 = \sum_j \omega_j z_j \mathbf{Y}_j$
Perform the QR decomposition $\mathbf{Q_0} = \mathbf{q}_{n\times m_0}\mathbf{r}_{m_0\times m_0}$
Compute $\mathbf{C}_{m_0\times m_0} = \mathbf{q^H Q_1 r^{-1}}$
Solve reduced eigenvalue problem $\mathbf{CW} = \mathbf{W\Lambda}$
Update $\mathbf{X}$=$\mathbf{qW}$, noting that $\mathbf{\Lambda} = \mathrm{diag}(\lambda_1, \ldots, \lambda_{m_0})$
Form $\mathbf{R} = \{\mathbf{r}_1, \mathbf{r}_2, \ldots, \mathbf{r}_{m_0}\}$ with $\mathbf{r}_i = \mathbf{T}(\lambda_i)\mathbf{x}_i$
Output: all m eigenpairs $\{\lambda_i, \mathbf{x}_i\}$ inside Γ

Thursday 9-10:30 2D Materials

Time	Type	Presenter	Title
9:00-9:30	**Keynote**	Eric Pop	Electro-Thermal Transport in 2D Materials, Devices, and Applications
9:30-9:45	Contributed	Anass Sebbar	Coherent thermal transport in isotopic graphene superlattices: a NEGF study
9:45-10:00	Contributed	Dongming Li	A New Method for Bandstructure Calculation and Its Application to Edge Termination Effects in Graphene
10:00-10:15	Contributed	Shoaib Mansoori	Theoretical Study of Carrier Transport in Bilayer Transition Metal Dichalcogenides
10:15-10:30	Contributed	Emeric Deylgat and William Vandenberghe	Electrostatic Model of Metal-Induced Gap States in Metal Edge, Top and Hybrid Contacts to MoS_2 transistors

Electro-Thermal Transport in 2D Materials, Devices, and Applications

Eric Pop*
Electrical Engineering, Applied Physics, Materials Science & Engineering, SLAC
Stanford University, Stanford, CA 94305, U.S.A.
*e-mail: epop@stanford.edu

Abstract

This talk will describe our group's recent work on two-dimensional (2D) materials and devices, with focus on electron and phonon transport. I will also describe some of their 'mainstream' as well as unconventional applications, which take advantage of the unique properties of 2D materials, including their anisotropy, band gap, and ultrathin nature.

Electronic Transport & Applications

From the point of view of electronic properties, 2D semiconductors have good mobility in ultrathin, sub-1 nm (i.e. monolayer) films. This indicates they could be used in applications where their ultrathin nature provides distinct advantages, such as flexible electronics [1], light-weight solar cells [2], or nanoscale transistors [3]. They may not be useful where conventional materials work well, or where their integration cost cannot be justified.

In the first part of this talk, I will focus on 2D materials for three-dimensional (3D) heterogeneous integration of electronics, which has major advantages for energy-efficient computing [4]. Here, 2D semiconductors (e.g. MoS_2, WSe_2) could be used as monolayer transistors with low leakage, used to access high-density memory [5], leveraging advances in topological interconnects [6], themselves based on ultrathin semimetallic NbP.

Recent efforts from our group [7-10] and others [11] have demonstrated well-behaved monolayer transistors which can rival conventional semiconductors, and we found the 2D performance can be further enhanced by strain [10,12]. Because experimental devices have defects and imperfections, we have also used simulations to understand quantum capacitance [8] and high-field transport in 2D semiconductors including strain and self-heating [13].

Thermal Transport & Applications

The thermal properties of 2D materials are of interest due to their anisotropic and tunable thermal conductivity. We have studied this behavior as part of transistors [14,15] and memory [5,16], where self-heating directly affects device operation and reliability. For instance, the electron saturation velocity in MoS_2 transistors is approximately doubled when self-heating is removed [13,17].

For monolayer 2D materials, molecular dynamics (MD) simulations suggest that their thermal conductivity on a substrate is always lower than in suspended films [18,19]. For multilayer 2D materials, we uncovered very long cross-plane phonon mean free paths, ~200 nm at room temperature in MoS_2 [20]. We have also layered heterogeneous 2D monolayers, achieving an effective cross-plane thermal conductivity ~3x lower than air [21]. A similar concept can be used with layered superlattices in phase change memory, enabling ultralow power operation [5]. Finally, I will also describe some applications of 2D materials as thermal switches [22] and heat spreaders in integrated circuits [23].

Combined, these studies reveal fundamental limits and some applications of 2D materials, which take advantage of their unique properties.

Acknowledgment

I would like to acknowledge the work of the entire Pop Lab (https://poplab.stanford.edu), as well as support from the SRC, NSF, DOE, the Stanford SystemX Alliance, Intel, TSMC, and Samsung.

References

[1] A. Daus et al., *Nat. Elec.* 4, 495 (2021). **[2]** K.N. Nazif, et al., *Comm. Phys.* 6, 367 (2023). **[3]** C. English et al., *IEDM* (2016). **[4]** M. Aly et al., *Computer* 48, 24 (2015). **[5]** X. Wu et al. *Nat. Comm*. 15, 13 (2024). **[6]** A.I. Khan et al. *Science* 387, 62 (2025). **[7]** C. McClellan et al. *ACS Nano* 15, 1587 (2021). **[8]** R. Bennett & E. Pop, *Nano Lett.* 23, 1666 (2023). **[9]** J.-S. Ko et al., *IEEE TED* 72, 1514 (2025). **[10]** I. Datye et al., *Nano Lett*. 22, 8052 (2022). [**11]** S. Das et al., *Nat. Elec*. 4, 786 (2021). **[12]** M. Jaikissoon et al., *Nat. Elec*. 7, 885 (2024). **[13]** M. Wang & E. Pop, in review (2025). **[14]** E. Yalon et al., *Nano Lett*. 17, 3429 (2017). **[15]** S. Islam et al., *IEEE EDL* 34, 166 (2013). **[16]** H. Su et al., *J. Appl. Phys*. 136, 013901 (2024). **[17]** K. Smithe et al., *Nano Lett.* 18, 4516 (2018). **[18]** A. Gabourie et al., *2D Mater.* 8, 011001 (2021). **[19]** A. Gabourie et al., *J. Appl. Phys.* 131, 195103 (2022). **[20]** A. Sood et al., *Nano Lett.* 19, 2434 (2019). **[21]** S. Vaziri et al., *Science Adv.* 5, eaax1325 (2019). **[22]** M. Chen et al., *2D Mater.* 8, 035055 (2021). **[23]** C. Koroglu & E. Pop, *IEEE EDL* 44, 496 (2023).

Coherent thermal transport in isotopic graphene superlattices: a NEGF study

A. Sebbar[1], N. Cavassilas[1], Y. Guo[2], A. Saul[3], M. Nomura[4,5], S. Volz[4,5], and M. Bescond[1,5]
(1) IM2NP UMR-CNRS, Aix Marseille Université, Université de Toulon, Marseille, France.
(2) School of Energy Science and Engineering, Harbin Institute of Technology, Harbin 150001, China.
(3) Aix-Marseille Université, CNRS, CINaM, Marseille, France
(4) LIMMS-CNRS, IRL 2820, Tokyo, Japan, (5) Institute of Industrial Science, University of Tokyo, Japan.

e-mail: anass.sebbar@univ-amu.fr, marc.bescond@cnrs.fr

ABSTRACT

We developed an in-house *ab initio* 2D Non-Equilibrium Green's Function (NEGF) code to study phonon transport in 2D materials. Based on this code, coherent phonon transport in isotopic ($^{12}C/^{13}C$) graphene superlattices is investigated.

INTRODUCTION

Nanoscale phononic crystals based on 2D materials provide a new opportunity to tune thermal properties using the wave nature of phonons. Constructive (resp. destructive) interferences could indeed induce high (resp. low) thermal conductivities [1].
In that context, atomistic Non-Equilibrium Green's Function (NEGF) approach is well suited, since it intrinsically describes the wave nature of thermal phonons by solving the atomic dynamical equation.

MODEL AND DISCUSSIONS

We extended our in-house NEGF code [2] to study 2D materials-based superlattices. The code solves the dynamical equation using the Retarded Green's function of phonons:

$$G^R(\omega,q_z) = [\omega^2 I - \tilde{\phi}(q_z) - \Sigma^R(\omega,q_z)]^{-1} \quad , \quad (1)$$

where ω denotes the phonon frequencies, I is the identity matrix, and q_z the wave vector along the z-axis, perpendicular to the transport direction. Σ^R represents the self-energies of the contacts while $\tilde{\phi}$ corresponds to the harmonic matrix, computed from the open-source packages Quantum ESPRESSO (QE) and PHONOPY (Figure 1).

Based on this method, we investigate the thermal properties of $^{12}C/^{13}C$ isotopic-superlattices of graphene (see Fig. 2). Since our initial NEGF code requires an orthogonal cell, we consider an orthorhombic unit cell whose resulting *ab initio* bandstructure is shown in Figure 3. Those results have been validated against phonon bandstructure considering a hexagonal unit cell (not shown).
Fig. 4, shows the thermal conductivity ratio γ ($=K_{isotope}/K_{pure}$) as a function of the central region length N for two superlattice (SL) period lengths M, where $K_{isotope}$ and K_{pure} are the thermal conductivity of SL and of pure ^{12}C graphene, respectively. We see that for a given N, *i)* the thermal conductivity of the SL is lower than the one of a pure ^{12}C graphene structure. The smaller the period, the more the thermal conductivity decreases. This expected trend is due to the interface scattering [2].

On the other hand, Figure 5 shows the ratio γ as a function of the SL period length M for three different central regions lengths N. It decreases with the SL period length until a critical value M=8. This is a signature of the wave-nature of phonon which overcomes the interface scattering when the SL period length is smaller than the dominant phonon wavelength. Similar phenomenon has also been found in carbon nanoribbons.

Finally, Figure 6 shows the spectral heat flows of pure graphene structure and SL at the critical length (M=8), where the interface scattering is maximum. We see that the heat flow decrease in SL is significant at 20 THz, which corresponds to a high-density mode in the bandstructure of Fig. 2.

Additional coherent effects will be discussed considering graded [2] and Golomb ruler SL.

REFERENCES

[1] Z. Zhang, *et al., Coherent thermal transport in nano-phononic crystals: An overview*, APL Materials **9** (8), 081102 (2021).
[2] Y. Guo, *et al., Thermal conductivity minimum of graded superlattices due to phonon localization*, APL Materials **9** (9), 091104 (2021).

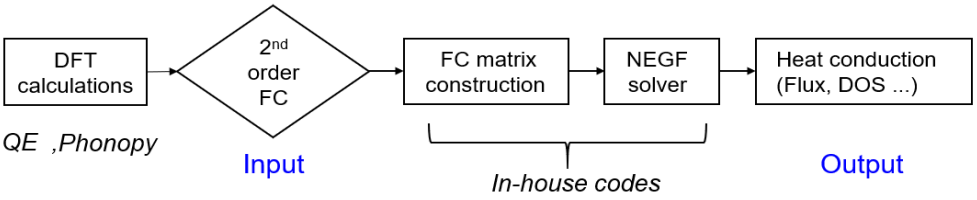

Fig. 1. Flowchart illustrating the structure of the 2D NEGF transport code.

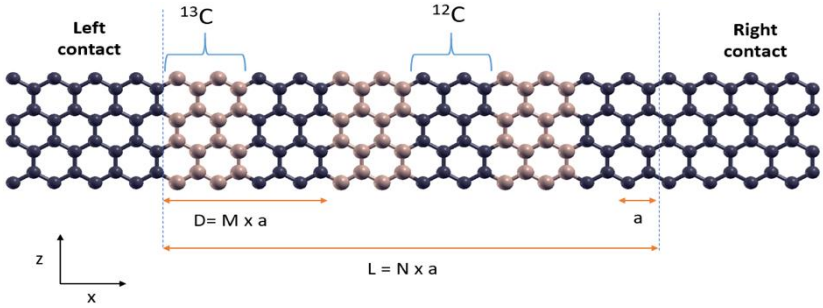

Fig. 2. Schematic of the considered graphene superlattice. The black and brown atoms represent the carbon 12 and 13 respectively, L is the length of the device, D is the period and a is the unit cell's lattice parameter.

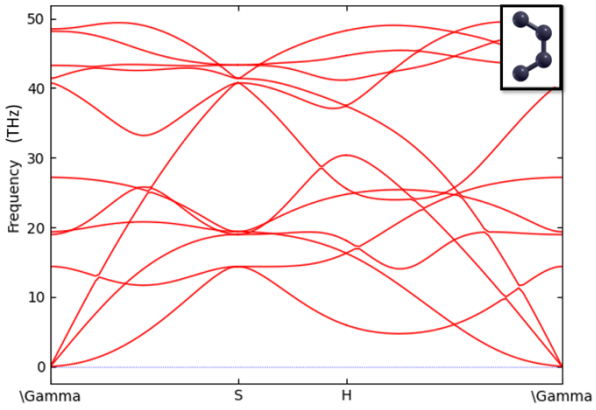

Fig. 3. DFT results of phonon bandstructure of graphene with an orthorhombic unit cell (shown in the top right corner).

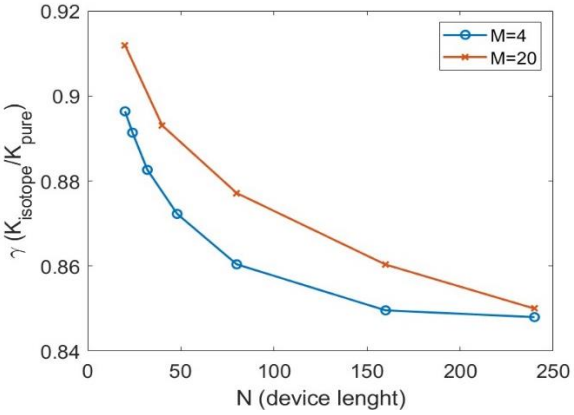

Fig. 4. Thermal conductivity ratio γ as a function of the device's length N for two superlattice period lengths M.

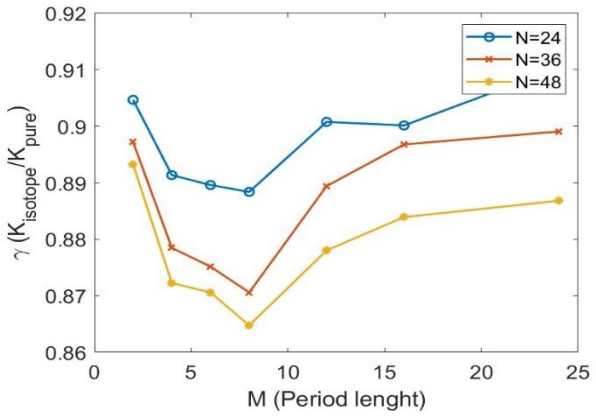

Fig. 5. Thermal conductivity ratio γ as a function of the superlattice period length M for three device lengths N.

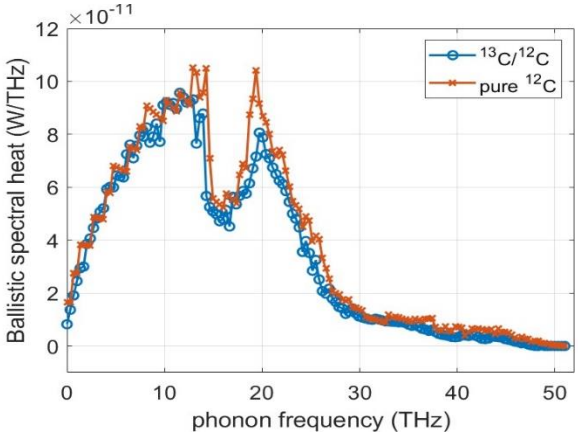

Fig. 6. Spectral heat flow comparison between pure graphene and the isotope superlattice with N=24 and M=8.

A New Method for Bandstructure Calculation and Its Application to Edge Termination Effects in Graphene

Dongming Li*, and Eric Polizzi*†
*Department of Electrical and Computer Engineering, University of Massachusetts, Amherst, MA, USA
†Department of Mathematics and Statistics, University of Massachusetts, Amherst, MA, USA
e-mail: dongmingli@umass.edu

Understanding the impact of surface terminations on the electronic properties of materials is crucial for designing tailored electronic and optoelectronic applications. In this study, we employ a recently developed real-space bandstructure calculation method—"A Method of Calculating Bandstructure in Real-Space with Application to All-Electron and Full Potential" [1]—to investigate the absolute band energies of graphene with three different passivations: hydrogen (H), fluorine (F), and hydroxyl (OH). Unlike conventional k-space methods, which rely on infinitely periodic boundary conditions and are unable to determine absolute band energies, this novel approach enables direct computation of band energies relative to the vacuum level by considering the potential of an extended finite system. The method leverages the combined contributions of nuclear and electron-electron interaction potentials, effectively eliminating the divergence of long-range effects and allowing for the extraction of a converged net potential within the unit cell. After obtaining the net potential from an extended finite system through self-consistent calculations, the band structure can be determined non-self-consistently using Bloch-periodic boundary conditions within the unit cell, enabling the identification of core, valence, and conduction bands.

The starting point is the Density Functional Theory (DFT) and Kohn-Sham one-electron equation described by v-representability to project in real space the one-electron wavefunction as follows:

$$-\frac{1}{2}\nabla^2\phi(r)+V_{nuclei}(r)\phi(r)+V_{hxc}(r)\phi(r)=\varepsilon\phi(r), \tag{1}$$

where V_{hxc} is the Hartree, Exchange and Correlation terms. In the case of infinitely repeated unit cells model, the nuclear potential $V_{nuclei}(r)$ is composed of an infinitely large number of potentials $V_{nuclei}(R_j-r)$ associated with atom j at position R_j. Therefore, in this model, because of the effect of long-range Coulomb potentials, $V_{nuclei}(r)$ term becomes infinitely large. However, in real situations, electrons are never really experiencing this infinitely large potential, and the potential energy felt by one electron can be better expressed by combining V_{nuclei} and V_{hxc} in equation (1) based on each unit-cell, as follows:

$$-\frac{1}{2}\nabla^2\phi(r)+\sum_{m}^{adjacent}\left\{\sum_{n}\left[V^n_{nuclei}(R_{m,n}-r)+V^n_{hxc}(R_{m,n}-r)\right]\right\}\phi(r)=\varepsilon\phi(r), \tag{2}$$

Using the aforementioned method, the band structure of any 1D, 2D, or 3D material can be computed, with examples illustrated in Fig. (1). We further investigated three distinct edge terminations of graphene, revealing that these terminations induce shifts in its absolute band energies shown in Fig. (2), with variations of up to approximately 0.7 eV among the studied cases. This work represents the first computational comparison and analysis of passivation effects on graphene's absolute band energies, highlighting the effectiveness of this method in accurately capturing such effects.

References

[1] Dongming Li, James Kestyn and Eric Polizzi, *A method of calculating bandstructure in real-space with application to all-electron and full potential*, Computer Physics Communications **295**, 109014 (2024).

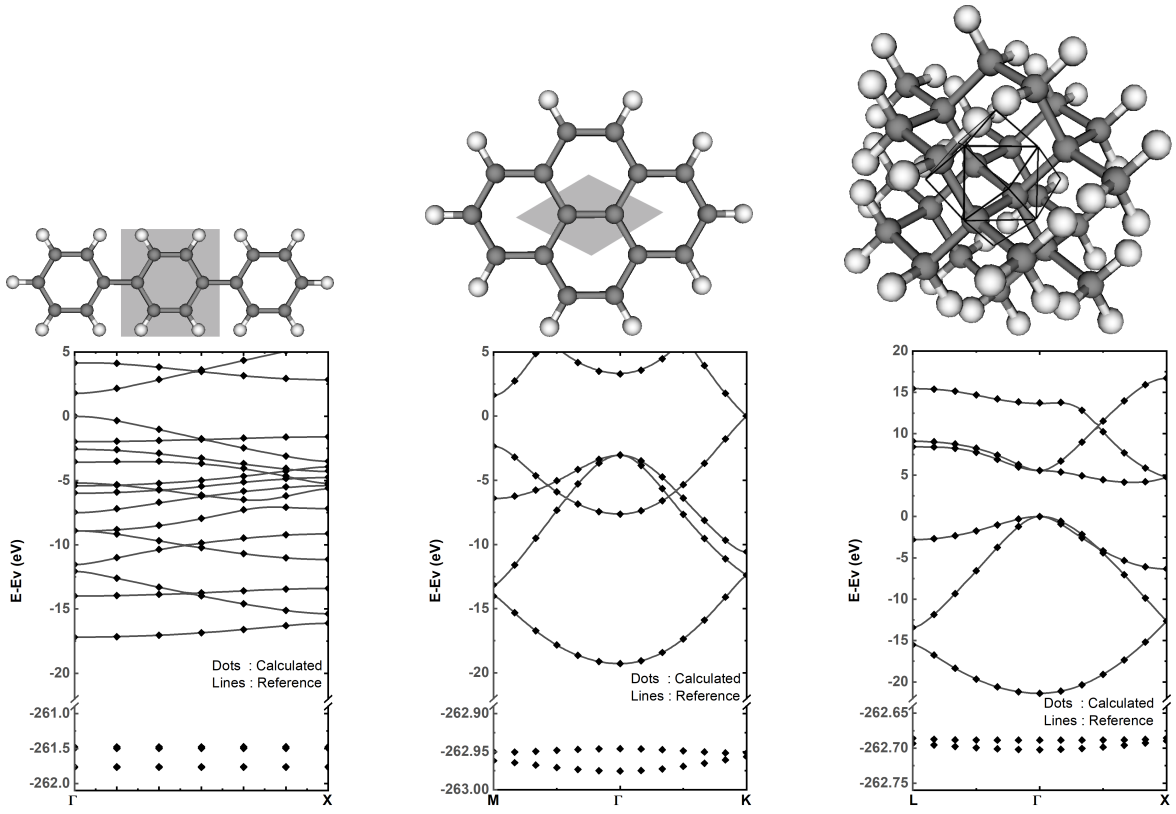

(a) (b) (c)

Fig. 1: Bandstructure calculations for 1D PPP (a), 2D Graphene (b) and 3D carbon Diamond (c). Our results for valence and conduction bands are compared with references obtained by k-space pseudopotential calculations. Core bands are also presented. The figures on top represent the finite systems that are used to extract the net potentials in their corresponding unit-cells. (Extracted from [1])

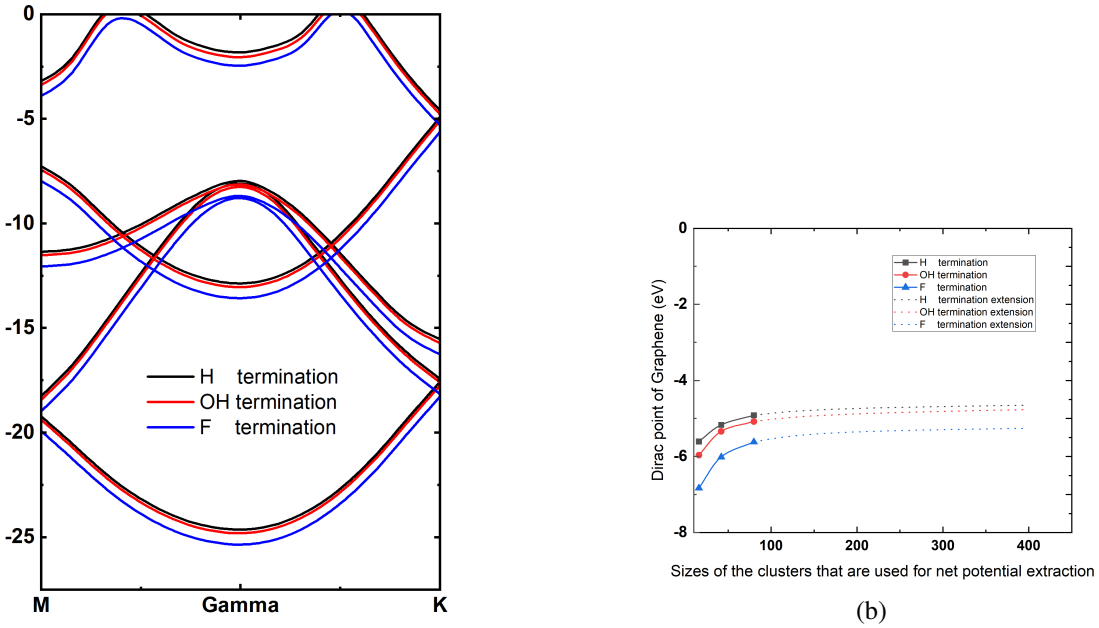

(a) (b)

Fig. 2: (a) Bandstructures of Graphene with -H, -OH and -F edge terminations at the LDA-1/2 density funcitonal physical model (energy level is given in eV), (b) Absolute Dirac Point extrapolation

Theoretical Study of Carrier Transport in Bilayer Transition Metal Dichalcogenides

Shoaib Mansoori, Edward Chen*, Massimo V. Fischetti
Department of Materials Science and Engineering, The University of Texas at Dallas
* Taiwan Semiconductor Manufacturing Company Limited (TSMC), Hsinchu, Taiwan
e-mail: shoaib.mansoori@utdallas.edu

In the past decade, transition metal dichalcogenides (TMDs) have emerged as promising materials for next-generation electronic devices [1], [2]. TMDs, with the chemical formula MX_2 (where M is a transition metal and X is a chalcogen, such as S, Se, or Te), consist of X-M-X layers stacked together. A single X-M-X layer (monolayer MX_2) has an M-atom layer sandwiched between two X-atom layers. The M-X bonds are strongly covalent, while the X-M-X layers are coupled by weak van der Waals forces.

The band structure of TMDs depends significantly on the number of X-M-X layers, as demonstrated by both theoretical and experimental studies on various MX_2 compounds (M = Mo, W; X = S, Se, Te) [3], [4], [5]. Through our work, we also find that in bilayer configurations, the interlayer distance determines whether the bandgap is direct or indirect. For field-effect transistor (FET) applications, TMDs are typically supported by an insulating substrate and may be gated. One critical factor is the interaction of electrons with hybrid plasmon/optical-phonon interface excitations (IPPs) [6], which can significantly affect the transport properties of TMDs, in addition to scattering with bulk phonons [6], [7], [8].

In this work, we examine TMD bilayers in a double-gate geometry, assuming a SiO_2 substrate and using HfO_2 or hBN as examples of high- and low-κ insulators, respectively. First-principles methods are used to compute the band structure (Quantum ESPRESSO) [9], phonon dispersion, and electron-phonon scattering rates (EPW) [10]. We employ the dielectric-continuum approximation to address dielectric screening and electron interactions with IPPs [6]. The carrier mobility was obtained using a full-band Monte Carlo method to solve the Boltzmann transport equation (BTE) [11], [12], [13]. Finally, for device calculations the Poisson Equation is solved and coupled with the BTE. In our device simulations we use 2,000–4,000 particles over a few ps to reach steady state and obtain statistically reliable estimators (e.g., density, velocity, current).

Our results show that WS_2 and WSe_2 bilayers achieve mobilities in the range of 1,000 to 2,000 $cm^2V^{-1}s^{-1}$. The subthreshold slope for bilayer TMDs is estimated $\approx$ 84 mV/dec and $I_{\rm ON}$ 1150 A/m at $V_{\rm DS}$ = 0.5 V, meeting the ITRS requirements. In addition, longer drain-extension regions introduce a high series resistance, which can significantly affect overall device performance. These findings highlight the importance of choosing the right channel and insulator materials and device architecture.

REFERENCES

[1] S. Li, K. Tsukagoshi, E. Orgiu, and P. Samori, Soc. Rev. **45**, 118–151 (2016).
[2] B. Radisavljevic, A. Radenovic, J. Brivio, V. Giacometti, and A. Kis., Nat. Nanotech. **6**, 147 (2011).
[3] Pandey SK, Das R, Mahadevan P, ACS Omega **25** (2020).
[4] A. Splendiani, et. al, Nano Lett. **10**, 1271 (2010).
[5] A. Kuc, N. Zibouche, T. Heine, Phys. Rev. B **83** (2011).
[6] S. Gopalan, M. L. Van de Put, G. Gaddemane, and M. V,. Fischetti, Phys. Rev. Appl. **18**, 054062 (2022).
[7] N. Ma and D. Jena, Phys. Rev. X **4**, 011043 (2014).
[8] A. Hauber and S. Fahy, Phys. Rev. B **95**, 045210 (2017).
[9] P. Giannozzi et al., J. Phys. Cond. Matt. **21**, 395502 (2009).
[10] S. Ponce, E. R. Margine, C. Verdi, and F. Giustino, Comp. Phys. Commun. **209**, 116 (2016).
[11] G. Gaddemane, W. G. Vandenberghe, M. L. Van de Put, S. Chen, S. Tiwari, E. Chen, M. V. Fischetti, Phys. Rev.B **98**, 115416 (2018).
[12] G. Gaddemane, S. Gopalan, M. L. Van de Put, M. V. Fischetti, J. Comp. Electron. **20**, 49-59 (2021).
[13] G. Gaddemane, M. L. Van de Put, W. G. Vandenberghe, E. Chen, M. V. Fischetti, J. Comp. Electron. **20**, 60–69 (2021).

	Freestanding	hBN/TMD/SiO_2	HfO_2/TMD/SiO_2
Bilayer WS_2	2300	1530	100
Bilayer MoS_2	50	35	7
Bilayer WSe_2	1300	1500	13
Monolayer WS_2	750	1500	70
Monolayer MoS_2	500		
Monolayer WSe_2	850		

Fig. 1. Calculated 300 K hole mobility (in $cm^2V^{-1}s^{-1}$) in freestanding TMD and double-gate stack, assuming SiO_2 as bottom insulator and different gate insulators. Both insulators are assumed to have an equivalent oxide thickness (EOT) of 0.7 nm. The results have been obtained assuming a TMD electron sheet-density of 5×10^{12} cm^{-2}

	Freestanding	hBN/TMD/SiO_2	HfO_2/TMD/SiO_2
Bilayer WS_2	161	172	30
Bilayer MoS_2	201	163	36
Bilayer WSe_2	400	340	63
Monolayer WS_2	170	152	20
Monolayer MoS_2	140		
Monolayer WSe_2	390		

Fig. 2. Calculated 300 K electron mobility (in $cm^2V^{-1}s^{-1}$) in freestanding TMD and double-gate stack, assuming SiO_2 as bottom insulator and different gate insulators. Both insulators are assumed to have an equivalent oxide thickness (EOT) of 0.7 nm. The results have been obtained assuming a TMD electron sheet-density of 5×10^{12} cm^{-2}

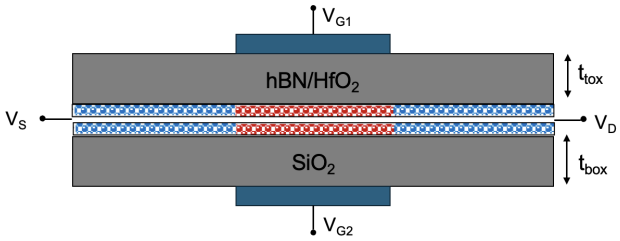

Fig. 3. Cross section of the double-gate TMD MOSFET used in the simulations

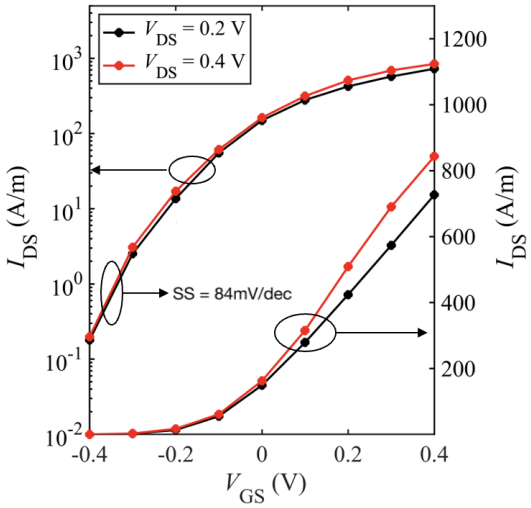

Fig. 4. The transfer characteristics ($I_{\rm DS}$ vs. $V_{\rm GS}$) for the double-gate device, plotted on linear and log scale

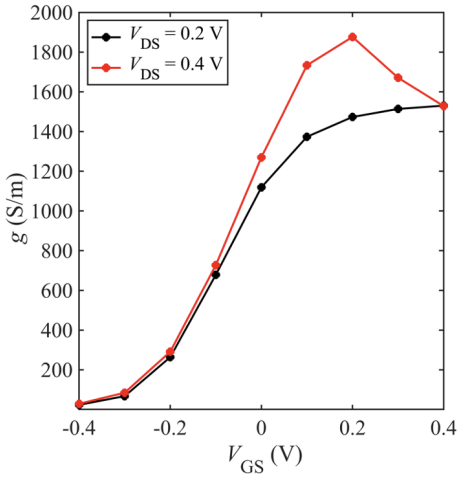

Fig. 5. The transconductances ($g_{\rm m}$ vs. $V_{\rm GS}$) for the double-gate device, plotted on linear and log scale

Electrostatic Model of Metal-Induced Gap States in Metal Edge, Top and Hybrid Contacts to MoS2 transistors

E. Deylgat[1,2,3], C.P. Chuu[4], E. Chen[4], B. Sorée[2,3,5] and W. Vandenberghe[1]
[1]Univerty of Texas at Dallas, Dallas, TX, USA, [2]Catholic University of Leuven, Leuven, BE, [3]IMEC, Leuven, BE,[4]Corporate Research, Taiwan Semiconductor Manufacturing Company Ltd., Hsinchu, Taiwan, [5]University of Antwerp, Antwerp, BE

Introduction: Two-dimensional (2D) semiconducting materials are a potential replacement for silicon-based channels in future transistor designs. Transition-metal dichalcogenides (TMDs) such as MoS_2, WS_2, and WSe_2 are some of the most promising candidates due to their relatively high band gaps and decent mobilities [1]. However, a key challenge of using 2D materials is the high contact resistance between the metal/TMD interface which is often characterized by so-called Schottky barriers. In the past, Schottky barriers were described by the Schottky-Mott rule in which the barrier height (BH) depends on the contact metal work function (WF). However, in many cases, the barrier is rather insensitive to the metal WF as the Fermi level (FL) is "pinned" to a certain energy level [2]. The pinning often occurs due to MIGS, due to which the FL is pinned to the charge neutrality level ECNL resulting in increased contact resistance.

In this paper, we model the MIGS in metal contacts with different geometries, the edge, top and hybrid contact (EC, TC and HC). From the model, we extract MIGS densities corresponding to different pinning parameters and compare to DFT and experiments. We calculate the contact resistance for back-gated contacts and determine current paths of different contact geometries.

Methods: Figure 1 shows a schematic of the EC, TC, and HC (top to bottom) and defines the 2D material thickness t_{2D} = 0.65 nm, the contact length L_C = 6 nm, the van-der-Waals (vdW) gap thickness as t_{vdW} = 0.3 nm and the back-gate distance as L_{BG} = 100 nm.

Figure 2 shows a schematic of the FL pinning mechanism due to MIGS described by Eq. (4, 5).

Figure 6 shows a schematic of the HC geometry where we indicate the location of the top and edge MIGS in the Poisson model.

Figure 3 shows a flowchart of the methodology of the BH model and transport calculation. We numerically solve the Poisson equation (Eq. (1)), self-consistently with the electron concentration in a 2D material (Eq. (2)) using finite element code [3]. We determine the IFBL by using an analytical expression (Eq. (3)) [4] which is added to the solution of the Poisson equation. To determine the FL pinning, we measure the BH in the center of the TMD and fit the S-parameter (Eq. (5)). We calculate the contact resistance by setting up an effective mass Hamiltonian (Eq. (6)) which is discretized with the finite-differences method. We use the quantum boundary transmission method (Eq. (7, 8)) [5, 6] to extract the transmission which is used in Eq. (9) to arrive at the contact resistance.

Results: Figure 4(a) shows the potential energy U of the EC, TC, and HC from top to bottom. The top dielectric is air, while the bottom dielectric is SiO_2. Figure 4(b) shows the solution of the Poisson equation (Eq. (1)) for the different geometries. Figure 4(c) shows the IFLB where we assume a homogeneous dielectric of SiO_2.

Figures 5(a) and (b) show the Schottky barrier height as a function of the difference between the metal WF and the MoS_2 electron affinity for contacts with different geometries and substrates. In the case of the EC (Fig. 5(a)), very high MIGS densities are needed to pin significantly. At a very high density of D_{IT} = 1e15 cm^{-2} eV^{-1}, we realize S = 0.67. Compare that to the pinning in the TC case (Fig. 7(b)), we see that full pinning is achieved at $D_{IT} > 10^{15}$ cm^{-2} eV^{-1} as S = 0.02 while very low pinning is achieved at $D_{IT} < 1\times10^{11}$ cm^{-2} eV^{-1} (S = 0.97). Previously, the BH was determined experimentally for Ti, Ni, and Pt in both EC and TC on SiO_2 substrates in ref. [7]. Pinning-free ECs were fabricated, and the extracted barrier heights are indicated in Fig. 5a. The corresponding S-parameter is S > 0.88 which translates to $D_{IT} <$ 1e14 cm^{-2} eV^{-1}. Pinning-free ECs can be fabricated if the interfaces are defect-free as the MIGS do not contribute much to pinning. In the case of the TC (Fig. 5(b)), the barriers from ref. [4] correspond to a $D_{IT} = 1.3\times10^{14}$ cm^{-2} eV^{-1}. Following Eq (3), we determine MIGS = 2.6×10^{13} cm^{-2}.

Figures 7(a) and (b) show the contact resistance as a function of carrier concentration for the different contact geometries in the case of a (a) Ni and (b) an Sb contact. The corresponding spatial current densities at the highest carrier densities are shown in Fig. (c) and (d), respectively. For the Sb contact, the contact resistance is close to the quantum limit (QL), since the barrier is low and MIGS are assumed to be low due to Sb being a semi-metal. The HC yields the lowest resistance since more current paths are available. The top contact has higher resistance because the current must tunnel through the vdW gap. For the Ni contact, the barrier is high. Therefore, the resistance is the lowest in the TC since the EC yields higher barriers in the x-direction. Most of the current goes through the metal corner of the hybrid and TCs. However, the HC has high resistance since the vicinity of the edge metal boundary increases the barrier.

Figure 8(a) shows the DFT structure of a top-contacted MoS_2 monolayer with a metal (Au). Figure 8 (b) shows the density of states (DOS) of the MoS_2 monolayer. The MIGS = 1.2×10^{13} cm^{-2} are extracted from DOS inside the bandgap of the monolayer induced by the metal. Figure 8(c) shows the DFT structure of an edge geometry. Figure 8(d) shows the MIGS as a function of x-coordinate along the length of the monolayer. At the edges, we find MIGS = 2.3×10^{13} cm^{-2}. The MIGS obtained from DFT is of the same order as the MIGS from the model fitted to the experimental data. Table 1 shows the values of the MIGS and E_{CNL} in the case of the EC and TC using the Poisson equation and the DFT.

Conclusion: We modeled the MIGS in EC, TC, and HC. MIGS pin the FL at much lower concentrations in TCs compared to ECs, allowing for easier pinning free edge contacts. However, EC do not yield the best performance. In low barrier scenarios, the HC gets closest to the QL, while the the TC yields the lowest contact resistance in high barrier scenarios.

References: [1] Y. Liu, *et al*. *Nature* **591**, 43–53 (2021). [2] A. Allain, *et al*. *Nat. Mat.* **14**, 1195–1205 (2015). [3] A. Logg, et al. ACM Trans. Math. Soft. **37** (2010). [4] S. R. Evans, *et al. Phys. Rev. Appl.* **20**, 044003 (2023). [5] M. Fischetti and W. Vandenberghe (2016). [6] C. S. Lent, et. al, JAP **67**, 6353–6359 (1990). [7] T. Y. T. Hung, *et al. IEDM* (2020).

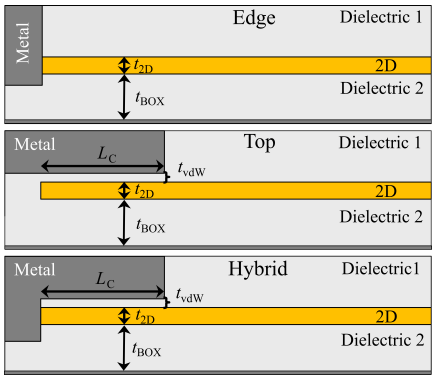

Fig. 1. Contact geometries considered in simulations.

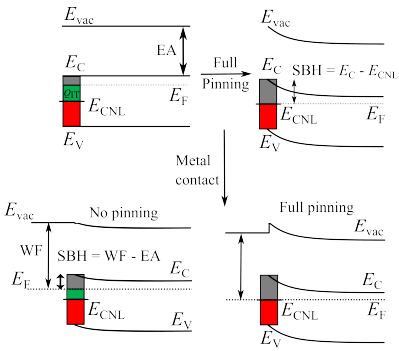

Fig. 2. Schematic Fermi level pinning of MoS_2 bands in the presence of MIGS.

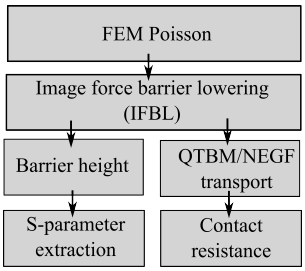

Fig. 3. Flow chart of the methodology of obtaining the barrier height for S-parameter extraction or obtaining contact

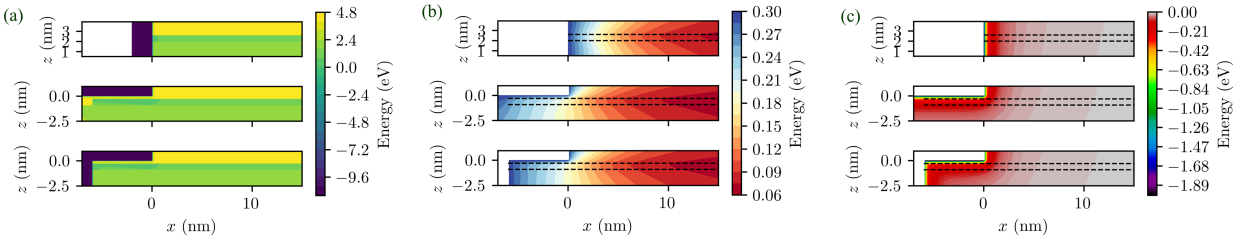

Fig. 4. (a) Energy landscape of the edge, top and hybrid contact (top to bottom). (b) Solution of Poisson equation for edge, top and hybrid contact (without MIGS). (c) Image-force barrier-lowering potential energy for edge, top and hybrid contact.

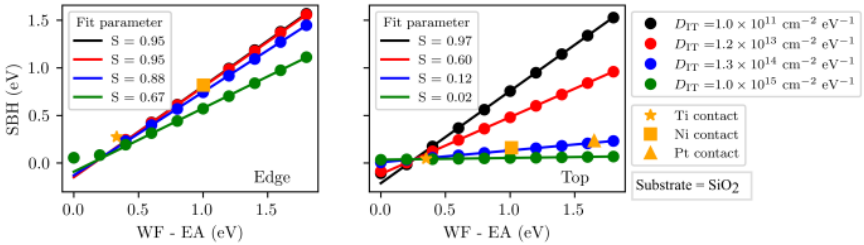

Fig. 5. Schottky barrier height vs. difference metal WF and MoS_2 EA for different MIGS. MoS_2 doping is 10×10^{12} cm^{-2} and E_{CNL}= 0.2 eV. The contact geometries are (a) edge contact and (d) top contact. We indicate the experimental barrier height of previously investigated devices [4] using yellow shapes.

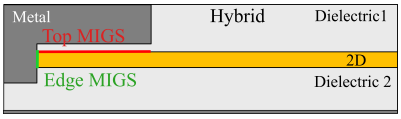

Fig. 6. Location of MIGS in a hybrid contact. Similar locations are used for edge and top contact.

Metal contact (Ti, Ni, Pt)	Edge	Top
D_{IT} (cm^{-2} eV^{-1})	~ 1.2×10^{14}	~ 1.3×10^{14}
E_{CNL}(eV)	0.2	0.2
MIGS (cm^{-2})	~ 2.4×10^{13}	~ 2.6×10^{13}
DFT MIGS (cm^{-2})	~ 2.3×10^{13}	~ 1.2×10^{13}

Table I. Contains the MIGS data of the different contact geometries

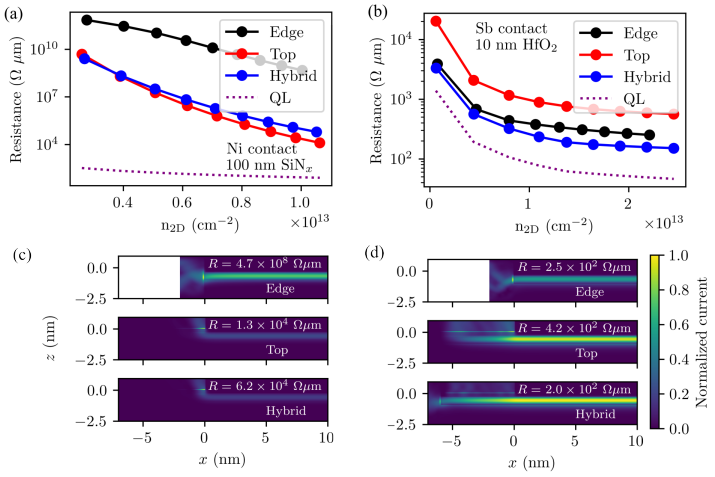

Fig. 7. Contact resistance vs. carrier concentration in an (a) Ni contact high barrier and pinning and (b) Sb contact for low barrier and pinning for different contact geometries. (c) and (d) show the corresponding current densities at the maximal carrier concentration according to (a) and (b).

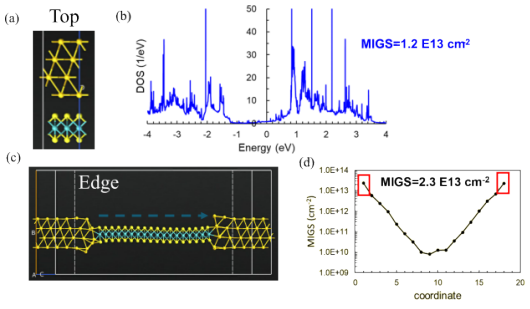

Fig. 8. (a) Structure of top contact in QuantumATK. (b) Density of states of the MoS_2 monolayer as function of energy. (c) Structure of edge contact in QuantumATK. (d) MIGS density as a function of x-coordinate.

Potentials:

$$\nabla\cdot(\bar{\epsilon}(x,z)\nabla V(x,z)) = e\left[N_D(x,z) + Q_{IT}(x,z) - n(x,z)\right] \quad (1)$$

$$n(x,z) = N\frac{m^* k_B T}{\pi\hbar^2 t_{2D}}\ln\left[1+\exp\left(\frac{E_F - eV(x,z)}{k_B T}\right)\right] \quad (2)$$

$$U_{IFBL}(r,\theta;\Omega) = \frac{-e^2}{8\pi\epsilon r}\int_0^\infty d\alpha \frac{\sinh(\alpha\pi)\cosh(2\alpha\theta) - \sinh(\alpha(\pi-\Omega))}{\sinh(\alpha\Omega)\cosh(\alpha\pi)} \quad (3)$$

MIGS:

$$\text{MIGS} = Q_{IT} = D_{IT}\cdot(E_F - E_{CNL}) \quad (4)$$

$$\text{SBH} = S\,(\text{WF} - \text{EA}) + (1-S)\,(E_C - E_{CNL}) \quad (5)$$

Transport:

$$H = -\frac{\hbar^2}{2}\nabla\cdot\left(\frac{1}{m^*(x,z)}\nabla\right) + \frac{\hbar^2 k_y^2}{2m^*(x,z)} + U(x,z) \quad (6)$$

$$[EI - H - \Sigma]\psi = B \quad (7)$$

$$T = 1 - \frac{|B_{out}^{-1}\psi_{out}|^2 v_{out}}{v_{in}} \quad (8)$$

$$\frac{1}{\rho_c} = \frac{2e^2}{h}N\int_{-\infty}^{\infty} dE\left|\frac{df(E)}{dE}\right|\int_{-\infty}^{\infty}\frac{dk_y}{2\pi}T(k_y,E) \quad (9)$$

Thursday 11:00-12:30 Emerging Devices

Time	Type	Presenter	Title
11:00-11:30	**Invited**	Wenhao Song	Diffusive and drift memristors for neuromorphic and analog computing
11:30-11:45	Contributed	Sylvester Wambua Makumi	Impact of Electrostatic Pressure on the TBC of 2D-Substrate Interfaces
11:45-12:00	Contributed	A. Alleysson	Quantum transport of excitons in lateral TMDs heterostructures
12:00-12:15	Contributed	Mauro Dossena	Influence of disordered oxides on the mobility of monolayer WS_2: an ab initio study
12:15-12:30	Contributed	Chieh-Yang Chen and Yiming Li	Effect of Random Nanosized Titanium Nitride Grains on Monolayer MoS_2 Field-Effect Transistors

Advancing Analog Precision: Memristor Technology for Scientific Computing

Wenhao Song, J. Joshua Yang

University of Southern California, Los Angeles, CA 90089, USA

Email: jjoshuay@usc.edu

Due to precision limitations, analog devices such as memristors have historically been confined to specialized, low-precision applications like neural networks. To overcome these constraints and extend their applicability into scientific computing, we comprehensively studied the sources of reading noise and successfully mitigated them, achieving up to 2048 stable conductance levels. Additionally, through a co-designed approach involving system circuit architecture and programming algorithms, we have significantly reduced device programming variability and improved overall precision. These advancements have enabled us to demonstrate high-precision computing applications with notably enhanced power efficiency, highlighting the expanding potential of memristors for next-generation computing paradigms.

Impact of Electrostatic Pressure on the TBC of 2D-Substrate Interfaces

Sylvester Wambua Makumi[1], Aidan Belanger[1], and Zlatan Aksamija[1*]
[1]Materials Science and Engineering, University of Utah, USA.
e-mail: *zlatan.aksamija@utah.edu

I. INTRODUCTION

While 2D materials offer exciting potential for application in electronic devices, their adoption is hindered by heating issues arising from increased component density in integrated circuits. Low thermal boundary conductance (G) of the 2D-substrate interfaces is a key bottleneck to the realization of efficient thermal management. Previous study has shown that G can be improved by applying hydrostatic pressure [1]. Likewise, electrostatic field (F) due to gate voltage (V_g) can produce pressure (P_{elec}) that can modulate phononic heat flow across interfaces [2]. However, the impact of P_{elec} on G at 2D/substrate interfaces is not well understood, particularly regarding the roles of the mechanical properties of 2D materials and substrate roughness.

To address this issue, we have employed a numerical modelling together with first-principles DFPT simulations to study the impact of P_{elec} on G. Our model involves generating rough surface with randomized roughness features that resemble the actual roughness of a material using an algorithm that is based on the inverse fast Fourier transform (IFFT) [3]. We then place a single layer of 2D material on the rough substrate (Fig. 1) and minimize the total energy to get the equilibrium 2D-substrate distances, h. Using h we determine vdW spring coupling constants (K_s) and then G.

II. RESULTS AND DISCUSSION

Our study shows that P_{elec} can improve G by more than 300 % when an electric field of 3e+9 V/m is applied. We find that G is enhanced more when the substrate has a roughness with large RMS roughness height (Δ_{rms}), small correlation length (L_{cor}), and the 2D material has a large bending stiffness (D_{bend}).

By applying V_g, we induce a net charge concentration on the 2D material that causes an attractive force (F_{elec}) hence P_{elec} that increases with increasing F. Unlike setups where hydrostatic pressure is used, here F_{elec} can cause the 2D sheet to bend and conform to the substrate roughness without destroying roughness peaks. However, the 2D sheet resists bending causing greater pressure at the roughness peaks. Consequently, K_s, and hence G, at roughness peaks is enhanced more as shown in Fig. 2. As illustrated in Fig. 3, the average TBC is enhanced more when surface slope, Δ_{rms}/L_{cor}, is large. G of interfaces with large surface slope increases by more than 300 % making it about 15 % larger than that of a flat interface. A large surface slope causes large delamination that result in weak adhesion energy, Γ_0, hence weak interfacial bond stiffness which is easier to compress and significantly reduce h values increasing K_s which leads to the enhancement in G.

As shown in Fig. 4, we observe that G increases more when D_{bend} is large. This is because if D_{bend} is small the 2D materials can easily bend and conform to the topography of the rough-substrate surface which leads to more uniform K_s values. However, if the 2D material has a large D_{bend}, it will resist bending. As a result high pressure concentrate at the roughness peaks so that h becomes very small hence, we get very large K_s values at these regions which leads to the high conductance. Finally, we show that induced electrons contributes through their interaction with phonons in the 2D material. As electrons get excited, they can effectively transfer heat energy to the lattice vibrations via electron-phonon coupling. We show that this additional pathway for heat transfer can contribute about 7% of the overall G.

III. CONCLUSIONS

In this study, we have demonstrated that electrostatic pressure (P_{elec}) due to a gate voltage is a viable approach to improve TBC. Our study reveals that TBC is enhanced more when the substrate has a large RMS roughness height, short correlation length, and the 2D material has a large stiffness. We show that P_{elec} can enhance the TBC of a very rough interface so that it is 15% greater than that of a flat interface. Thus, this study provides information on how P_{elec}, substrate roughness, and mechanical properties of 2D materials can be leveraged to enhance thermal performance in electronic devices made of 2D materials.

IV. ACKNOWLEDGMENT

The authors acknowledge financial support from the National Science Foundation (NSF). This research was supported by NSF under Grant No. DMR-2302879.

REFERENCES

[1] Wen-Pin Hsieh, Austin S. Lyons, Eric Pop, Pawel Keblinski, and David G. Cahill. Pressure tuning of the thermal conductance of weak interfaces. *Physical Review B*, 84(18):184107, November 2011. Publisher: American Physical Society.

[2] Yee Kan Koh, Austin S. Lyons, Myung-Ho Bae, Bin Huang, Vincent E. Dorgan, David G. Cahill, and Eric Pop. Role of Remote Interfacial Phonon (RIP) Scattering in Heat Transport Across Graphene/SiO_2 Interfaces. *Nano Letters*, 16(10):6014–6020, October 2016. Publisher: American Chemical Society.

[3] Claudio Buran, Marco G Pala, Marc Bescond, Mathieu Dubois, and Mireille Mouis. Three-dimensional real-space simulation of surface roughness in silicon nanowire FETs. *IEEE Transactions on Electron Devices*, 56(10):2186–2192, 2009.

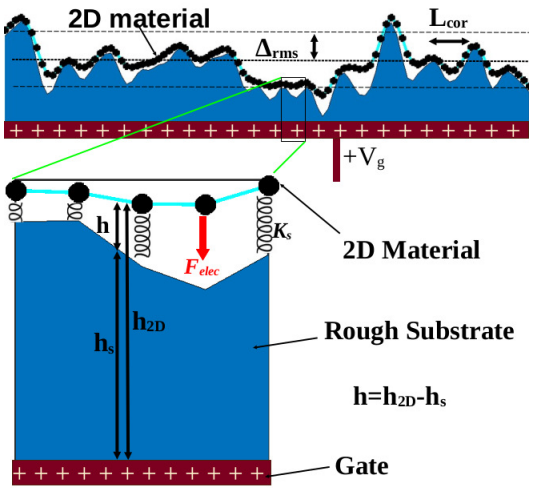

Fig. 1. A schematic showing a single layer of 2D material on a rough substrate and a gate. Electrostatic field due to a gate voltage produces a force that pull the 2D sheet towards the substrate and tries to make it conform to the topography of the rough substrate. However, the 2D sheet resists bending and cannot bend enough to conform fully to the rough substrate. As a result, we have regions that are in contact and others that are delaminated. This leads to variation in the 2D-substrate distance across the interface.

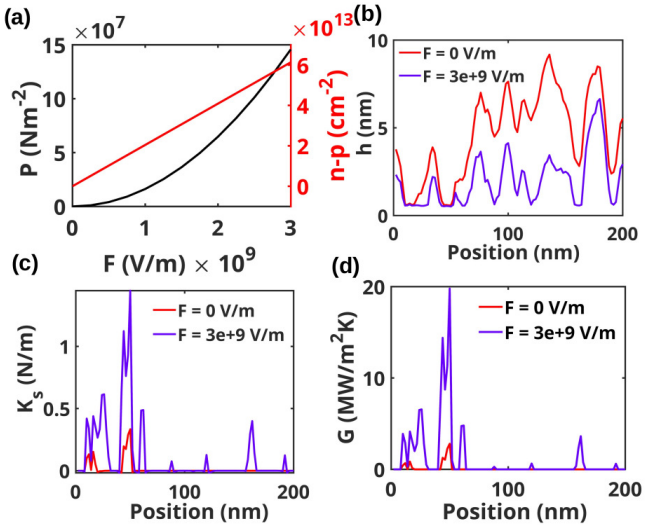

Fig. 2. Analysis of graphene/a-SiO_2 interface at 300 K. (a) Electrostatic pressure, P_{elec}, and the induced charge density, $(n-p)$, as a function of field (F). (b) The 2D-substrate distance, h, (c) vdW spring coupling constant, K_s, and (d) thermal boundary conductance, G, as a function of position for a substrate with Δ_{rms} of 2.5 nm and L_{cor} of 8.8 nm. Larger pressure at the roughness peaks significantly increases K_s hence phonon coupling at these regions. As a reult we find that G at contact regions is enhanced more upon application of P_{elec}.

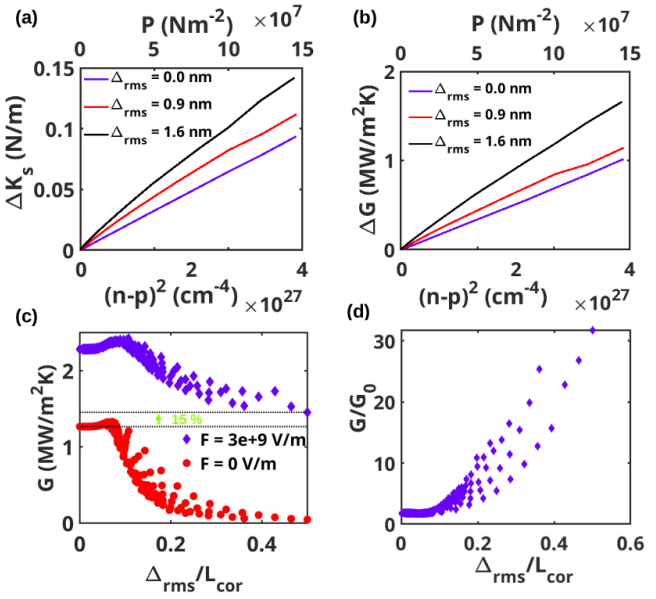

Fig. 3. Analysis of K_s and G of graphene/a-SiO_2 interface at 300 K. (a) The difference between K_s at an electric field of 3e+9 V/m and at 0 V/m, ΔK_s, and (b) the difference between G at an electric field of 3e+9 V/m and G_0 at 0 V/m, ΔG, as a function of the square of charge concentration density, $(n-p)^2$, and P_{elec} for interface with different Δ_{rms} values and L_{cor} of 10.8 nm. We observe a maximum increase in G of 333 % for interface with Δ_{rms} of 1.6 nm when an electric field of 3×10^9 V/m is applied. (c) G as a function of surface slope, Δ_{rms}/L_{cor}, before and after applying electric field. G of very rough interfaces become 15 % larger than that of a flat interface. (d) The ratio of G and G_0 as a function of surface slope showing that electrostatic pressure enhances G of interfaces with large surface slope more.

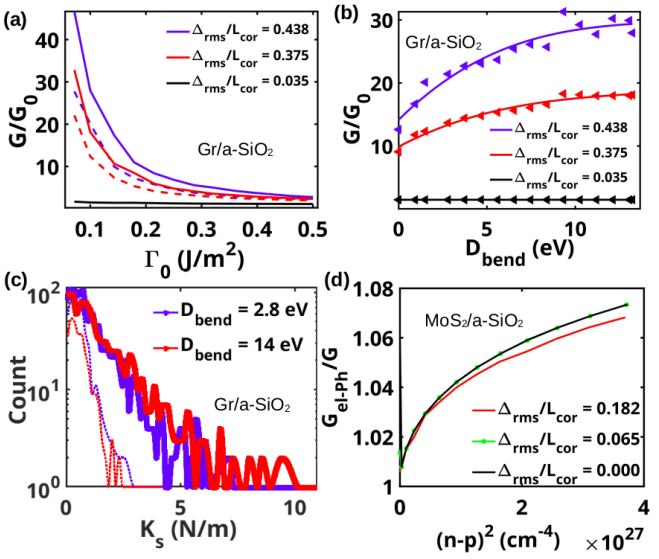

Fig. 4. The ratio of G (at an electric field of 3×10^9 V/m) and G_0 (no electric field) as a function of adhesion, Γ_0, for bending stifness, D_{bend}, of 1.5 eV (broken lines) and 13.24 eV (full lines) showing that G is enhanced more when Γ_0 is weak and surface slope is large. (b) The ratio of G and G_0 as a function of D_{bend} for different values of surface slope and Γ_0 of 0.1 J/m^2. We observe that G is enhanced more when D_{bend} and surface slope are large. (c) The K_s values when an electric field of 3×10^9 V/m is applied (full lines) and when there is no electric field (dotted lines) showing that in a stiffer 2D sheet, application of electric field leads to many-large K_s values than when the 2D sheet is flexible. (d) The ratio of the TBC when there is el-ph coupling, G_{el-ph}, and the TBC without el-ph as a function of the square of charge concentration. We observe that the el-ph coupling contributes about 7 % of the total G.

Quantum transport of excitons in lateral TMDs heterostructures

A. Alleysson[1], F. Michelini[1], M. Lannoo[1], S. Volz[2,3], and M. Bescond[1,3]
(1) IM2NP UMR-CNRS, Aix Marseille Université, Université de Toulon, Marseille, France.
(2) LIMMS-CNRS, IRL 2820, Tokyo, Japan, (3) Institute of Industrial Science, University of Tokyo, Japan.

e-mails: anais.alleysson@univ-amu.fr, fabienne.michelini@univ-amu.fr, marc.bescond@cnrs.fr

ABSTRACT

We theoretically investigate exciton transport in lateral TMD's heterostructures within the Non-Equilibrium Green's Function (NEGF) formalism. An original self-energy is developed to describe the crucial exciton-phonon interactions.

INTRODUCTION

Excitonic devices, which are based on carriers made of bound electron-hole pairs, are very promising for energy-efficient operation. In that context, 2D materials transition metal dichalcogenides (TMDs), in which binding energy of excitons is much larger than in common semiconductors (few hundreds of meV), represent a great opportunity to develop that kind of devices operating at room temperature. However, most of the theoretical transport studies reported so far rely on classical physics: they are mainly based on fluid mechanics or empirical models [1].

MODEL AND DISCUSSIONS

We develop a NEGF quantum transport approach for the bosonic nature of excitons to investigate the dynamics of excitons in the TMDs lateral heterostructure shown in Fig. 1. Excitons are generated by a laser in the left reservoir, and we calculate the number of excitons collected in the right reservoir in which they recombined. The left reservoir boson statistics is estimated from the laser power.

Based on the tight-binding triangular lattice exciton model proposed in Ref. [2], we calculate the electronic band structure which reproduces the main features of typical transition metal dichalcogenides for the valence (v) and conduction (c) band (see Fig. 2 in the case of WSe_2).
The exciton bands are then obtained including the Coulomb interaction between the electron and the hole (Fig. 3a)). Typical binding energies of the first four optical excitons are between 100 and 500 meV. The corresponding square modulus of their wave-function is shown on Fig. 4 for the first four states. We also observe that simple effective mass scheme remains very accurate to determine the energy band of the first exciton state. The extracted effective masses of the first excitonic state at Γ point for the two TMDs are given in Fig. 3b).

Using those effective masses, we computed the transport properties of the first excitonic state of the TMD heterostructure shown in Fig. 1. Two incident laser powers have been considered. At low laser power (*i.e.* 3 mW), the resulting chemical potential μ is located at 0.11 eV below the excitonic band, leading a Boltzman character of the exciton distribution. As shown in Fig. 5, the exciton density is very close to the one obtained with a Fermi-Dirac distribution for electrons. However, at higher laser power (*i.e.* 10 mW), μ rises up to 0.017 eV below the bottom of the band. The Bose-Einstein character becomes now crucial to describe the exciton transport (see Fig. 6).

Exciton-phonon coupling is negligible in a given exciton state. It becomes however predominant when considering multiple bands (see Fig. 3). Based on the work of Antonius and Louie [3], we have developed a real-space exciton-phonon self-energy with a similar expression as the one of the electron-phonon coupling. Impact on TMDs heterostructures will be discussed.

REFERENCES

[1] A. Granados del Águila, *et al.*, *Ultrafast exciton fluid flow in an atomically thin MoS2 semiconductor*, Nat. Nanotechnol. **18**, 1012 (2023).
[2] D. Gunlycke and F. Tseng, *Triangular lattice exciton model*, Phys. Chem. Chem. Phys. **18**, 8579 (2016).
[3] G. Antonius, S. G. Louie, *Theory of exciton-phonon coupling*, Phys. Rev. B **105**, 085111 (2022).

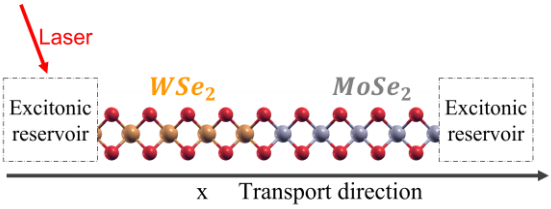

Figure 1. Lateral heterostructure of WSe_2-$MoSe_2$. Excitons are generated by an incident laser in the left reservoir.

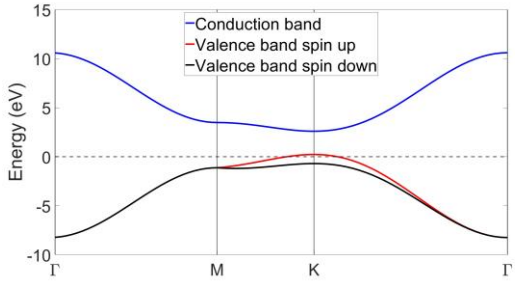

Figure 2. WSe_2 band structure without Coulomb interaction. The two spin channels are degenerate for the conduction band, while for the valence band, there is a splitting of the up and down spins due to spin-orbit coupling.

a)

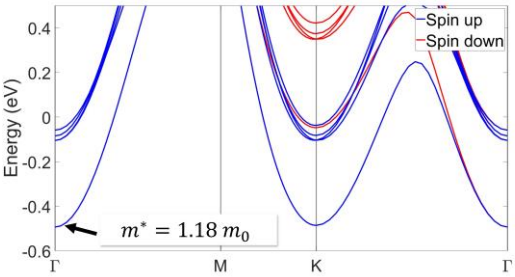

b)

	WSe_2	$MoSe_2$
Effective mass (m^*)	$1.18m_0$	$1.63m_0$

Figure 3. a) WSe_2 exciton band structure with Coulomb interaction for the different spin states. b) Effective mass estimated from the exciton band structure obtained using the triangular model of Ref. [2].

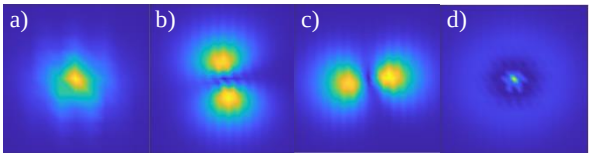

Figure 4. Probability of presence of the fourth exciton states at Γ: a) $E_1 = -0.4935$ eV, b) $E_2 = -0.1050$ eV, c) $E_3 = -0.1050$ eV, and d) $E_4 = -0.0847$ eV. For the first and fourth states (spin up), the central location between hole and electron emphasizes tightly bound exciton states.

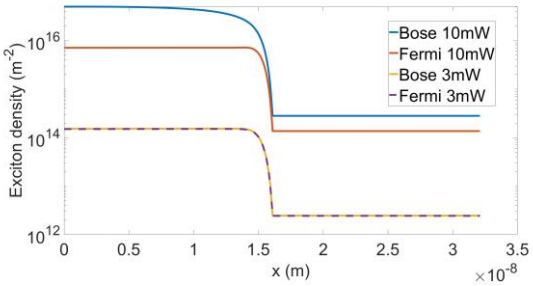

Figure 5. Exciton densities along the TMD heterostructure of Figure 1 for two incident laser powers applied in the left contact: P_{low}= 3 mW, P_{high}= 10 mW, and two assumed distributions (Fermi-Dirac and Bose-Einstein).

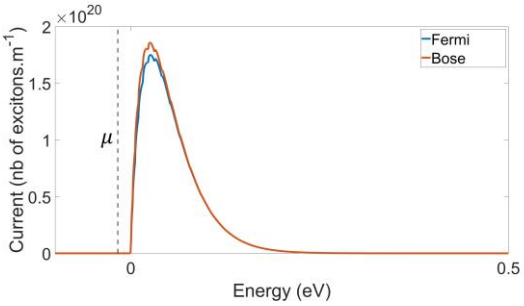

Figure 6. Exciton current spectra of the TMD heterostructure under a high incident laser power (10 mW) assuming Bosonic (red line) and Fermionic (blue line) transport.

Influence of disordered oxides on the mobility of monolayer WS_2: an *ab initio* study

M. Dossena*, B. Van Troeye†, F. Ducry†, J. Cao*, A. Afzalian†, G. Pourtois†, and M. Luisier*
*Integrated Systems Laboratory (IIS), ETH Zurich, Zurich, Switzerland; †Imec, Leuven, Belgium
email: mdossena@iis.ee.ethz.ch

Introduction Transition metal dichalcogenides (TMDc) such as WS_2 or MoS_2, especially in their monolayer form, are widely considered as promising 2D materials to extend Moore's scaling law and equip future nano-sheet field-effect transistors [1]. Their carrier mobilities, while greater than those of silicon at ultra-scaled thicknesses, are extremely sensitive to the dielectric environment around them. For example, the electron mobility of monolayer WS_2, which was theoretically predicted to be up to 300 cm^2/(Vs) [2], does not exceed a few tens of cm^2/(Vs) when surrounded by amorphous dielectric materials [3]. Here, we investigate the influence of different models of amorphous Al_2O_3 and HfO_2 on the electron mobility of monolayer WS_2 from first-principles, identify limiting factors, and examine two optimization scenarios.

Methods: Oxide-WS_2-oxide cells are first generated and relaxed with density functional theory (DFT) [4]. Their Hamiltonian and overlap matrices are then computed with the CP2K package [5] and upscaled to form large-scale devices of different lengths. By combining non-equilibrium Green's function (NEGF) calculations, as implemented in the OMEN code, [6] and the dR/dL method [7], the electron mobility of the targeted samples can be accurately determined. Phase coherence is eliminated by a phenomenological electron-phonon scattering model, whose parameters are adjusted to reproduce the mobility of pristine WS_2. Our developed simulation framework is presented in Fig. 1.

Results: All created structures (see Fig. 2 (a)-(d)), are characterized by a clear bandgap of around 2 eV (Fig. 2(e)). To assess the impact of the different oxides on the transport properties of WS_2, the electrostatic potential modulations they induce in the semiconductor channel are considered. The latter come from the inhomogeneity of the semiconductor-oxide interface and from defects located close to this surface. As an example, the electrostatic potential modulation for the WS_2-Al_2O_3 stack is shown in Fig. 2(f). Localized potential barriers and wells can be observed. Depending on their height or depth, they significantly affect the propagation of electrons and holes. In Fig. 3(a) the conduction band of pristine WS_2 is compared to that of the same material embedded between two amorphous Al_2O_3 layers. The potential modulation leads to a flatter band dispersion and thus poorer transport. To quantify this phenomenon, we compute the electron mobility of all stacks in Fig. 2(a) with the dR/dL method. The applicability of this approach is demonstrated in Fig. 3(b), i.e., the resistance linearly increases with the sample length. From the values reported in Fig. 3(c), it can first be concluded that Al_2O_3 and HfO_2 oxides massively reduce the mobility of WS_2. Secondly, the inclusion of one or two hBN layers between WS_2 and Al_2O_3 boosts this quantity by a factor between 2.5 and 4×. Finally, optimizing the HfO_2 oxide surface by redistributing the H passivation atoms leads to a three times increase of the mobility, compared to the original HfO_2 oxide.

Conclusions: Through DFT and NEGF calculations, we highlighted the impact of different oxide configurations on the electron mobility of WS_2 and proposed two solutions to increase this parameter (hBN interfacial layers and optimized passivation).

Acknowledgment: This research was supported by the NCCR MARVEL (SNSF Grant No. 205602) and by CSCS under projects s1119 and s1212.

References: [1] D. Jayachandran et al., Nat. 625, 276 (2024) [2] J. Backman et al., Phys. Rev. Appl. 21, 054017 (2024). [3] Y. G. You et al., Nanotech. 32, 505702 (2021). [4] B. V. Troeye et al., under review. [5] T. D. Kuhne et al., J. Chem. Phys. 152, 194103 2020). [6] A. N. Ziogas et al., SC19, 1 (2019). [7] Y.-M. Niquet et al., J. Appl. Phys. 115, 054512 (2014).

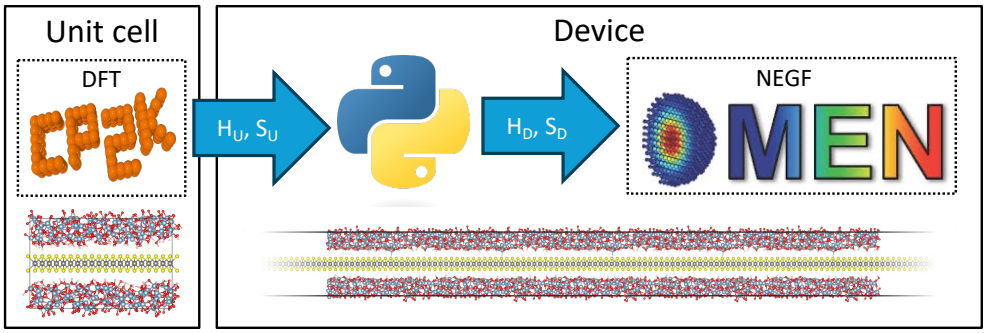

Fig. 1. Overview of the developed *ab initio* mobility modeling framework. A unit cell composed of monolayer WS_2 encapsulated between amorphous oxides is first simulated with CP2K (geometry relaxation and electronic properties), producing its Hamiltonian H_U and overlap S_U matrices. A full device structure is constructed by repeating the same unit cell and upscaling the Hamiltonian and Overlap matrices. The obtained device Hamiltonian H_D and Overlap S_D matrices serve as inputs to an NEGF solver, OMEN, from which the electrical current, corresponding resistance, and finally mobility can be extracted.

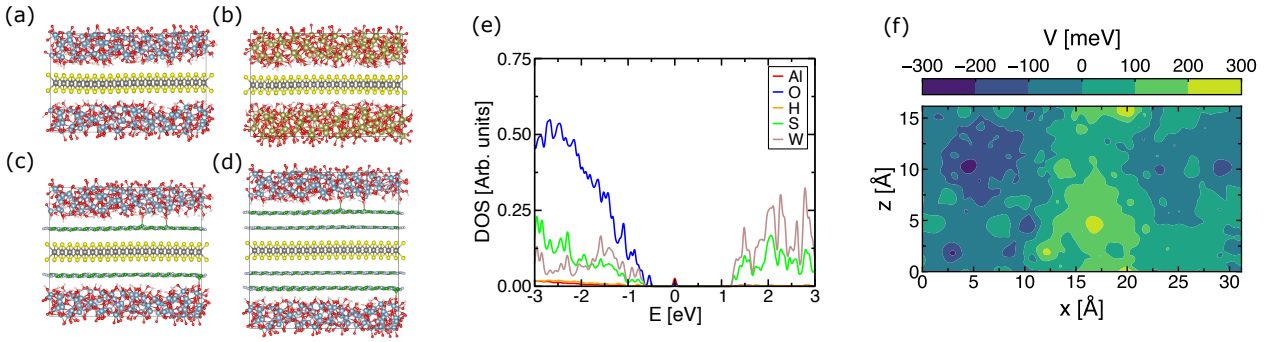

Fig. 2. Schematic view of the oxide-WS_2-oxide structures investigated in this work: (a) Al_2O_3; (b) HfO_2; (c) Al_2O_3 with 1 hBN layer between the semiconductor and the oxide; (d) Same as (c), but with two 2 hBN layers in between WS_2 and Al_2O_3. (e) Density-of-states for the WS_2 - Al_2O_3 structure in (a) projected onto the different atomic species that make up this stack. (f) Electrostatic potential modulation extracted in the W plane of monolayer WS_2, as induced by the surrounding amorphous Al_2O_3 oxides.

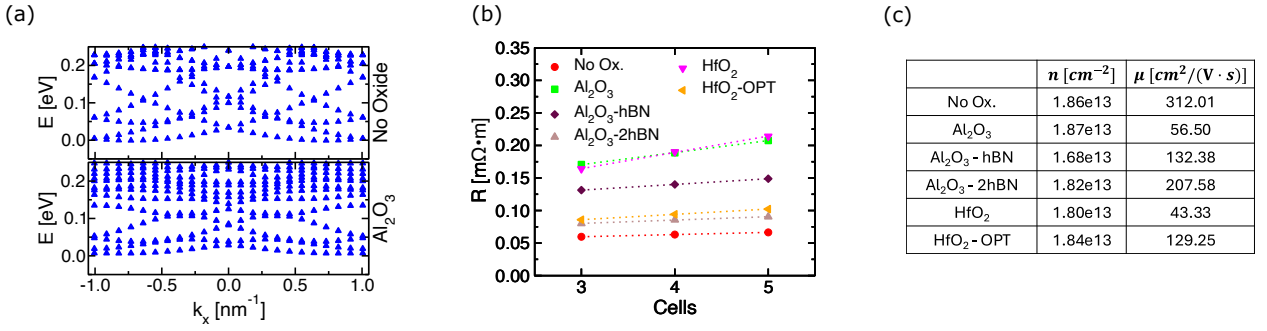

	n [cm^{-2}]	μ [$cm^2/(V \cdot s)$]
No Ox.	1.86e13	312.01
Al_2O_3	1.87e13	56.50
Al_2O_3 - hBN	1.68e13	132.38
Al_2O_3 - 2hBN	1.82e13	207.58
HfO_2	1.80e13	43.33
HfO_2 - OPT	1.84e13	129.25

Fig. 3. (a) Conduction band structure of monolayer WS_2 without oxide around it (top) and when it is surrounded by amorphous Al_2O_3 layers (bottom). The band dispersion flattens when Al_2O_3 is inserted. (b) Resistance (R) of oxide-WS_2-oxide samples as a function of their length (expressed in terms of the number of repeated cells) for all stacks considered in this work. A clear linear increase of the resistance with respect to the device length is observed in all cases, indicating diffusive transport. (c) Extracted electron mobility (μ) and corresponding charge concentration (n) for all structures in (b).

Effect of Random Nanosized Titanium Nitride Grains on Monolayer MoS_2 Field-Effect Transistors

Chieh-Yang Chen[1,2], Kuan-Lin Lee[1,2], Szu-Huan Hsu[1,2], Min-Hui Chuang[1,2], Yueh-Ju Chan[1,2], and Yiming Li[1-3,*]
[1]Parallel and Scientific Computing Laboratory; [2]Institute of Communications Engineering; [3]Department of Electronics and Electrical Engineering, National Yang Ming Chiao Tung University, 1001 Ta-Hsueh Rd., Hsinchu 300093, Taiwan. *E-mail: ymli@nycu.edu.tw

ABSTRACT

This work first studies effects of work function fluctuation (WKF) of nanosized titanium nitride (TiN) grains via device simulation on monolayer (ML) molybdenum disulfide (MoS_2) back-gate (BG) and nanosheet (NS) field-effect transistors (FETs). Density functional theory (DFT) calculated data are calibrated with experimental results in order to provide proper accuracy of device simulation. The results indicate that the off-state current and the threshold voltage exhibit the most significant variations. NS FETs are 5% and 2.06% lower variability of these parameters than that of BG FETs.

INTRODUCTION

During the fabrication process of semiconductor devices, work function fluctuation [1-2] is a critical factor associated with process variation effect and intrinsic parameter fluctuation. As researches are focus on two-dimensional (2D) materials for device applications [3-7], challenges of WKF remain difficult to mitigate. Although WKF has been studied in advanced silicon-based devices, study of the effect of WKF on ML MoS_2 devices has not been reported yet.

In this study, to examine the effect of WKF on 2D material-based devices, we first advance the DFT-simulated material parameters for statistical device simulation of ML MoS_2 FETs with nanosized TiN grain of gate.

MODEL AND METHODOLOGY

The 3D device simulation is mainly based on parameters obtained from DFT and calibrated using experimental data. First, DFT calculations are performed to extract key material properties of MoS_2, such as the band gap (E_g), effective mass (m_e^*), and electron affinity (χ_e), which are list in Table 1. The nominal gate metal is TiN with WK = 4.52 eV. To account for fluctuation, the high and low WK values are set to 4.6 and 4.4 eV, respectively, with corresponding probabilities of 0.6 and 0.4, where the grain size is set close to $(4\ nm)^2$, as shown in Fig. 1. For each of above devices, 300 samples are simulated statistically [8] for key DC characteristics, the on-/off-state current (I_{ON} and I_{OFF}), the threshold voltage in linear (V_{th_lin}) and saturation (V_{th_sat}) regions, subthreshold swing (SS), and the drain-induced barrier lowering (DIBL).

RESULTS AND DISCUSSION

First, a BG FET simulation is constructed for calibration with the experimental I_D-V_G curve [7], as shown in Fig. 2. Then, the nominal case of MoS_2 BG FET for the WKF study as well as NS FET are designed, as shown in Figs. 2 and 3. The geometric parameters and DC characteristics are listed in Table 2. Figure 4 shows the fluctuation in results for MoS_2 BG FET and NS FET at V_D = 0.7 V. In the nominal case, V_{th_sat} for both devices is fixed at 140 mV. The standard deviation of the V_{th_sat} for BG FETs is 9.40 mV, which is higher than that of NS FETs (5.84 mV). Furthermore, we estimate the relative standard deviation (RSD), defined as the ratio of the standard deviation to the mean value, for the most significant DC characteristics, as shown in Fig. 5. Figure 6 presents the relationship between the electric potential and the distribution pattern of high/low work function (WKF) metals. In extreme cases where effective WK = 4.52 eV, the BG FET is primarily affected by high WK metal near the source side. In contrast, the NS FET mitigates this effect due to its multi-gate structure.

CONCLUSION

In summary, the analysis of WKF in ML MoS_2 FETs has been studied by using random assigned TiN grains in 3D device simulation. For the given TiN grain size of $(4\ nm)^2$, the NS FET shows enhanced robustness against external variations, as evidenced by its reduced standard variability in DC characteristics compared to the BG FET.

ACKNOWLEDGMENT

This work was supported in part by the National Science and Technology Council (NSTC), Taiwan, under Grant NSTC 113-2221-E-A49-094 and Grant NSTC 113-2218-E-006–019-MBK, and in part by the 2025 JDP of TSMC.

REFERENCE

[1] W.-L. Sung *et al*., *IEEE TED*, vol. 71, pp. 350–358, 2024.
[2] N. Seoane *et al*., *IEEE EDL*., vol. 42, pp. 1416–1419, 2021.
[3] Y.-Y. Chung *et al*., in IEDM, p. 34.5.1-34.5.4, 2022.
[4] B. Radisavljevic *et al*., Nature Nanotech, vol. 6, pp. 147–150, 2011.
[5] X. Xiong *et al*., in *IEDM*, p. 7.5.1-7.5.4, 2021.
[6] J. Xu *et al*., *Nanotechnology*, vol. 29, p. 345201, 2018.
[7] W.-C. Wu *et al*., in *VLSI*, pp. 1–2, 2024.
[8] Y. Li *et al*., in *IEDM*, p. 34.4.1-34.4.4., 2015.

Table 1. The extracted bandgap, electron affinity, and effective mass of ML MoS_2 from DFT simulation.

Material Properties	ML MoS_2
Band gap (E_g)	1.78 eV
Electron affinity (χ_e)	4.26 eV
Effective mass (m_e^*)	4.59 m_0

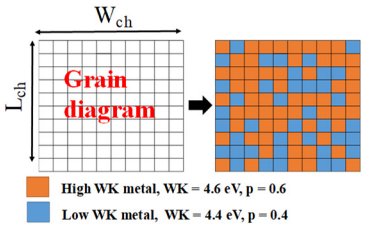

Fig. 1. Illustration of WKF setting.

Table 2. The critical device dimensions and electrical characteristic for MoS_2 BG FET and NS FET without WKF.

Parameter	BG FET	NS FET
L_{ch} (nm)	100	
EOT (nm)	2.448	
W_{ch} (nm)	25	
t_{ch} (nm)	0.42	
EWK (eV)	4.52	
V_{th_lin} (mV)	195	178
V_{th_sat} (mV)	140	140
I_{on} ($\times 10^{-6}$ A)	7.83	3.67
I_{off} ($\times 10^{-11}$ A)	4.66	3.76
SS (mV/dec.)	131	121
DIBL (mV/V)	84.3	60.2

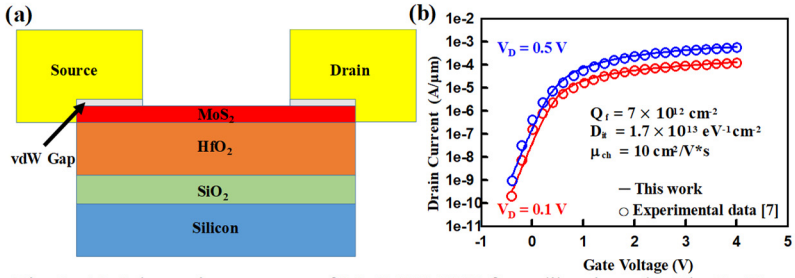

Fig. 2. (a) Schematic structure of MoS_2 BG FET for calibration. (b) The I_D-V_G curves calibrated with fabrication result [7].

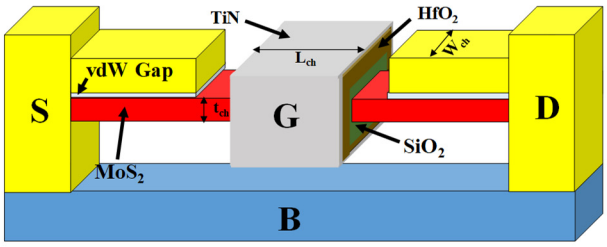

Fig. 3. Schematic of 3D MoS_2 NSFET structure.

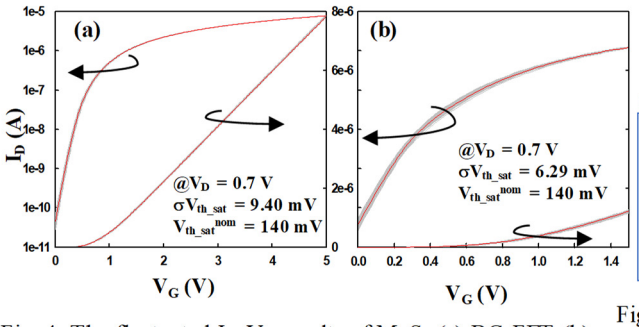

Fig. 4. The fluctuated I_D-V_G results of MoS_2 (a) BG FET (b) NS FET in saturation (V_D = 0.7 V).

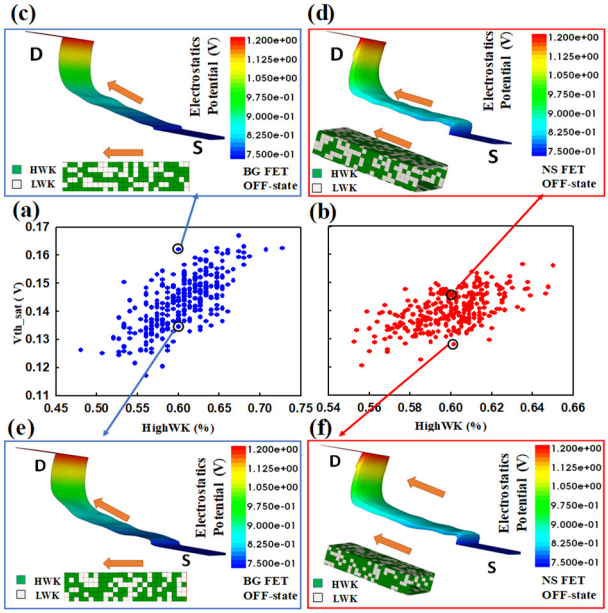

Fig. 6. V_{th} vs the probability of high WK metal for (a) BG FET and (b) NS FET, where (c) and (d) represent high V_{th} case, and (e) and (f) represent low V_{th} case.

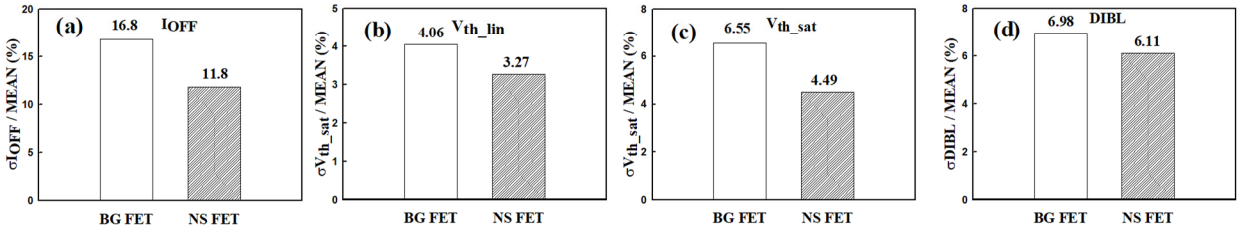

Fig. 5. Normalized fluctuation values comparison between BG FET and NS FET for DC characteristics: (a) OFF-state current, threshold voltage under (b) linear and (c) saturate region, and (d) drain-induce barrier lowering.

Thursday 2:00-3:30 pm Device Simulation

Time	Type	Presenter	Title
2:00-2:30 pm	**Invited**	Blanka Magyari-Kope	Innovating Tomorrow's Semiconductor Technology: Computational Strategies for Material Optimization
2:30-2:45	Contributed	Ashwin Tunga	A full 3D TCAD framework for nanosheet transistors including quantum-confined channels
2:45-3:00	Contributed	Min-Hui Chuang	Performance Boost of GAA Si NS CFET via Tungsten Source/Drain Sidewalls
3:00-3:15	Contributed	Dallin Nielsen	Thermalization and Effects of Radiation-Induced Charge-Carriers in Semiconductors and GaN/$Al_{0.25}Ga_{0.75}N$ HEMTs
3:15-3:30	Contributed	Jianshi Sun	Unlocking high hole mobility in diamond over a wide temperature range via efficient shear strain

Innovating Tomorrow's Semiconductor Technology: Computational Strategies for Material Optimization

Blanka Magyari-Köpe

Technical Manager in R&D, TCAD Division at TSMC, San Jose, CA

Email: blankamk@tsmc.com

Recent advancements in computational material optimization strategies are unveiling innovative solutions to address the stringent demands of advanced technology nodes, constrained by fundamental physical, chemical, and electrical limitations. By leveraging advanced material property simulations, computational material exploration, and AI-driven or -enhanced process modeling, significant strides have been made in alleviating bottlenecks that impact critical process yield and device performance metrics. Focus areas include next-generation interconnect materials, optimization of low-k dielectrics, and enhancements in process reliability - all recognized as pivotal in overcoming scaling limitations and enabling the progression of next-generation semiconductor technologies.

Copper-based back-end-of-line (BEOL) interconnects, historically foundational to semiconductor architecture, are increasingly limited at nanoscale dimensions due to resistivity escalation. This phenomenon degrades signal integrity and significantly reduces the scaling benefits of RC delay and power reduction. Reliability concerns, such as electromigration and dielectric breakdown, further underscore the inadequacy of conventional interconnect materials. To address these constraints, high-throughput screening using quantum mechanical computations has enabled the identification and evaluation of novel interconnect solutions, such as intercalated graphene, which exhibits superior electrical and thermal properties. In parallel, advancements in optimizing amorphous low-k dielectric materials to reduce parasitic capacitance, unlock further transformative opportunities for improved device performance and scalability.

Amorphous materials, in general, are emerging as critical enablers of semiconductor technologies due to their distinctive electronic, optical, and mechanical properties. The low-k dielectric materials mentioned above, essential for reducing parasitic capacitance, continue to face persistent challenges related to growth kinetics, thermodynamic stability, and reliability. Systematic exploration of the density-stability-property optimization landscape using novel methods has led to the discovery of new bonding configurations and defect mechanisms, exemplified by advancements in the synthesis of amorphous boron nitride.

The integration of machine learning (ML)-driven methodologies into predictive technology computer-aided design (TCAD) workflows is fundamentally transforming semiconductor optimization paradigms. Hierarchical AI frameworks, which synergistically combine neural networks with quantum mechanical simulations, are enhancing the capability and precision of material property predictions and process optimizations. These frameworks are also used in modeling complex reaction mechanisms that improve thin-film deposition processes. By bridging atomistic insights with feature-scale simulations, generalized solutions applicable across diverse semiconductor manufacturing workflows are being developed, pushing towards the ultimate virtual fab paradigm.

In summary, material optimization strategies and AI-driven methodologies both represent paradigm shifts in addressing longstanding challenges associated with semiconductor scaling. Advances highlighted here—in interconnect technologies, low-k dielectric optimization, and deposition process reliability, combined with predictive modeling capabilities—are expected to enable the semiconductor industry to achieve unprecedented levels of performance, efficiency, and scalability in the development of next-generation technologies.

A full 3D TCAD framework for nanosheet transistors including quantum-confined channels

A. Tunga, M. Grupen*, and S. Rakheja
Electrical and Computer Engineering, University of Illinois Urbana-Champaign, Urbana, IL, 61801, USA
*AFRL Sensors Directorate, WPAFB, OH, 45433, USA
e-mail: tunga2@illinois.edu

Introduction

Nanosheet FETs utilizing ultrathin, quantum-confined semiconductor channels, offer a promising solution for sub-10 nm scaling for high-speed digital logic [1] and may also provide a path to high-speed RF power electronics using wide bandgap materials such as GaN. Simulating nanosheet FETs in TCAD is essential for understanding their physics and guiding device design. While previous approaches using NEGF and Monte Carlo methods are accurate, their high computational cost limits their practicality for device design exploration. This paper introduces a computationally efficient 3D TCAD framework for simulating nanosheet FETs, taking into account the quantum confinement in the channel. The presented framework integrates the Schrödinger equation to account for quantum subbands in the channel and couples the real-space transport of 2D electrons in these subbands with 3D charge transport in the surrounding bulk materials.

TCAD Framework

Figure 1 presents the schematic of a test GaN nanosheet HEMT structure, featuring a 12 nm GaN channel and a 5 nm $Al_{0.3}Ga_{0.7}N$ barrier, with n^+ GaN bulk regions beneath the source/drain contacts. The 3D transport in the bulk is modeled by solving the moments of the Boltzmann Transport Equation (BTE) using the Fermi Kinetics Transport (FKT) solver, a TCAD framework developed at the Air Force Research Laboratory [2]. Unlike conventional BTE solvers, FKT employs an alternative formulation of electronic heat flow based on heat capacity of ideal Fermi gas, offering superior numerical stability and convergence properties. In the quantum-confined channel, the Schrödinger is solved along confinement direction self-consistently with Poisson's equation to compute the subbands (see Figure 2 for wavefunctions). The 2D transport along the channel length is treated classically by adapting the FKT framework to two dimensions using the 2D moments of the BTE. The 3D bulk transport and the 2D channel transport are coupled through ballistic thermionic emission, linking the bulk conduction band with the channel subbands, as shown in Figure 3. Furthermore, FKT can incorporate the full bandstructure with transport simulations taking into account the various scattering mechanisms [3]. The 3D transport model utilizes bulk GaN band structure derived from empirical pseudopotential method (EPM), while the integration of 2D band structure with the 2D transport will be addressed in future work (the methodology to do so is indicated in Figure 4).

Results

To demonstrate the superior electrostatics of the nanosheet device particularly for scaled gate lengths, we compare the subthreshold characteristics of nanosheet HEMTs with bulk HEMTs for gate lengths ranging from 100 nm to 10 nm. As illustrated in Figures 5-7, nanosheet HEMT consistently demonstrates reduced leakage currents and improved subthreshold swing as gate length decreases, outperforming the bulk HEMT. The on-current of the nanosheet device can be improved in structures where multiple sheets are integrated in parallel, providing additional conduction channels [4]. The nanosheet HEMT was simulated using the effective mass approximation with constant mobility, which is reasonable for estimating the subthreshold characteristics; nevertheless, the inclusion of the full bandstructure in 2D FKT is currently ongoing and will be presented in the future.

Conclusion

This work introduced a 3D TCAD framework to simulate nanoscale devices with quantum-confined channels. By incorporating Schrödinger's equation and coupling it with real-space Boltzmann transport, the framework accurately captures the essential quantum and classical transport phenomena. This versatile approach is well-suited for designing next-generation nanosheet-based devices. As a case study, the simulator was used to highlight the superior electrostatics of a GaN nanosheet HEMT over its bulk counterpart at reduced gate lengths.

References

[1] Ajayan, J., et al. "Nanosheet Field Effect Transistors-A next Generation Device to Keep Moore's Law Alive: An Intensive Study," in Microelectronics Journal, vol. 114, pp. 105141, 2021.

[2] Tunga, A., et al. "A Comparison of a Commercial Hydrodynamics TCAD Solver and Fermi Kinetics Transport Convergence for GaN HEMTs," in Journal of Applied Physics, vol. 132, no. 22, pp. 225702, 2022.

[3] Grupen, M., "Energy Transport Model with Full Band Structure for GaAs Electronic Devices," in Journal of Computational Electronics, vol. 10, no. 3, pp. 271–290, 2011.

[4] Tunga, A., Li, X., Rakheja, S., "Modeling-Based Design and Benchmarking of Al-rich AlGaN 3D Nanosheet MOSFET and MOSHEMTs for RF Applications," in 2021 Device Research Conference (DRC), 2021, pp. 1–2.

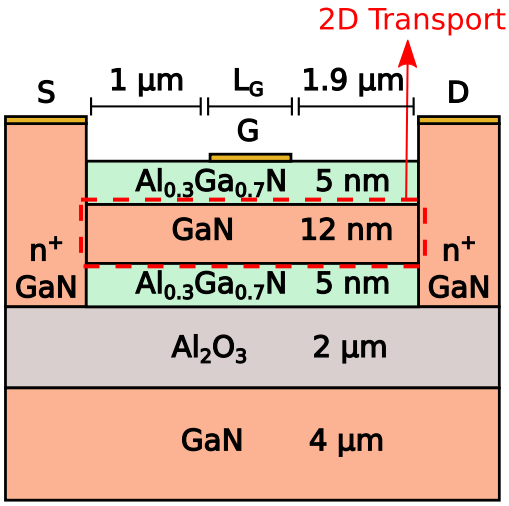

Fig. 1. Schematic of nanosheet GaN HEMT. The dotted box indicates the region where 2D transport is solved. L_G is varied from 100 nm to 10 nm in the simulations.

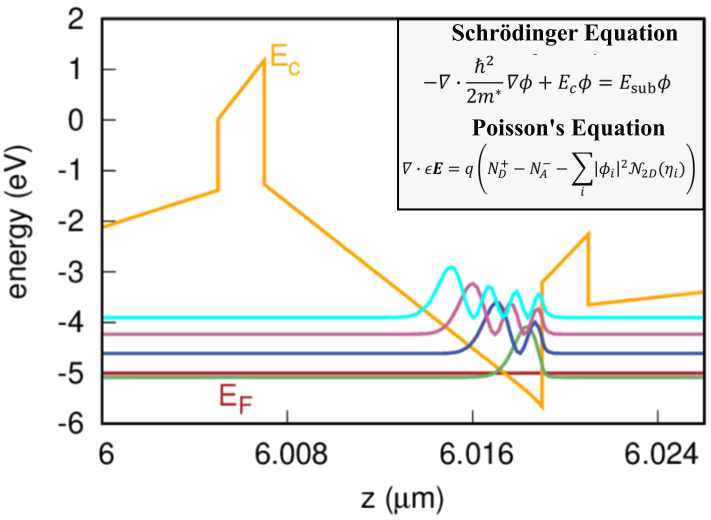

Fig. 2. Wavefunctions in the channel at the center of the gate at equilibrium, obtained from self-consistent solution of coupled Schrödinger-Poisson equation.

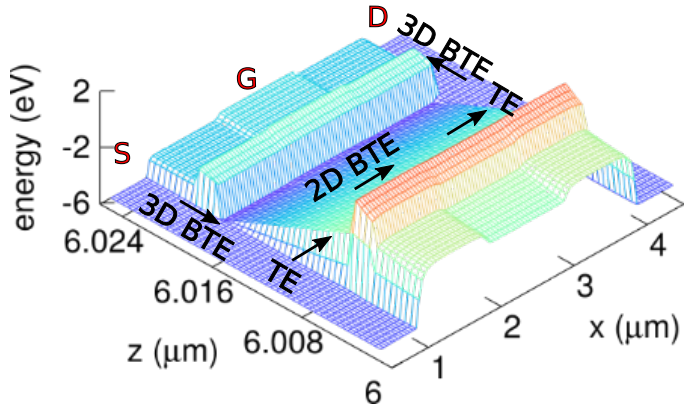

Fig. 3. Coupling 3D BTE in the bulk region with the 2D BTE in the nanosheet channel through thermionic emission (TE). The horizontal plane represents the device cross-section, and the vertical axis is the conduction band energy.

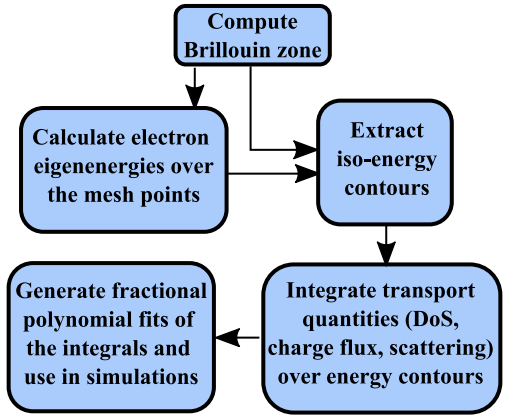

Fig. 4. Methodology to incorporate full band-structure in transport simulations.

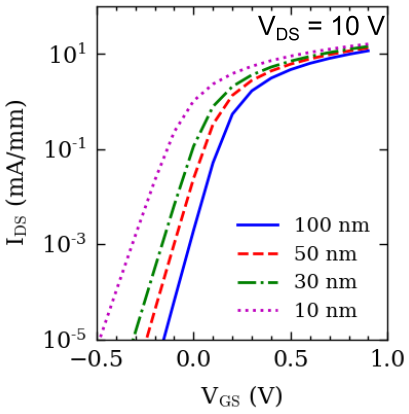

Fig. 5. Transfer characteristics of nanosheet GaN HEMT for varying gate lengths.

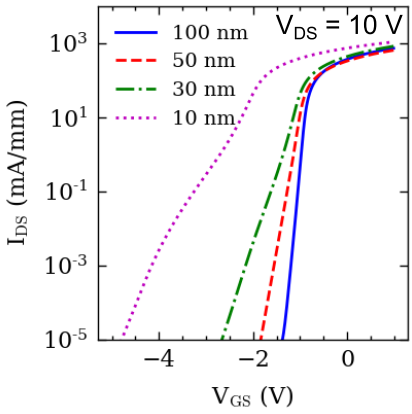

Fig. 6. Transfer characteristics of bulk GaN HEMT for varying gate lengths.

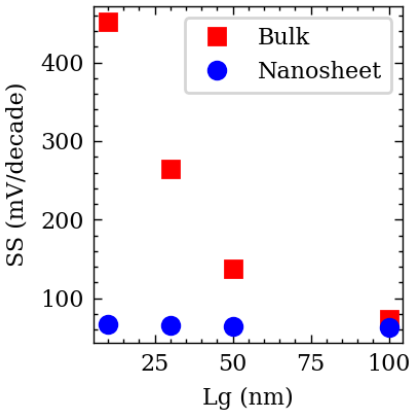

Fig. 7. Subthreshold swing of bulk and nanosheet HEMTs with varying gate lengths.

Performance Boost of GAA Si NS CFET via Tungsten Source/Drain Sidewalls

Min-Hui Chuang[1,2], Sekhar Reddy Kola[1,2], and Yiming Li[1-4,*]
[1]Parallel and Scientific Computing Laboratory, [2]Institute of Communications Engineering; [3]Department of Electronics and Electrical Engineering, [4]Institute of Biomedical Engineering, National Yang Ming Chiao Tung University, Hsinchu 300093, Taiwan. Tel: +886-3-5712121 ext. 52974; Fax: +886-3-5726639; *E-mail: ymli@nycu.edu.tw

ABSTRACT

This study computationally analyzes the electrical performance of vertically stacked Gate-All-Around (GAA) Si nanosheet (NS) complementary FETs (CFETs) with (w/) and without (w/o) metal sidewall (MSW) structures in the source/drain (S/D) regions. MSW integration significantly reduces contact resistance and enhances drive current (I_{on}), though it slightly increases intrinsic capacitance. Without MSW, device and circuit performance are limited to a maximum of four channels due to weakened electrostatic potential from the top contact to the bottom S/D regions. In contrast, MSW structures, leveraging tungsten's low resistivity (5.6×10^{-6} Ω·cm), support higher I_{on} and improved scalability, enabling performance gains beyond four channels. For instance, a 10-channel CFET with MSW achieves a 56.9% higher ring oscillator (RO) frequency compared to w/o MSW devices. These results highlight the critical role of MSW in optimizing advanced designs of emerging GAA Si NS CFETs.

INTRODUCTION

Due to the severe short-channel effects (SCEs) and weakened gate controllability, scaling of devices has caused a sizeable leakage current. To overcome this bottleneck, GAA devices, such as NS, have been of special interest because they can reduce supply voltages, sustain gate drivability, and achieve high performance for advanced technology nodes. The stacking of N- and P-FETs vertically is one of the primary benefits of using CFETs, which allows for a considerable reduction in active area [1]-[7]. However, to minimize the DC performance loss by NS resistance, there were many efforts to reduce the contact resistivity at the semiconductor/silicide interface.

In this study, we numerically investigate the impact of MSW integration on electrical characteristics of both N/P-FETs in CFET and three-stage CFET ring oscillators.

3-D COMPUTATIONAL DEVICES

Fig. 1(a) presents a 3-D schematic, and Fig. 1(b) is a 2-D schematic of the GAA Si NS CFET, consisting of a bottom P-FET and a top N-FET [8], [9]. The device simulation employs the quantum-mechanically corrected transport models, along with four mobility models: the high-field saturation, the Philips unified model, the Lombardi model, and the ballistic mobility. In addition, Hurkx band-to-band tunneling and Shockley-Read-Hall recombination are included to account for generation and recombination effects.

RESULTS AND DISCUSSION

Figure 2 shows the SCEs in CFETs w/ and w/o MSW, considering varying number of channels in N- and P-FETs. Fig. 2(a) highlights the off-state current (I_{off}) trends, revealing a 35.8% reduction for N-FETs and a 22.4% reduction for P-FETs in devices w/ MSW compared to those w/o MSW. This reduction in I_{off} with increasing number of channels in w/ MSW devices is primarily attributed to enhanced electrostatic control, reduced parasitic resistance, and improved charge confinement, which collectively suppress SCEs and minimize leakage currents. Enhanced gate-to-channel coupling in GAA structures w/ MSW ensures more effective control over the channel potential, mitigating drain induced barrier lowing (DIBL) and subthreshold leakage. Fig. 2(b) demonstrates a 68.7% increase in I_{on} for 10-channel N-FETs w/ MSW compared to w/o MSW devices. This improvement stems from the reduced series resistance at the S/D contacts due to the integration of low-resistivity tungsten in the sidewalls, which enhances carrier injection efficiency and minimizes voltage drop at the S/D junctions. Additionally, improved electrostatic control ensures a more uniform potential profile across vertically stacked channels, optimizing carrier transport and drive strength. Furthermore, Fig. 2(c) analyzes DIBL, demonstrating that variations number of channels have minimal impact on DIBL in both w/ MSW and w/o MSW devices, indicating stable threshold voltage (V_{th}) control across multiple channels. Fig. 3(a) further confirms that the V_{th} remains constant as the number of channels increases, a characteristic attributed to the strong electrostatic confinement provided by the GAA architecture.

Gate capacitance (C_G) is a critical AC parameter, directly extracted from the AC response curves of N- and P-FETs. As shown in Fig. 3(b), C_G increases with the number of channels due to the larger cumulative channel surface area, allowing greater charge accumulation and facilitating linear capacitance scaling. This increase is further supported by parallel capacitance addition and improved electrostatic coupling between the gate and channel, which collectively enhance carrier confinement and mitigate SCEs. Fig. 4 presents a 2-D current density profile at the middle of the channel in the on-state for N- and P-FETs w/ and w/o MSW. The significantly higher current density in w/ MSW devices is attributed to enhanced electrostatic control and reduced series resistance (Fig. 5), resulting in improved carrier velocity and overall current conduction efficiency. Fig. 6 compares the RO frequency vs. number of channels. Beyond four channels, the frequency decreases for devices w/o MSW due to increased parasitic resistance and capacitance, which degrade signal propagation speed. In contrast, w/ MSW devices exhibit a 56.9% increase in frequency, driven by improved electrostatic control, lower resistance. The performance boost highlights the effectiveness of MSW in mitigating channel-induced degradation, making it essential for high-speed applications.

CONCLUSION

In summary, GAA Si NS CFETs w/ MSW outperform w/o MSW configurations due to reduced S/D resistance from the low-resistivity tungsten sidewalls. While both I_{on} and parasitic capacitance increase number of channels, I_{on} growth slows and saturates for w/o MSW devices when the number of channels exceeds four, due to diminished electrostatic potential from top to bottom channels.

ACKNOWLEDGMENT

This work was supported in part by the National Science and Technology Council (NSTC), Taiwan, under Grant NSTC 113-2221-E-A49-094 and Grant NSTC 113-2218-E-006–019-MBK, and in part by the 2025 JDP of TSMC.

REFERENCES

[1] S. R. Kola *et al.*, *IEEE T. Nano*, vol. 23, pp. 382–392, 2024.
[2] X. Yang *et al.*, *IEEE T. ED*, vol. 70, pp. 3935–3942, 2024.
[3] X. R. Yu *et al.*, *IEDM*, pp. 487–490, 2022.
[4] B. Vincent *et al.*, *IEEE J. EDS*, vol. 8, pp. 668–673, 2020.
[5] Y. Li *et al.*, *IEDM*, pp. 887–890, 2015.
[6] X. Yang *et al.*, *IEEE T. ED*, vol. 69, pp. 4029–4036, 2022.
[7] C. Y. Huang *et al.*, *IEDM*, pp. 20.6.1-20.6.4, 2020.
[8] S. R. Kola *et al.*, *ISQED*, pp. 1-6, 2023.

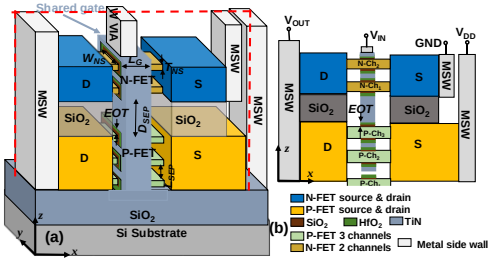

Fig. **1**. (a) 3-D schematic of the GAA Si NS CFET w/ MSW. (b) 2-D cross-sectional view (cut-C_1) of the device. The channel count is further increased to ten.

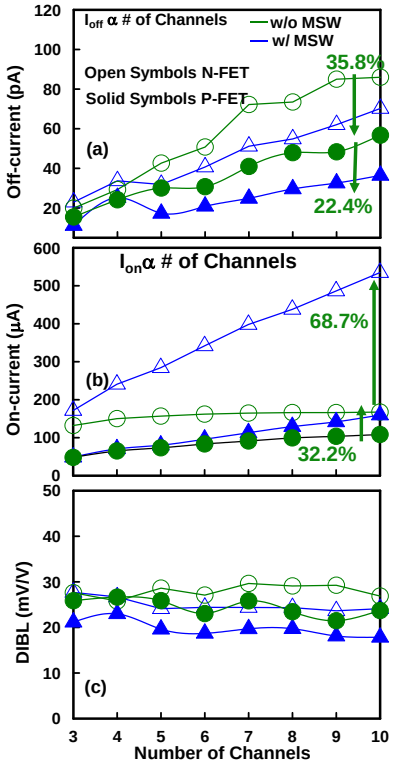

Fig. **2**. The impact of number of channels on SCE parameters in GAA Si NS CFETs. (a) I_{off} and (b) I_{on} vs. the number of channels. For devices w/ MSW, the I_{on} is enhanced by 68.7% for N-FETs and 32.2% for P-FETs compared to devices w/o MSW. This improvement highlights the effectiveness of MSW in boosting carrier transport and overall device performance. (c) DIBL vs. the number of channels.

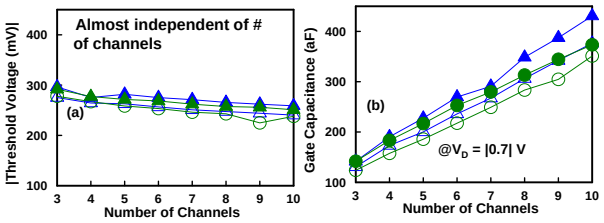

Fig. **3**. (a) The V_{th} versus the number of channels for both N- and P-FETs in CFET devices, demonstrating that V_{th} remains largely unaffected by number of channels, indicating stable electrostatic control. (b) C_G increases with number of channels due to expanded channel surface area, allowing for greater charge accumulation and enhanced electrostatic coupling between the gate and channel.

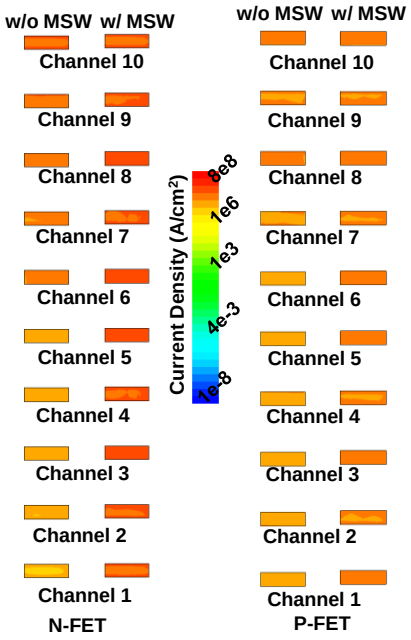

Fig. **4**. The 2-D current density distribution profile at the middle of the channel in the on-state condition ($|V_G| = |V_D| = 0.7$ V), illustrating carrier transport characteristics and highlighting the impact of electrostatic control on current flow in the device.

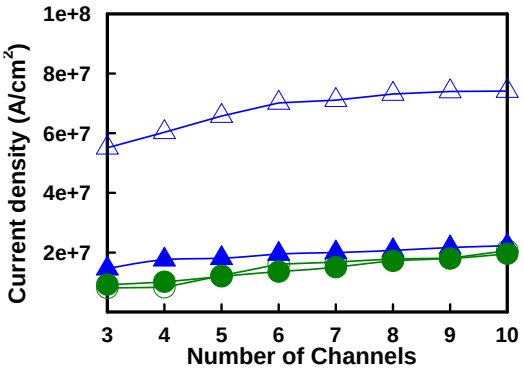

Fig. **5**. The current density vs. the number of channels at the middle of the channel under on-state conditions. Devices w/ MSW exhibit a significant increase in current density, attributed to reduced S/D resistance and enhanced electrostatic control.

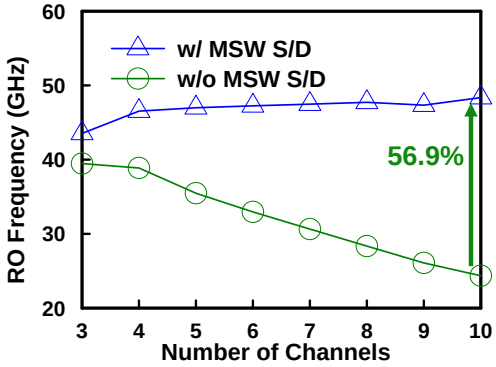

Fig. **6**. The RO frequency vs. the number of channels for the devices w/ and w/o MSW. In the w/o MSW, frequency declines as number of channels increases, primarily due to higher resistance in the top S/D regions.

Thermalization and Effects of Radiation-Induced Charge-Carriers in Semiconductors and GaN/$Al_{0.25}Ga_{0.75}N$ HEMTs

D. O. Nielsen[1], L. R. Nichols[2], S. T. Pantelides[2,3], X.-G. Zhang[4], R. D. Schrimpf[3], D. M. Fleetwood[3], C. G. Van de Walle[5], and M. V. Fischetti[1]
[1]Department of Materials Science and Engineering, University of Texas at Dallas, Dallas, TX
[2]Department of Physics and Astronomy, Vanderbilt University, Nashville, TN
[3]Department of Electrical and Computer Engineering, Vanderbilt University, Nashville, TN
[4]Department of Physics, University of Florida, Gainesville, FL
[5]Materials Department, University of California Santa Barbara, Santa Barbara, CA
Email: dallin.nielsen@utdallas.edu

Charge-Carrier Thermalization

We present here extensions of our *ab initio* study of the energy-loss processes and thermalization of radiation-generated hot charge-carriers, originally performed for GaN, to other semiconductors (β-Ga_2O_3, C (in the diamond structure), SiC, AlN, and Si) and to how these hot carriers affect devices. As discussed in the past [1,2], we focus on the 10-100 eV range of kinetic energy since this range is poorly understood. Indeed, the nuclear/particle physics community has a long-standing track record of understanding the thermalization in the higher-energy range (above about 100 eV) [3], whereas the electronic-device community has studied extensively carrier transport in the lower-energy range (below ~10 eV) [4]. However, the 10-100 eV gap has been studied only using the free-electron approximation and semi-empirical models for the energy-loss processes [5-7].

We have employed the density functional theory (DFT) package Quantum ESPRESSO to obtain the band structure and the dielectric function of the materials, obtaining information about the electron dispersion and energy-loss function for energies up to about 100 eV. We have used DFT perturbation theory and Fermi's Golden Rule/first Born approximation to calculate the charge-carrier scattering rates for the major charge-carrier interactions (phonon scattering, impact ionization, and plasmon emission). A full-band Monte Carlo solution of the Boltzmann transport equation is then used to study the thermalization of electrons with kinetic energies as high as 100 eV. Considering for example C and β-Ga_2O_3, the results show that the full thermalization of electrons is complete within ~ 0.4 and 1.0 ps, respectively (Fig. 1). Hot electrons dissipate about 90% of their initial kinetic energy to the electron-hole gas during the first ~ 0.1 fs, due to rapid plasmon emission and impact ionization at high energies. The remaining energy is lost at a much slower rate via phonon emission at lower energies (below ~ 10 eV). During the thermalization, hot electrons generate pairs with an average energy of ~ 12.9 and 11.2 eV/pair for C and β-Ga_2O_3, respectively. Additionally, during the thermalization, the maximum electron displacement from its original position is found to be on the order of 100 nm [1,2] (Fig. 2).

Device Simulation

Using the spatial and energetic distributions of the radiation-induced pairs, we have also performed full-band Monte Carlo simulations of electronic transport in devices. Considering a GaN/$Al_{0.25}Ga_{0.75}N$ high electron mobility transistor (HEMT) as an example, we simulate a "streak" of charge carriers generated by an energetic ion traversing the device (Fig. 3). We collect information regarding the time-scale of the diffusion, thermalization and current transient. This constitutes an advancement of the state of the art, which currently involves the use of TCAD software to simulate the streak, assuming a thermal distribution of carriers. We compare our results to an identical calculation with such a thermal distribution.

Additionally, we have calculated the damage induced by these hot electrons at the GaN/AlGaN interface. As the primary mechanism for damage generation, we consider the activation of defects, formed during fabrication, via dehydrogenation. To determine the defect activation rate, we use parameters (cross sections and density of defect precursors) either determined experimentally [8] or calculated using an H-release methodology [9] that is an extension of a recently developed theory of non-radiative carrier-capture by defects [10]. We find that the damage is primarily confined to the region near the upper tip of the streak. In particular, if the proton strikes on the source-side of the device, this leads to a more rapid threshold voltage shift.

Acknowledgment

This work was supported by the Air Force Office of Scientific Research: Award FA9550-21-0461, and through the Center of Excellence in Radiation Effects: Award FA9550-22-1-0012.

References

1. D. O. Nielsen, C. G. Van de Walle, S. T. Pantelides, R. D. Schrimpf, and M. V. Fischetti, Phys. Rev. B **108**, 155203 (2023).
2. D. O. Nielsen and M. V. Fischetti, Appl. Phys. Lett. **123**, 252107 (2023).
3. P. E. Dodd, IEEE Trans. Device Mater. Rel. **5**, 343 (2005).
4. M. V. Fischetti, S. E. Laux, Phys. Rev. B **38**, 14 (1988).
5. D. Pines, Rev. Mod. Phys. **28**, 184 (1956).
6. A. Rothwarf, J. Appl. Phys. **44**, 752 (1973).

7. R. C. Alig, S. Bloom, and C. W. Struck, Phys. Rev. B **22**, 5565 (1980).
8. S. Mukherjee, Y. Puzyrev, J. Chen, D. M. Fleetwood, R. D. Schrimpf, and S. T. Pantelides, IEEE Trans. Electron Devices **63**, 1486 (2016).
9. L. R. Nichols, W. Perry, D. O. Nielsen, G. Li, M. V. Fischetti, S. T. Pantelides, X.-G. Zhang, to be published.
10. L. R. Nichols, G. Li, Y. Yu, J. Jiang, A. O'Hara, G. D. Barmparis, S. T. Pantelides, and X.-G. Zhang, Phys. Rev. B **111**, 045201 (2025).

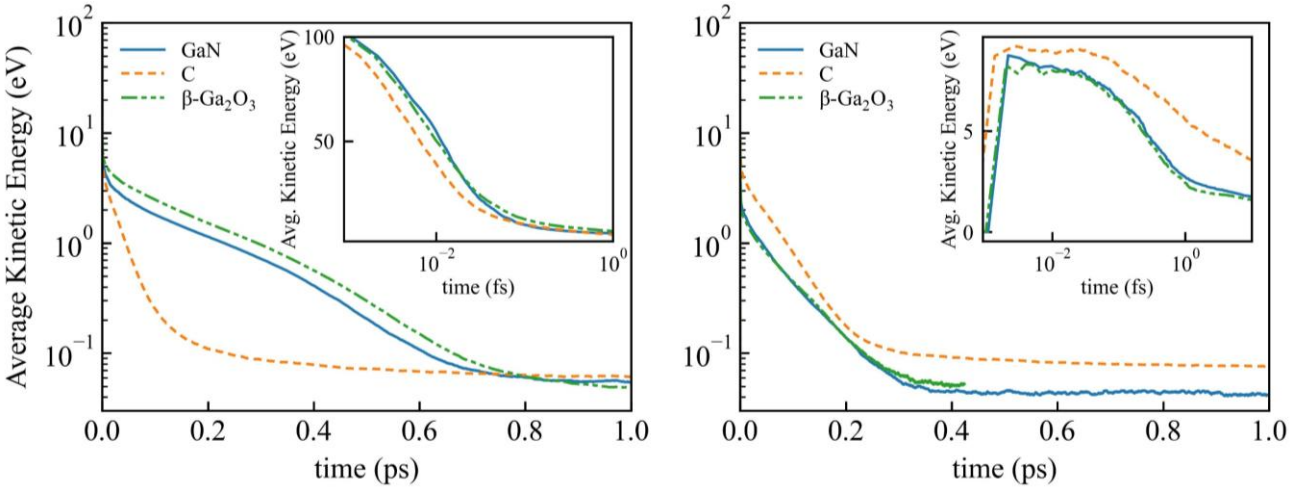

Fig. 1. Average electron (left) and hole (right) kinetic energies as a function of time for GaN, C (diamond), and β-Ga_2O_3. Electrons begin at 100 eV and thermalize by plasmon emission, impact ionization, and eventually phonon emission.

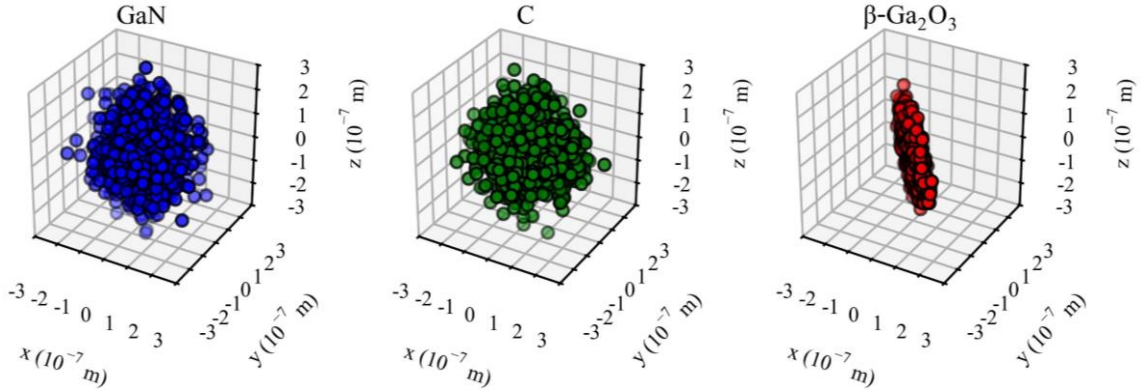

Fig. 2 Real-space positions of simulated electrons after ~1 ps in GaN, C (diamond), and β-Ga_2O_3.

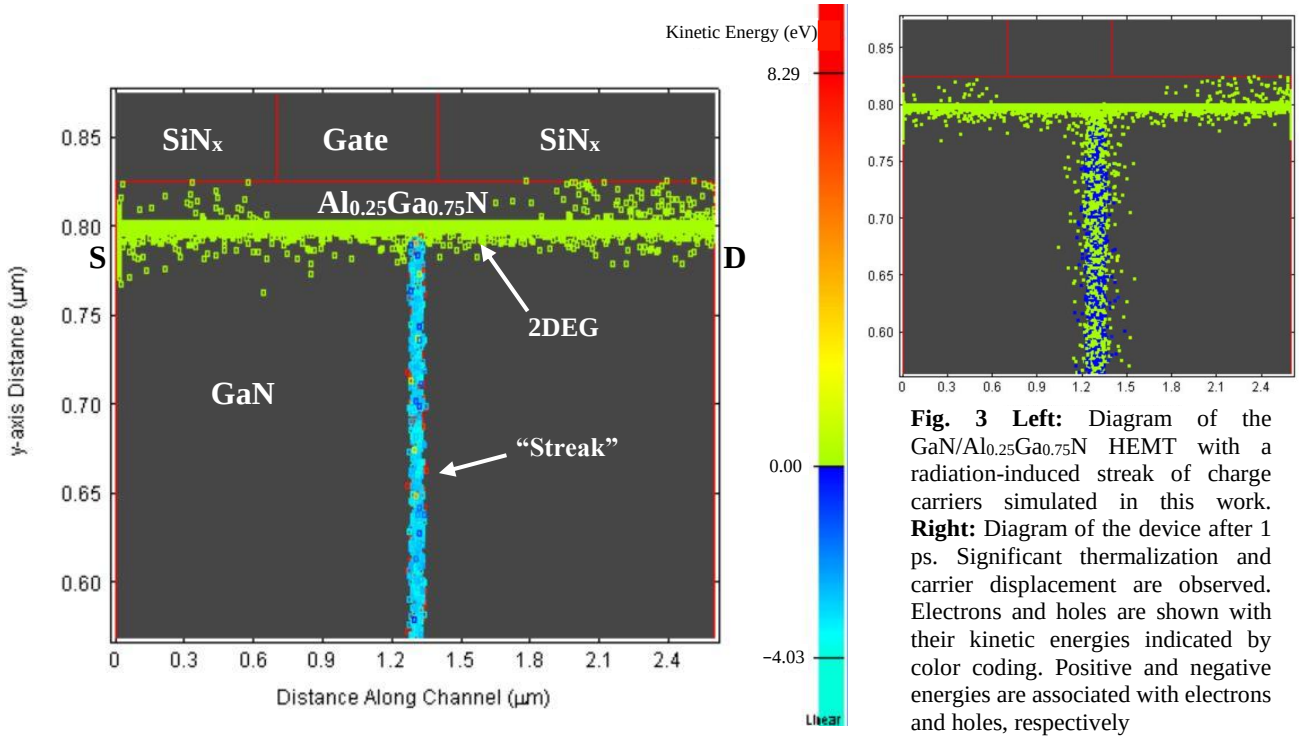

Fig. 3 Left: Diagram of the GaN/$Al_{0.25}Ga_{0.75}N$ HEMT with a radiation-induced streak of charge carriers simulated in this work. **Right:** Diagram of the device after 1 ps. Significant thermalization and carrier displacement are observed. Electrons and holes are shown with their kinetic energies indicated by color coding. Positive and negative energies are associated with electrons and holes, respectively

Unlocking high hole mobility in diamond over a wide temperature range via efficient shear strain

Jianshi Sun†, Xiangjun Liu†, and Shouhang Li*
†Institute of Micro/Nano Electromechanical System and Integrated Circuit,
College of Mechanical Engineering, Donghua University, Shanghai 201620, China
*Centre de Nanosciences et de Nanotechnologies, CNRS, Université Paris-Saclay,
10 Boulevard Thomas Gobert, 91120 Palaiseau, France
e-mail: shouhang.li@universite-paris-saclay.fr

ABSTRACT

As a wide bandgap semiconductor, diamond holds both excellent electrical and thermal properties, making it highly promising in the electrical industry. However, its hole mobility is relatively low and decreases with increasing temperature, which severely limits further applications. Herein, we proposed that the hole mobility can be efficiently enhanced via slight compressive shear strain along the [100] direction. The shear strain breaks the symmetry of the crystalline structure and lifts the band degeneracy near the valence band edge, resulting in a significant suppression of interband electron-phonon scattering. Moreover, the hole mobility becomes less temperature-dependent due to the decrease of electron scatterings from high-frequency acoustic phonons.

INTRODUCTION

Enhancing carrier mobility is essential for improving the performance and reducing the power consumption of next-generation electronic devices, particularly in high-frequency and high-power applications.[1] Diamond is a rising star semiconductor owing to its ultra-wide bandgap, ultra-high thermal conductivity, and high saturation carrier velocity.[2] However, the hole mobility of diamond is relatively lower compared to its electron mobility and dramatically decreases with increasing temperature.[3] These drawbacks in hole mobility significantly constrain the potential of diamonds in CMOS, high-power LEDs, and detectors.[4]

Strained silicon technology[5] is effective in promoting the hole mobility of silicon, which has been extensively utilized in industry and drives the ongoing progress of Moore's law. Although the strain engineering on the hole mobility of Si, Ge, and Ge-Sn alloy has been extensively studied, research on the diamond, which possesses a similar face-centered cubic (*fcc*) structure, remains relatively scarce. This may be attributed to the extreme hardness and strength of diamond which are widely considered to render strain implementation nearly impossible. Recently, Dang *et al.*[6] realized uniform elastic strain along the [100], [101], and [111] crystal directions by fabricating micron-nanometer scale bridge structures, thereby making it possible for the widespread application of "strained diamond" in electronic devices. It remains unclear whether strain engineering effectively promotes the hole mobility of diamond and shares a similar mechanism with other group IVA *fcc* semiconductors.

RESULTS AND DISCUSSIONS

The crystalline geometry of the relaxed diamond is *fcc* (space group $Fd\bar{3}m$, no. 227) and its first Brillouin zone (BZ) is a truncated octahedron. The SOC removes the triple degeneracy at the VBM, resulting in the double degeneracy of the heavy-hole (*hh*) and light-hole (*lh*) bands, while the split-off hole (*sh*) band lies 13.4 meV lower in energy, as shown in the insets of Fig. 1(a). In contrast, the crystal symmetry is broken with the slight shear strain applied to the *fcc* diamond. The space group is changed to $I4_1/amd$ (no. 141). As a result, the double degeneracy of the *hh* and *lh* bands is lifted under a 2% shear strain along the [100] directions, arousing a large energy splitting of ~ 0.3 eV (highlighted by light green ribbons in Fig. 1(b).)

Fig. 1(c) shows the phonon-limiting hole drift mobility and Hall mobility of the relaxed diamond. The room-temperature hole mobility of the relaxed diamond is 2820 $\mathrm{cm}^2/(\mathrm{Vs})$. There is a dramatic enhancement in hole mobility when shear strain is applied, as shown in Fig. 1(d). Specifically, the in-plane mobility is increased to 14148 $\mathrm{cm}^2/(\mathrm{Vs})$ under 2% compressive (-2%) shear strain along the [100] direction. Correspondingly, the out-of-plane mobility reaches 8252 $\mathrm{cm}^2/(\mathrm{Vs})$ for the -2% shear strain case. As the shear strain increases to 8%, the enhancement in hole mobility gradually approaches saturation. The in-plane hole mobility reaches 24190 $\mathrm{cm}^2/(\mathrm{Vs})$, which is one order of magnitude larger than that of relaxed diamond and is the highest recorded value in bulk semiconductors. The hole mobility typically decreases exponentially with temperature ($\mu \sim T^{-n}$) since phonons are significantly activated, which degrades the performance of electronic devices. For the relaxed case, the value of exponent *n* in the temperature dependence is -2.01. We show that hole mobility becomes less temperature-dependent for diamonds with shear strains. The exponent *n* values of in-plane hole mobility are located in the range of -1.52 to -1.61.

To understand the increase in the hole mobility induced by shear strains, we further project the interband electron-phonon scattering rates onto the band structure for diamonds without/with strain, as shown in Figs. 1(e) and 1(f). There is a significant reduction in the interband electron-phonon scattering rates for the shear-strained diamond, attributed to the substantial energy splitting in the valence bands. This energy splitting prohibits energy conservation and diminishes the available electron-phonon scattering channels. Moreover, intraband electron-phonon scattering processes are primarily mediated by low-frequency acoustic phonons, while the interband scattering processes are mainly assisted by high-frequency acoustic phonons. The relative increase in the number of low-frequency acoustic phonons with temperature is not as significant as that of high-frequency acoustic phonons. Therefore, the hole mobility for strained diamonds becomes less temperature-dependent.

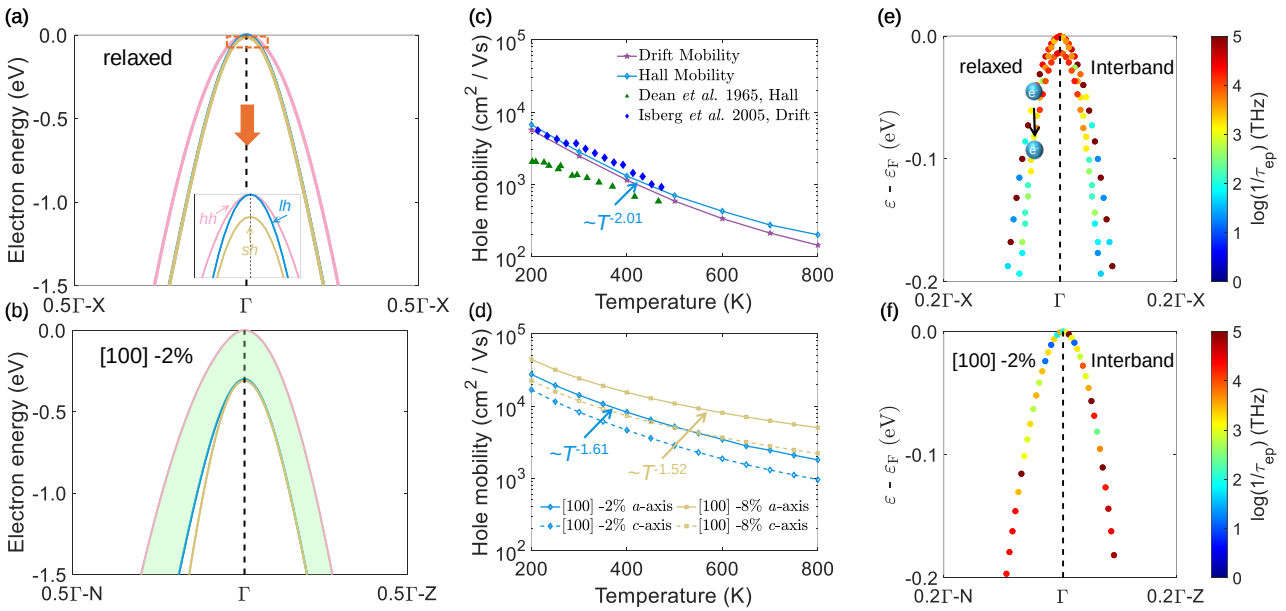

Fig. 1. Valence bands of (a) relaxed structure, (b) the structure with -2% shear strain along the [100] direction. (c) Drift mobility and Hall mobility as a function of temperature for relaxed diamond. The scatters are experimental data reported by Dean *et al.*[7] (triangle) and Isberg *et al.*[8] (diamond). (d) In-plane (*a*-axis) and out-of-plane (*c*-axis) Hall mobilities for shear strains along the [100] directions. Projection of interband electron-phonon scattering rates onto the band structure for (e) relaxed and (f) -2% shear-strained diamond.

ACKNOWLEDGMENT

S.L. was supported by the National Natural Science Foundation of China (Grant No. 12304039). X.L. was supported by the National Natural Science Foundation of China (Grants Nos. 52150610495 and 12374027). J.S. was supported by the Fundamental Research Funds for the Central Universities (Grant No. CUSF-DH-T-2024061).

REFERENCES

[1] "International roadmap for devices and systems (IRDS), https://irds.ieee.org/editions/2023."

[2] C. J. Wort and R. S. Balmer, "Diamond as an electronic material," *Materials Today*, 11, 22–28, 2008.

[3] J. Isberg, J. Hammersberg, E. Johansson, T. Wikström, D. J. Twitchen, A. J. Whitehead, S. E. Coe, and G. A. Scarsbrook, "High carrier mobility in single-crystal plasma-deposited diamond," *Science*, 297, 1670–1672, 2002.

[4] N. Kurinsky, T. C. Yu, Y. Hochberg, and B. Cabrera, "Diamond detectors for direct detection of sub-Gev dark matter," *Physical Review D*, 99, 123005, 2019.

[5] S. E. Thompson, G. Sun, Y. S. Choi, and T. Nishida, "Uniaxial-process-induced strained-Si: Extending the CMOS roadmap," *IEEE Transactions on Electron Devices*, 53, 1010–1020, 2006.

[6] C. Dang, J.-P. Chou, B. Dai, C.-T. Chou, Y. Yang, R. Fan, W. Lin, F. Meng, A. Hu, J. Zhu *et al.*, "Achieving large uniform tensile elasticity in microfabricated diamond," *Science*, 371, 76–78, 2021.

[7] P. Dean, E. Lightowlers, and D. Wight, "Intrinsic and extrinsic recombination radiation from natural and synthetic aluminum-doped diamond," *Physical Review*, 140, A352, 1965.

[8] J. Isberg, A. Lindblom, A. Tajani, and D. Twitchen, "Temperature dependence of hole drift mobility in high-purity single-crystal CVD diamond," *Physica Status Solidi (a)*, 202, 2194–2198, 2005.

Thursday 4:00-5:30 pm Monte Carlo

Time	Type	Presenter	Title
4:00-4:15 pm	Contributed	Josef Gull and Hans Kosina	Electron-Electron Scattering in Monte Carlo-based Device Simulations
4:15-4:30	Contributed	Tobias Reiter	GPU-based Monte Carlo Ray Tracing for Flux Calculation in Process Simulation
4:30-4:45	Contributed	Caroline dos Santos Soares	The impact of oxide-traps on n-NWFET using a quantum-corrected Monte Carlo simulator
4:45-5:00	Contributed	Orazio Muscato	Signed particle Monte Carlo quantum simulation of thermionic cooling devices based on resonant tunneling heterostructure
5:00-5:15	Contributed	Rémi Helleboid	Self-Consistent Advection-Diffusion Monte Carlo Simulation of Quenching in Single-Photon Avalanche Diodes
5:15-5:30	Contributed	Siddhant Gangwal	Hierarchical Framework for Modeling Electrostatics and Mobility in $Ge_{1-x}Sn_x$/Ge Heterostructures

Electron-Electron Scattering in Monte Carlo-based Device Simulations

Josef Gull and Hans Kosina
Institute for Microelectronics, TU Wien, Gußhausstraße 27–29/E360, 1040 Wien, Austria
e-mail: gull@iue.tuwien.ac.at

Introduction

Understanding reliability issues and degradation mechanisms is key to improving device quality. Hot carrier degradation (HCD) occurs when electrons of high kinetic energy cause material damage. An important requirement for modeling HCD is good knowledge of the local carrier distribution function. An accurate calculation of the high-energy tail should take into account electron-electron scattering (EES) [1] and a realistic band structure model.

Recently, a Monte Carlo (MC) algorithm for solving a two-particle kinetic equation has been developed, which treats both single-particle scattering and two-particle scattering in a consistent way [2]. In this work, we present a statistical enhancement method for the two-particle MC algorithm and the treatment of EES in a non-parabolic band.

Model

The basic idea is to simulate the time evolution of two electron states simultaneously. Each electron can individually undergo phonon scattering or both electrons can simultaneously experience EES [2].

In an EES event, both energy and momentum are conserved. For a parabolic band, the allowed momentum transfer vectors $\vec{q}$ are located on a sphere, and the EES rate can be obtained by analytical integration. In the case of a non-parabolic band that surface becomes an ellipsoid of rotation (Fig. 1), and analytical integration of the transition rate is no longer feasible. To simplify the integrand, we use an upper bound that allows for an analytic evaluation. The upper bound of the EES rate obtained in this way is used in a rejection technique. A specific transition is accepted with the given acceptance probability; otherwise, self-scattering is selected [3].

The distribution function varies by many orders of magnitude. To resolve the high-energy tail of the distribution in a MC simulation, statistical enhancement is required. Methods successful in the one-particle picture, such as particle splitting and gathering, cannot be used in the two-particle picture. Instead, we exploit the fact that any result of a stationary MC simulation represents a time average:

$$\langle A \rangle = \frac{1}{T} \int_0^T A(\vec{k}(t), \vec{r}(t)) \, \mathrm{d}t \, . \qquad (1)$$

We split the simulation period T into time frames. If a rare event of interest occurs in a certain time frame, simulation of that frame is repeated, and its statistical weight is reduced accordingly.

Results and Conclusion

Figure 2 shows the energy distribution function (EDF) on the surface of a planar MOSFET. In the transition region between channel and drain, electrons reach energies higher than those that ballistic trajectories passing the potential maximum would allow. This effect is described in [1]. Figure 3 illustrates the influence of carrier concentration and the dispersion relation on the EDF at the channel/drain junction. The slope of the high-energy tail increases with the carrier density. The parabolic transport model predicts a larger enhancement of the tail than the nonparabolic model does.

Figure 4 shows the distribution of the sampling points in the energy domain. The repeated time frame approach has been applied in a cascade of three steps. Figure 5 demonstrates that the statistical enhancement algorithm allows us to calculate three more orders of magnitude of the EDF. At lower energies, the EDFs calculated with standard and statistically enhanced MC are virtually identical.

Acknowledgment

This work has been supported by the Austrian Research Promotion Agency (FFG), contract 880672.

REFERENCES

[1] Childs, P. A., and C. C. C. Leung, *A one-dimensional solution of the Boltzmann transport equation including electron–electron interactions*, Journal of Applied Physics 79.1 (1996): 222-227.

[2] J. Gull and H. Kosina, *Monte Carlo study of electron–electron scattering effects in FET channels*, Solid-State Electronics **208** (2023).

[3] J. Gull, L. Filipovic and H. Kosina, *Electron-electron scattering in non-parabolic transport models*, SISPAD, (2024), doi: 10.1109/SISPAD62626.2024.10733120.

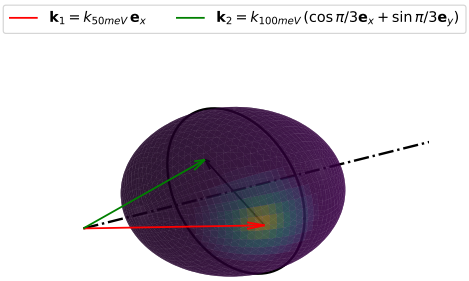

Fig. 1. For a non-parabolic dispersion the final states are located on an ellipsoid. The colour maps the transition rate $T(\vec{q})$ as a function of the momentum transfer vector $\vec{q} = \vec{k}_1' - \vec{k}_1 = \vec{k}_2 - \vec{k}_2'$. The transition rate is not symmetric with respect to the principal axes of the ellipsoid, complicating analytical integration.

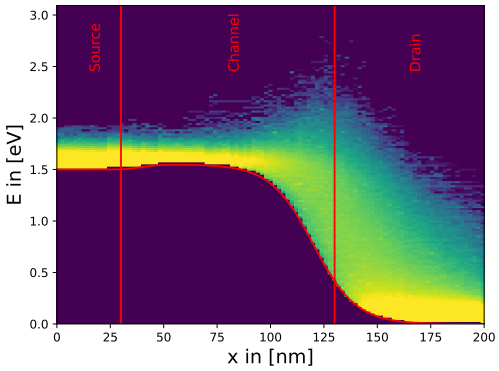

Fig. 2. EDF along a MOSFET channel, assuming a Kane dispersion and $n = 1 \times 10^{19}\,\mathrm{cm}^{-3}$: The population of electron states with high kinetic energy at the channel/drain junction increases due to EES. Adopting the Kane dispersion accelerates energy relaxation toward the drain.

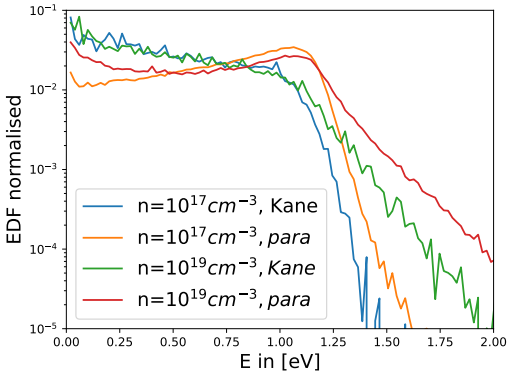

Fig. 3. EDF at the channel/drain junction: Higher carrier densities n lead to an increased population of high-energy states, which can contribute to device degradation.

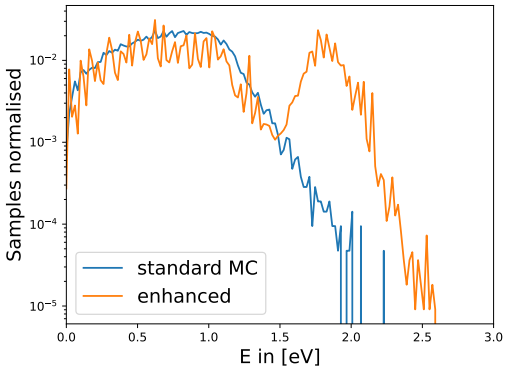

Fig. 4. Statistical enhancement increases the sampling of high-energy states and enables the study of the distribution at even higher energy levels.

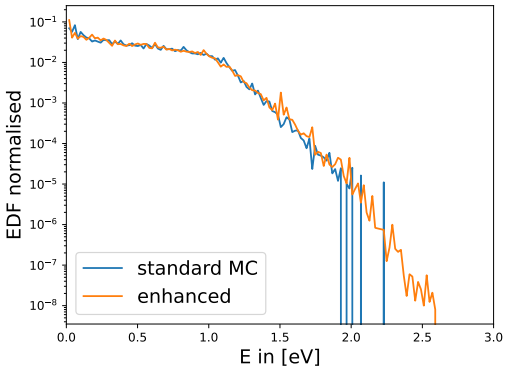

Fig. 5. Enhanced energy resolution: By cascading the statistical enhancement approach, the EDF can be resolved over additional three orders of magnitude.

GPU-based Monte Carlo Ray Tracing for Flux Calculation in Process Simulation

T. Reiter[†*], P. Manstetten[†] and L. Filipovic[†]
[†]Christian Doppler Laboratory for Multi-Scale Process Modeling of Semiconductor Devices and Sensors,
Institute for Microelectronics, TU Wien, 1040 Vienna, Austria
[*]Email: reiter@iue.tuwien.ac.at

I. Introduction

Simulating semiconductor fabrication is particularly challenging when three-dimensional (3D) structures with high aspect ratios (HAR) are involved, such as in 3D NAND flash memory [1]. Accurate modeling of plasma processes requires determining the flux of reactive and charged species reaching the structures on the wafer surface, which serves as input for physical process models. For HAR structures, conventional analytical models or semi-empirical models are often limited to specific geometries and fail to capture the full range of particle-surface interactions and reflections occurring within deep trenches [2]. Monte Carlo (MC) ray tracing provides a powerful alternative by simulating the trajectories of pseudo-particles—each representing hundreds of atomic particles—from a plasma source to the substrate.

Furthermore, process simulation is rarely a one-time computation. Optimizing a fabrication process requires running numerous simulations under varying input conditions to explore process windows, improve yield, and ensure robustness against manufacturing variations. Since each optimization cycle may involve evaluating hundreds or even thousands of different scenarios, computational efficiency is crucial [3]. Traditional CPU-based MC ray tracing, while accurate, can be prohibitively slow when modeling particle fluxes for complex 3D structures with extensive particle interactions. To address this challenge, we present a GPU-based framework for highly efficient flux calculations in complex 3D geometries. This method allows for highly accelerated modeling, compared to traditional CPU approaches, without losing accuracy.

We utilize NVIDIA OptiX™ [4], a multi-purpose GPU ray tracing engine, to simulate particle fluxes within a plasma processing chamber. The implementation is embedded within ViennaPS [5], an open-source process simulation framework from the Institute for Microelectronics. The GPU acceleration dramatically reduces computation time, making previously time-consuming simulations feasible. By significantly accelerating flux calculations, the bottleneck of physical simulations, our approach enables rapid exploration of process parameters, facilitating iterative design and optimization without requiring expensive computational clusters or excessive runtime on a regular workstation. Additionally, we investigate different surface representations for ray tracing, assessing their impact on both performance and accuracy within our framework.

II. Top-Down Monte Carlo Flux Calculation

For top-down MC flux calculations, a large number of pseudo-particle trajectories are traced from a source plane to the surface of a structure, with the possibility of adsorption or reflection (cf. Fig. 1). Since the simulation domain is confined to a region near the sample surface, where ballistic transport can be assumed, the trajectories are independent of each other. This independence makes the method well-suited for parallelization of surface intersection calculations, offering the potential for high computational efficiency.

Tracing trajectories through a given domain is a well-established problem, particularly in computer graphics, where highly efficient ray tracing algorithms have been developed for this purpose [6]. Due to its straightforward parallelization, it is also ideally suited for GPU acceleration. To leverage this advantage, we integrate OptiX™ into our framework for particle flux calculation.

The program structure of our flux calculation framework is shown in Fig. 2. First, an explicit surface is extracted from the native Level-Set representation from ViennaPS, and used to build the geometry acceleration structure (GAS). The shader binding table (SBT) is configured to link user-defined programs to the ray tracing pipeline. The OptiX™ ray tracing engine then handles fast geometry traversal and intersection calculations, while user-provided programs manage flux accumulation and particle reflection in the closest-hit shader. If no intersection occurs, the miss shader discards the particle and generates a new one on the source plane until the desired ray count is achieved.

III. Surface Representation

Initially, the surface is stored in a Level-Set, which is used for topography simulation and surface evolution. The Level-Set employs an implicit representation, storing only the signed distance to the surface on a regular grid. Since ray tracing is more efficient with explicit surface representations, we test two different approaches: *disk meshes* and *triangle meshes* (cf. Fig. 3 a,b). The disk mesh represents the surface as a point cloud with normals defining disk orientations [7], while the triangle mesh is generated via Marching Cubes. Disk extraction is fast and well-suited for Level-Set methods, while triangle mesh extraction is typically slower. Fluxes on disk meshes can be directly used for Level-Set advection, whereas fluxes on triangle meshes require conversion back to points on a rectilinear grid. However, for GPU ray tracing, disk meshes require a custom intersection kernel, whereas triangle meshes benefit from built-in GPU support, making them significantly faster for this task.

Additionally, disk meshes are typically designed with a diameter that extends beyond a single grid spacing to ensure a continuous and hole-free surface representation. However, this can introduce an issue at the edges of trench or hole openings, where disks may extend beyond the intended boundary, leading to unintended shadowing of

incoming particles. This effect is illustrated in Fig. 3(c) and Fig. 4 which shows the flux distribution on the sidewall and bottom of a cylindrical hole. Coarser geometry representations amplify this issue, causing increased shadowing and reduced flux inside the cylinder when using disks. However, as the geometry resolution increases, the flux values for disk and triangle meshes converge, aligning with the analytical radiosity calculation [8].

IV. Performance

We evaluated the performance using both CPU and GPU implementations, utilizing the faster disk mesh extraction for the CPU and triangular meshes for the GPU. Benchmarking was performed using a cylindrical hole geometry, resolved with approximately 110,000 triangles, or 50,000 disks. A total of 50 million initial rays were emitted from the source plane, with a sticking coefficient of 0.1, resulting in approximately 200 million total traces, including reflections. The GPU shows a 45× overall speedup compared to the CPU, which aligns with expectations, as GPUs are significantly more efficient for ray tracing workloads than CPUs. The resulting flux in a cylinder is shown in Fig. 4, while benchmark results are presented in Table I and Fig. 5.

We then simulate the etching of a three-dimensional cylinder with the above dimensions in a few minutes on the GPU, making a 100-step optimization feasible. In contrast, when using a CPU-based ray tracer each simulation takes about one hour, significantly limiting the number of possible optimization runs.

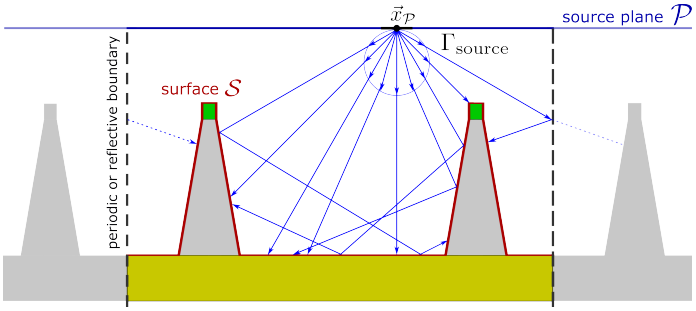

Fig. 1. Schematic depiction of rays being traced from a point on the source plane $\vec{x}_{\mathcal{P}}$ to the surface using reflective or periodic boundary conditions.

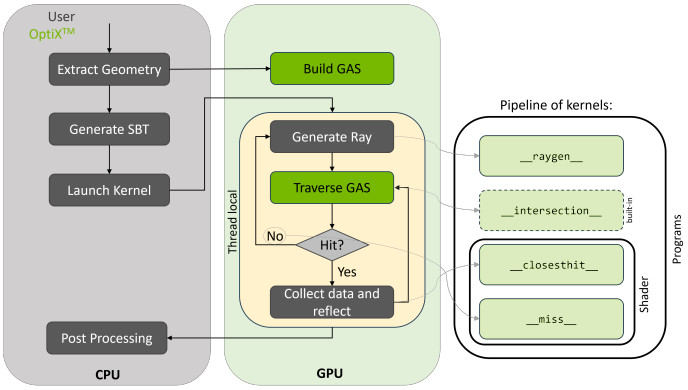

Fig. 2. Overview of the program structure for ray tracing with OptiX™, illustrating the interaction between CPU and GPU components, including geometry extraction, ray generation, traversal, and shader execution.

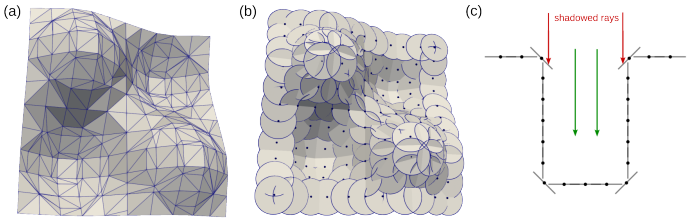

Fig. 3. Mesh representations used for comparison. (a) Triangle mesh representation. (b) Disk mesh representation. (c) The 2D view of the disk mesh in the hole geometry illustrates the overextension of disks at the hole opening.

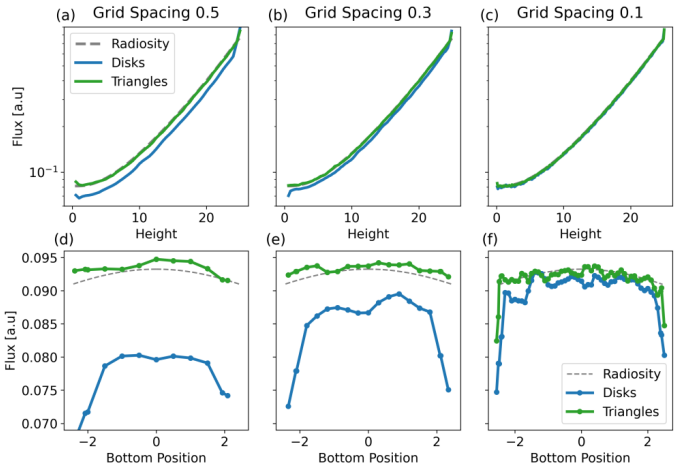

Fig. 4. Flux distribution in a cylindrical hole. (a–c) show the flux on the sidewall of the hole for different geometry resolutions, while (d–f) depict the flux on the bottom, where 0 marks the center of the hole. The results compare flux computed using triangle and disk surface representations to the analytical radiosity solution.

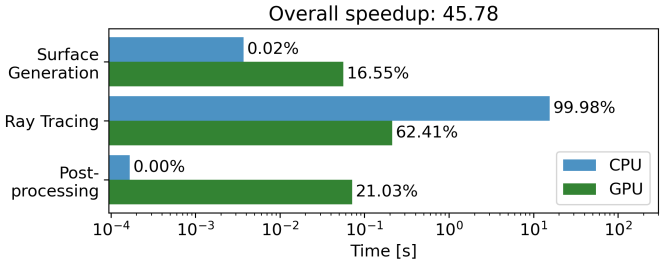

Fig. 5. Benchmark comparison of CPU and GPU execution times. The bar chart shows the time distribution for surface generation, ray tracing, and post-processing on CPU (blue) and GPU (green). Percentages indicate the relative contribution of each stage to the total runtime. All results were obtained by taking the median of ten simulation runs.

TABLE I
Timing results for CPU and GPU ray tracing.

Device	Total Time [s]	MRays / s
CPU (i7-12700K, 16 Threads)	15.57	12.30
GPU (RTX 4070 Ti Super)	0.21	1052.85

References

[1] Y. Li, *IEEE J. Solid-State Circuits*, vol. 12, pp. 56–65, 2020. DOI: 10.1109/MSSC.2020.3021841

[2] G. S. Oehrlein *et al.*, *J. Vac. Sci. Technol. B* vol. 42, pp. 041501, 2024. DOI: 10.1116/6.0003579

[3] F. Krüger *et al.*, *J. Vac. Sci. Technol. A* vol. 42, pp. 043008, 2024. DOI: 10.1116/6.0003554

[4] S. Parker *et al.*, *ACM Trans. Graph.*, vol. 29(4), pp. 1–13, 2010. DOI: 10.1145/1778765.1778803

[5] T. Reiter *et al.*, ViennaPS-3.2.0. URL: https://github.com/ViennaTools/ViennaPS

[6] E. Vasiou *et al.*, *Vis. Comput.* vol. 34, pp. 875–885, 2018. DOI: 10.1007/s00371-018-1532-8

[7] O. Ertl and S. Selberherr, *Comput. Phys. Commun.*, vol. 180(8), pp. 1242–1250, 2009. DOI: 10.1016/j.cpc.2009.02.002

[8] P. Manstetten *et al.*, *Solid-State Electron.*, vol. 128, pp. 141–147, 2017. DOI: 10.1016/j.sse.2016.10.029

The impact of oxide-traps on n-NWFET using a quantum-corrected Monte Carlo simulator

C.S. Soares, A.C.J. Rossetto*, D. Vasileska and G.I. Wirth†
School of Electrical Computer and Energy Engineering, Arizona State University, Tempe, AZ, USA
*Centro de Desenvolvimento Tecnológico Universidade Federal de Pelotas, Pelotas, Brazil
†Universidade Federal do Rio Grande do Sul, Porto Alegre, Brazil
e-mail: cdossan2@asu.edu

The continuous scaling of FinFETs is a challenge to reproduce in high-volume manufacturing. Because of that, the industry projects to change the transistor architecture shortly. Ref. [1], [2] suggest the tri-gate SOI nanowire FET (SOI NWFET) is a promising architecture. Ref. [2] showed that, at high temperatures, the Gate-Induced Drain Leakage (GIDL) in SOI NWFET is smaller than in SOI nanosheet FET. This work studies the effect of a charged oxide trap on the current of n-SOI NWFET. Ref. [3] has accessed the current variability of this transistor caused by random dopants. Charged oxide traps are another relevant source of intrinsic variability and contributes to BTI and RTN.

This work uses the 3D quantum-corrected Monte Carlo device simulator presented in Ref. [4], which employs the effective potential approach to account for size-quantum effects. Phonon scatterings are treated in k-space, surface roughness scattering is modeled in r-space, using Fuchs' model, and Coulomb interactions accounted for by solving the Poisson equation and using a very fine mesh. The width and height of the NW are 10 nm and the equivalent oxide thickness is 1.3 nm. The channel is undoped, and its length is 40 nm. Fig. 1 shows the experimental and simulated $I_{DS} \times V_{GS}$ curves obtained by our group at $V_{DS} = 0.7$ V. The excellent agreement demonstrates that our model is accurate. This study models oxide traps as charged particles. The simulations were carried out at $V_{GS} = 0.5$ V and $V_{DS} = 0.7$ V. The current and its standard error (SE) of the device without a oxide trap is 4.387 ± 0.027 μA (with 95% confidence interval). An ensemble of 100 SOI NWFET was investigated. In each NWFET, a charged trap was placed in the oxide at (x, y, z). The schematic of the n-SOI NWFET is presented on the left-hand side of Fig. 2, and the dashed planes cut the x-position of the trap. The right-hand side of Fig. 2 shows the cross-section of the n-SOI NWFET, the red and blue arrows define, respectively, the regions in the top and side oxide where traps were placed. The traps can assume five different positions along these regions. The tail and the head represent, respectively, the 0-y/0-z-positions and 4-y/4-z-positions. Fig. 3 shows five curves, one for each trap z-position, of the current deviation as a function of the trap x-position, and the y-position of all the traps is 0.26 nm from the top Si/SiO_2 interface, while Fig. 4 shows the curves for the traps whose y-position is 0.52 nm from this interface. Fig. 5 shows the curves of the current deviation as a function of the trap x-position, and the z-position of these traps is 0.26 nm from the side Si/SiO_2 interface, while Fig. 6 shows the curves for the traps whose z-position is 0.52 nm from this interface. The presence of a charged oxide trap affects the electron transport and its density in the channel. The results show the impact of the trap depends on its position. When the trap is far from the source and drain its effect is significant. A trap in the top oxide causes the highest variability when the trap is closer to this interface and in the center of the NW width. A trap in the side oxide causes the highest degradation when the trap is closer to this interface and around the BOX.

REFERENCES

[1] S. Barraud, et al., IEEE Electron Device Letters (2012), doi: 10.1109/LED.2012.2212691
[2] M. de Souza, et al., 2022 IEEE LAEDCm(2022). doi: 10.1109/LAEDC54796.2022.9908212
[3] C. S. Soares, et al. IEEE Transactions on Electron Devices (2024).doi: 10.1109/TED.2024.3440276

[4] C. S. Soares, et al. Journal of Computational Electronics (2024). doi:10.1007/s10825-024-02145-w

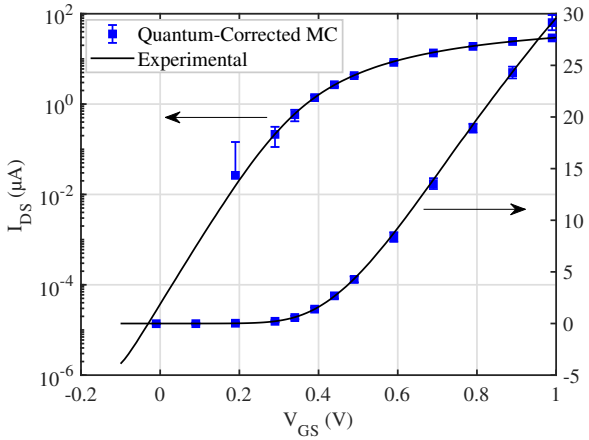

Fig. 1. Experimental and simulation $I_{DS} \times V_{GS}$ curves

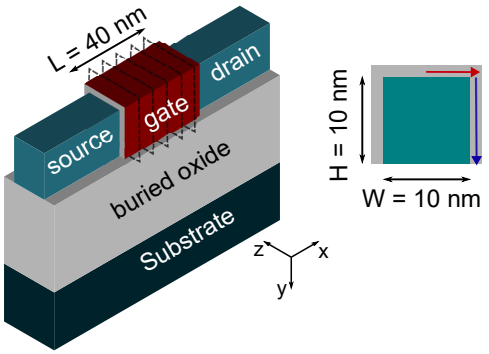

Fig. 2. Schematic of the SOI n-NWFET.]

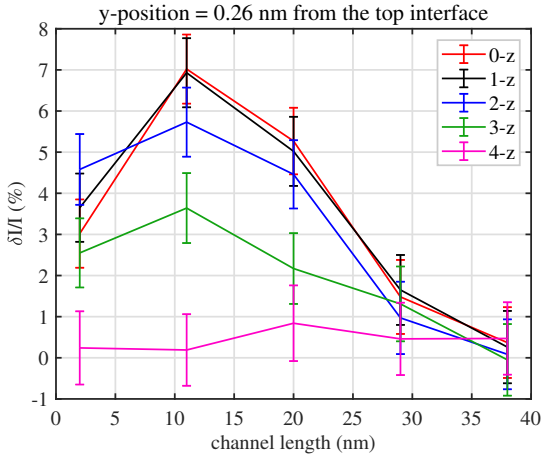

Fig. 3. Current deviation × trap x-position for distinct z-positions. y-position = 0.26 nm from the top interface

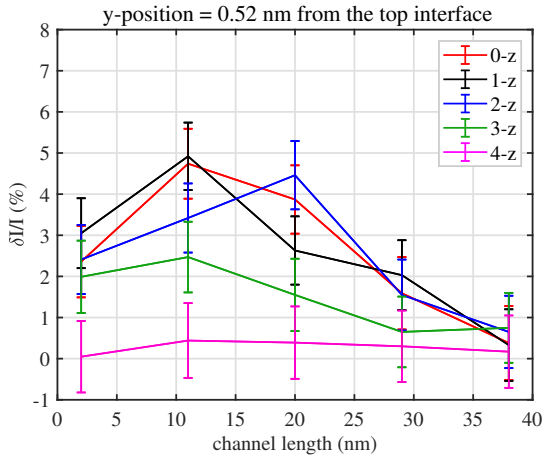

Fig. 4. Current deviation × trap x-position for distinct z-positions. y-position = 0.52 nm from the top interface

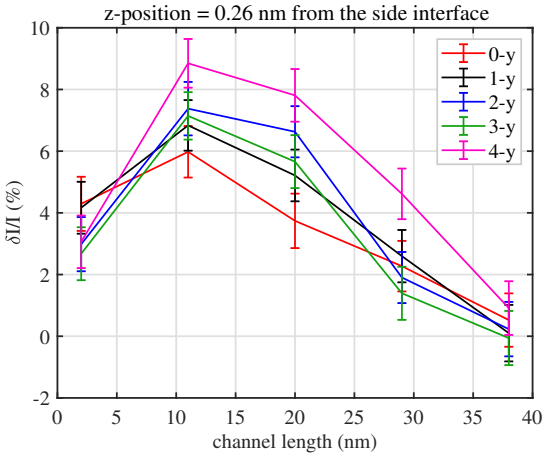

Fig. 5. Current deviation × trap x-position for distinct y-positions. z-position = 0.26 nm from the side interface

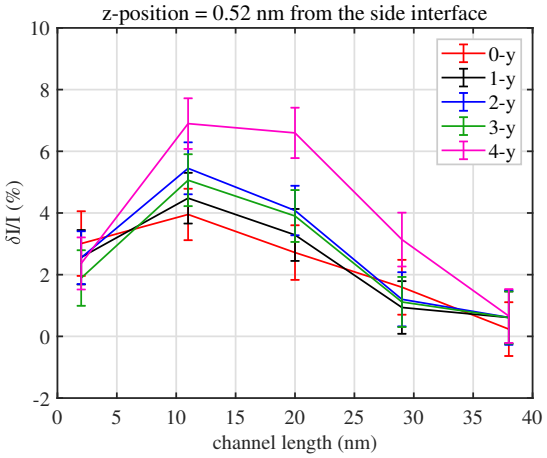

Fig. 6. Current deviation × trap x-position for distinct y-positions. z-position = 0.52 nm from the side interface

Signed particle Monte Carlo quantum simulation of thermionic cooling devices based on resonant tunneling heterostructure

O. Muscato, and V. Di Stefano
Department of Mathematics and Computer Science, University of Catania, Viale A. Doria 6, 95125 Catania, Italy
email : orazio.muscato@unict.it

INTRODUCTION

Refrigeration ever-smaller integrated circuits is major scientific and industrial issue, because self-heating effects result, indeed, in significant reductions of both transistor efficiency and lifetime. An interesting mechanism for refrigeration is the thermionic effect. If we consider two metals separated by a vacuum region, electrons with high thermal energy (greater than the work function of the metal) can escape from the metal, transferring their kinetic energies to the anode to give rise to refrigeration in the cathode. In the 1990s, room-temperature thermionic refrigerators emerged using semiconductor heterostructures, where quasiballistic electron transport replaces the vacuum region. Cooling of 1–5 K was observed. This paper studies the AlGaAs/GaAs resonant heterostructure shown in Fig. 1, proposed in [1] and analyzed via non-equilibrium Green's functions in [2], [3]. The structure features a quantum well (QW) between two potential barriers: a thin, tall emitter barrier (b_1) enabling resonant tunneling of cold electrons into the QW, and a thick, low collector barrier (b_2) that prevents electron escape. When subband energy in the QW matches polar optical phonon energy, electrons absorb phonons, overcome b_2 via thermionic emission, and cool the QW while minimizing heat backflow. This paper adopts the Wigner-Boltzmann transport equation (WBTE) for numerical simulation of this structure.

ELECTRO-THERMAL TRANSPORT

Quantum transport phenomena are described by the Wigner-Boltzmann transport equation (WBTE), solved in conjunction with the Poisson equation.

The WBTE is addressed using the Signed Particle Monte Carlo (SPMC) method [4], [5], where the Wigner potential is treated as an additional scattering source, alongside phonon scattering.

Thermal, self-consistent device characteristics are determined by solving the heat diffusion equation based on the power distribution derived from the electronic SPMC simulation. This iterative approach, called Electro-Thermal Monte Carlo method, alternates between Monte Carlo simulations and a steady-state heat equation solver to compute phonon temperatures, until convergence is reached.

In this study, we focus on acoustic and polar optical phonons and employ the parabolic band approximation.

RESULTS

In the Figure 2 we show the acoustic phonon temperatures along the device, for some values of the applied bias voltage V_b. The temperature decreases in the left region and increase on the right side of the device, for small values of V_b. The lowest temperatures are observed in the QW, with the minimum value of 299.4 K occurring at V_b = 0.2 V. This modest value is primarily due to the high lattice thermal conductivity of AlGaAs and GaAs, which efficiently equalize the temperature throughout the device. Since the QW is cooled, but the collector region heats, there is therefore a risk of heat backflow towards the QW which could be overcame considering a material in the collector barrier with a very weak electron-phonon coupling and a low thermal conductivity.

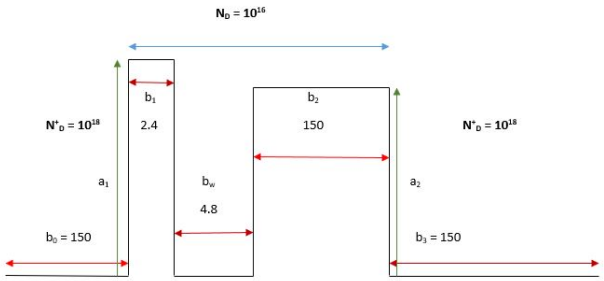

Fig. 1. Band diagram profile of the device. The GaAs regions b_0 and b_1 are 150 nm wide, with a doping concentration of $10^{18}\,cm^{-3}$. The Al_xGaAs_{1-x} barriers b_1 and b_2 are 2.4 nm and 150 nm wide, respectively. The Al mole fractions are x = 0.3 (b_1) and x = 0.12 (b_2). The QW (made with GaAs) thickness b_w is 4.8 nm

REFERENCES

[1] K.A. Chao and M. Larsson, *Room-temperature semiconductor heterostructure refrigeration*, Appl. phys. letters **87**, 0022103 (2005).

[2] M. Bescond, D. Logoteta, F. Michelini, N. Cavassilas,A. Yangui, M. Lannoo and K. Hirakawa, *Thermionic cooling devices based on resonant-tunneling $AlGaAs/GaAs$ heterostructure*, J. Phys.: Condens. Matter **30**, 064005 (2018).

[3] A. Philippe, F. Carosella, X. Zhu, C. Salhani, K. Hirakawa, M. Bescond, R. Ferreira and G. Bastard, *Rate equations description of the asymmetric double barrier electronic cooler*. J. Applied Physics, **134**(12), 124305, (2023).

[4] M. Nedjalkov, J. Weinbub, M. Ballicchia, S. Selberherr, I. Dimov and D.K. Ferry, *Wigner equation for general electromagnetic fields: The Weyl-Stratonovich transform*, Physical Review B **99**(1), 014423 (2019).

[5] O. Muscato, *Wigner ensemble Monte Carlo simulation without splitting error of a GaAs resonant tunneling diode*, J. Comput. Electr. **20**, 2062-2069 (2021).

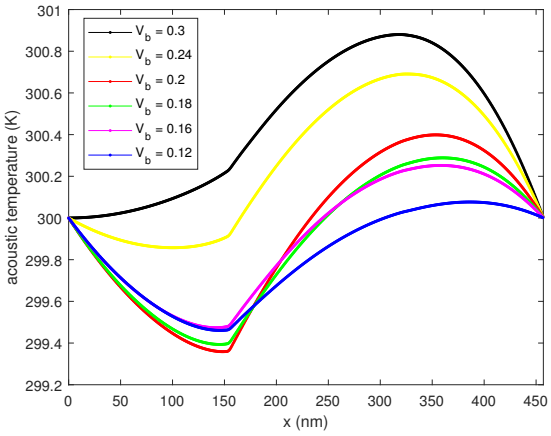

Fig. 2. The acoustic phonon temperatures T_{ac} along the device for some values of the applied bias V_b.

Self-Consistent Advection-Diffusion Monte Carlo Simulation of Quenching in Single-Photon Avalanche Diodes

R. Helleboid*, K. Morel-Handa*, I. Nicholson†, G. Mugny†, D. Rideau†
M. Pala*, P. Dollfus*, J. Saint-Martin*,
*C2N, CNRS and Univ. Paris-Saclay, France
†STMicroelectronics, France and United Kingdom

***Abstract*—This paper introduces a self-consistent Advection-Diffusion Monte Carlo (ADMC) method for transient modeling of Single-Photon Avalanche Diodes (SPADs), coupling carrier transport with electrostatics via the Poisson equation to simulate avalanche and quenching dynamics. The approach employs a Finite Element Method (FEM) framework for 3D field calculations and explores key phenomena such as the build-up field effect, quenching mechanisms, and quenching time distributions.**

I. Introduction

Single-Photon Avalanche Diodes (SPADs) are highly sensitive photodetectors capable of detecting individual photons by leveraging avalanche multiplication in a reverse-biased p-n junction. Their ability to provide precise timing resolution and single-photon sensitivity makes them indispensable in applications such as quantum computing, LiDAR, and biomedical imaging. Efficient simulation of SPAD transient behavior, including avalanche dynamics and quenching processes, is crucial for optimizing device performance, as these phenomena directly influence timing accuracy, detection efficiency, and noise characteristics [1]. Accurate modeling tools are therefore essential to advance SPAD technology and enable their integration into next-generation systems. Standard SPAD simulation tools, such as TCAD software, typically rely on drift-diffusion models to simulate carrier transport and avalanche dynamics. While these models are computationally efficient, they lack the features needed to capture the stochastic nature of the avalanche and thus quenching dynamics. To address this limitation, self-consistent Monte Carlo, based on solving the Boltzmann equation with the Monte Carlo method (MC), has been proposed to model SPAD dynamics [2]. Those approaches are computationally intensive and require significant computational resources, which limits their practicality for simulating large-scale SPAD and limits the amount of statistics that can be gathered, which is crucial for the study of quenching. In [3] an efficient MC method was proposed to simulate the transport and impact ionization of carriers in SPADs, based on the Fokker-Planck equation. The method was shown to accurately capture the avalanche multiplication process. In this work, we couple the MC method with a Finite Element Method (FEM) framework to solve the Poisson equation self-consistently, enabling the simulation of avalanche and quenching dynamics in SPADs. The proposed methodology is summarized hereafter.

II. Modeling and simulation

The transport of carriers is modeled using an advection-diffusion MC method, where carriers are driven according to the drift velocity and diffused according to the Einstein's law. It results in a Fokker-Planck-like equation for the probability density function of the carriers that is solved using a particle MC approach with the following dynamics [3]:

$$\begin{cases} \mathbf{X}^0 = \mathbf{x}_0 \\ \mathbf{X}^{n+1} = \mathbf{X}^n + [-\mathbf{v}(\mathbf{X}^n, t_n) + \mathrm{div}(\mathbb{D}(\mathbf{X}^n, t_n))]\, dt + \boldsymbol{\sigma}(\mathbf{X}^n, t_n)\mathbf{W}^{n2} \end{cases}$$

where $\mathbf{X}$ is the position of the carrier, $\mathbf{v}$ is the drift velocity, $\mathbb{D}$ is the diffusion tensor, $\boldsymbol{\sigma}$ is the square root of the diffusion tensor, and $\mathbf{W}$ is a vector of independent standard normal random variables. The impact ionization and particle generation are simulated concurrently with the carrier transport, using the method proposed in [3].

The Poisson equation:

$$\mathrm{div}(\varepsilon \nabla \Phi) = -q(p - n + N_D - N_A)$$

where ε is the permittivity, Φ is the electrostatic potential, q is the elementary charge, p and n are the hole and electron densities, and N_D and N_A are the donor and acceptor densities is solved using a FEM framework. The carrier densities are calculated from the particle positions using a point-in-cell method, and smoothed when setting the element quantities over the nodes. We use a simple external R-C quenching circuit (see Fig. 5), which enables us to compute the voltage across the SPAD directly from the SPAD current, calculated using the Ramo-Shockley theorem.

III. Results and discussion

To illustrate the appearence of a build up field effect during the avalanche, we show in Fig. 2 an avalanche in a SPAD at three different times: when the particle is injected, after 20 ps and after 100 ps. We observe that the depletion region is flooded with carriers, which creates an important change in the density and thus on the electrostatics. This impact is shown in Fig. 3 where the carrriers densities, the electrostatic potential and the electric field are plotted before and during the avalanche along the x direction. We observe an important drop in the electric field in the avalanche region, which we call the avalanche build-up field effect (ABUE). This effect strength is highly dependent on the device geometry, as illustrated in Fig. 4.

Quenching is a crucial process in SPADs, as it determines the timing resolution and the afterpulsing probability. Fig. 6 shows the quenching process in a SPAD quenched by a R-C circuit. The figure shows that in some cases, the quenching fails, leading to multiple avalanches. Fig. 7 shows the impact of the ABUE on the quenching process, it lowers the peak current and the voltage sweep, hence the time during which the voltage is below the diode breakdown voltage. This results in poor quenching efficiency. The ABUE is desactivated in the simulation by assigning a zero 'Poisson-weight' to carriers generated by impact ionization.

Finally, the quenching statitistics are investigated. Fig. 8 shows 1000 quenching events. We observe that some simulations take up to 5 ns to quench, in contrast with the 200 ps standard quenching time. The detection of such events was made possible by the statistically signficant amount of data provided by the MC method, itself enabled by the efficient implementation of the method.

References

1 Cova, S. *et al.*, "Avalanche photodiodes and quenching circuits for single-photon detection," *Applied Optics*, vol. 35, no. 12, pp. 1956–1976, Apr. 1996, number: 12 Publisher: Optica Publishing Group.
2 Dollfus, P. *et al.*, "Avalanche breakdown and quenching in Ge SPAD using 3D Monte Carlo simulation," *Solid-State Electronics*, vol. 194, p. 108361, 2022, publisher: Elsevier.
3 Helleboid, R. *et al.*, "A Fokker-Planck-based Monte Carlo method for electronic transport and avalanche simulation in single-photon avalanche diodes," *Journal of Physics D: Applied Physics*, vol. 55, Oct. 2022.

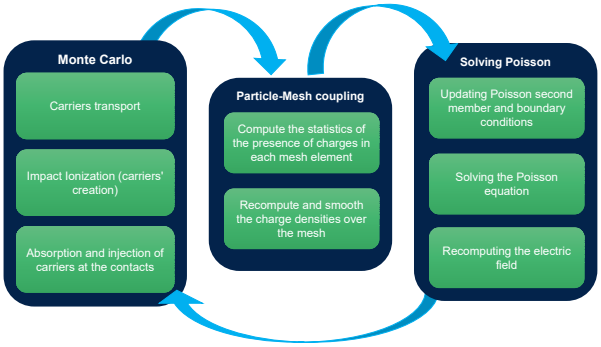

Fig. 1. Flowchart of the self-consistent Monte Carlo method for SPAD simulation.

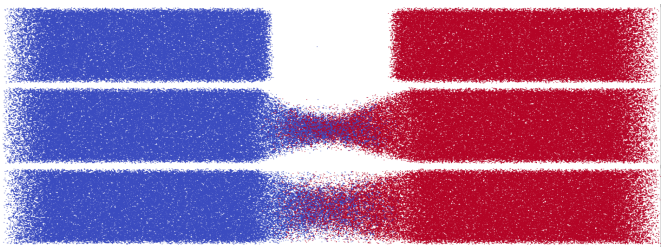

Fig. 2. Avalanche in a SPAD at three different times: when the particle is injected, after 20 ps and after 100 ps. Electrons and holes are shown in blue and red, respectively.

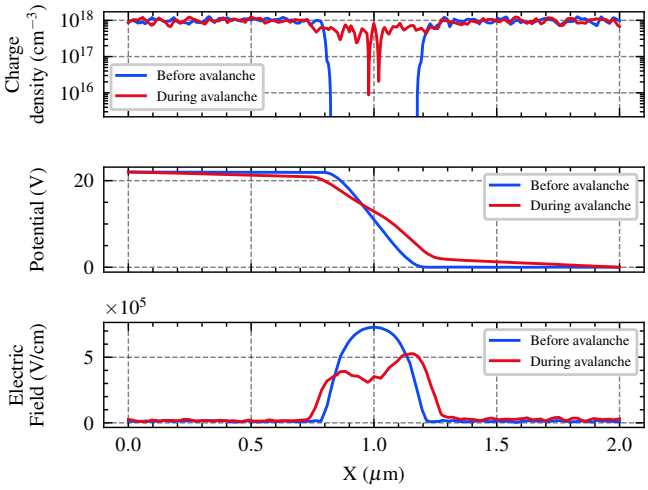

Fig. 3. Longitudinal cut in the center of the 3D SPAD structure showing the carrier density (top), electrostatic potential (middle), and electric field (bottom) at equilibrium and during the avalanche.

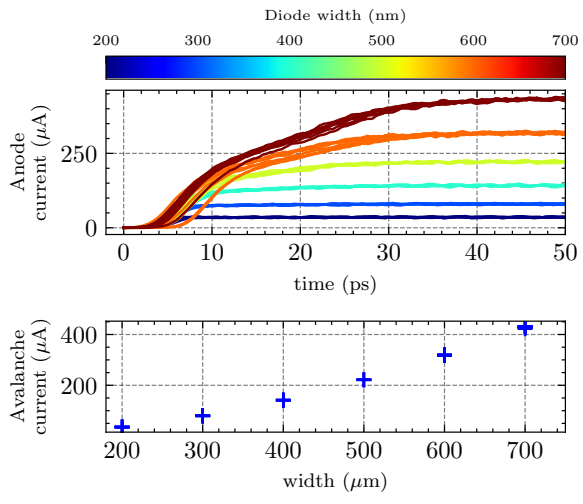

Fig. 4. Top: current from multiple simulations of a SPAD with different widths (latteral dimension y/z of the diode structure). Bottom: avalanche saturation current as a function of the SPAD width

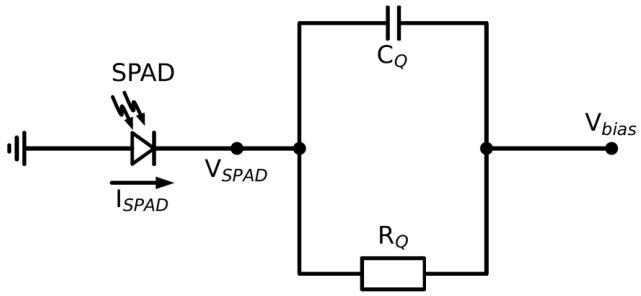

$$V^{i+1}_{anode} = V^{i}_{anode} + \frac{\Delta t}{R_q C_q}\left[-R_q \mathrm{I} + (V_{bias} - V_{anode})\right]$$

Fig. 5. Quench circuit used in the simulation. The quenching is done by an R-C circuit in series with the SPAD. The voltage evolution across the SPAD is calculated using Kirchhoff's law.

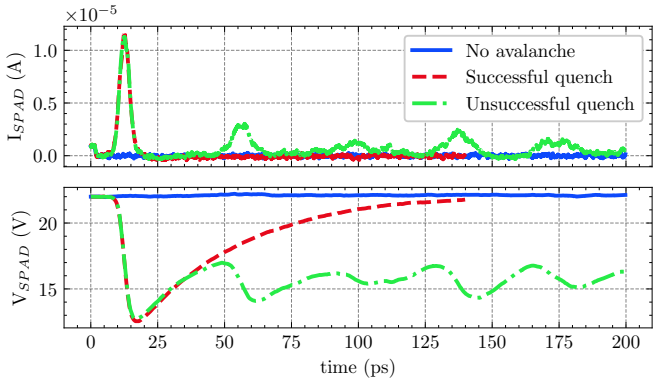

Fig. 6. Voltage and current evolution during three different types of simulation outcomes: no avalanche, single avalanche with successful quenching, and failed quenching.

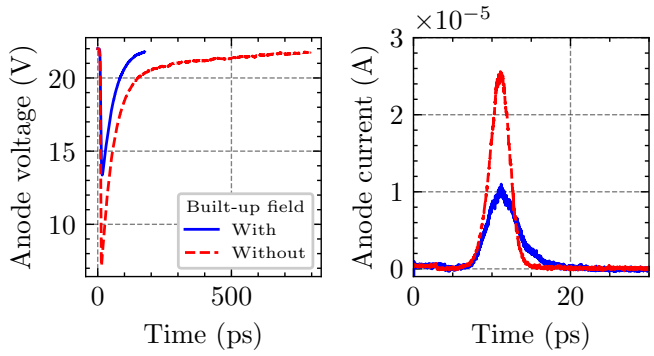

Fig. 7. Voltage and current evolution during a quenching event with and without the avalanche build-up field effect.

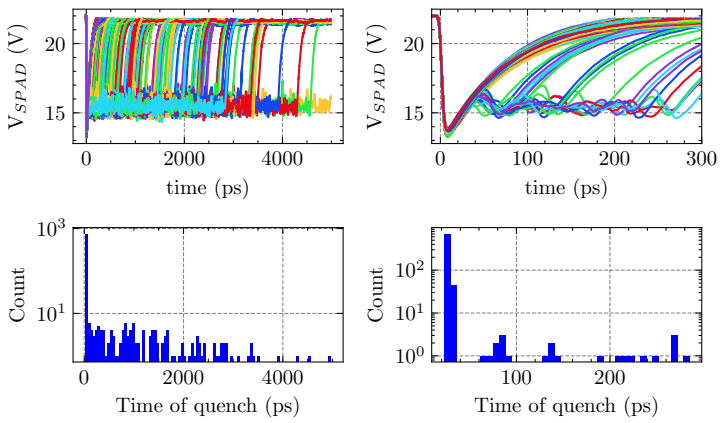

Fig. 8. Voltage evolution during 1000 quenching events (top) and the corresponding quenching time distribution (bottom), extracted from the time when the voltage reaches 99% of its initial value.

Hierarchical Framework for Modeling Electrostatics and Mobility in $Ge_{1-x}Sn_x$/Ge Heterostructures

S. Gangwal*, T.–M. Lu†, S. Chen‡, T. Li‡, M. Povolotskyi§, and D. Vasileska*
*School of Electrical, Computer and Energy Engineering, Arizona State University, Tempe, AZ, USA
†Center for Integrated Nanotechnologies, Sandia National Laboratories, Albuquerque, NM, USA
‡Department of Civil and Environmental Engineering, George Washington University, Washington DC
§Amentum Solutions, Hanover, MD, USA

Group IV alloys present a versatile material system attracting significant interest due to the possibility of electronic structure manipulation in compounds that are isoelectronic with Si. Although Si is extensively used for the development of electronics, its use in photonics is limited due to its indirect bandgap. $Ge_{1-x}Sn_x$ offers the potential to develop a tunable Group-IV semiconductor alloy, with a fundamentally direct bandgap, and compatibility with existing Si infrastructure [1]. Furthermore, the study of Group-IV alloys reveals the possibility of short-range ordering (SRO) which can be used to manipulate electronic bandstructure [2]. Given the wide possibility of its applications, it is important to investigate electrostatics and electrical transport in structures fabricated in the Group-IV alloy system.

This work presents a hierarchical framework that allows the study of hole transport in heterostructures fabricated in the Group-IV alloy system (see Fig. 1). Simulation results are validated with experimentally measured data (conducted at Sandia National Lab) for $Ge_{1-x}Sn_x$ heterostructures with different doping profiles as shown in Fig. 2.

Within this framework, the first step is to calculate the electronic bandstructure and phonon dispersions. The effective masses for holes are determined using first-principles DFT calculations that utilize the Vienna ab initio simulation package (VASP), based on the projector augmented wave method. This work uses the special quasi-random structure (SQS) to represent $Ge_{1-x}Sn_x$ random solid solution, with a simulation cell containing 128 atoms. The folded electronic bandstructure for 8% $Ge_{1-x}Sn_x$ random alloy is shown in Fig. 3.

The next step in the simulation framework is the self–consistent solution of the Schrödinger – Poisson problem for heterostructures with an arbitrary number of layers. Furthermore, the solver uses arbitrary doping profiles, temperature-dependent material parameters, partial ionization of dopants and Fermi–Dirac statistics. The solution of the Schrödinger equation is formulated for a generalized non–diagonal effective mass tensor.

The results of the Schrödinger – Poisson solver are fed into the 2D Monte Carlo transport kernel to investigate hole transport in this heterostructure. The theoretical model includes acoustic, non-polar optical phonon, alloy disorder, and interface roughness scattering mechanisms. Coulomb scattering, relevant at very low temperatures and highly doped samples has not been implemented yet.

Simulation results for the sheet hole density (Fig. 4), and the effective hole mobility (Fig. 5) as a function of temperature agree well with the experimentally measured values. These results demonstrate the modeling capabilities of the solver to simulate electrical properties for a wide range of temperatures. The solver is further improved to facilitate simulations at cryogenic temperatures (2K).

References

[1] S. Gangwal, S. Chen, T. Li, T.-M. Lu, and D. Vasileska, IEEE Journal of Selected Topics in Quantum Electronics, vol. 31, no. 1 (2025).
[2] S. Chen, X. Jin, W. Zhao, and T. Li, Physical Review Materials 8, 043805 (2024).

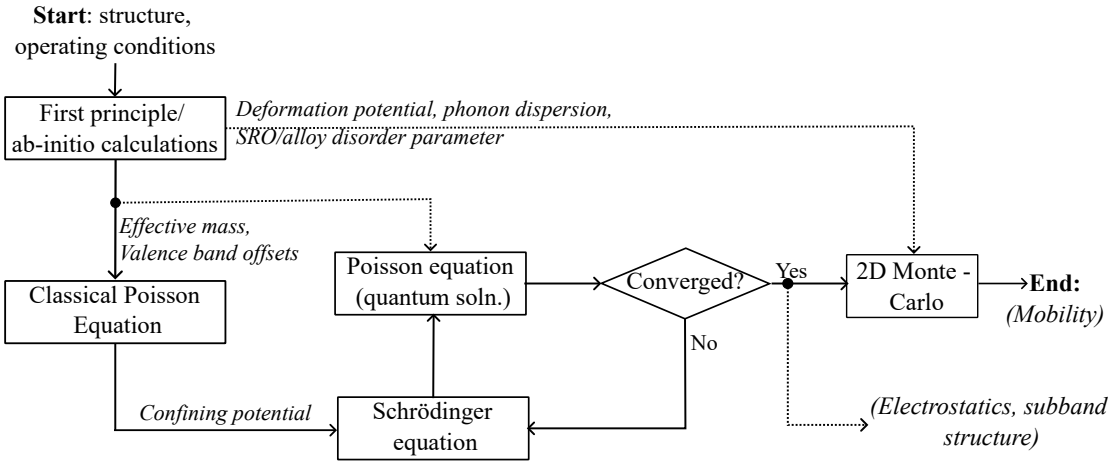

Fig. 1. Flowchart explaining the implemented hierarchical framework.

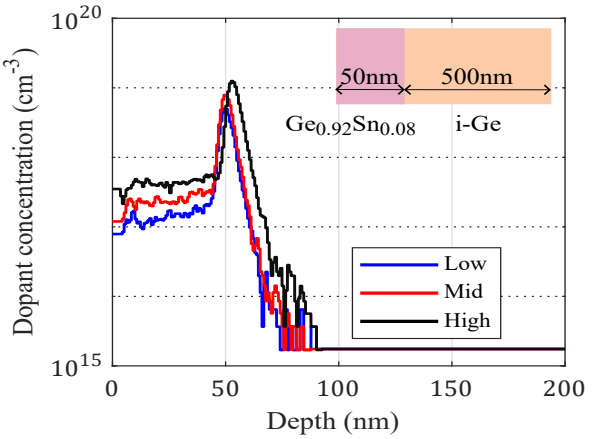

Fig. 2. Doping profiles for different $Ge_{1-x}Sn_x$ /Ge heterostructures.

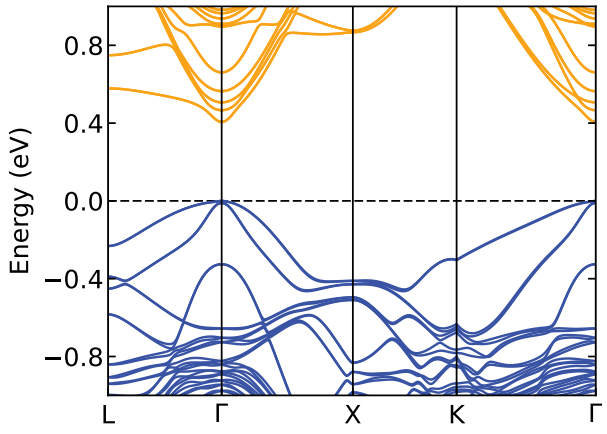

Fig. 3. Folded electronic bandstructure of $Ge_{1-x}Sn_x$ (8% Sn) calculated using 128-atom SQS supercell with DFT.

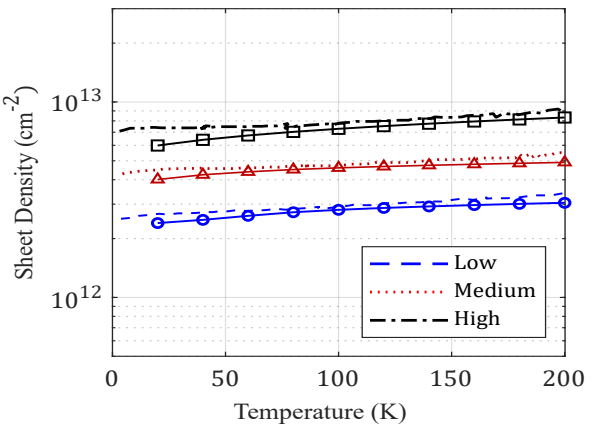

Fig. 4. Sheet carrier densities for the three different doping profiles from Fig. 2. Dashed lines represent the experimentally measured sheet carrier densities and solid lines with symbols represent simulated results.

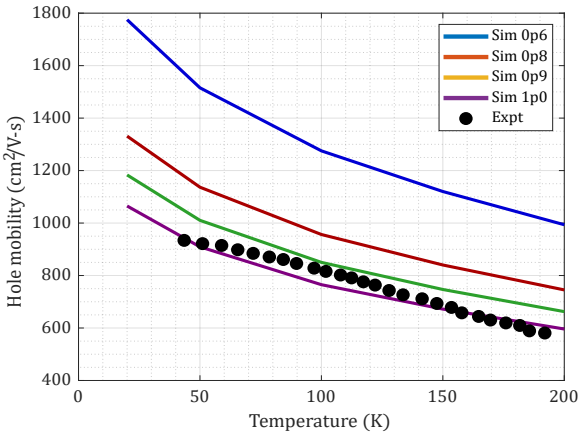

Fig. 5. Temperature variation of the hole mobility in the low-doped GeSn/Ge heterostructure. Solid circles are experimental data and solid lines show simulation results for different alloy disorder scattering parameters.

Friday 9-10:30 Quantum Transport I

Time	Type	Presenter	Title
9:00-9:30	**Invited**	William Frensley	Design Principles for Discrete Models of Nanoelectronic Systems
9:30-9:45	Contributed	M. Pech	Time-resolved Quantum Transport in Open Systems: Phase Versus Real-Space Methods
9:45-10:00	Contributed	Filippo Passeri	Implementation of quantum transmitting boundary method in a 1D electron transport code
10:00-10:15	Contributed	A. Martinez	Scaled 1D NEGF model for 3D Oxide Barriers and Resonant Tunneling Diodes
10:15-10:30	Contributed	Jeongwon Lee, Ryong-Gyu Lee, Hyeonwoo Yeo, and Yong-Hoon Kim	Effects of the internal dipole alignment on the quantum transport properties of two-dimensional halide perovskite devices

Design Principles for Discrete Models of Nanoelectronic Systems

William R. Frensley
University of Texas at Dallas, Richardson, TX

Abstract

This is a summary of insights that the author has accumulated over five decades of work in computationally-oriented semiconductor physics. The principle conclusion is that, for stable devices and systems described by partial-differential (PDE) and integro-differential equations (IDE), there will always exist a robust discrete model that does not exhibit spurious solutions or growing errors, and whose convergence in iterative processes is generally reliable. There are several requirements by which such models may be constructed, but they are largely at odds with widspread practices in this field.

The first requirement is to discretize differential operators in the lowest order. A notorious example is the centered-difference (CD) expression for the gradient, which is guaranteed to create computational problems. The gradient occurs in **k**·**p** Hamiltonians used to define envelope-function models of heterostructures. Use of the CD leads to spurious states showing shorter wavelengths than the true states. If we examine the dispersion relation of the CD expression in comparison to nearest-neighbor differences the reason is apparent. Let $\hat{K}$=$-i\partial_x$, and $\hat{K}_C$, $\hat{K}_L$ and $\hat{K}_R$ be, respectively the centered, left- and right-hand differences in the discrete space. The dispersion relations are compared in Fig. 1.

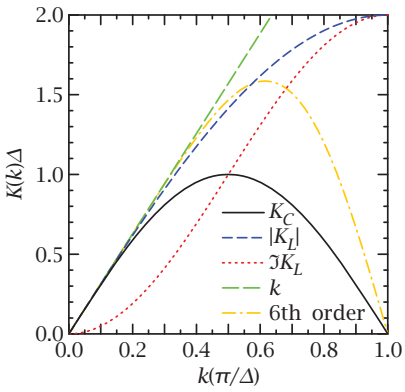

Fig. 1. Dispersion relations for different treatments of $\hat{K}$.

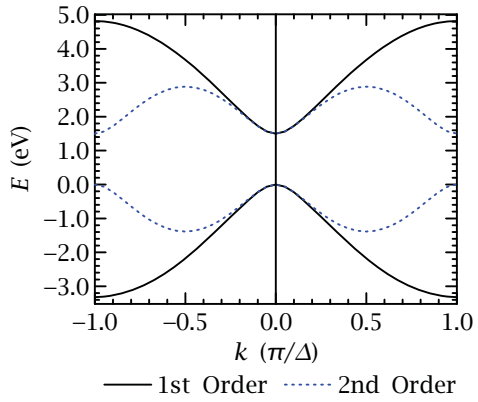

Fig. 2. Simple 2-band structures.

Because the $\hat{K}_{L,R}$ terms appear off the diagonal in the Hamiltonian, the first-order differences appear in adjoint pairs, and enter into the eigenvalue expression as $\hat{K}_L\hat{K}_R = \hat{K}_R\hat{K}_L = \hat{L}$, $\hat{L}$ being the normal three-point discrete Laplacian. Thus it is the magnitude of $\hat{K}_{L,R}$ that determines $E(k)$. This removes the retgrograde regions of $E(k)$, as seen in Fig. 2.

Similarly, the use of $\hat{K}_{L,R}$ in the Dirac Hamiltonian for graphene, $\hat{H} = \hbar v_F(\hat{K}_x\hat{\sigma}_x + \hat{K}_y\hat{\sigma}_y)$, removes the spurious Dirac points that occur when CD is used.

In classical transport formulaations the gradient appears in the drift term, and here stability is achieved by replacing the centered difference with an upwind difference. The Scharfetter-Gummel approach to calculating inter-node currents works because it naturally leads to a bias toward the upstream difference.

A second requirement for the construction of robust models is that the discrete formulation must exactly satisfy the physical conservation laws (or vector identities). This cannot be done if one tries to attach both scalar and vector quantities to the mesh points. The Yee discretization for the Maxwell fields (Fig. 3) provides the prototype for conservative discretizations. We place the mesh points at the center of a cubic lattice, and associate scalar functions s with those points, axial vectors v with

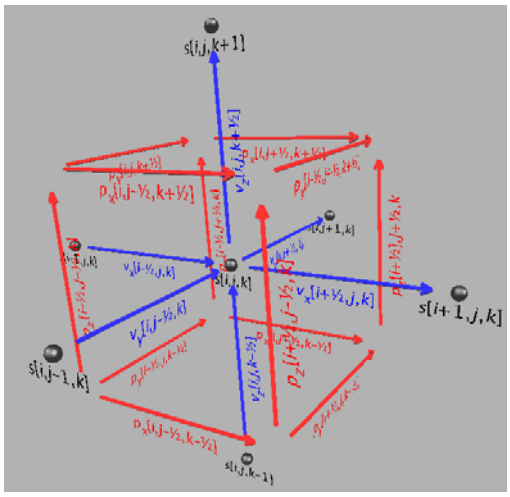

Fig. 3. The Yee discretization.

the centers of the faces, and pseudovectors p with the edges of the cube.

The conservation laws are the conditions that confine the eigenvalues of the discrete difference operator to those regions of the complex plane that assure the stability of the solution. Small violations of them are what permit the odd eigenvalue to creep across the stability boundary and create components which grow with each iteration. Unfortunately, it appears that not all of these constraints can be guaranteed with irregular triangle meshes [1].

Schemes such as the transfer-matrix method for transmission probabilities, which reduce the size of the problem by applying partial analytic soltuitions, are prone to a different mode of failure, observable as an excessive sensitivity to arithmetic roundoff errors. This particularly occurs when highly damped evanescent modes are present, resulting in very ill-conditioned matrices. Such a situation arises in multi-band tight-binding descriptions of heterostructures, where, at any energy, the total number of propagating and evanescent bands must equal the number of basis states.

The solution is to explicitly represent the Hamiltonian as a block-tridiagonal matrix with a number of blocks equal to the number of unit cells in the structure. Then, direct soltution of the resulting inhomogeneous system is entirely stable and accurate. (The recursive Greeen function algorithm is also used, but it is simply a repeated inversion by partitioning of the block matrix.)

In C-family programming languages one can easily represent block-sparse matrices as four-indexed objects, with empty blocks represented by null values in the two-index object. It is then straightforward to code the Crout LU-decomposition algorithm for this data structure, and the LU decomposition preserves the tridiagonal sparsity structure. In particular, the Crout algorithm is carried out exactly as it would be for a full matrix, but knowing that the algorithm will create no "fill" elements outside the tridiagonal blocks allows the code to ignore those elements. Thus, one obtains a useful sparse representation of the dense full Green function.

Possession of a block matrix solver permits one to satisfy the final requirement for robust models: the use of direct rather than iterative matrix soltuion procedures, in a wide variety of physical problems. This is particularly important for implementing electrostatic self-consistency using multi-dimensional Newton iterations. In self-consistent drift-diffusion simulations the fully-coupled Jacobian can be constructed and solved for one-dimensional models and in two spatial dimensions we can easily deal with partially-coupled Jacobians.

At the stage where one has a converged self-consistent solution to an active device using this scheme, it is easy to evaluate the set of "terminal influence functions" for the device, defined by $u_j(\mathbf{r}) = \partial\phi(\mathbf{r})/\partial\mathbf{V_j}$. Then one can use a generalization of the Shockley-Ramo theorem to evaluate the terminal currents by integrating over the volume of the device:

$$I_j = \int \mathbf{J}_c \cdot \nabla u_j \, d^3\mathbf{r},$$

where $\mathbf{J}_c(\mathbf{r})$ is the total conduction current at $\mathbf{r}$. This provides a robust way to evaluate the terminal currents. We will show this by comparing two simulations of a simple bipolar transistor, one using a mesh spacing that resolves the depletion layers, and one with an absurdly coarse mesh. The resulting characteristic curves are indistinguishable.

The use of direct solution is also the key to achieving stability in time-propagation calculations, where some form of implicit time stepping is necessary to guarantee stability. One should use the fully implicit algorithm for dissipative systems and the semi-implicit Crank-Nicholson or Cayley algorithms for Hamiltonian systems.

References

[1] M. Wardetzky, *et al.*, *Discrete Laplace Operators: No Free Lunch*, Eurographics Symposium on Geometry Processing (2007).

Time-resolved Quantum Transport in Open Systems: Phase Versus Real-Space Methods

M. Pech, and D. Schulz
Chair for Communication Technology, TU Dortmund, Dortmund, Germany
e-mail: mathias.pech@tu-dortmund.de

Introduction

Density matrix based simulation methods can offer great insights into the time-resolved quantum charge carrier transport in nanoscale devices with open boundaries such as tunneling diodes, multigate FETs or 2D material based transistors. The most widely applied methods are based on the Wigner Transport Equation (WTE) and have been in use for the analysis of transient carrier transport phenomena for almost 40 years now. Results are consistent with those obtained by using non-equilibrium Greens function (NEGF) methods, though the latter continues being plagued by extreme computational demands in the transient case. More recently, however, our research has shown that studying the density matrix directly in real space can provide several advantages. As such, a comparison of the strengths and limitations of the phase space and real space methods is given here.

Phase space based methods

The preference for the WTE and similar methods such as quantum Liouville-type equations (QLTE) naturally follows from the ease of distinguishing between in- and outgoing waves when setting up the necessary inflow boundary conditions. The wealth of research conducted over the years encompasses the use of a variety of discretization methods, including the finite volume method visualized in Fig. 1, efficient finite element methods and Monte Carlo sampling [1]. Results can be obtained for a variety of devices such as resonant tunneling diodes (Fig. 2) and gate-all-around FETs (Fig. 3). Nevertheless, the conventional discretization methods approach their limits when applying such continuum models onto devices just few atoms in dimension [2] (see Fig. 4).

Real space based methods

While the already mentioned discretization methods can also be applied onto the von Neumann equation, the real space formulation naturally lends itself to the use of atomistic models such as tight-binding Hamiltonians [3]. If inserted into an equation of motion along with the density operator defined in terms of field operators, a density matrix formalism in second quantization can be obtained that retains the atomistic description appropriate for nanoscale devices (Fig 1). Instead of the arbitrarily chosen computational grid used with the WTE, the density matrix elements are defined on the same lattice points as those of the Hamiltonian that is used. The resulting equation of motion can not only reproduce results obtained by the WTE (Fig. 2 and Fig. 3), but also account for otherwise hard to include effects, such as varying lattice spacings [3], nonparabolic band structures or rapid change in device geometry (Fig. 4).

Discussion

The WTE provides an easy to implement and efficient model that is applicable to numerous devices. However, while numerical challenges must still be addressed, the real-space method seems to be the more capable method for bridging the gap between established atomistic methods (NEGF) and time-resolved models (WTE).

References

[1] J. Weinbub and D. K. Ferry, "Recent advances in Wigner function approaches," *Appl. Phys. Rev.*, vol. 5, no. 4, 2018.
[2] M. Luisier, A. Schenk, and W. Fichtner, "Quantum transport in two- and three-dimensional nanoscale transistors," *J. Appl. Phys.*, vol. 100, 2006.
[3] M. Pech, A. Abdi, and D. Schulz, "Density matrix based transport in heterostructure devices utilizing tight-binding approaches," *SISPAD 2024*.

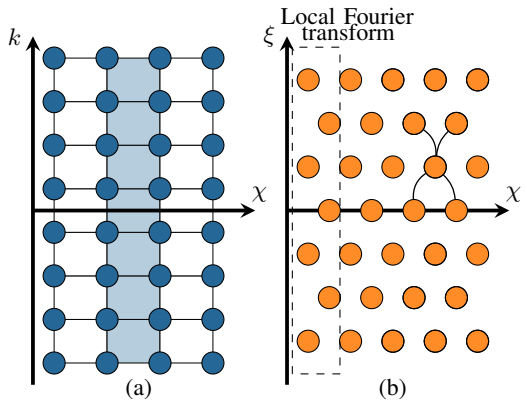

Fig. 1. The schematic representation of the Wigner function discretized by a finite volume scheme is shown in (a) with the blue circles representing the locations at which the Wigner function is defined. By nature of the discretization scheme, the blue shaded area connects the vectors to its left and right and needs to be integrated over, possibly introducing a numerical error in the case of discontinuities. With the real space formulation shown in (b), the density matrix elements are defined on the same lattice sites as the Hamiltonian and discontinuities can easily be taken into account. The resulting grid does not have to be uniform within the device, thus allowing for spatially varying lattice distances as the Fourier transform is only needed at the contacts as is indicated in (b).

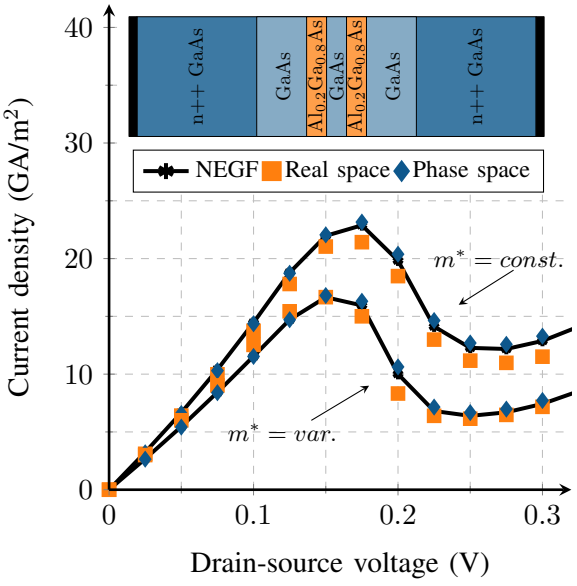

Fig. 2. The current densities from the NEGF method, the WTE solved in phase space and the tight-binding density matrix solved in real space [3] all agree well with each other for the flatband simulation of a GaAs/AlGaAs resonant tunneling diode with spatially constant (upper graphs) and spatially varying (lower graphs) effective masses. Additionally, the higher sparsity of the real space system matrix leads to faster computation times and lower memory requirements.

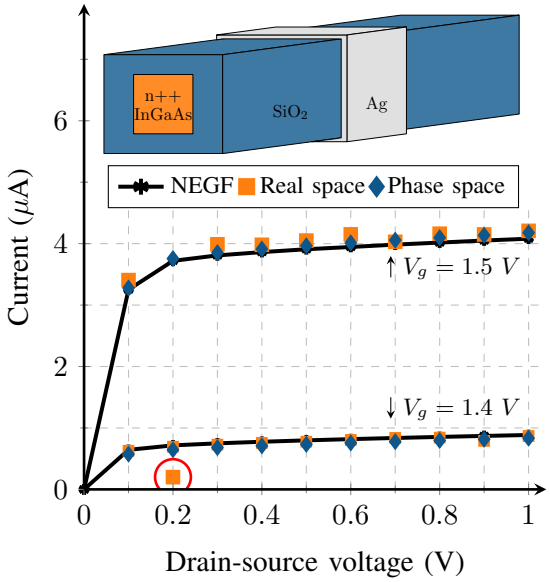

Fig. 3. For gate-all-around FETs the previously mentioned approaches can be combined with the mode-space approximation [2]. The self-consistent results from the real space formulation are in good agreement with the other methods for both gate voltages V_g, except for one bias point where convergence issues are apparent (circled red), requiring further improvements of the boundary conditions.

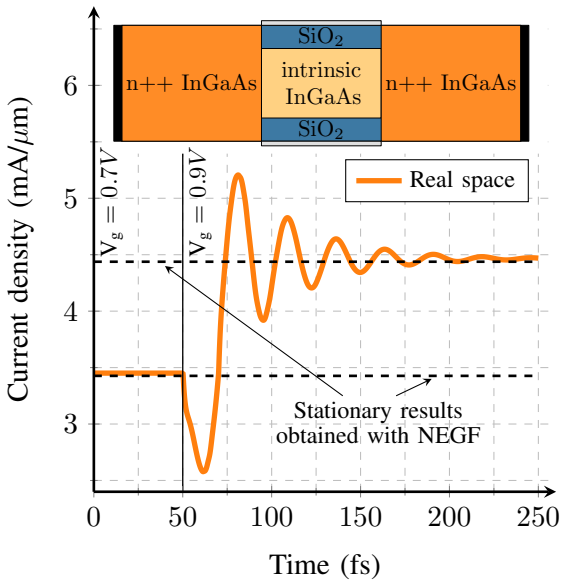

Fig. 4. A constriction in the dual-gate FET leads to strongly varying coupling terms at the interface [2] and coupling between the modes. As such, the real space method is better suited for these problems and no solution using the WTE could be obtained. At $t = 50$ fs, the gate voltage V_g is switched from 0.7 V to 0.9 V. As it can be seen, the self-consistent current density perfectly converges from its initial state to the reference result for $t \to \infty$.

Implementation of quantum transmitting boundary method in a 1D electron transport code

Filippo Passeri*§, Antonio Martinez*, Roberto Grassi† and Karol Kalna*
*Nanoelectronic Devices Computational Group, Dept. of Electronic & Electrical Eng., Swansea University, Swansea, Wales, United Kingdom, §e-mail: 2007991@swansea.ac.uk
†Silvaco France, Montbonnot Saint-Martin, France

INTRODUCTION

Dissipative quantum transport simulations of 3D nanoscale semiconductor devices are computationally expensive, necessitating various approximations [1]. The Quantum Transmitting Boundary Method (QTBM) in conjunction with the Pauli master equation allows efficiently incorporate scattering [2], unlike usually employed Non-Equilibrium Green's Functions (NEGF) formalism. This work presents and benchmarks a preliminary 1D QTBM implementation. This code allows for an efficient and accurate calculation of resonant tunnelling diodes (RTDs) characteristics, and tunnelling in general. The code can be used in combination with other transport methods such as Monte Carlo or drift-diffusion method to accurately model tunnelling.

QUANTUM TRANSMITTING BOUNDARY METHOD

The QTBM solves a weak variational form of the time-independent Schrödinger equation with open boundary conditions on a mesh representing the device. Simple leads enable setting Cauchy boundary conditions on the lead-device interface. The finite element method [3] is then used to derive a system of linear equations, which can be solved to determine the wave functions within the device:

$$(\mathbf{T} + \mathbf{V} + \hat{\mathbf{C}})u = \hat{\mathbf{P}} \tag{1}$$

where $\mathbf{T}$, $\mathbf{V}$, and $\hat{\mathbf{C}}$ are $n \times n$ matrices and n is the amount of nodes in the mesh. The vector u contains the wave function. The elements of the matrix $\mathbf{T}$:

$$T_{j,k} = \frac{\hbar^2}{2m^\star} \int_0^L \partial_x \phi_j(x) \partial_x \phi_k(x) dx \tag{2}$$

represent the kinetic term of the system. Value of the wave function at or between mesh points is represented by a shape function $\phi(x)$.

The effective mass $m^\star$ is assumed not to vary across the device. $\mathbf{V}$ accounts for the total energy at or between points of the mesh as:

$$V_{j,k} = \int_0^L [V(x) - E]\phi_j(x)\phi_k(x) dx \tag{3}$$

$\hat{\mathbf{C}}$ is a non-hermitian matrix with diagonal elements. Eq. (4) in Table I represents contact nodes. For non-contact nodes, $C_{j,j} = P_j = 0$. The boundary value of the wave number k_j is defined by the injection energy E_{inj} and the potential V_j at the node. The $\hat{\mathbf{P}}$ vector, whose elements define the amplitude a_l by Eq. (5) in Table I, represents the injection from the contacts.

RESULTS

To verify accuracy, a numerical square barrier transmission profile is compared to its analytical solution in Fig 1[4]. Its height and width is $U_0 = 0.4\,eV$ and $L_0 = 6\,nm$ respectively. From the transmission profile, the magnitude squared of the first totally transmitted mode a is compared to a damped mode b in Fig. 2. The transmission profile of a double barrier RTD (barrier height $U_1 = 0.3\,eV$ and widths $L_1 = 2\,nm$) is evaluated and shown in Fig. 4. Its resonant modes I, II and III are highlighted and plotted as squares of the magnitude in Fig. 5 alongside the RTD barrier potential. All numerical simulations were set with effective mass of $m^\star = 0.067\,m_0$.

The numerical convergence for the double barrier RTD is shown in Fig. 3. Mesh node resolution M_{res} is defined as nodes per unit nanometre. Wave numbers higher than the mesh's Nyquist frequency (half the mesh node resolution) are distorted from undersampling. If the injected wave number k_{inj} exceeds $\pi\, Mres$, it becomes imaginary in the mesh, resulting in exponential wave functions. This because the wave number is defined by a first order dispersion relation Eq. (6) in Table I. By using an energy dispersion relation beyond the first order, this error can be avoided.

In future work, we will extend the code to treat 3D structures, with the prospect of more efficient device simulations.

ACKNOWLEDGMENT

Funding from the EPSRC CASE Award and Silvaco Group is acknowledged.

REFERENCES

[1] E. Pop, *Energy Dissipation and Transport in Nanoscale Devices*, Nano Res. **3** (2010) 147–169.
[2] P. B. Vyas, M. L. Van de Put, and M. V. Fischetti, *Master-Equation Study of Quantum Transport in Realistic Semiconductor Devices Including Electron-Phonon and Surface-Roughness Scattering*, Phys. Rev. Appl. **13** (2020) 014067.
[3] C. S. Lent and D. J. Kirkner, *The quantum transmitting boundary method*, J. Appl. Phys. **67** (1990) 6353-6359.
[4] D. Vasileska, S. M. Goodnick and G. Klimeck, *Computational Electronics: Semiclassical and Quantum Device Modeling and Simulation* CRC Press (1st ed.) (2010).

$$C_{j,j} = -\frac{\hbar^2}{2m^\star} i k_j \quad (4)$$

$$P_j = -\frac{\hbar^2}{2m^\star} i 2 a_j k_j \quad (5)$$

$$\text{where} \quad k_j = \sqrt{\frac{2m^\star (E_{inj} - V_j)}{\hbar^2}} \quad (6)$$

TABLE I

DEFINITION OF BOUNDARY MATRIX AND VECTOR $\hat{\mathbf{C}}$ AND $\hat{\mathbf{P}}$.

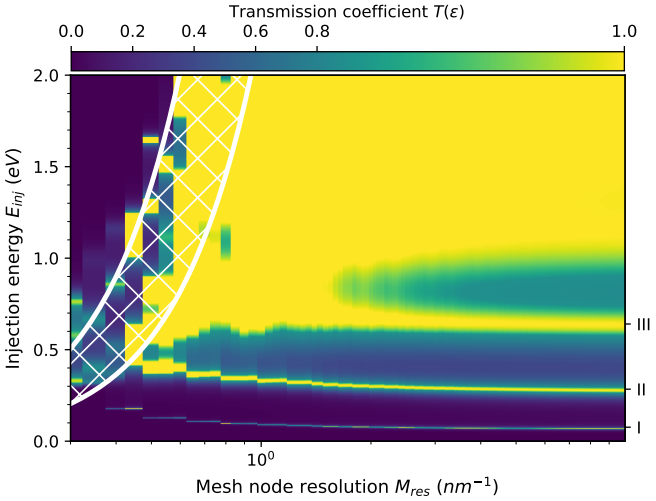

Fig. 3. Convergence evaluation for a double barrier RTD. Transmission coefficient of energies injected at various node resolutions is mapped on to a colour scale. Transmission of wave numbers exceeding the mesh's Nyquist frequency are distorted (hatched area). Evaluations where $k_{inj} > \pi M_{res}$ are exponential and do not transmit (above hatched area).

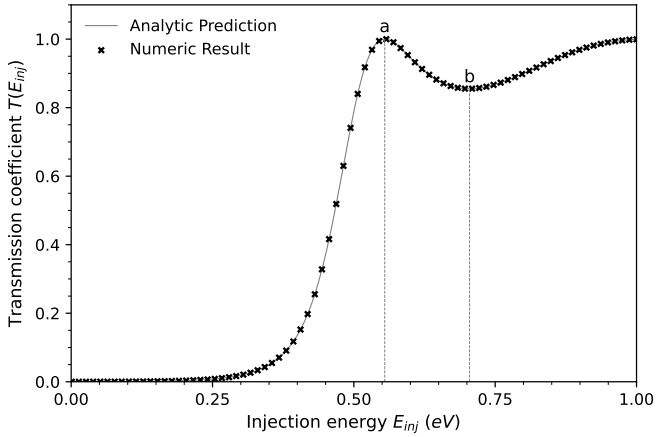

Fig. 1. Transmission coefficient vs energy for a square barrier with width $L_0 = 6\ nm$ and height $U_0 = 0.4\ eV$. A resonant mode and the first damped mode are highlighted as *a* and *b*, respectively.

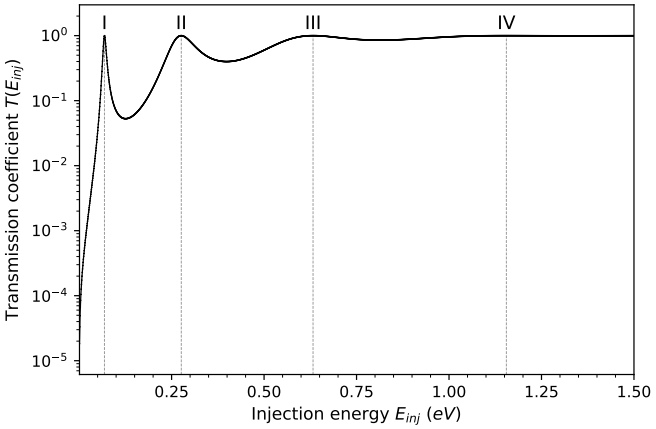

Fig. 4. Transmission coefficient vs energy for a double barrier RTD with height $U_1 = 0.3\,eV$ and equal widths $L_1 = 2\,nm$. The first three resonance peaks E_{inj} are highlighted as I, II, and III, respectively. Mesh resolution used was $50\,nm^{-1}$.

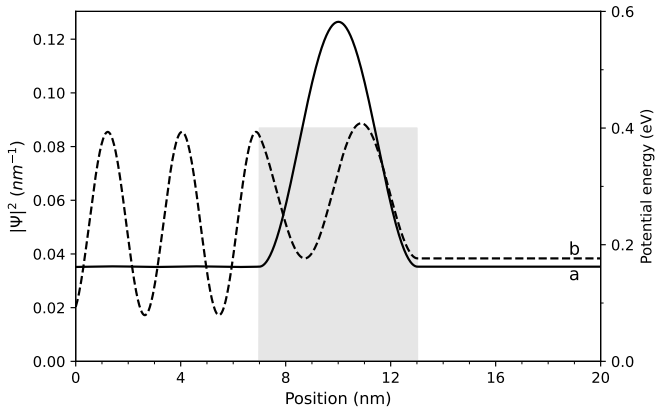

Fig. 2. The square of highlighted mode magnitudes *a* and *b* from Fig. 1. Injected from the left as plane waves, the two modes either fully transmit (a) or are partly reflected, leading to oscillations (b).

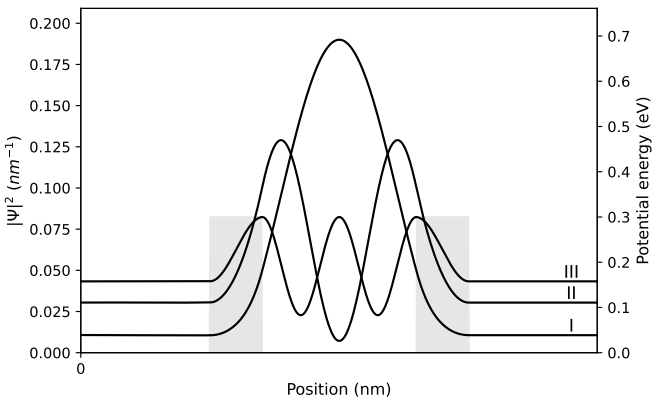

Fig. 5. Square of magnitudes corresponding to the resonant modes from Fig. 4. Note the number of crests increasing per resonant mode akin to the modes of a particle in a box. The potential energy is depicted beneath.

Scaled 1D NEGF model for 3D Oxide Barriers and Resonant Tunneling Diodes

A. Martinez and J. R. Barker*
Dept of Electronics and Electrical Engineering, Swansea University, Bay Campus, Swansea UK
* James Watt School of Engineering, University of Glasgow, Glasgow G12 8LT, UK
e-mail: a.e.martinez@swansea.ac.uk

ABSTRACT

We apply a novel scaling algorithm that projects the full 3D NEGF steady state formalism to a scaled 1D formulation (S-NEGF) that permits the study of the current through realistic 3D structures with appropriate symmetry. Our results for oxide barriers are compared with the well-known Fowler-Nordheim expression and a more general expression using WKB. The impact of trapped holes and the effect of temperature are being considered. The method is also applied to a resonant tunneling diode, where the results agree with previous 3D calculations of R. Lake and S. Datta (L&D) using a more accurate formulation. Using a simple 1D Einstein phonon model we are able to accurately predict the peak-valley current of L&D. The S-NEGF results reproduces 3D NEGF ballistic results for space invariant systems. Scattering is introduced phenomenologically, but it is current conserving.

MODEL AND SIMULATIONS

Wide band gap materials such as SiC used in vertical power MOSFETs operate at high voltages (high fields) that cause stresses in the gate oxide, shortening its lifetime. The estimation of the lifetime is done by projecting high temperature measurements to room temperature. This projection depends on the model and field considered. High fields are beneficial as the channel resistance is reduced and therefore the power dissipation, however this implies shorter lifetimes. The estimation of this trade-off requires accurate identification of tunnelling current and dielectric breakdown mechanisms. Fowler-Nordheim (FN)[1] tunnelling is widely used to describe tunneling in dielectrics at high fields. A more general model is the Sommerfeld-Bethe (SB) model that considers temperature. We compare S-NEGF [2] with the above models. Fig. 1 and fig. 2 show the current at 300K and 450K respectively, assuming $0.4m_e$ (m_e is the electron mass) in the oxide [3]. The formation of hole traps in the oxide are one of the mechanisms contributing to the dielectric breakdown [4]. These traps can form resonant paths to induce breakdown [4]. Fig. 3 shows the current at 450K and m_e=0.65me including two different types of trapped hole (wider and thinner). In addition, at low temperatures and small Fermi energies the FN is not accurate. We have developed an expression (denoted FNG as Fowler-Nordheim Generalized), which agrees with SB and S-NEGF but is analytical. Fig. 4 shows the current, comparing FN, SB and FNG at different Fermi energies, showing the agreement between SB and FNG. Finally, we have used our methodology to reproduce NEGF simulation of a 3D double barrier resonant tunnelling diode presented in [5]. In the ballistic regime the two simulations agree. When considering scattering our results reproduce the peak/valley current quantitatively, by using similar Einstein phonons as in [5].

CONCLUSION

The S-NEGF methodology presented in [2] has been successfully validated by reproducing 3D NEGF results [5] including complex resonances. We conclude that for triangular barriers FN is a good approximation at relative low temperature, however at small Fermi energies it is not accurate. The S-NEGF method is applicable to very general barrier profiles likely to occur in highly stressed dielectrics. Trapped holes can lead to sufficient enhancement of the current to cause dielectric breakdown. Prohibitive “3D NEGF” large computations for realistic structures can now be circumvented using the S-NEGF formalism that uses recursive algorithms.

REFERENCES

[1] A. Sommerfeld and H. Bethe, *Elektronentheorie der Metalle* (Springer - Verlag, 1967).

[2] A. Martinez and J. R. Barker, *A phenomenological method to reduce NEGF simulation from 3D to 1D for lateral translation invariant systems.* IWCN2023, Barcelona.

[3] R. K. Chanana et al, *Fowler–Nordheim hole tunneling in p-SiC/SiO2 structures*, Appl. Phys. Lett. 77, 2560-2562 (2000)

[3] Ricco, M. Ya Azbel, and M. H. Brodsky, *A novel mechanism for tunneling and breakdown in thin SiO2 films*, Phys. Rev. Lett., vol. 51, p. 1795, (1983).

[5] R. Lake and S. Datta, *Nonequilibrium Green's-function method applied to double-barrier resonant-tunneling diodes*, Phys. Rev. B 45, 6670**,** (1992**).**

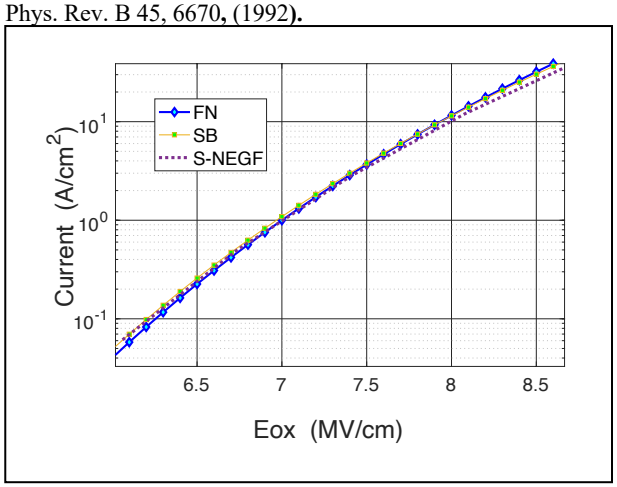

Fig. **1**. Current vs field through an oxide dielectric using different models at 300K; the mass of the carrier in the oxide is 0.40 times the electron mass.

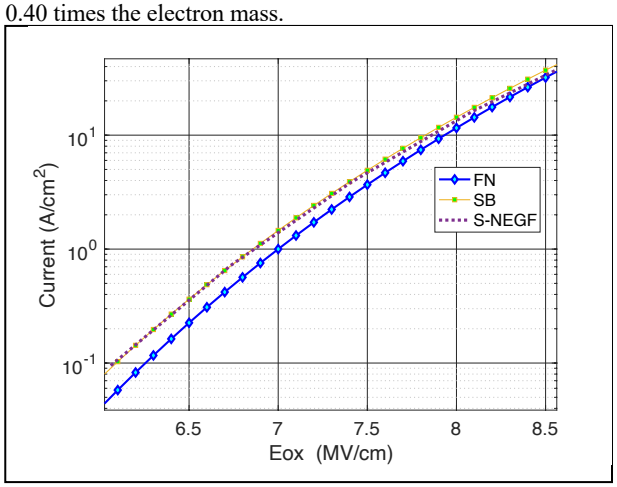

Fig. 2. Current through a triangular barrier at 450K; the mass of the carrier in the oxide is 0.40 times the electron mass.

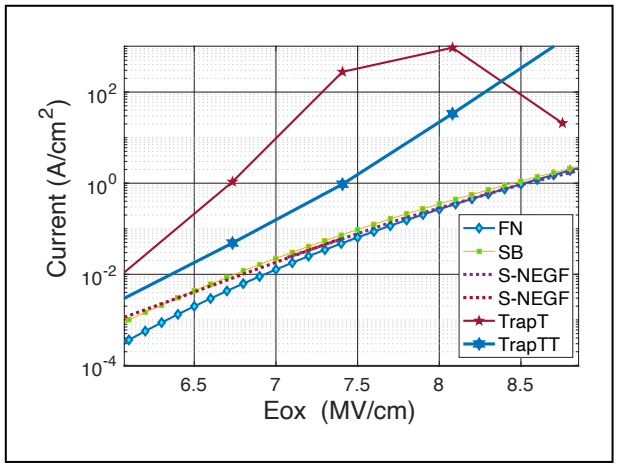

Fig. 3. Current vs Electric field for different models, FN, SB and NEGF with oxide mass of 0.65me and 450K. S-NEGF calculations with a wide Trap width, W and thinner Trap width, T, inside the oxide are also depicted. Note the resonant characteristic for the wide trap current.

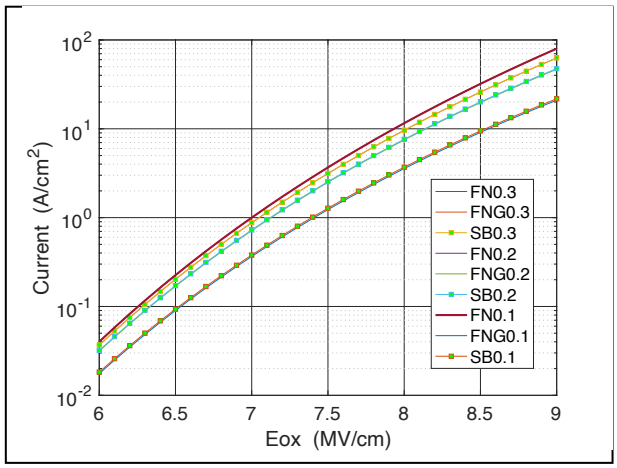

Fig. 4. Currents from FN, FNG and SB for different Fermi energies: 0.3eV, 0.2eV, 0.1eV. The SB and FNG agree as expected. The FN is not accurate for low Fermi energy values.

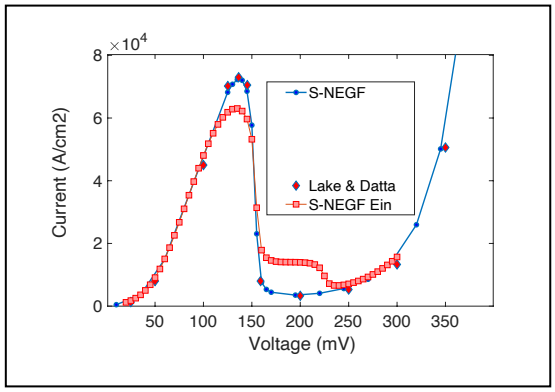

Fig. 5. Current vs voltage for the resonant tunnelling diode of ref. 4 (Lake & Datta). S-NEGF and S-NEGF Ein (Einstein phonons) denoted the calculations of this work.

Effects of the internal dipole alignment on the quantum transport properties of two-dimensional halide perovskite devices

Jeongwon Lee, Ryong-Gyu Lee, Hyeonwoo Yeo, and Yong-Hoon Kim*
School of Electrical Engineering, Korea Advanced Institute of Science and Technology (KAIST), 291 Daehak-ro, Daejeon, 34141, Korea
e-mail: jeongwon.lee@kaist.ac.kr

INTRODUCTION

Ferroelectricity was suggested as a mechanism that contributes to the excellent optoelectronic properties of halide perovskites such as high light absorption rates, long charge carrier diffusion lengths, and strong photoluminescence [1-3]. However, research on the ferroelectricity of halide perovskites has been scarce, and an atomistic understanding remains elusive. In this study, carrying out multi-space constrained-search density functional theory (MS-DFT) calculations [4] for the junction models based on two-dimensional (2D) $MAPbBr_3$, we study effects of the internal dipole alignment on finite-bias quantum transport properties.

COMPUTATIONAL DETAILS

All calculations were performed within SIESTA package, in which MS-DFT is implemented, to describe equilibrium and finite bias non-equilibrium conditions. We used the generalized gradient approximation PBEsol, double ζ-plus-polarization-level numerical atomic orbital basis sets, and the Troullier-Martins type norm-conserving pseudopotentials. The k-point mesh was 3 x 3 x 1 Monkhorst-Pack grid.

RESULT

Here, we consider two different dipole alignments of MA, parallel (P) configurations (4 MA dipoles in the unit cell are aligned in the same direction) and antiparallel (AP) configurations (4 MA dipoles adopt alternating orientations) as shown in Fig. 1. To investigate the influence of dipole moment configurations on transport, we performed MS-DFT calculation. We present current-voltage (I-V) characteristics of each case and analyze their electronic structures. In Fig. 2, the P model exhibits asymmetric transport behavior, whereas the AP model shows no measurable current. To explain this disparity, we obtained projected local density of states and energy-resolved current in Fig. 3. Due to the higher energy level of valence band maximum (VBM) states in the P case, these states (marked by left triangles) in the P case are positioned closer to the bias window than those in the AP case under both bias conditions. Therefore, the VBM states of the P case come into the bias window at +0.8 V compared to those in the AP configuration. This early entry of HOMO states facilitates the flow of charge carriers and contributes to the observed increase in current. Since MA dipoles have the same (opposite) orientation in the P (AP) case, MA alignments enhance (offset) their internal electric field. In Fig. 4, dipole effects can be seen by potential and density of states (DOS). The red box in the left panel indicates that the gradient of Hartree potential within the MA layer, indicating that the MA alignments induce an internal electric field. It results in an upward shift of 0.11 eV in the VBM states for the P-up configuration compared to the AP case, as shown in the right panel of Fig. 4. This shift plays a crucial role in the asymmetric transport behavior, and it can be evidence of ferroelectricity.

REFERENCES

[1] Fan, Z., et al., *Ferroelectricity of $CH_3NH_3PbI_3$ Perovskite.* J. Phys. Chem. Lett. **6**(7), 1155-61 (2015).
[2] Garten, L.M., et al., *The existence and impact of persistent ferroelectric domains in $MAPbI_3$.* Sci. Adv. **5**(1), eaas9311 (2019).
[3] Rakita, Y., et al., *Tetragonal $CH_3NH_3PbI_3$ is ferroelectric.* Proc. Natl. Acad. Sci. U S A. **114**(28), E5504-E5512 (2017).
[4] Lee, J., H.S. Kim, and Y.H. Kim, *Multi-Space Excitation as an Alternative to the Landauer Picture for Nonequilibrium Quantum Transport.* Adv. Sci. **7**(16), 2001038 (2020).

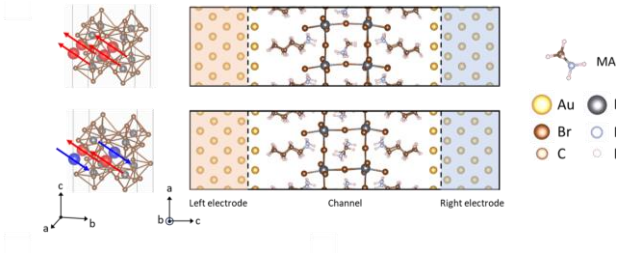

Fig 1. Structures of 2D MAPbBr3 with two different dipole alignment

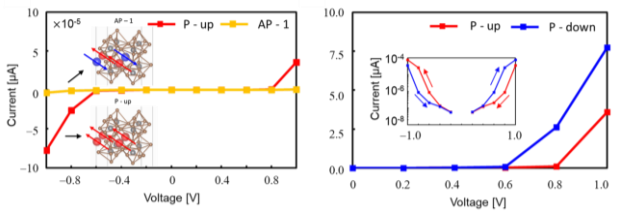

Fig 2. I-V characteristics depending on the dipole moment directions.

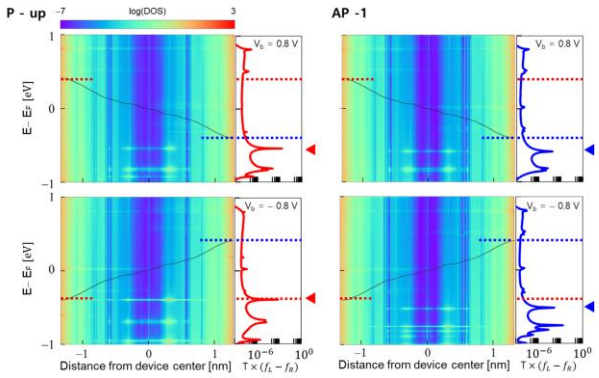

Fig 3. Non-equilibrium projected local density of states and energy-resolved current of P-up and AP-1

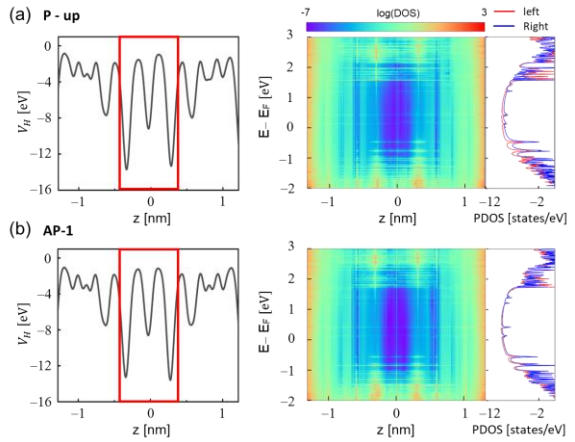

Fig 4. Equilibrium Hartree potential, DOS of (a) P-up and (b) AP-1.

Friday 11:00-12:30 Quantum Transport II

Time	Type	Presenter	Title
11:00-11:15	Contributed	Massimo Macucci	Phase noise model for qubit control
11:15-11:30	Contributed	Andrzej Kolek	Interband tunneling in a superlattice absorber
11:30-11:45	Contributed	Juan Pedro Mendez Granado	Predictive quantum transport simulations for advanced nano-scale FET-based sensors
11:45-12:00	Contributed	Juan José Seoane	Exploring quantum technologies through THz polaritonic semiconductor devices

Phase noise model for qubit control

A. Barsotti, P. Marconcini, G. Procissi, and M. Macucci
Dipartimento di Ingegneria dell'Informazione, Università di Pisa, via Caruso 16 56122 Pisa, Italy
e-mail: massimo.macucci@unipi.it

INTRODUCTION

The evolution of superconducting qubits is controlled by means of properly shaped microwave pulses. Such pulses are unavoidably affected by phase noise, which is the consequence of instabilities of the reference oscillators, resulting from various sources of nonidealities. We present an improved approach to the generation of phase noise sequences, that can be used for the numerical simulation of the time evolution of the state of a qubit, in order to analyze and understand the effect of phase noise on the achievable fidelity of quantum gates.

NUMERICAL METHOD

We have developed the numerical procedure illustrated in Fig. 1 to generate sequences of baseband phase noise values with arbitrarily shaped power spectral density (PSD). We start with the generation of a sequence of pseudorandom noise values with a gaussian amplitude distribution and a white spectrum. We synthesize the finite impulse response of a FIR filter, characterized by the desired frequency behavior (by means of an inverse Fourier transform). Then, the white gaussian noise sequence is convolved with the impulse response to obtain the desired phase noise. To speed up the evaluation of the convolution, we transform it into a multiplication in the frequency domain, exploiting the FFT (Fast Fourier Transform) for the conversion from the time to the frequency domain and vice versa. A proper zero-padding is performed to obtain vector lengths that are a power of 2.

RESULTS AND DISCUSSION

In Fig. 2 we report the PSDs for flicker-like phase noise with different corner frequencies, while in Fig. 3 and Fig. 4 we show the phase noise behavior in the time domain (we see that within the duration of a typical experiment the lowest frequency components give a limited contribution, while they are relevant over the longer time interval). To understand the contribution of single frequency components we use gaussian narrow-band filters. In Figs. 5 and 6, we report the impulse response and the frequency response (respectively) for such filters. The effect of control-signal nonidealities on qubit coherence and on error rates has been discussed in the literature by various authors, in particular Ball and Biercuk [1] have performed a Hamiltonian analysis based on the expressions derived by Green et al. [2]. While in Ref. [1] they conclude that higher frequency components of phase noise give the largest contribution, we find, with Qiskit-Dynamics simulation in which we exploit our phase noise sequences, that a well defined spectral interval contributes, depending on the duration of the experiment and coupling with the qubit.

ACKNOWLEDGMENT

Partial support by the Italian Ministry of the University and Research (MUR), in the framework of the CrossLab and the FoReLab projects (Departments of Excellence), is acknowledged. Financial support is also acknowledged from the European Union, NRRP, Mission 4 Comp. 2 Investment N. 1.4, CUP N. I53C22000690001, through the National Centre for HPC, Big Data and Quantum Computing ("Spoke 10: Quantum Computing"). This work was supported also by the U.S. Department of Energy, Office of Science, National Quantum Information Science Research Centers, SQMS under Contract No. DEAC02-07CH11359.

REFERENCES

[1] H. Ball, W. Oliver and M. Biercuk, npj Quantum Information **2**, 16033, (2016), doi:10.1038/npjqi.2016.33

[2] T. J. Green, J. Sastrawan, H. Uys, M. J. Biercuk, New J. Phys. vol. 15, 905004 (2013) doi:10.1088/1367-2630/15/9/095004

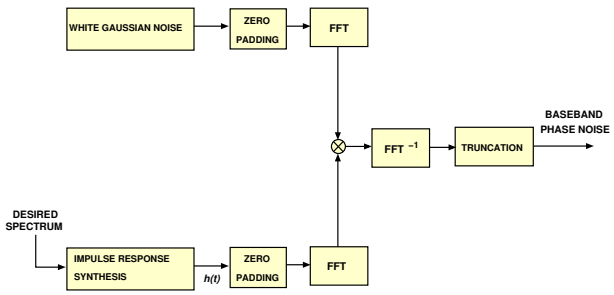

Fig. 1. Block diagram of the numerical procedure to generate baseband phase noise.

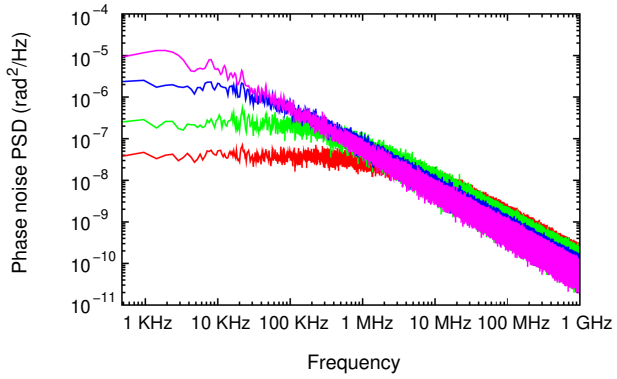

Fig. 2. Flicker phase noise PSD for different corner frequencies: 1.59 kHz (magenta), 15.9 kHz (blue), 159 kHz (green) and 1.59 MHz (red).

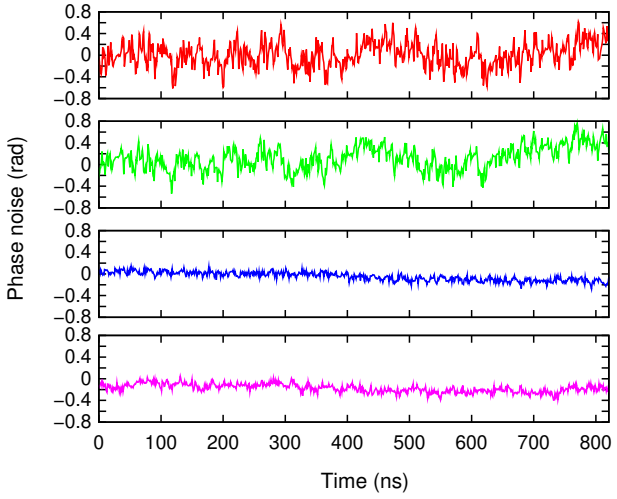

Fig. 3. Phase noise as a function of time, over an interval equal to the duration of the experiment, 820 ns.

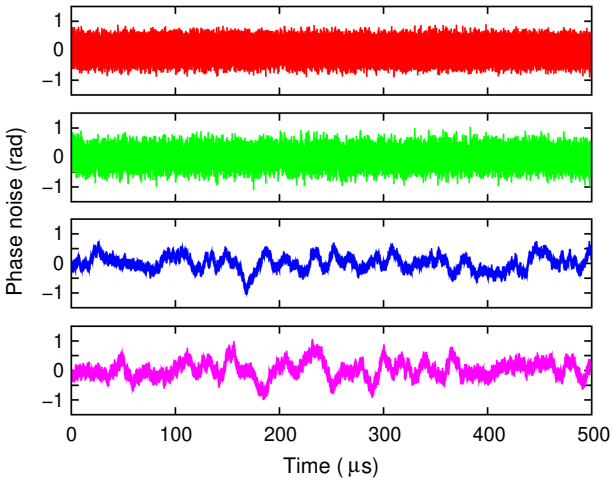

Fig. 4. Phase noise as a function of time, over an interval of 500 μs.

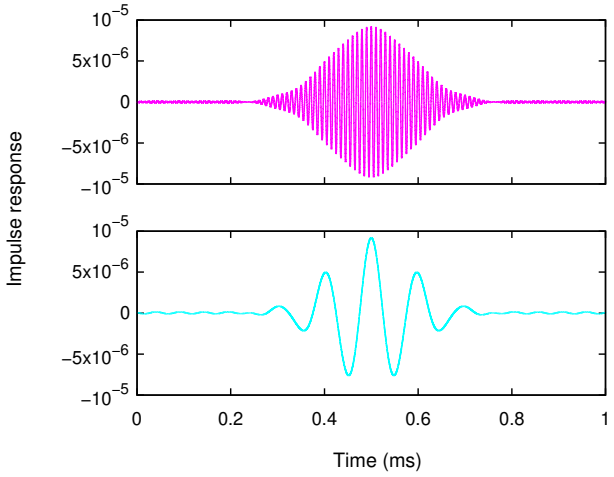

Fig. 5. Impulse response for gaussian filters with the same bandwidth (3 kHz), but different center frequencies: 10 kHz (cyan) and 100 kHz (magenta).

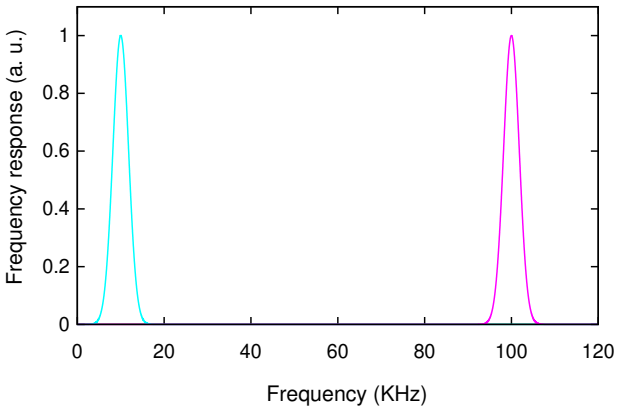

Fig. 6. Frequency response of two gaussian filters centered at 10 kHz (cyan) and at 100 kHz (magenta).

Interband tunneling in a superlattice absorber

Andrzej Kolek
Department of Electronics Fundamentals, Rzeszów University of Technology, Rzeszów, Poland
e-mail: akoleknd@prz.edu.pl

INTRODUCTION

Superlattice (SL) photodiodes are now widely used to detect radiation, especially in the infrared region. However, in many cases their theoretical description merely adopt 'homogeneous' models [1]. In particular, the band-to-band (btb) tunneling is usually described with the Kane formula which was derived for a homojunction device [2]. This is because the vertical transport under high electric fields is almost unexplored for SL devices. In this paper the nonequilibrium Greens function (NEGF) method is used to study btb tunneling in SL absorber, with the aim of verifying the justification for the approaches that use 'homogeneous' models.

MODEL & METHOD

As the aim of the work is of qualitative rather than quantitative nature, the device is modelled with the two-band Hamiltonian

$$H = \begin{bmatrix} E_c(z,k) & \hbar\sqrt{\frac{E_p}{2m_0}}\frac{d}{dz} \\ \hbar\sqrt{\frac{E_p}{2m_0}}\frac{d}{dz} & E_\upsilon(z,k) \end{bmatrix}, \quad (1)$$

where z is the growth direction, k is the in-plane momentum norm, and $E_i(z, k) = E_i(z) \pm \hbar^2k^2/2m_{\|i}$, $i = c, \upsilon$, are k-dependent band edges. Calculations are made for a toy p-i-n diode made of 9 SL periods terminated with bulk n-InAs and p-GaSb leads. The leads, and adjacent to them parts of the SL region are doped to $n = p = 1\times10^{18}$ cm^{-3}. The band diagram of the device is shown in Fig. 1.

In the NEGF formalism the scatterings due to optical and acoustic phonons, and rough interfaces were included. The equations of the formalism, completed by the Poisson equation, were solved self-consistently (Born approximation).

RESULTS & CONCLUSIONS

Results of the simulations are shown in Figs. 1-4. Fig.1 illustrates, that at sufficiently high electric field F, the minibands break into the ladder of localized Wannier-Stark (WS) states [3]. They act as resonant centers for the btb tunneling process; each time the WS state in the conduction band (CB) aligns energetically with the WS state in the valence band (VB), the btb current is enhanced. The resulting, oscillatory structure of current-field characteristic is shown in Fig. 2. Similar effects were observed in real devices made of high-quality materials, in which defect-assisted tunneling did not hide the direct btb tunneling current, e.g. in ref. [4]. This means that the formulas derived for btb tunneling in a bulk material can hardly be used for SL materials. Further analyses performed on the simulation data, and illustrated in Fig. 3 and Fig. 4 allow to propose a new analytic formula for btb tunneling current in SL materials [5]. Namely,

$$J_{BTB} = N\frac{em_{\|,h}\delta E}{\pi\hbar^2 t_{tun}(m_F, \Delta E_F)}, \quad (2)$$

where N is the number of btb transitions (≅ SL periods), δE is the energetic width of tunneling current, t_{tun} is the (field-dependent) tunneling time of the dominant btb transition which spans m_F SL periods, and ΔE_F is the mismatch of WS energies.

ACKNOWLEDGMENT

This research was supported by the National Science Centre, Poland, project No. UMO-2020/35 /B/ST7/01830 (OPUS-19).

REFERENCES

[1] Delmas, M., Rodriguez, J. B., Rossignol, R., Licht, A. S., Giard, E., Ribet-Mohamed, I. & Christol, P. *Identification of limiting mechanism in GaSb-rich superlattice midwave infrared detector*. J. Appl. Phys. **119**, 174503 (2016).
[2] Pan, A., Chui, C., *Modeling direct interband tunneling. I. Bulk semiconductors*, J. Appl. Phys. **116**, 054508 (2014).
[3] Wacker, A. *Semiconductor superlattices: a model system for nonlinear transport*. Physics Reports **357**, 1 (2002).
[4] Kazemi, A., Myers, S., Taghipour, Z., Mathews, S., Schuler-Sandy, T., Lee, S. & Krishna, S. *Mid-wavelength infrared unipolar nBp superlattice photodetector*. Infrared Physics & Technology **88**, 114 (2018).
[5] Kolek, A. *Interband Tunneling in a Type-II Broken-gap Superlattice*, Phys. Rev. Applied **19,** 024059 (2023).

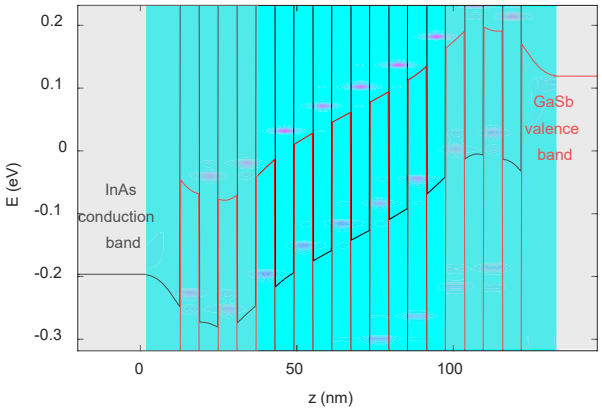

Fig. **1**. Band diagram of the p-i-n SL device with 6 nm InAs/6 nm GaSb period. Doped regions are shadowed. The undoped central part resembles the absorber in a real photodiode. The color map shows local density of states for the vanishing in-plane momentum, $k = 0$, calculated with the NEGF method.

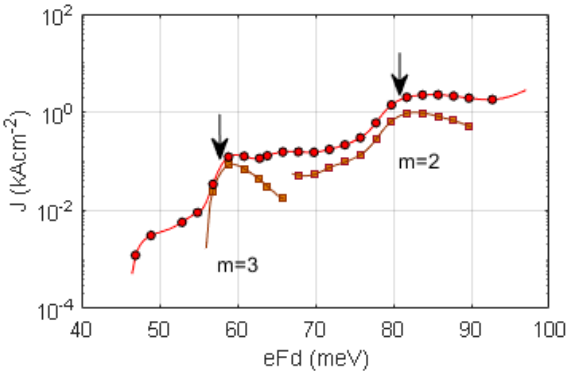

Fig. 2. Current-filed (I-V) characteristic (calculated). Arrows indicate the positions of the resonances, determined by the equation: $eF(m + 1/2)d = \Delta E_{SL}$ (d is the SL period, ΔE_{SL} is the C1-H1 bandgap and $m + 1/2$ is the number of SL periods spanned by the tunneling process) for $m = 2$ and $m = 3$. Series correspond to: circles - total current, squares/crosses - individual btb transitions between Wannier-Stark states.

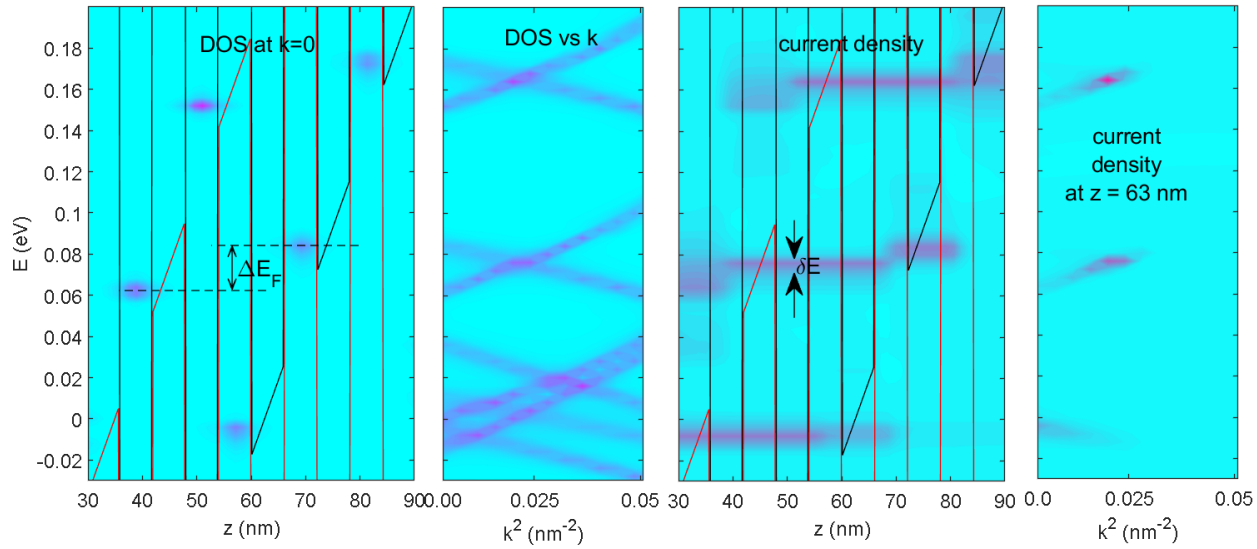

Fig. 3. (a) Band diagram and DOS for vanishing in-plane momentum $k = 0$ in the central part of the absorber under high electric field. Minibands are broken into WS states. ΔE_F is the (field dependent) mismatch between WS states involved in the interband tunneling transition (b) DOS as function of in plane momentum k; lines show hole and electron subbands formed by the WS states in C1 and H1 minibands. (c) Position resolved energetic spectrum of the current density; δE is energy width of the current strip (d) Momentum-energy resolved current density at $z = 63$ nm; current flows at k's for which electron and hole WS subbands cross.

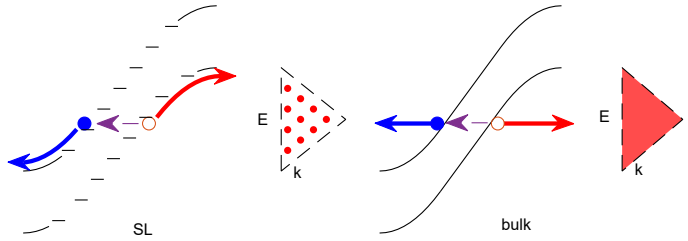

Fig. 4. Diagrams illustrating fundamental differences in btb tunneling current in bulk and SL devices in real and energy-momentum space: (i) the continuous vs discrete grid of energy-momentum pairs available for btb tunneling transitions (ii) ballistic vs inelastic extraction of created e-h pairs, which in SL is the LO-phonon dominated WS hopping within minibands [3].

Predictive quantum transport simulations for advanced nano-scale FET-based sensors

J.P. Mendez and D. Mamaluy
Cognitive & Emerging Computing, Sandia National Laboratories, Albuquerque, USA
e-mail: jpmende@sandia.gov

Sensors are indispensable components in our lives nowadays. Among all existing types, Field Effect Transistor (FET)-based sensors offer significant advantages for detecting: label-free, real-time, small in size and weight, and integration on a chip. FET-based sensors have been widely reported for various applications, including the SARS-CoV-2 virus, nucleic acids such as DNA or RNA, prostate-specific antigen (PSA), etc. In addition, novel materials, structures or nano-scale devices can unlock new opportunities in sensing applications by exploiting novel quantum-mechanical effects.

In particular, recent advances in Atomic Precision Advanced Manufacturing (APAM) have enabled the creation of novel quasi-2D highly-doped regions (a.k.a. δ-layers) in a semiconductor with single-atom precision and high conductivity (Fig.1a). Previous experimental and computational work has demonstrated that these structures possess exotic quantum-mechanical properties. Among all them, it has been observed that the conduction band of δ-layers is strongly quantized, resulting in quasi-discrete states in the low-energy conduction band. These quantized conduction subbands vanishes as the thickness of the δ layers increases.

In this talk, we will present a predictive open-system quantum transport framework to investigate the use of APAM devices as FET-based sensor (Fig. 1b) by exploiting the quantized conduction band in δ layers.

Our quantum transport framework[1,2,3] relies on a self-consistent solution of Poisson-open system Schrödinger equation in the effective mass approximation and the Non-Equilibrium Green's Function (NEGF) formalism. To reduce the computational cost of these intensive calculations, we utilize the Contact Block Reduction (CBR) method, which is an efficient method to calculate the electronic transmission function of an arbitrarily shaped, multi-terminal open device and scales linearly with the size of the system.

Fig. 2 shows the study of the sensitivity of the device when a positive/negative charge is present near the tunnel junction. The sensitivity S, defined as the ratio of the change in current caused by the presence of the single charge to the nominal current. Fig. 3 shows the study of how far these devices might sense a single charge at 4 and 300K. Fig. 4 shows the sensitivity of the device as a function of the thickness of the δ-layer.

By employing predictive simulations, we have demonstrated the extreme sensitivity of APAM FET devices for charge sensing in the low-concentration limit, i.e., for detecting single charges. Our results show that APAM FET-based sensors achieve superior sensitivity, with a maximum sensitivity is around 6.9 at 4K and 0.86 at 300K for a single negative charge –significantly higher than the theoretical upper bound of sensitivity for TFET-based sensors, which is typically S=6e-3 for low charge concentrations[4]. Additionally, we have shown that simulations can create opportunities to explore advanced nanoscale sensors by leveraging exotic quantum-mechanical effects.

SNL is managed and operated by NTESS under DOE NNSA contract DE-NA0003525.

REFERENCES

[1] H. R. Khan, et al., 3D NEGF quantum transport simulator for modeling ballistic transport in nano FinFETs, Journal of Physics: Conference Series 54, 784–796 (2007).
[2] D. Mamaluy, and X. Gao, The fundamental downscaling limit of field effect transistors, Appl. Phys. Lett. 106, 193503 (2015).
[3] X. Gao, et al., Efficient self-consistent quantum transport simulator for quantum devices, Appl. Phys. 115, 133707 (2014).
[4] D. Sarkar, et al., Proposal for tunnel-field-effect-transistor as ultra-sensitive and label-free biosensors, Appl. Phys. Lett., 100, 143108 (2012).

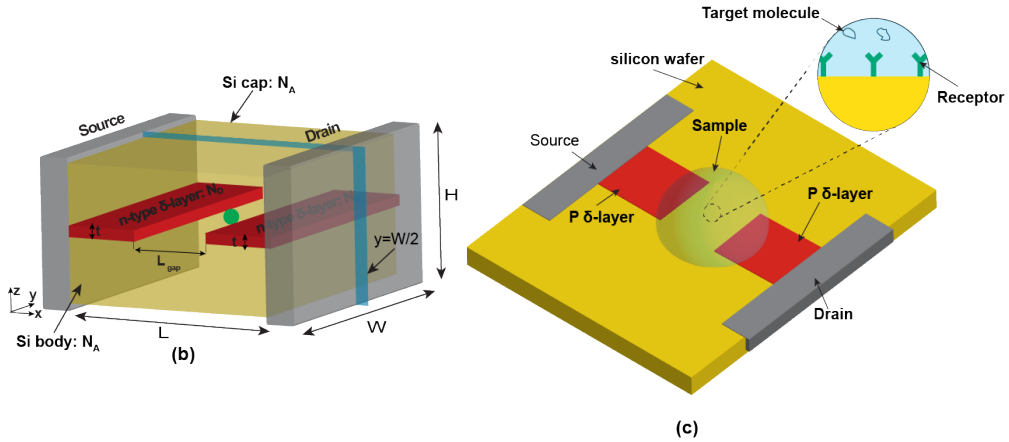

Fig. **1**. (a) Schematic of the δ-layer tunnel junction, consisting of two very thin, highly n-type-doped layers separated by an intrinsic semiconductor gap and embedded in silicon. (b) Example of an APAM FET-based sensor for biological application.

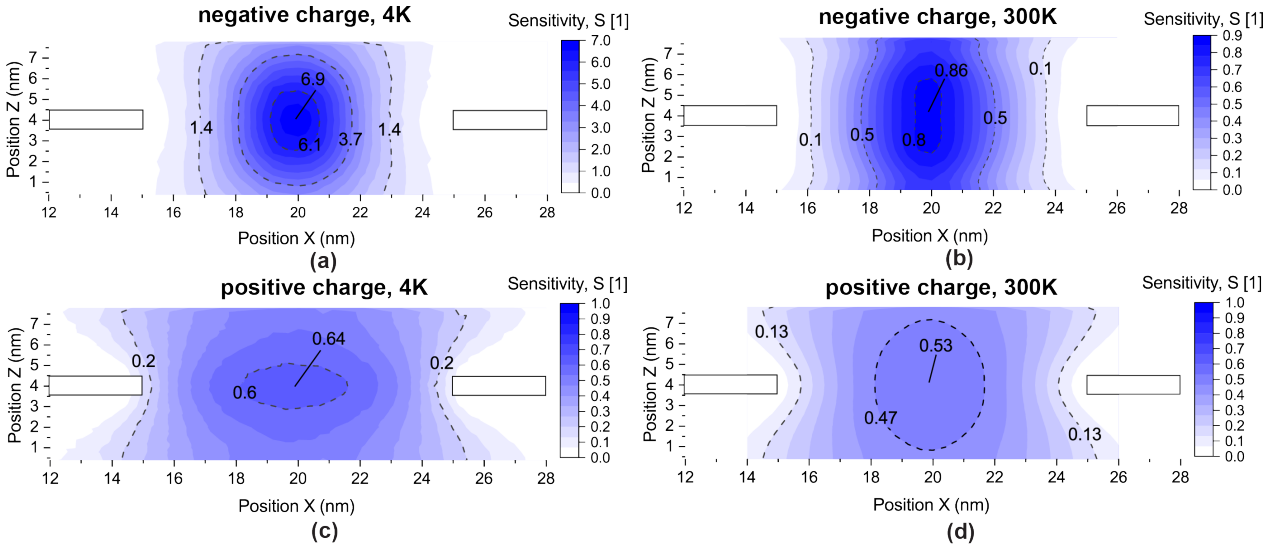

Fig. **2**. Sensitivity of the device due to the presence of a single negative charge located at different positions (x,z) in the middle plane of the device (y=W/2), see Fig. 1a, at 4K in (a) and at 300K in (b), as well as for a single positive charge at 4K in (c) and at 300K in (d). A voltage of 1mV is applied between the source and drain. The device dimensions are: L=40nm, W=15nm, H=8nm, and t=1nm.

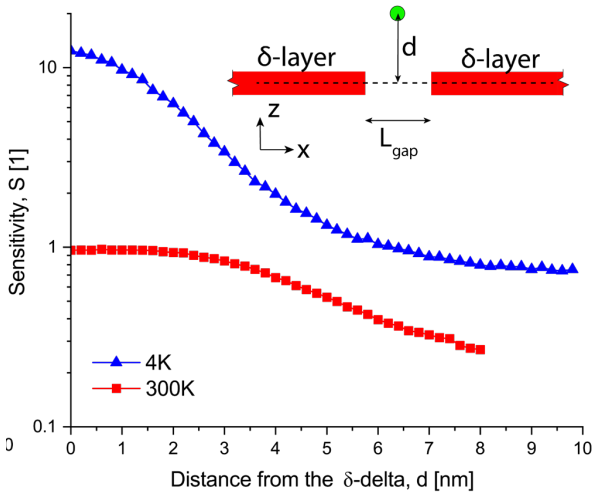

Fig. **3**. Sensitivity of the device to the presence of a single negative charge located at different distances d from the δ-layers, along the line (x, y, z)=(L/2, W/2, d), at both temperatures 4 and 300K. The green sphere represents an electrical charge. A voltage of 1mV is applied between the source and drain.

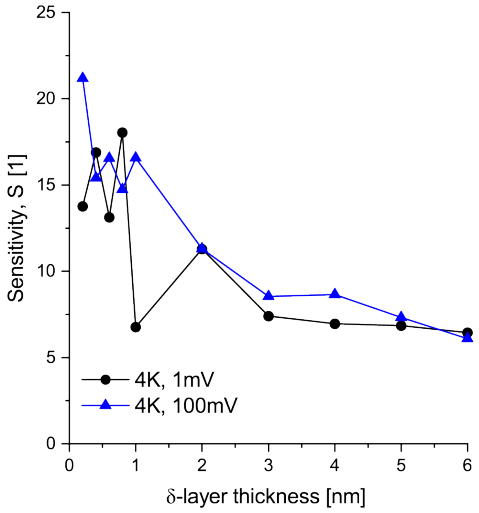

Fig. **4**. Sensitivity vs. δ-layer thickness study when a single negative charge is placed between the δ-layers.

Exploring quantum technologies through THz polaritonic semiconductor devices

Juan José Seoane, Abdelilah Benali, Xavier Cartoixà, Xavier Oriols
Universitat Autònoma de Barcelona, 08193 Bellaterra SPAIN

e-mail: JuanJose.Seoane@uab.cat

INTRODUCTION

The understanding of the interaction between electrons and electromagnetic fields has been a constant topic of research in electronics. The electrons ("matter") and the electromagnetic field ("light") are usually treated as independent yet interacting physical quantities. This independence is well suited in the modeling of most electronic devices (within the so-called weak light-matter interaction regimes). However, when light and matter reach the strong couple regime, they can no longer be treated as independent entities, but as an hybridized light-matter state named polariton [1].

Polaritons appear in a wide variety of platforms. For example they occur when electrons are confined within a "matter" cavity (or a quantum well) and THz radiation is confined within an "optical" cavity (or a resonant THz cavity)[2]. In this work, we focus on the so-called intersubband polaritons [3].

Although the quantum optics community has developed a robust understanding of such phenomenology and some experimental prototypes of polaritons operating at room temperature have been documented [4], the electronics community has largely overlooked the device possibilities of these phenomena.

MODEL

In this work, we explore how several electrons (each insde a double barrier seen in Fig 1 representing a two-level system with states $\psi_1(x_1), \psi_2(x_2)$) strongly interacting with a single-mode electromagnetic field $\phi(q)$ can be used to develop novel quantum applications when equipped with electrodes to provide a flexible configurability (Fig. 1). For instance, each quantum well can be seen as a qubit, and their entanglement can enable the realization and manipulation of an N-qubit entangled system. On the other hand, since the entanglement originates from the interaction with the electromagnetic field, it could be harnessed over large distances, enabling some type of quantum communications. In Fig. 2, we draw the mentioned polaritonic system coupled to a measuring apparatus represented by a degree of freedom y to measure both electron's energies. We study such measurement process within the Bohmian framework, which has shown that quantum phenomena can be consistently explained in terms of well-defined (ontologically determined) properties of physical systems [5], and enable multiscale modeling (Fig. 2) when the electromagentic field generated inside the quantum well needs to be coupled to the optical cavity for realistic self-consistent simulations.

CONCLUSIONS

We argue that this emerging phenomenon holds the potential to revolutionize electronics by naturally bridging electronics and photonics. Furthermore, it offers a new platform compatible with traditional electronics fabrication techniques for advancing quantum technologies.

ACKNOWLEDGMENTS

We acknowledge support from the Spain's Ministerio de Ciencia, Innovacion y Universidades under Grants PID2021-127840NB-I00 (MICINN/AEI/FEDER, UE) and PDC2023-145807-I00 (MICINN/AEI/FEDER, UE.

REFERENCES

[1] C. Ciuti, G. Bastard, and I. Carusotto, Phys. Rev. B, vol. 72, no. 11, p. 115303, Sep. 2005

[2] C. F. Destefani, M. Villani, X. Cartoixà, M. Feiginov, and X. Oriols, Phys. Rev. B, vol. 106, 2022

[3] A. A. Anappara et al., Phys. Rev. B, vol. 79, no. 20, p. 201303, May 2009

[4] M. Jeannin et al., ACS Photonics, vol. 6, no. 5, pp. 1207–1215, May 2019

[5] X. Oianguren-Asua, C. F. Destefani, M. Villani, D. K. Ferry, and X. Oriols, Springer International Publishing, 2024

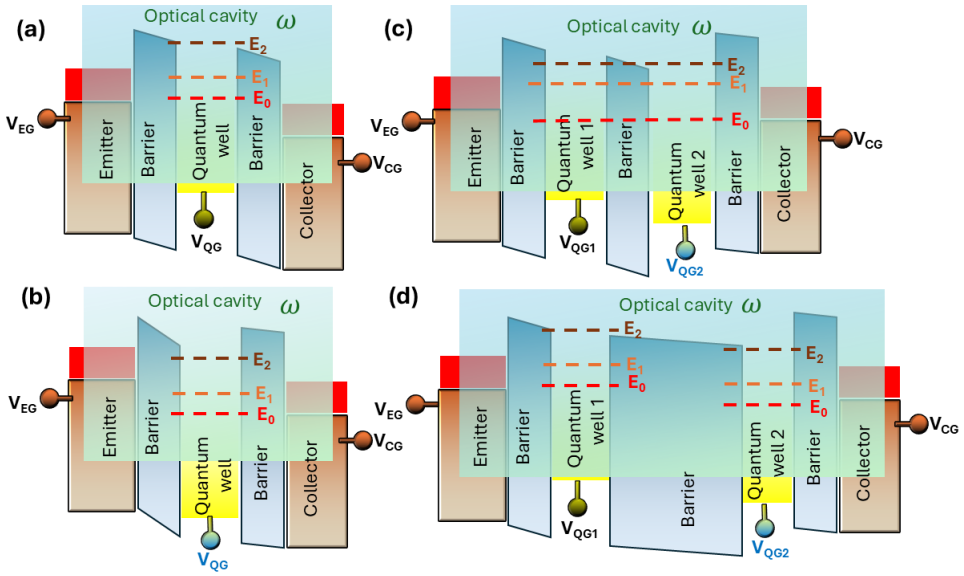

Fig. 1. Different realizations of the polaritonic semiconductor device. (a) and (b) show polaritonic devices with just one electron, whereas (c) and (d) show a two electron system. The quantum wells of system (c) are close enough so electrons can interact directly between them. The device in (d) has the central barrier width enough to prevent electron's direct coupling. In this case, the entanglement among them is due to their interaction with the electromagnetic field.

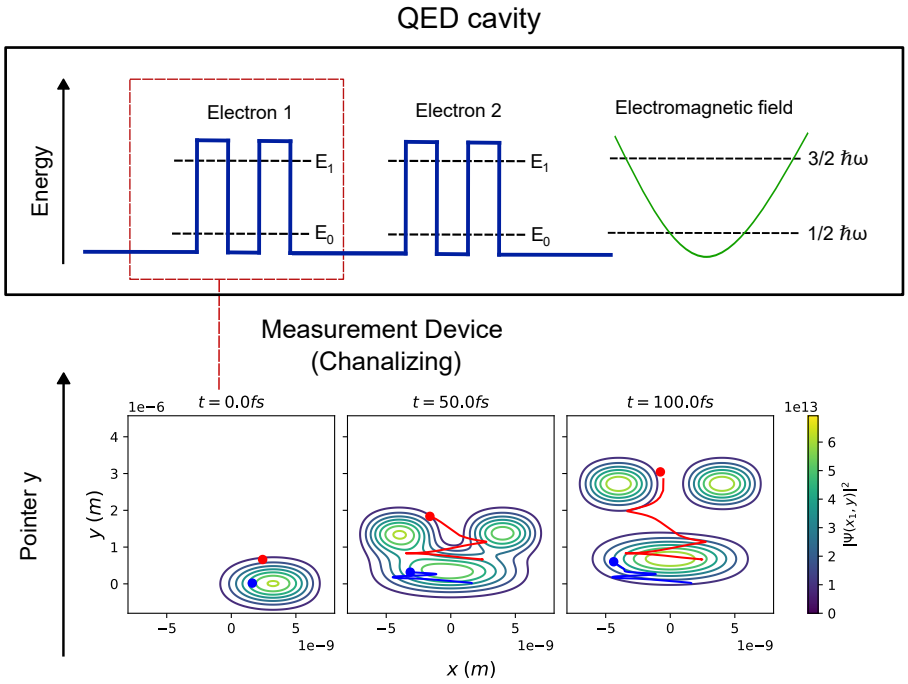

Fig. 2. Scheme of the polaritonic device model depicted in Fig 1(d) including a measuring apparatus. Two quantum wells, each containing a single electron with two discrete energy levels, are embedded within a larger "light" cavity that supports a single-mode electromagnetic field strongly coupled to the electrons. Additionally, a measuring device is coupled to the system, enabling the measurement of the electrons' energies. The measuring apparatus channalizes the system as shown in the bottom image. The evolution of the 2D wavefunction $\Psi(x, y)$ (contour plot) is represented together with Bohmian trajectories (solid lines) from two different experimental outcomes: the blue trajectory corresponds to a measurement in the ground state, while the red trajectory corresponds to a measurement in the excited state.